## QUANTUM LIQUIDS AND QUANTUM CRYSTALS

# Study of phase separation kinetics of $^3$He−$^4$He solid mixtures by precision pressure measurements

A. N. Ganshin, V. A. Maidanov, N. F. Omelaenko, A. A. Penzev, E. Ya. Rudavskii, and A. S. Rybalko

*B. Verkin Institute for Low Temperature Physics and Engineering, National Academy of Sciences of the Ukraine, 310164 Kharkov, Ukraine*[*)]

The kinetics of isotopic phase separation of $^3$He−$^4$He solid mixtures for various molar volumes has been studied by precision pressure measurements at a constant volume. It is found that the attainment of equilibrium between coexisting phases formed as a result of stratification is described correctly by an exponential dependence for various modes of crystal cooling and heating. The characteristic phase separation time decreases with temperature, thus confirming the athermal quantum nature of the growth of a new phase during the phase transition. The phase separation time is found to increase considerably with crystal pressure. It is shown that the prevailing theory can provide only a qualitative description of the established regularities. A quantitative description of experimentally observed decay times requires an analysis of diffusion processes in a gas of impurity excitations in the presence of a concentration gradient. © *1998 American Institute of Physics.* [S1063-777X(98)00109-1]

### INTRODUCTION

It is well known that the phase separation of dilute solid mixtures of $^3$He in $^4$He at quite low temperatures leads to the formation of clusters of the concentrated phase consisting almost entirely of pure $^3$He. In contrast to the phase separation in liquid $^3$He−$^4$He mixtures where the lighter concentrated phase floats in the gravity field, the clusters of $^3$He in solid mixtures are distributed all over the host matrix, and a unique interface does not exist. Under these conditions, the growth of the concentrated phase is mainly determined by diffusion processes in such a system.

Another distinguishing feature of $^3$He−$^4$He solid mixtures is that owing to a large amplitude of zero-point vibrations, the $^3$He impurity atoms are delocalized as a result of quantum tunneling and are transformed into quasiparticles (impuritons). For a low impurity concentration, we can treat them as a rarefied gas of quasiparticles moving practically freely over the entire crystal. This results in a special type of diffusion processes in $^3$He−$^4$He solid mixtures.

In spite of the fact that some aspects of the kinetics of isotopic phase separation of $^3$He−$^4$He solid mixtures have been studied for over 30 years,[1–12] the correlation between the growth kinetics for the concentrated phase and diffusion processes in the solid mixture has been established only recently.[13–15] It was shown that the characteristic phase separation time decreases with temperature, which means that the diffusion processes are not thermally activated. An agreement with the experimental results was attained under the assumption that the evolution of new phase clusters is determined by quantum diffusion[16] of delocalized impurity

excitations in the mixture. As expected, the process depends significantly on the concentration of $^3$He in the mixture.

A unique feature of helium crystals associated with their extremely high compressibility leads to another factor which may change the kinetic behavior of the system radically. It was shown experimentally in Ref. 17 that pressure is the factor responsible for such a behavior. Since the exchange energy of the pair of atoms $^3$He and $^4$He (nearest neighbors) decreases sharply with increasing pressure, an increase in pressure at a constant concentration suppresses quantum diffusion of $^3$He quasiparticles and leads to their localization.

This circumstance affects the kinetics of isotopic phase separation. The present publication marks the beginning of systematic experimental studies of the effect of pressure on growth kinetics of the concentrated phase through precision measurements of pressure during isotopic phase separation of $^3$He−$^4$He solid mixtures at a constant volume.

### EXPERIMENTAL TECHNIQUE

We studied a mixture with initial concentration 2.04 at. % $^3$He. The crystalline sample was grown by capillary blocking method. Samples were annealed at a temperature near the melting point for two days to improve the quality of the crystal, which was estimated from the reproducibility of the temperature dependence of pressure in the single-phase region before phase separation as a result of multiple cooling. The experimental cell is shown schematically in Fig. 1. The sample was taken in the form of a flat cylinder of diameter 9 mm and height 1.5 mm to facilitate cooling of the crystal. The coupling between the measuring cell and the
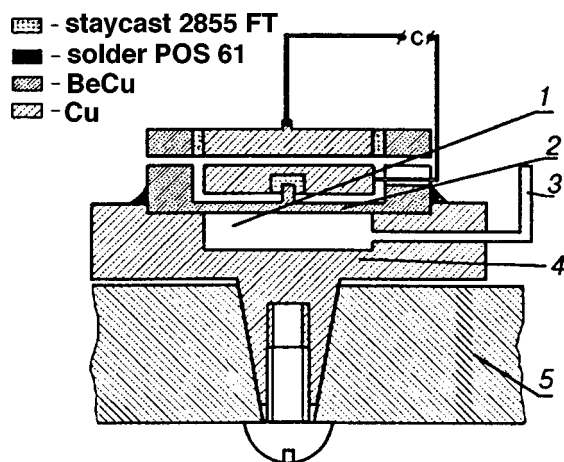
FIG. 1. Schematic diagram of the experimental cell: sample (*1*), membrane of capacitive pressure gauge (*2*), inlet capillary tube (*3*), body of the cell (*4*), dilution chamber plate (*5*).

dilution chamber was ensured through a detachable conic thermal contact.[18] We did not use a sintered heat exchanger in the measuring cell since fine pores may considerably affect the phase separation process.[19]

The thermal relaxation time for the sample associated with its finite thermal resistance is estimated at ~1 s, while the relaxation time associated with Kapitza resistance is estimated as 25–50 s.

Ultralow temperatures were attained by using a new indigenous powerful $^3$He–$^4$He dilution refrigerator distinguished by outer circulation of $^3$He forced by a mechanical pump NVPR–16, as well as by cryogenic circulation created by two adsorption pumps. The dual circulation system enables a rapid attainment of the desired temperature with the help of two adsorption pumps, which can then be maintained just by the mechanical pump. Such a working cycle considerably decreases the consumption of helium in the outer bath. The minimum temperature attained by cooling with an empty experimental cell (without heat leakage through the filling capillary) was 4.2 mK.

The sample temperature was measured by a melting curve thermometer[20] mounted on the dilution chamber plate. The temperature resolution of the thermometer was 0.3 mK. Several resistance thermometers were also used at the same time, and their readings were recorded by using an a.c. cryobridge R441 and a specially designed digital a.c. bridge with a power dissipation below $10^{-15}$ W.[21] Temperature was stabilized by a heater which was mounted on the dilution chamber plate and connected to the outlet circuit of the digital bridge.

The phase transition was studied by cooling the sample in the phase separation region in small steps with temperature stabilization at each step. In some cases, cooling in a single large step was carried out for comparison.

Isotopic phase separation kinetics was studied by recording the pressure variation in the sample. For this purpose, we used a Straty–Adams pressure gauge in which one of the experimental cell walls served as the mobile membrane (Fig. 1). The pressure variation in the sample was recorded by using an a.c. bridge General Radio 1615-A. In the entire
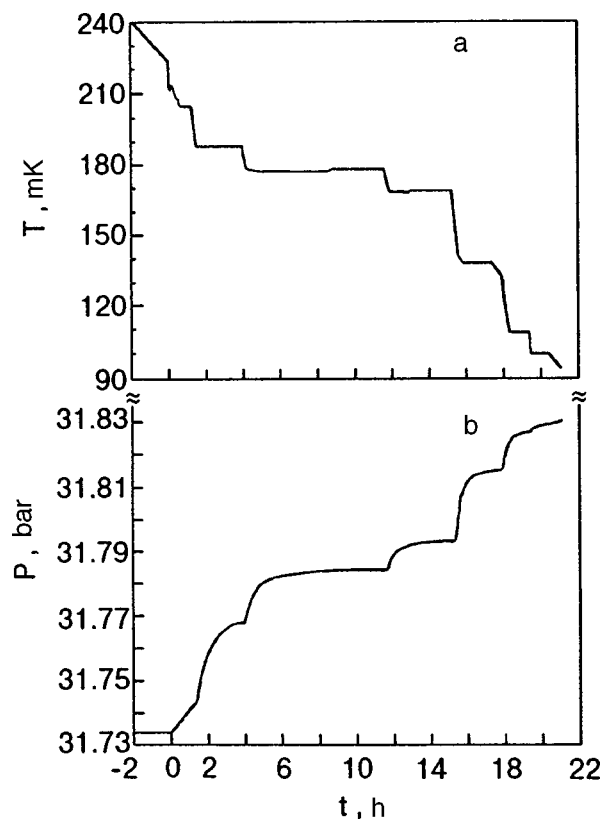


FIG. 2. Cooling kinetics of sample *3* (a) and the corresponding dependence of crystal pressure on time (b) (molar volume 20.54 cm³/mole).

working pressure range, the pressure gage has a resolution better than 8 Pa.

## COOLING THERMOGRAMS AND KINETICS OF PRESSURE VARIATION

After growth and annealing, the samples were cooled to a temperature close to the phase separation point $T_s$ at a rate of $34\pm10$ mK/h. Below ~400 mK, the pressure in the crystal practically did not change right down to the temperature $T_s$, at which a sharp increase in pressure indicating the phase transition was observed. Subsequent cooling of the sample in the phase separation region was carried out in small steps followed by temperature stabilization. Figure 2 shows a typical cooling thermogram of the sample in the phase separation region, as well as the corresponding pressure variation in the crystal reflecting the growth kinetics for the concentrated phase.

In each step, the equilibrium state between the coexisting phases was established after a certain time $\tau$, characterizing the attainment of a plateau. The value of this time decreases as we go over to steps at lower temperatures. Such a behavior was also observed in NMR experiments.[12,13]

Some samples were studied in the phase separation region during cooling, as well as during subsequent warming (also in small temperature steps) right up to transition of the decomposed mixture into a homogeneous state. Such a thermogram and the corresponding temperature variation are shown in Fig. 3. It can be seen that there is no significant difference in the pressure jump during phase separation and
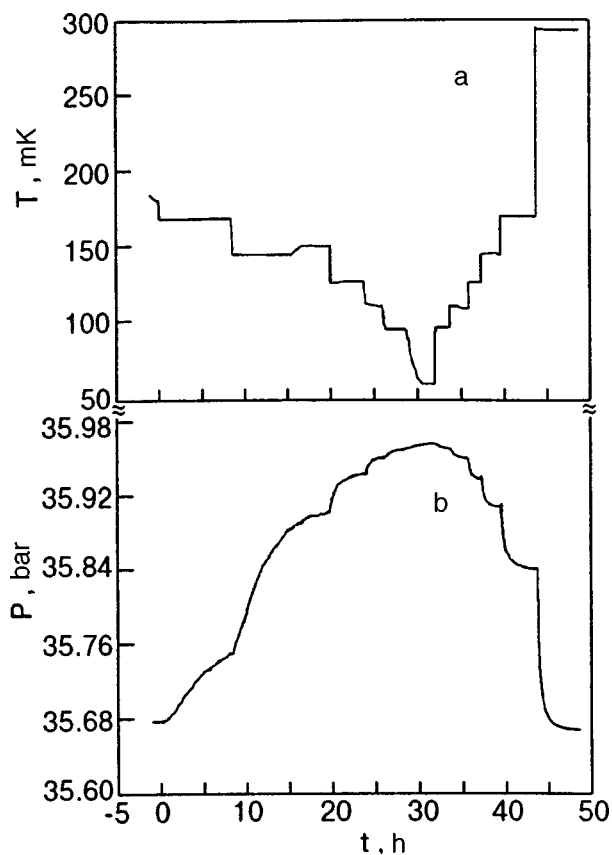
FIG. 3. Kinetics of cooling followed by warming of sample 8(a) and the corresponding time dependence of the variation of crystal pressure (b) (molar volume 20.28 cm$^3$/mole).

closed volume. After this, the pressure in the cell was lowered or increased by using a vaporizer filled with an identical mixture. The newly formed crystal was then subjected to annealing once again in order to eliminate possible heterogeneities and stresses. For comparison, some crystals were investigated before and after annealing.

Table I also shows the phase separation temperatures $T_s$ recorded at the instant of pressure variation during cooling of the crystal. Note that the phase transition in samples grown without preliminary annealing begins at higher temperatures than in properly annealed samples. The highest values of $T_s$ were obtained during cooling of the samples after a transition from a two-component system into a homogeneous mixture. This points towards the existence of metastable phase regions, which is a characteristic feature of first-order phase transitions.

## CHARACTERISTIC PHASE SEPARATION TIME DURING STEPWISE COOLING. COMPARISON WITH THEORY

In order to describe qualitatively the kinetics of the isotopic phase separation, the time variation of pressure for the $n$th step was approximated by the exponential dependence

$$P_n = P_{n0} \pm A \exp(-t/\tau), \tag{1}$$

where the minus sign corresponds to cooling and the plus sign to heating, $\tau$ is the characteristic time determining the kinetics of decomposition or homogenization within one step, the parameter $P_{n0}$ corresponds to the final equilibrium pressure for each step, and parameter $A$ to the difference in final and initial pressures.

The obtained experimental data are described quite well by formula (1), as shown in Fig. 4 on a magnified scale for the case of cooling of a two-phase mixture within one temperature step. Approximation was carried out by the method of least squares, and Table II contains the values of parameters obtained for each crystal.

homogenization in a single temperature step (irrespective of its variation) and over the entire pressure variation during multiple stratification followed by homogenization.

Table I shows the basic characteristics of the investigated samples. A transition from one sample to another was carried out by heating the crystal up to the melting point in a

TABLE I. Characteristics of investigated samples.

| Sample No. | Pressure at $T = T_s$, bar | Molar volume, cm$^3$/mol | $T_s$, mK | Type of cooling | Remark |
|---|---|---|---|---|---|
| 1 | 31.66 | 20.54 | 180 | Rapid (1 step) | Annealing for 3 days; cooling and heating |
| 2 | 31.72 | 20.54 | 216 | Rapid (2 steps) | Cooling after homogenization of sample 1 and repeated heating |
| 3 | 31.73 | 20.54 | 215 | Step-wise | Step-wise cooling after homogenization of sample 2 |
| 4 | 30.18 | 20.64 | 202 | Rapid | Without preliminary annealing; cooling and heating |
| 5 | 35.61 | 20.29 | 207 | Rapid | Without preliminary annealing; cooling and heating |
| 6 | 35.61 | 20.29 | 221 | Rapid | After homogenization of sample 5; cooling and heating |
| 7 | 31.28 | 20.56 | 200 | Rapid | Without preliminary annealing; cooling |
| 8 | 35.67 | 20.28 | 194 | Step-wise | Annealing for 1.5 days; cooling and heating |
| 9 | 35.67 | 20.28 | 220 | Rapid | After homogenization of sample 8; cooling and heating |
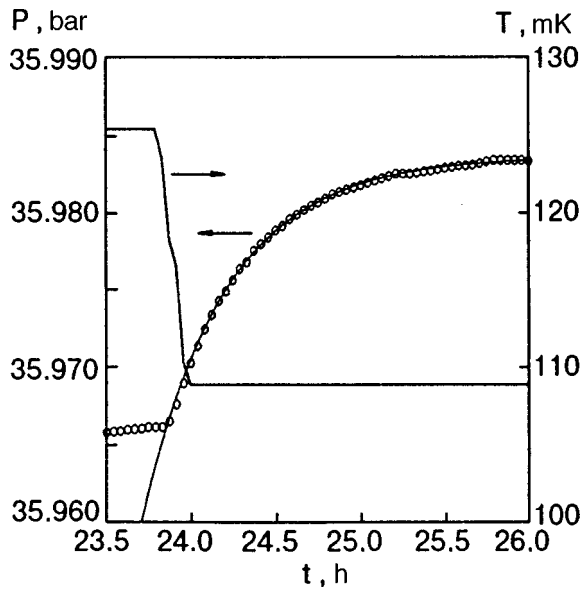
FIG. 4. Variation of crystal pressure as a result of cooling within a step ($T_i = 100$ mK, $T_f = 99$ mK). Circles correspond to the experimental measurements and the solid curve to formula (1).
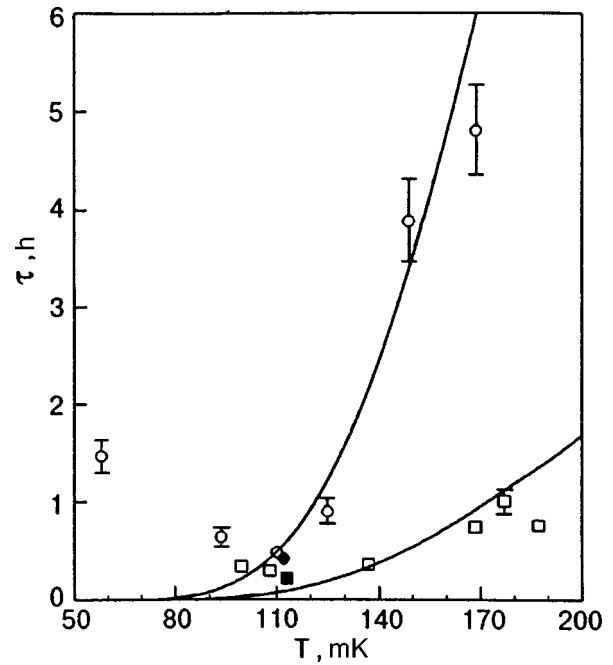


FIG. 5. Temperature dependence of the characteristic isotopic phase separation time for different molar volumes: 20.54 cm$^3$/mole (circles), 20.28 cm$^3$/mole (squares). Dark symbols correspond to cooling in one step, and the solid curves to calculations using formula (2).

Figure 5 shows the temperature dependence of the isotopic phase separation times $\tau$ obtained in this way. As expected, the isotopic phase separation is considerably slowed down upon an increase in pressure (decrease in molar volume). Upon a change in temperature in the course of phase separation, the concentration of the dilute phase changes in conformity with the equilibrium phase diagram[22] defining the concentration dependence of the time $\tau$ which is found to be nearly linear and in accord with the results presented in Ref. 13.

It should be remarked that, according to rough estimates, the heat of phase transition[11] liberated during isotopic phase separation does not alter the kinetics of the process

significantly. We assume that the rate of liberation of heat of phase transition is determined by the growth of the new phase in accordance with formula (1) and that the Kapitza resistance is the bottleneck in the process of heat removal. It then follows from the heat balance equation that on account of the liberation of heat of phase transition, the time dependence of the sample temperature has a small peak of about 2.5 mK as a result of abrupt cooling and about 0.5 mK during stepwise cooling. This peak corresponds to the first minutes of phase separation, when the sample temperature has not attained stabilization. After the peak, the sample temperature levels out according to an exponential law.

The experimental data shown in Fig. 5 can be compared with the recently developed theory[14] describing the mobility of interface in a quantum crystal. According to the authors of this theory,[14] the experimentally observed growth of the new phase is associated with the movement of the interphase boundary. The characteristic time of phase separation was calculated from the interface velocity for the case when the temperature step $\Delta T$ is much smaller than the temperature $T$:

$$\tau = \frac{\pi\sqrt{2}}{6x_0 d}\frac{aR_0}{D_0}\left(\frac{T_c}{T}\right)^3 \exp\left(-\frac{2T_c}{T}\right), \tag{2}$$

where $x_0$ is the concentration of the decomposed mixture, $a$ the separation between atoms. $d$ the dimensionality of clusters of the concentrated phase, $T_c$ the critical temperature of phase separation, and $R_0$ the cluster size which is equal to the radius of a sphere for $d=3$ (spherical clusters), radius of a cylinder for $d=1$ (cylindrical clusters), and half the plate thickness for $d=2$ (flat clusters). The parameter $D_0$, which depends on pressure, appears in the expression for the diffusion coefficient:

TABLE II. Parameters characterizing phase separation.

| Sample No. | Initial and final $T$ of a step, mK | $P_{n0}$, bar | $\tau$, h | Final equilibrium concentration, % $^3$He |
|---|---|---|---|---|
|   | 216–188 | 31.768 | 0.76 | 1.0 |
|   | 188–177 | 31.784 | 1.07 | 0.76 |
| 3 | 177–168 | 31.793 | 0.74 | 0.6 |
|   | 168–139 | 31.814 | 0.40 | 0.2 |
|   | 139–110 | 31.827 | 0.27 | 0.04 |
|   | 110–100 | 31.829 | 0.37 | 0.017 |
|   | 194–169 | 35.772 | 5.07 | 0.67 |
|   | 169–148 | 35.910 | 3.69 | 0.28 |
|   | 148–125 | 35.942 | 0.90 | 0.11 |
|   | 125–110 | 35.959 | 0.42 | 0.04 |
|   | 110–99 | 35.967 | 0.65 | 0.02 |
| 8 | 99–62 | 35.974 | 1.20 | 0.0002 |
|   | 62–95 | 35.968 | 0.73 | 0.015 |
|   | 95–107 | 35.958 | 0.54 | 0.035 |
|   | 107–124 | 35.937 | 0.33 | 0.11 |
|   | 124–143 | 35.907 | 0.37 | 0.26 |
|   | 143–169 | 35.842 | 0.67 | 0.7 |
|   | 169–294 | 35.672 | 0.61 | 2.0 |

$$D(x) = \frac{D_0}{x} \left( \frac{x_c - x}{x_c} \right)^\nu, \qquad (3)$$

which follows from the theory[23] and was confirmed by NMR measurements of the coefficient of quantum spin diffusion in solid mixtures containing 0.12–4.98% $^3$He in the range 19.9–20.7 cm$^3$/mole of molar volumes.[24] The quantity $x_c$ in formula (3) corresponds to the critical concentration marking the suppression of the band motion of impuritons which leads to quantum diffusion, and the onset of localization of $^3$He quasiparticles. It has been shown in experiments[24] that the value of $x_c$ increases with molar volume and amounts to 3.2–7.0% $^3$He depending on pressure variation, the critical exponent $\nu$ being 1.7±0.3 everywhere.

A comparison of the experimental data with formula (2) shows that the theory[14] can describe qualitatively the temperature dependence of $\tau$. The solid curves in Fig. 5 were obtained by calculations according to formula (2) for both molar volumes. The quantity $R_0/D_0 d$, which is equal to $4.9 \times 10^{11}$ s/cm for $V = 20.28$ cm$^3$/mole and $9.8 \times 10^{10}$ s/cm for $V = 20.54$ cm$^3$/mole was chosen as the fitting parameter. Assuming that the radius of the spherical cluster $R_0 = 2 \times 10^{-4}$ cm for $d = 3,$[5,9,25] the obtained values of the fitting parameter correspond to the value $D_0 \sim 10^{15}$ cm$^2$/s. This is about three orders of magnitude lower than the analogous values of the constant obtained from NMR measurements of the spin diffusion coefficient $D(x)$[24] for the corresponding values of the molar volume.

Note that at temperatures below ~110 mK, the time $\tau$ remains practically unchanged upon a decrease in temperature. In some cases, even a slight increase in the decay time was observed. Theory[14] does not predict such a low-temperature dependence.

The pressure dependence of the phase decay time $\tau$ is found to be only in qualitative agreement with the theory[14] (see Fig. 5). Apparently, the quantitative disagreement is associated with the fact that the value of the parameter $D_0$ appearing in formula (2) should not be taken from the NMR measurements. This means that the growth of the new phase in the process of isotopic phase separation is determined by the diffusive process occurring under conditions different from those of the NMR experiment. It would probably be appropriate to use the coefficient of heterodiffusion occurring in a two-phase solid mixture in the presence of a concentration gradient. It was mentioned by Antsygina *et al.*[15] that strong elastic stresses may appear at the interface between coexisting phases due to different crystal structures and molar volumes of these phases. Under such conditions, the diffusion coefficient must also vary significantly. Unfortunately, these aspects of the quantum crystal mixtures have not been subjected to theoretical or experimental investigation so far.

### PHASE SEPARATION UNDER RAPID COOLING

Figure 6 shows an example of pressure variation upon a rapid cooling of the sample following its thermal cycling (one large step) and subsequent heating to the homogeneous state. The asymmetry in the pressure variation upon cooling
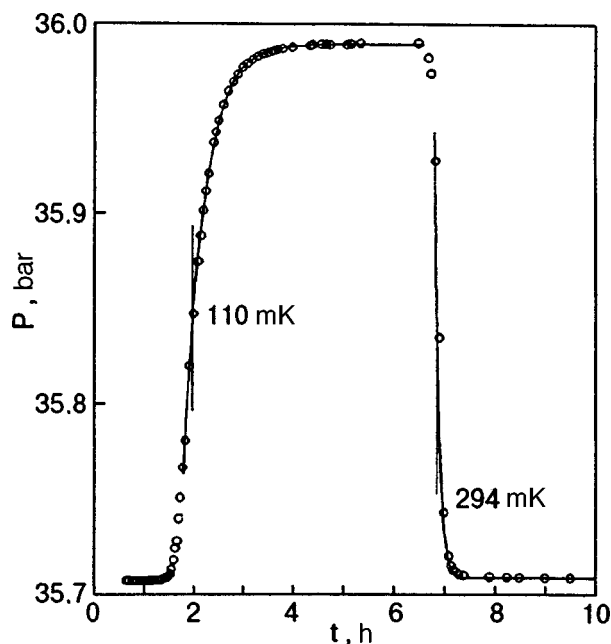


FIG. 6. Change in the crystal pressure during a one-step cooling and warming of sample 9 (molar volume 20.28 cm$^3$/mole). The solid curve corresponds to calculations based on formula (1).

and heating can be clearly seen in this case. Note that a similar asymmetry is also observed during stepwise cooling and heating (Fig. 3).

An analysis of the kinetics of pressure variation during the isotopic phase separation shown in Fig. 6 indicates that the attainment of equilibrium between coexisting phases is described correctly by a single exponential dependence. Table III shows the corresponding values of the characteristic phase separation time $\tau$ for this as well as other samples. The characteristic time $\tau^*$ corresponding to the reverse transition from a dissociated two-phase mixture to the homo-

TABLE III. One-step cooling and warming of samples.

| Sample No. | Initial and final temperature of step | Separation time, h | | Remark |
|---|---|---|---|---|
| | | $\tau^*$, during cooling | $\tau$, during heating | |
| 1 | 184–113 | 0.33 | | After annealing for 3 days |
| 2 | 216–198 | 0.76 | | After sample homogenization |
| | 198–103 | 0.20 | | |
| 5 | 207–112.5 | 0.64 | | Without annealing |
| | 112.5–300 | | 0.10 | |
| 6 | 84–300 | | 0.12 | Values of $\tau$ measured only during heating |
| 7 | 200–115 | 0.30 | | Without annealing |
| 9 | 230–110 | 0.42 | | After homogenization of sample 8 |
| | 110–296 | | 0.11 | |

geneous single-phase state is also given in the Table. It can be seen that $\tau^*$ is always much smaller than $\tau$.

The values of the phase separation time under rapid cooling are also shown in Fig. 5 where they can be compared with the corresponding values obtained during stepwise cooling. Experiments show that the values of $\tau$ coincide in both cases for the same value of the final temperature.

Some of the investigated samples were subjected to isotopic phase separation without preliminary annealing. In this case, the phase separation time was found to be much longer than for samples after annealing.

Note that phase transition under conditions of rapid cooling or heating always occurs under conditions of a large concentration gradient which, in addition, varies rapidly in time. Apparently, this circumstance must affect significantly the process of transport of $^3$He from the surrounding mixture to the clusters of the concentrated phase. Assuming that such a transport is only diffusive in nature, we can estimate, the diffusion coefficient for a phase separation with characteristic time $\tau$.

Suppose that stable clusters of the concentrated bcc phase with a mean radius $2 \times 10^{-4}$ cm are formed in an hcp mixture containing $x = 2.04\%$ $^3$He for a molar volume 20.28 cm$^3$/mole. In this case, the mean cluster density can be defined as

$$n = \frac{3x}{4\pi R^3} \frac{V_c}{V_d}, \tag{4}$$

where $V_c$ and $V_d$ are the molar volumes of the concentrated and dilute phase respectively. Assuming half the mean separation between clusters $l = n^{-1/3}$ as the diffusion length, we can write the effective diffusion coefficient in the form

$$D_{\text{eff}} = \left(\frac{\pi V_d}{6 V_c}\right)^{2/3} \frac{R^2}{\tau x^{2/3}}. \tag{5}$$

Using this equation, we can estimate the value $D_{\text{eff}} \sim 10^{10}$ cm$^2$/s, which is about an order of magnitude higher than the diffusion coefficient measured by the NMR method in the solid mixture $^3$He–$^4$He.[24] This also indicates that the quantum diffusion of impuritons during phase separation may occur in a different manner than in NMR experiments with a homogeneous mixture.

Transport of $^3$He atoms may occur diffusively as well as through hydrodynamic flow of $^3$He quasiparticles. These questions also require additional experimental and theoretical studies.

*)E-mail: rudavskii@ilt.kharkov.ua

[1] D. O. Edvards, A. S. McWilliams, and J. G. Daunt, Phys. Rev. Lett. **9**, 195 (1962).

[2] M. F. Panczyk, R. A. Scribner, J. R. Gorano, and E. D. Adams, Phys. Rev. Lett. **21**, 594 (1968).

[3] W. J. Mullin, Phys. Rev. Lett. **20**, 254 (1968).

[4] P. N. Henriksen, M. F. Panczyk, and E. D. Adams, Solid State Commun. **8**, 735 (1970).

[5] A. S. Greenberg, W. C. Thomlinson, and R. C. Richardson, J. Low Temp. Phys. **8**, 3 (1972).

[6] M. Uwaha, J. Phys. Soc. Jpn. **48**, 1921 (1980).

[7] I. Iwasa and H. Suzuki, Proc. LT-17, North Holland Phys. Publ. **1**, 531 (1984).

[8] V. A. Mikheev, V. A. Maidanov, and N. P. Mikhin, Fiz. Nizk. Temp. **12**, 658 (1986) [Sov. J. Low Temp. Phys. **12**, 375 (1986)].

[9] V. A. Mikheev, V. A. Maidanov, N. P. Mikhin *et al.*, Fiz. Nizk. Temp. **14**, 563 (1988) [Sov. J. Low Temp. Phys. **14**, 309 (1988)].

[10] V. A. Mikheev, A. A. Golub', V. A. Goncharov *et al.*, Fiz. Nizk. Temp. **15**, 540 (1989) [Sov. J. Low Temp. Phys. **15**, 304 (1989)].

[11] R. Schrenk, O. Friz, Y. Fujii *et al.*, J. Low Temp. Phys. **84**, 133 (1991).

[12] S. C. J. Kingsley, I. Kosarev, L. Roobol *et al.*, J. Low Temp. Phys. **110**, 359 (1998).

[13] V. A. Shvarts, N. P. Mikhin, E. Ya. Rudavskii *et al.*, Fiz. Nizk. Temp. **21**, 717 (1995) [Low Temp. Phys. **21**, 556 (1995)].

[14] T. N. Antsygina, V. A. Slusarev, and K. A. Chishko, Fiz. Tverd. Tela (St. Petersburg) **38**, 1906 (1996) [Phys. Solid State **38**, 1062 (1996)].

[15] T. N. Antsygina, K. A. Chishko, N. P. Mikhin *et al.*, J. Low Temp. Phys. **111**, 19 (1998).

[16] V. N. Grivor'ev, B. N. Esel'son, V. A. Mikheev, and Yu. E. Shulman, Pis'ma Zh. Éksp. Teor. Fiz. **17**, 25 (1973) [JETP Lett. **17**, 16 (1973)]; V. N. Grivor'ev, Fiz. Nizk. Temp. **23**, 5 (1997) [Low Temp. Phys. **23**, 1 (1997)].

[17] V. A. Mikheev, V. A. Maidanov, and N. P. Mikhin, in *Abstracts of Papers to the 23rd Conf. Low Temp. Phys.*, Tartu, (1984).

[18] A. S. Rybalko and M. B. Sterin, Fiz. Nizk. Temp. **22**, 1095 (1996) [Low Temp. Phys. **22**, 837 (1996)].

[19] D. N. Bittner and E. D. Adams, Low Temp. Phys. **97**, 519 (1994).

[20] G. Schuster, A. Hoffmann, and D. Hechtfischer, Vol. **19**, doc. CCT/96-25, Bureau International des Poids et Mesures, St. Vres, France (1996).

[21] G. A. Mikhailov, in *Proceedings 14th Int. Cryogen. Engg. Conf. and Int. Cryogen. Mater. Conf.*, Kiev (1992).

[22] V. A. Shvarts, N. P. Mikhin, E. Ya. Rudavskii *et al.*, Fiz. Nizk. Temp. **20**, 645 (1994) [Low Temp. Phys. **20**, 505 (1994)].

[23] Yu. Kagan and L. A. Maksimov, Phys. Lett. A **95**, 242 (1983).

[24] V. A. Mikheev, N. P. Mikhin, and V. A. Maidanov, Fiz. Nizk. Temp. **9**, 901 (1983) [Sov. J. Low Temp. Phys. **9**, 465 (1983)].

[25] A. E. Burgess and M. J. Crooks, Phys. Lett. **A39**, 183 (1972).

Translated by R. S. Wadhwa

## SUPERCONDUCTIVITY, HIGH-TEMPERATURE SUPERCONDUCTIVITY

# Mixed state stability range in a YBaCuO single crystal

K. I. Kugel' and A. L. Rakhmanov

*Scientific Center for Applied Problems in Electrodynamics, Russian Academy of Sciences, 127412 Moscow, Russia*

L. G. Mamsurova and K. S. Pigal'skiǐ

*N. N. Semenov Institute of Chemical Physics, Russian Academy of Sciences, 117977 Moscow, Russia**
(Submitted February 2, 1998; revised April 6, 1998)
Fiz. Nizk. Temp. **24**, 823–831 (September 1998)

The range of applied magnetic field $H$ corresponding to the stability of mixed state with a fixed magnetic induction $B$ is determined for a high-$T_c$ superconducting $YBa_2Cu_3O_x$ single crystal for $H \perp c$-axis. For this purpose, the field dependences of the contribution $\mu_v$ to the dynamic magnetic permeability $\mu'_{ac}$ are analyzed for the hysteresis loops $\mu_v(H)$ in the temperature range from 70 to 84 K. It is shown that the $\mu_v(H)$ hysteresis can be interpreted in terms of the interaction between the vortex lattice and the surface and is associated with the $B(H)$ hysteresis as a manifestation of the Bean–Livingston surface barrier. As a result, the $\mu_v(H)$ hysteresis loops corresponding to different temperatures can be described by a universal curve in dimensionless coordinates. The obtained estimates and the available experimental data reveal a significant suppression of the surface barrier in actual YBaCuO single crystals as compared to the barrier predicted for a perfect surface. The lower branch of the $\mu_v(H)$ hysteresis loop, which corresponds to increasing $H$, is found to be close to the equilibrium $\mu_v(H)$ curve, and the surface barrier appreciably affects the behavior of $\mu_v(H)$ only for decreasing field, i.e., the emergence of magnetic vortices from the sample surface. © *1998 American Institute of Physics.* [S1063-777X(98)00209-6]

### INTRODUCTION

Abrikosov's vortices interact with the surface of a superconductor. One of the results of this interaction is the emergence of a surface (Bean–Livingston)[1] barrier hampering free vortices entering or emerging from the sample surface. For example, when the applied magnetic field $H$ increases from zero, the magnetic flux starts entering the sample with a perfect surface when the value of $H$ becomes equal to the thermodynamic critical field $H_c$ (rather than the lower critical field $H_{c1}$ as in the absence of the Bean–Livingston surface barrier).

However, an analysis of a large number of available data suggests to a high confidence level that the Bean–Livingston barrier in high-$T_c$ superconductors (HTSC) is noticeably lower than predicted for a perfect surface. Nevertheless, this fact is not trivial since the value of $H_c$ in HTSC is much higher than $H_{c1}$ in view of a considerable value of the Ginzburg–Landau parameter $\kappa \simeq 100$. For this reason, strong local fields associated with the roughness of the surface can suppress the surface barrier by not more than 10–20% of its value for a perfect surface according to estimates.[2] Some authors attribute the barrier suppression effect to the presence of surface defects (see, for example, Ref. 3). However, quantitative estimates concerning this problem have not been obtained as yet.

In this connection, an analysis of effects associated with peculiarities in the behavior of vortex lattice near the superconductor surface is of special importance. One of such phenomena (which is very sensitive to the structure and dynamics of surface vortices) is the magnetic hysteresis of dynamic magnetic permeability.

This effect was observed for $YBa_2Cu_3O_x$ single crystals and studied by a number of authors[4–7] who investigated the response of HTSC to an ac magnetic field of low frequency ($\omega/2\pi = 3$ kHz) and small amplitude ($h < 10$ Oe) in the presence of a constant parallel magnetic field $H$. In these publications, the real component of the fundamental harmonic $\mu'_{ac}$ of the complex magnetic permeability $\mu^*_{ac}$ is the object under investigation. The quantity $\mu'_{ac}$ is defined as a coefficient in the Fourier expansion of the volume-averaged magnetic induction $B(t)$ varying periodically with time. In a magnetic field $H(t) = H + h \sin(\omega t)$, we can write the following expression for $\mu'_{ac}$ (which will be henceforth referred to as permeability $\mu$ for the sake of brevity):

$$\mu = \frac{1}{2\pi h} \int_0^{2\pi/\omega} \cos(\omega t) \frac{dB}{dt} dt. \tag{1}$$

It was proved in Ref. 4 that the change in the magnetic induction in the sample due to the varying component of the

magnetic field (and hence permeability) can be represented as the sum of two terms. The first term $\mu_m$ associated with Meissner's current oscillations is defined as

$$\mu_m = 2\lambda/D, \tag{2}$$

where $\lambda$ is the London penetration depth and $D$ the sample thickness in the direction perpendicular to the magnetic field. The second term $\mu_v$ is associated with displacements of vortices in the superconductor. For large values of the amplitude $h$ of the ac magnetic field, vortices get separated from pinning centers and can enter and leave the sample. For small $h$, vortices perform small vibrations near equilibrium positions, their total number in the volume remaining unchanged. The vibrational contribution $\mu_v$ is due to a strong dependence of the surface flow of vortices on their position relative to the surface. The analysis carried out in Refs. 4–7 revealed that it is the contribution from vortex vibration that determines the hysteresis loop in the magnetic permeability of YBaCuO appearing upon a cyclic variation of the constant field $H$. It was found that all the changes occurring in $\mu_v$ during the application or removal of the field are completely determined by the variation of distance $x_1$ between the first row of vortices and the surface. The shape of the $\mu_v(x_1)$ curve was also determined. However, the origin of the hysteresis loop in the vibrational contribution $\mu_v(H)$ (i.e., the reason for which the hysteresis of $x_1(H)$ takes place) has not been clarified completely.

In this publication, we analyze this effect in terms of interaction between the vortex lattice and the surface and derive an analytic expression connecting the contribution $\mu_v$ to dynamic permeability from the vibrations of vortices with the induction of the vortex lattice in the surface layer of a single crystal.

It will be proved that a comparison of the theoretical curves with the experimentally obtained hysteresis loops of $\mu_v(H)$ makes it possible to reconstruct the range of the applied magnetic fields $[H_{\max}(B) - H_{\min}(B)]$ in which the mixed state with a fixed value of magnetic induction can exist. This allows us to estimate the height of the surface barrier in actual HTSC single crystals and compare it with the value for a perfect surface.

## EXPERIMENT

Permeability measurements on $YBa_2Cu_3O_x$ single crystals in the temperature range 70–84 K were made with the help of an ac bridge by using the technique described in detail in Ref. 4. The constant field $H$ (varying from 0 to 1 kOe) was applied parallel to the ac field of amplitude $h$ (0.1–10 Oe) and frequency 3 kHz. The $c$-axis of a $YBa_2Cu_3O_x$ single crystal ($T_c = 92$ K) having the shape of a $1.18 \times 1.26 \times 1.67$ mm parallelepiped was oriented at right angles to the field $H$ ($H \perp c$). In order to measure the field dependences of permeability, the bridge was balanced at the minimum ac field amplitude after sample cooling to $T < T_c$ in zero constant magnetic field. The real component of the first harmonic was determined from the disbalance voltage induced as a result of application of the field $H$ by using a selective amplifier and a phase detector. The signal obtained
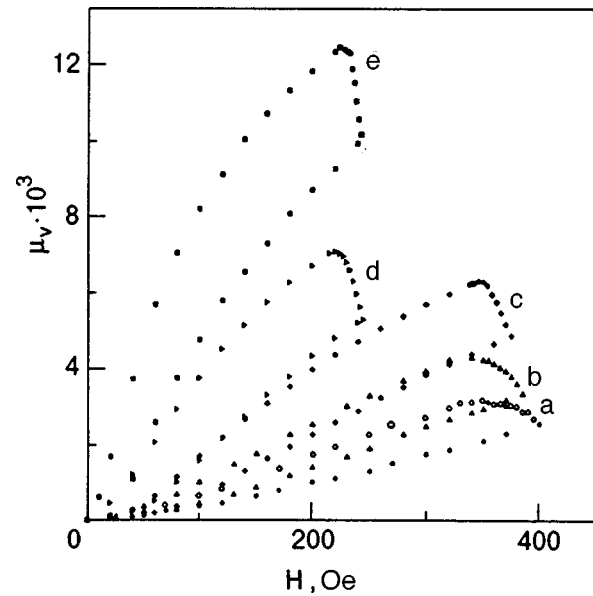


FIG. 1. Field dependences of the vibrational contribution to dynamic permeability $\mu_v$ of a $YBa_2Cu_3O_x$ single crystal at different temperatures $T$, K: 70 (a), 73.4 (b), 77.3 (c), 80 (d), and 83.8 (e). Lower branches of the hysteresis loops correspond to field application and the upper branches to field removal.

in this way is proportional to the real component $\mu'_{ac}$ of the complex permeability. This technique, which ensures complete compensation of the diamagnetic signal associated with sample shielding by Meissner surface currents, makes it possible to detect relatively weak effects associated with vortex dynamics in the surface layer at the ac magnetic field penetration depth.

The magnitude of the sought vibrational contribution $\mu_v$ (which is independent of amplitude) was determined for each value of the constant field $H$ during its increase as well as decrease by extrapolating the experimental curve $\mu'_{ac}(h)$ to zero amplitude according to the procedure described in detail in Ref. 4.

Figure 1 shows the $\mu_v(H)$ hysteresis loops obtained for a $YBa_2Cu_3O_x$ single crystal at temperatures varying from 70 to 84 K. It can be seen that the vibrational contribution $\mu_v$ to dynamic permeability increases noticeably with temperature, the width of the hysteresis loop varying insignificantly. It can also be noted that the width of segments formed upon a transition from one hysteresis branch to the other upon a change in the direction of field sweep becomes considerably smaller (from ~50 to ~15 Oe) upon heating.

In the case when the effects under investigation can be described in terms of interaction of vortices with one another and with the sample surface, and the pinning of vortices and their thermal activation are insignificant, it is convenient to use dimensionless units introduced in the London or the Ginzburg–Landau theory. In this case, with an ''appropriate'' normalization from the physical point of view, we can expect that the magnetic field dependences $\mu_v(H)$ measured at different temperatures behave similarly. We measure length in the units of $\lambda$ and the magnetic field in the units of $H_{c1} = (\varphi_0/4\pi\lambda^2) \times (\ln \kappa + 0.5)$, where $\varphi_0$ is the magnetic flux quantum. For the corresponding normalization of the
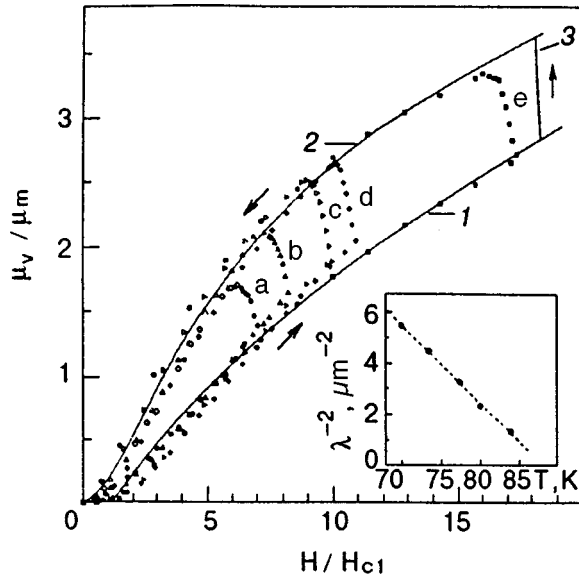
FIG. 2. Normalized field dependences of the vibrational contribution to dynamic permeability $\mu_v$ of a YBa$_2$Cu$_3$O$_x$ single crystal at different temperatures $T$, K: 70 (a), 73.4 (b), 77.3 (c), 80 (d), and 83.8 (e). The symbols correspond to the experimental data. Solid curve *1* corresponds to calculations for a thermodynamically equilibrium state, *2* to averaged $\mu_v(H)$ dependence for field removal, corresponding to curve *3* in Fig. 3, *3* to calculations for the region of transition from one hysteresis branch to the other under the condition $B_v$=const. The arrows show the directions of field variation. The inset shows the temperature dependence of the magnetic field penetration depth in the surface layer of a YBa$_2$Cu$_3$O$_x$ single crystal.

vibrational contribution to the permeability $\mu_v$, it is reasonable to use the Meissner contribution $\mu_m$ to the permeability, which depends on $\lambda$ according to formula (2). (The physical meaning of such a normalization will be clarified in the subsequent analysis.)

It should be noted that, in our geometry ($H \perp c$), vortices anisotropic in cross section are characterized by the values of $\lambda_{ab}$ and $\lambda_c$ along the crystallographic axis $c$ and in the $ab$-plane, respectively. For this reason, we must describe the experimental data by using the mean values of the magnetic field penetration depth $\lambda = \lambda_{av} = \sqrt{\lambda_{ab}\lambda_c} = \sqrt{5}\lambda_{ab}$ (considering that the anisotropy parameter for YBaCuO is $\gamma = \lambda_c/\lambda_{ab} = 5$).[8] In the same geometry ($H \perp c$), the Ginzburg–Landau parameter is $\kappa = \kappa_{av} = \sqrt{\lambda_{ab}\lambda_c}/\sqrt{\xi_{ab}\xi_c} = \lambda_c/\xi_{ab} \cong 350$. The size of an anisotropic sample (the values of $d_c$ and $d_{ab}$ along the $c$-axis and in the $ab$-plane, respectively) should be recalculated to the size of its isotropic analog: $D_c = d_c\sqrt{\gamma}$; $D_{ab} = d_{ab}/\sqrt{\gamma}$. Besides, we must take into account the possibility of penetration of vortices from the end faces of the sample (in view of its finite size). In this case, the quantities $D_c$ and $D_{ab}$ are connected with the thickness $D$ of a model plate through the relation

$$D = D_{ab}D_c/(D_{ab}+D_c) = \sqrt{\gamma}d_{ab}d_c/(\gamma d_c + d_{ab}).$$

Figure 2 shows the experimental $\mu_v(H)$ curves obtained at different temperatures in normalized coordinates. It can be seen that all the curves indeed behave similarly, i.e., we observe the scaling behavior associated with the values of magnetic field penetration depths for each temperature.

It should be noted that the procedure of ''scaling'' the experimental dependences $\mu_v(H)$ in this case presumed the measurement of magnetic field penetration depths (as fitting parameters) only to within the scaling factor. In order to determine the absolute values of $\lambda$, we had to use additional information, e.g., concerning the value of $\lambda$ at a certain temperature, or refer to a certain theoretical curve $\mu_v(H)$ whose shape is known. The value of $\lambda$ shown by way of an example on the inset to Fig. 2 correspond to the latter case, i.e., the reference to an equilibrium $\mu_v(H)$ curve (see below for details). It will be clear from subsequent analysis that these values of $\lambda$ are of special importance for interpreting experimental data.

The scaling behavior of $\mu_v(H)$ suggests that the vortex dynamics near the surface is in all probability determined by the interaction between vortices as well as their interaction with the surface rather than by interactions with pinning centers.

It would be interesting to obtain the theoretical $\mu_v(H)$ curves for HTSC single crystals, correctly describing the experimental behavior of this quantity and thus clarifying the nature of the observed effect.

## THEORY

In our previous publication,[5] we investigated the contribution of vortex vibrations near their equilibrium positions to permeability and derived an analytic expression for $\mu_v$:

$$\mu_v = \frac{2\varphi_0}{Da\lambda} \frac{\exp(-x_1/\lambda)}{1-\exp(-d/\lambda)} \left(\frac{\partial x_1}{\partial H}\right)_{B_v}, \qquad (3)$$

where $x_1$ is the equilibrium position of the first row of vortices near the sample surface, $a$ the vortex lattice constant in the rows, and $d = \sqrt{3}a/2$ the separation between rows of vortices in a regular triangular lattice. The differentiation is carried out for a constant number of vortices in the sample or (which is the same) for a constant magnetic induction $B_v$ of the vortex lattice, which is defined as

$$B_v = \varphi_0/da. \qquad (4)$$

While deriving formula (3), we assumed that vortex rows near the surface (starting from the second one) are arranged regularly with the same separation $d$. This statement is valid to a high degree of accuracy for a perfect surface with which vortices interact strongly.[9,10] Such an approximation is the more so valid for a ''damaged'' surface with which they interact much less intensely. Thus, in conformity with (3), the permeability hysteresis is completely determined by the hysteresis of the equilibrium position of the first row of vortices $x_1(H)$ as a result of magnetic field application and removal. The hysteresis in the position of the first row of vortices can be associated with the interaction of vortices either with pinning centers, or with the surface. Let us consider the first case.

When vortices move from the surface to the bulk or back, they are trapped in the pinning centers, which obviously leads to a decrease in the distance between the $i$th row and the surface as a result of entrance and to an increase in this distance as a result of exit of vortices. In accordance

with (3), such a process leads to a hysteresis loop, but with a polarity opposite to that observed in experiments. Besides, the magnitude of the effect is quite small since the critical current density $j_c \leqslant 10^4$ A/cm$^2$ associated with pinning is smaller than the density of Meissner currents: $j_c \ll cH/4\pi\lambda$ for $H \geqslant 100$ Oe (even if we assume that the effective value of $\lambda$ near the "damaged" surface is an order of magnitude larger than in the bulk of the single crystal). Thus, the effect of pinning on the hysteresis of $x_1(H)$ is weak.

Let us now consider the second possible reason behind the hysteresis in the position of the first row of vortices relative to the surface, and hence in the quantity $\mu_v$, i.e., the interaction of vortices with the surface. The position of the first vortex row near the surface was calculated by different methods[5,10–12] either numerically, or by using various approximations. It would be expedient to obtain a simple analytic expression for $x_1$ and $\mu_v$ by direct summation of the contributions of vortices to the Gibbs energy of the vortex lattice near the surface, following the approach developed in Ref. 12.

We write the Gibbs free energy for a vortex in the first row (per unit length)[10]:

$$G_v = \frac{\varphi_0}{4\pi}\left[\sum_{l=2}^{\infty} H_v(x_l - x_1) - \sum_{l=1}^{\infty} H_v(x_l + x_1)\right]$$
$$- \frac{\varphi_v(x_1)H}{4\pi} + G_0, \tag{5}$$

where $H_v(x) = (\varphi_0/2a\lambda)\exp(-|x|/\lambda)$, $\varphi_v = \varphi_0[1 - \exp(-x/\lambda)]$ the summation is carried out over vortex rows, the first and second term in the braces describe the interaction of the first vortex row with the remaining rows and with their images (including its own image) respectively, and the third term in (5) corresponds to the interaction with Meissner's current. The quantities $H_v(x)$ and $\varphi_v(x)$ are the magnetic field created by a vortex row at a distance $x$ from it and the magnetic flux of a vortex separated by the distance $x$ from the surface respectively. The constant $G_0$ contains all the terms independent of $x_1$ (including the internal energy of a vortex).

It was mentioned above that in accordance with the results of analysis,[9,10] we can put $x_l = x_1 + (l-1)d$ to a high degree of accuracy. Consequently, we obtain after summation the following expression for the force acting on a unit length of a vortex in the first row:

$$F = -\frac{\partial G_v}{\partial x_1} = \frac{\varphi_0}{4\pi\lambda}\left[\frac{\varphi_0}{2a\lambda}\frac{\exp(-d/\lambda) + \exp(-2x_1/\lambda)}{1 - \exp(-d/\lambda)}\right.$$
$$\left. - H\exp(-x_1/\lambda)\right]. \tag{6}$$

In accordance with experimental conditions, the magnetic field varies according to the law $H + h\sin(\omega t)$. We shall assume that the system corresponds to the minimum of Gibbs' free energy for each value of the constant component of the magnetic field $H$, i.e., $F(H) = 0$. Under the condition $H \gg h$, we obtain the following equation for the equilibrium position of the first vortex row $x_1(H)$:

$$\frac{\varphi_0}{2a\lambda}\frac{\exp(-d/\lambda) + \exp(-2x_1/\lambda)}{1 - \exp(-d/\lambda)} - H\exp(-x_1/\lambda) = 0,$$
$$x_1 = x_1(H), \tag{7}$$

and the periodic force acting on a vortex in the first row is given by

$$F = \frac{\varphi_0 h}{4\pi\lambda}\exp[-x_1(H)/\lambda]\sin(\omega t). \tag{8}$$

Equation (7) is quadratic in $\exp(-x_1/\lambda)$. Solving this equation, we obtain

$$\exp(-x_1/\lambda) = \exp(-d/2\lambda)\left\{\frac{H}{\tilde{B}_v} \pm \left[\left(\frac{H}{\tilde{B}_v}\right)^2 - 1\right]^{1/2}\right\}, \tag{9}$$

where the following notation has been introduced:

$$\tilde{B}_v = B_v \frac{d}{2\lambda\sinh(d/2\lambda)}. \tag{10}$$

It can be easily seen that the Gibbs free energy minimum corresponds to the larger value of $x_1$, i.e., the plus sign in Eq. (9). Finally, we can write the following expression for the position of the first row corresponding to $G_{\min}$:

$$x_1(H) = \frac{d}{2} + \lambda\operatorname{arccosh}\left(\frac{H}{\tilde{B}_v}\right). \tag{11}$$

Thus, the hysteresis loop can emerge on the $x_1(H)$ curve due to the hysteresis in the magnetic induction $B_v(H)$ appearing as the magnetic flux enters and leaves the sample.

In accordance with formula (3), the calculation of permeability in the case of a small amplitude of the sinusoidal external field is reduced to the problem of small oscillations of the position of the first vortex row near its equilibrium position corresponding to the Gibbs free energy minimum for a given value of $H$. In the low-frequency limit, in which the amplitude of forced oscillations is independent of frequency, we can use formula (8) for obtaining the expression for the coercive force:

$$x_1(t,H) = x_1(H) + \frac{\varphi_0 h\exp[-x_1(H)/\lambda]}{4\pi k\lambda}\sin(\omega t). \tag{12}$$

Here $k$ is the retrieving force corresponding to small harmonic oscillations of the first vortex row in the effective potential well. Substituting (11) and (12) into expression (3) for $\mu_v$, we obtain

$$\mu_v = \frac{\varphi_0}{2\pi Dk\lambda}\exp(-d/2\lambda)\frac{\tilde{B}_v^3}{[H + (H^2 - \tilde{B}_v^2)^{1/2}]^2}. \tag{13}$$

This formula expresses permeability in terms of the vortex lattice induction and the retrieving force $k$. Thus, in order to describe the behavior of $\mu_v$ upon a change in the applied magnetic field, we must first of all know the form of the $B_v(H)$ dependence. If we assume that vortices penetrate the plate in a quasi-equilibrium way (i.e., in the absence of any mechanisms of overcoming of the barrier by vortices), this dependence assumes the form[12]

$$H = (H_s^2 + \widetilde{B}_v^2)^{1/2}, \tag{14}$$

where $H_s$ is the field corresponding to the penetration of vortices in the plate for $B_v = 0$. In fact, formula (14) is a generalization of the expression for the Bean–Livingston barrier to the case of a nonzero magnetic induction of the vortex lattice. It should be recalled that $H_s = H_c$ for a perfectly smooth surface,[13] while in the general case $H_{c1} < H_s < H_c$. The condition for the emergence of vortices from the plate is given by the relation[12]

$$H = \widetilde{B}_v. \tag{15}$$

This leads to the hysteresis behavior of $\mu_v(H)$, the width of the hysteresis loop being a function of the form of $B_v(H)$ as well as the value of the parameter $k$.

If we assume that $k$ is mainly determined by the interactions of vortices with one another and with Meissner currents rather than by pinning (which is natural just for the vortex row nearest to the surface, where the Meissner current exceeds $j_c$), it can easily be proved that expression (13) assumes the form

$$\mu_v = \frac{2\lambda}{D} \frac{\widetilde{B}_v^2}{(H^2 - \widetilde{B}_v^2)^{1/2}[H + (H^2 - \widetilde{B}_v^2)^{1/2}]}. \tag{16}$$

Here we assume that $k$ is determined by the second derivative of the Gibbs free energy (5) with respect to the position of the first row for a fixed magnetic induction. Formula (16) establishes a simple analytic relation between the permeability and the vortex lattice induction, which allows us to use this formula for describing experimental data. It can be seen that the quantity $\mu_m = 2\lambda/D$ is the natural scaling factor in the dependence of $\mu_v$ on $H$, which justifies the above normalization used for plotting experimental results in dimensionless units (see Fig. 2).

It should be noted that expression (16) is formally inapplicable for calculating $\mu_v(H)$ for a sample with a perfect surface with a magnetic flux emerging from it since condition (15) is satisfied in this case, and $\mu_v(H)$ turns to infinity. In this case, we must take into account the contribution from pinning centers to the retrieving force $k$ and/or deviation of the $B_v(H)$ dependence from the quasi-equilibrium law (15).

## COMPARISON OF THEORY WITH EXPERIMENT. DISCUSSION OF RESULTS

Thus, according to (16), we can obtain the theoretical curves $\mu_v(H)$ by assuming a definite form of the $B_v(H)$ dependence upon an increase or decrease in the magnetic field. For example, we can use for this purpose expressions (14) and (15) obtained by us earlier[12] and corresponding to ''superheating'' and ''supercooling'' of the Meissner state due to the existence of an appreciable surface barrier for vortices entering and leaving the superconductor. However, direct substitution of (14) and (15) into (16) and a comparison of the theoretical values of $\mu_v(H)$ with the experimental data suggests that the surface barrier in a YBaCuO single crystal (if it exists) is much lower than the one predicted for a perfect surface. Indeed, as the magnetic field increases, the value of the field $H_s$ corresponding to penetration of vortices
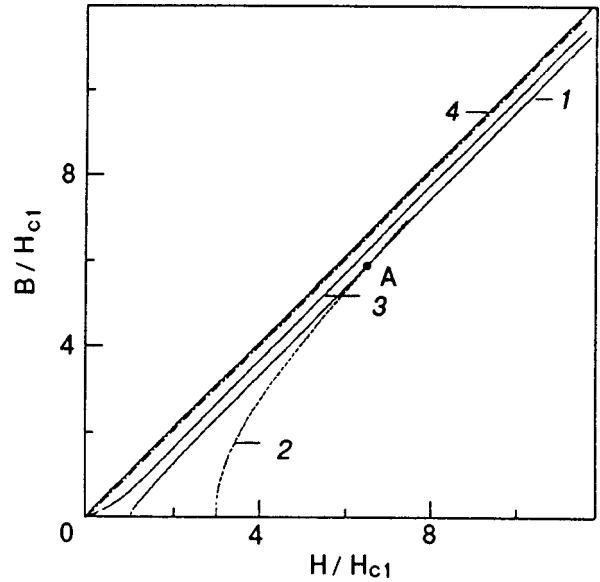


FIG. 3. Magnetic induction as a function of the applied magnetic field. Curve *1* corresponds to a thermodynamically equilibrium state of the vortex lattice, curve *2* is the $B(H)$ dependence (14) corresponding to the entrance of vortices in the sample for $H_S = 3H_{c1}$, curve *3* is reconstructed from a comparison of experimental values of $\mu_v(H)$ for field removal with dependences calculated by formula (16), and curve *4* is the lower stability boundary for the mixed state in the case of an ideal barrier. The dot-and-dash line corresponds to $B = H$, and *A* is the point of intersection of curves *1* and *2*.

(and playing the role of fitting parameter) is close to the lower critical field: $H_{c1} \lesssim H_s \lesssim 3H_{c1}$, while for a decreasing magnetic field we have finite values of $\mu_v$ instead of the expected sharp increase in $\mu_v$ corresponding to condition (15): $H = \widetilde{B}_v$.

This result allows us to draw several conclusions. First, the closeness of the values of $H_s$ and $H_{c1}$ suggests that in an increasing field the values of $\mu_v(H)$ can correspond to a magnetic induction in the sample, which is close to the equilibrium value.

We can obtain this $\mu_v(H)$ curve by putting in (16) the $B_v(H)$ dependence corresponding to thermodynamic equilibrium: $B = B_{eq}(H)$. [An approximate formula correctly describing the equilibrium dependence $H(B)$ is given in Ref. 5, and the $B_{eq}(H)$ curve is shown in Fig. 3 (curve *1*).] The results of calculation of $\mu_v(H)$ for the equilibrium curve $B = B_{eq}(H)$ are presented in Fig. 2 in the normalized coordinates chosen by us (curve *1*). It was noted above and follows from Fig. 2 that the scaling experimental dependences shown in the same figure and observed for increasing magnetic field can be matched with the given equilibrium theoretical curve $\mu_v(H)$ for the values of magnetic field penetration depth illustrated in the inset to Fig. 2.

Let us consider in greater detail the values of $\lambda$ obtained as a result of such a procedure. The absolute values of this quantity are slightly larger than the available data (see, for example, Refs. 14 and 15): the difference amounts approximately to 10% at $T = 70$ K and increases with temperature, attaining $\sim 40\%$ at $T = 84$ K. Such a result appears as quite reasonable if we assume that slightly larger values of magnetic field penetration depth than bulk values are realized for

some reason in the surface layer (whose response is observed in experiments). For example, this can be due to oxygen deficiency in the surface layer. Qadri *et al.*,[16] who measured local values of the crystal lattice parameter $c$ in the bulk of the sample proved that the oxygen content at the surface does not exceed $x = 6.82$ even in high-quality $YBa_2Cu_3O_x$ single crystals. Using the results obtained by Zimmermann *et al.*[17] and establishing the relation between the values of $\lambda_{ab}(0)$ and the oxygen content $x$, we can verify that this value of oxygen index indeed corresponds to the values of $\lambda$ increased by 30–40% as compared to the value in the bulk for which $x = 6.95$.

The above arguments suggest that the experimental values of $\mu_v(H)$ obtained upon an increase in the field can be quite close to the equilibrium dependence $\mu_v(H)$, and hence the surface barrier for vortices entering the sample is actually not observed. It should be noted that the equilibrium curve in the range of weak fields still lies slightly higher than experimental points, and hence the statement that $H_s$ and $H_{c1}$ coincide exactly is not quite correct. However, estimates show that even an insignificant surface barrier (if it exists) makes the root dependence (14) approach the equilibrium $B_{eq}(H)$ dependence very rapidly. For example, if $H_s = 3H_{c1}$, this is observed for fields $H \approx 6H_{c1}$, which indicates an inevitable transition to the equilibrium dependence for $H > 6H_{c1}$ (curve *2* in Fig. 3). Consequently, the application of formula (14) with $2H_{c1} \leqslant H_s \leqslant 3H_{c1}$ instead of the equilibrium dependence $B_{eq}(H)$ for calculating $\mu_v(H)$ by formula (16) changes the theoretical dependence $\mu_v(H)$ insignificantly.

The other conclusion concerns the upper branch of the hysteresis loop $\mu_v(H)$ corresponding to a decreasing magnetic field. Let us reconstruct the $B_v(H)$ dependence observed for vortices leaving the superconductor by comparing the experimental data with formula (16). The results of calculations are presented in Fig. 3 (curve *3*).

The existence of a barrier for vortices leaving the sample suggests that the number of vortices does not change upon the reversal of the direction of magnetic field scanning in a certain transition region. This only shifts vortices towards the surface, while $B_v = const$. The transition region obviously corresponds to a transition from the lower branch of the $\mu_v(H)$ hysteresis loop to the upper branch. The substitution of the condition $B_v = const$ into Eq. (14) gives the theoretical curve (curve *3* in Fig. 2) for the given region. It should be noted that this curve is characterized by a comparatively large steepness, which is in qualitative agreement with experimental data.

The transition region exists until the repulsive force exerted by the Meissner current becomes smaller that the force of interaction between vortices. At this value of $H = H_{min}$, the barrier for vortices emerging from the sample must vanish. The lower stability boundary for the mixed state corresponds to the position of the vortex row nearest to the surface, in which it is at the point of inflection of the Gibbs free energy (for a perfect surface, this point corresponds to $\tilde{B} = H$; curve *4* in Fig. 3), i.e., at the point of instability to small variations of $H$. It was noted above that the value of $\mu_v$ in this case much increase abruptly (formally tending to infinity). Finite and not very large experimental values of $\mu_v(H)$ observed during field removal indicate that vortices leave the sample in the case when the position of the row closest to the surface still corresponds to the minimum of the Gibbs free energy (and not to the point of inflection). A possible mechanism of such an emergence of vortices in the case of an insignificant barrier is apparently the thermally activated process.

The region bounded by curves *1* (or a combination of curves *1* and *2*) and curve *3* in Fig. 3 can apparently be regarded on the whole as the region of mixed state with a fixed value of $B$ in an actual YBaCuO single crystal (for $H \perp c$). We can assume that the existence of this region, i.e., the hysteresis behavior of $B_v(H)$ due to the surface barrier for vortices leaving the sample is mainly responsible for the hysteresis loop observed in $\mu_v(H)$. (Taking into account our experimental geometry as well as the size and shape of the sample, we can conclude that barriers other than the Bean–Livingston one (e.g., a geometrical barrier[18]) cannot make any noticeable contribution to the magnetic flux distribution in the range of magnetic fields $H > H_{c1}$ under investigation).

It should be noted that the results obtained above for the stability region of the vortex state in YBaCuO single crystals are very close to the results obtained earlier[19] for small-grain samples of the same composition. These data suggest the existence of an objective reason associated in all probability with peculiarities in the boundary conditions observed for HTSC (and not with technological conditions determined by the method of sample preparation), which is responsible for such a strong suppression of the surface barrier in HTSC. As a result, an increase in magnetic field in such objects leads to a virtually equilibrium value of magnetic induction.

## CONCLUSION

An analysis of peculiarities in the behavior of a vortex lattice near the surface leads to an analytic expression for the magnetic field dependence of the vibration contribution $\mu_v$ to the dynamic permeability, which correctly describes the experimental data under the following conditions: for increasing field, the values of $\mu_v(H)$ virtually correspond to equilibrium values $B_{eq}(H)$, while for decreasing field there exists a small barrier for vortices leaving the sample, which is responsible for the observed hysteresis behavior of $\mu_v(H)$ in a $YBa_2Cu_3O_x$ single crystals.

Thus, a comparison of experimental curves $\mu_v(H)$ with theoretical dependences makes it possible to estimate quantitatively the stability region for the mixed state for a given value of induction and indicates that magnetic field penetration depth in the surface layer of the single crystal under investigation has slightly higher values than in the bulk.

This probably explains the origin of a considerable suppression of the surface barrier, but this question requires further detailed investigations.

*E-mail: mamsurova@chph.ras.ru

[1] C. P. Bean and J. D. Livingston, Phys. Rev. Lett. **12**, 14 (1964).

[2] F. Bass, V. D. Freilikher, B. Ya. Shapiro, and M. Shvartser, Physica C **260**, 231 (1996).

[3] L. Burlachkov, M. Konzykowski, Y. Yeshurun, and F. Holtzberg, J. Appl. Phys. **70**, 5759 (1991).

[4] L. G. Mamsurova, K. S. Pigalskiy, V. P. Sakun, and L. G. Scherbakova, Physica C **200**, 175 (1992).

[5] L. G. Mamsurova, K. S. Pigalskiy, V. P. Sakun, and L. G. Scherbakova, Fiz. Tverd. Tela (St. Petersburg) **37**, 2954 (1995) [Phys. Solid State **37**, 1630 (1995)].

[6] V. P. Sakun and K. S. Pigalskiy, Khim. Fiz. **15**, 3 (1996).

[7] L. G. Mamsurova, K. S. Pigalskiy, V. P. Sakun, and L. G. Scherbakova, Supercond., Phys. Chem. Technol. **5**, 1811 (1992).

[8] B. Pumpin, H. Keller, W. Kundig *et al.*, Phys. Rev. B **42**, 8019 (1990).

[9] V. V. Shmidt and G. S. Mkrtchyan, Usp. Fiz. Nauk **112**, 459 (1974) [Sov. Phys. Usp. **17**, 170 (1974)].

[10] F. F. Ternovskii and L. N. Shekhata, Zh. Éksp. Teor. Fiz. **62**, 2297 (1972) [Sov. Phys. JETP **35**, 1202 (1972)].

[11] J. R. Clem, in *Proc. 13th Conf. on Low Temperature Physics (LT13)*, vol. **3**, Plenum, New York (1974).

[12] K. I. Kugel and A. L. Rakhmanov, Physica C **251**, 307 (1995).

[13] P. G. de Gennes, Solid State Commun. **3**, 127 (1965).

[14] J. Y. Lee, K. M. Paget, T. R. Lemberger *et al.*, Phys. Rev. B **50**, 3337 (1994).

[15] S. Kamal, D. A. Bonn, N. Goldenfeld *et al.*, Phys. Rev. Lett. **73**, 1845 (1994).

[16] S. B. Qadri, M. S. Osofsky, V. M. Browring, and E. F. Skelton, Appl. Phys. Lett. **68**, 2729 (1996).

[17] P. Zimmermann, H. Keller, S. L. Lee *et al.*, Phys. Rev. B **52**, 541 (1995).

[18] E. H. Brandt, Rep. Prog. Phys. **58**, 1465 (1995).

[19] K. S. Pigalskiy and L. G. Mamsurova, Fiz. Tverd. Tela **39**, 1943 (1997) [Phys. Solid State **39**, 1737 (1997)].

Translated by R. S. Wadhwa

## LOW-TEMPERATURE MAGNETISM

# Effects of nonlocal interlayer exchange in spin dynamics of a magnetic metal superlattice

S. V. Tarasenko

*A. Galkin Physicotechnical Institute, National Academy of Sciences of the Ukraine, 340114 Donetsk, Ukraine**
(Submitted September 22, 1997; revised May 5, 1998)
Fiz. Nizk. Temp. **24**, 832–838 (September 1998)

It is shown that a consistent analysis of the nonlocal interlayer exchange in semi-confined metallic magnetic superlattice of the ferromagnet–nonmagnetic metal type with antiferromagnetic coupling between ferromagnetic layers leads to the formation of new types of collective dipole–exchange spin-wave excitations near the surface of the magnetic superlattice. © *1998 American Institute of Physics.* [S1063-777X(98)00309-0]

The conductivity of the layers of a nonmagnetic metal in magnetic superlattices (MSL) of the magnet–nonmagnetic type determines the most fascinating properties of such magnetic systems, which are associated with magnetic dipole interaction, as well as spin–spin interaction between magnetic layers due to conduction electrons of the nonmagnetic layer.[1] It was shown, in particular, that indirect interaction of magnetic moments of adjacent magnetic layers can be of the ferro- or antiferromagnetic type depending on the thickness of the nonmagnetic interlayer. However, in spite of a large number of publications devoted to an analysis of resonant properties of MSL, the role of this type of magnetic interlayer interaction was taken into account only in an analysis of equilibrium spin configuration.[2,3] At the same time, this type of interlayer exchange also contains the spatially nonhomogeneous component in view of its nonlocal nature, but the effect of this component on spin dynamics of metallic MSL has been disregarded so far.

In this communication, we shall show for the first time that the inclusion of spatially nonhomogeneous component of interlayer spin–spin exchange along with magnetic dipole interaction in addition to the spatially homogeneous component leads to the emergence of qualitatively new anomalies in the surface as well as volume dipole–exchange spin dynamics of the MSL of the type ''ferromagnetic–nonmagnetic metal.''

### BASIC RELATIONS

By way of an example, we consider an $N$-periodic ($N \gg 1$) superlattice formed by a system of isotropic ferromagnetic layers of thickness $d_1$ each, which are connected through layers of a nonmagnetic metal of thickness $d_2$ (for example, Y–Gd system).[2] We shall henceforth assume that the interlayer exchange through conduction electrons is antiferromagnetic by nature, and the external magnetic field **H** is applied in the plane of the layers (**H**$\|0Y$) whose normal **n** to the interface is parallel to $0Z$. Strictly speaking, the

calculation of the spectrum of collective spin–wave excitations in such a magnetic system on the basis of simultaneous analysis of the exchange and magnetic–dipole mechanisms of interlayer exchange and corresponding boundary conditions (between the layers and at the edges) involves the application of the method of T-matrix.[4] For this reason, the calculations and the subsequent analysis of the results become extremely cumbersome. However, we can confine our analysis to the long-wave range of magnon spectrum of the MSL under investigation since the thickness of magnetic layers in them varies from a few tens to several hundreds angströms [Ref. 1], and assume that magnetic layers are ultrathin in their dynamic properties ($k_\perp d_1 \ll 1$, $\mathbf{k}_\perp$ being the wave vector of magnetic oscillations in the plane of a magnetic layer). Besides, it was shown by Bass *et al.*[5] that since the interval between two eigenfrequencies in the case of spin–wave resonance in an individual ferromagnetic layer with the saturation magnetization $M_0$ is equal to $gM_0\tilde{\alpha}(\pi/d_1)^2$ ($\tilde{\alpha}$ is the nonuniform exchange constant and $g$ the gyromagnetic ratio), oscillations of magnetization over the film thickness can be regarded as quasi-uniform if the following relation holds:

$$d_1 \ll \pi c_0 \Delta^{-1}, \tag{1}$$

where $c_0$ is the velocity of light and $\Delta$ the frequency of uniform ferromagnetic resonance (FMR). Thus, the magnetization of each ferromagnetic film constituting the MSL and magnetized to saturation in its $XY$ plane (**n**$\|0Z$) can be represented in the form[5]

$$\mathbf{M}_j(x,y,z) = \mathbf{M}_s(x,y)d_1\delta(z). \tag{2}$$

In this case, the exchange interaction of identical uniformly magnetized ferromagnetic layers $j$ and $j+1$ with magnetizations $M_j = m_s$ ($|\mathbf{M}_j| = M_0$) through conduction electrons of the nonmagnetic interlayer in MSL under investigation can be represented in the form $\delta M_j M_{j+1}$ in the phenomenological theory of magnetism.[1,2] In the applied magnetic field **H**, the magnetizations of magnetic layers with labels $j$ and $J$

$\pm 2\nu$ ($\nu = 1,2,...$) in the equilibrium state have the same spatial orientation. If we describe the direction of equilibrium magnetization in the $j$th layer of the MSL in the spherical system of coordinates with the polar axis directed along $\mathbf{n}$ ($\mathbf{n} \| 0Z$): $M_j = M_0(\sin\theta_j \cos\varphi_j; \sin\theta_j \sin\varphi_j; \cos\theta_j)$ the following relations hold for the magnetic moments of adjacent magnetic layers[2]:

$$M_j = M_0(\sin\varphi; \ \cos\varphi; \ 0);$$

$$M_{j\pm 1} = M_0(-\sin\varphi; \ \cos\varphi; \ 0), \quad \sin\varphi = H/2\delta M_0. \tag{3}$$

If we confine our analysis to collective spin-wave excitations which are quasi-uniform over the superlattice period $L = d_1 + d_2$, i.e.,

$$k_\perp L \ll 1, \tag{4}$$

the analysis of the magnon spectrum of such an MSL can be carried out on the basis of the concept of effective medium developed in Refs. 2 and 3 for calculating the spectrum of collective spin-wave excitations of the magnetostatic type under conditions (4). By virtue of (3), the magnetic layers with labels $j\pm 2\nu$ and $j\pm 2(\nu+1)$ ($\nu = 1,2,...$) can be combined into two magnetic sublattices $M_{j\pm 2\nu} = M_1$; $M_{j\pm(2\nu+1)} = M_2$ ($|M_1| = |M_2| = M_0$). In this case, under conditions (1)–(4), the density of thermodynamic potential $W$ of a metallic MSL with spatial inhomogeneity of interlayer exchange can be represented in the form

$$W = \delta \sum_{j=1}^{N} M_j M_{j\pm 1} + \frac{\alpha_\perp}{2}(\nabla_\perp M_j)^2 - (M_j, H + H_{mj}). \tag{5}$$

Here $\delta$ is the exchange integral of interlayer exchange ($\delta = \delta(d_2) > 0$), $\alpha_\perp$ the constant of nonuniform spin–spin exchange in the plane of ferromagnetic layers, $\nabla_\perp \equiv (\partial/\partial x, \partial/\partial y)$, $H$ the applied magnetic field, and $H_{mj}$ the magnetic-dipole field in the $j$th magnetic layer of the MSL. In view of the concept of effective (fine-layered) medium, the expression for the $\gamma$ component of the magnetic induction vector $\mathbf{B}$ ($\gamma = x,y,z$) averaged over the period $L$ of the MSL can be presented in the form

$$\langle B_\gamma \rangle = \frac{d_1}{2L}[h_{1\gamma} + h_{2\gamma} + 4\pi(M_{1\gamma} + M_{2\gamma})]$$

$$+ \frac{d_2}{2L}(h_{a\gamma} + h_{b\gamma}), \tag{6}$$

(indices $a$ and $b$ correspond to adjacent nonmagnetic layers of thickness $d_2$ each, separated by a ferromagnetic layer of thickness $d_1$).[2]

In this case, taking into account the standard electrodynamic boundary conditions at the interfaces in the MSL, relation (5) can be transformed to

$$W = \frac{\delta}{2}\mathbf{m}^2 + \frac{\alpha_\perp}{2}\left[\left(\frac{\partial \mathbf{l}}{\partial x}\right)^2 + \left(\frac{\partial \mathbf{l}}{\partial y}\right)^2\right] + \frac{\alpha}{2}\left(\frac{\partial \mathbf{l}}{\partial z}\right)^2$$

$$- \frac{\alpha}{2}\left(\frac{\partial \mathbf{m}}{\partial z}\right)^2 + \frac{\alpha_\perp}{2}\left[\left(\frac{\partial \mathbf{m}}{\partial x}\right)^2 + \left(\frac{\partial \mathbf{m}}{\partial y}\right)^2\right] + \frac{b}{2}l_z^2$$

$$+ \frac{a}{2}m_z^2 - \mathbf{M}(\mathbf{H} + \mathbf{H}_m), \tag{7}$$

where

$$a = 4\pi d_2/L; \quad b = 8\pi; \quad \alpha = \delta d_2^2;$$

$$\mathbf{m} = \mathbf{M}_1 + \mathbf{M}_2; \quad \mathbf{l} = \mathbf{M}_1 - \mathbf{M}_2.$$

Thus, in the concept of effective medium with the antiferromagnetic type of interlayer exchange, the density of thermodynamic potential (7) of the MSL under investigation has a structure corresponding to the model of an easy-plane (EP) antiferromagnet ($0Z$ being the difficult axis) in the external magnetic field $\mathbf{H} \| 0Y$ applied in the easy plane $XY$.[6–9] The dipole–exchange spin dynamics of such a magnetic medium is determined by a coupled system of dynamic equations consisting of the Landau–Lifshitz equation for the magnetization vector $\mathbf{M}_{1,2}$ and magnetostatic equations. The standard procedure of calculations (see, for example, Ref. 6) shows that the magnetic susceptibility tensor $\hat{\chi}(\omega,\mathbf{k})$ for the MSL under investigation with nonlocal inter- and intralayer exchange in the limit (4) can be presented in the form

$$\hat{\chi}(\omega,\mathbf{k}) = \begin{pmatrix} \chi_{xx} & 0 & \chi_{xz} \\ 0 & \chi_{yy} & 0 \\ \chi_{zx} & 0 & \chi_{zz} \end{pmatrix}, \tag{8}$$

where

$$\chi_{xx} = \frac{\Delta_{xx}}{\omega_F^2 - \omega^2}; \quad \chi_{yy} = \frac{\Delta_{yy}}{\omega_{AF}^2 - \omega^2}; \quad \chi_{zz} = \frac{\Delta_{zz}}{\omega_F^2 - \omega^2};$$

$$\chi_{xz} = -\chi_{zx} = \frac{i\omega\Delta}{\omega_F^2 - \omega^2};$$

$$\omega_F^2 = g^2(\delta + a + \beta_{ii}k_i^2)\alpha_{ii}k_i^2 l_0^2 + g^2(H + \beta_{ii}k_i^2 m_0)$$

$$\times (H + \beta_{ii}m_0 k_i^2 + am_0);$$

$$m_0 = H/\delta; \quad l_0^2 = (2M_0)^2(1 - m_0^2);$$

$$\omega_{AF}^2 = g^2[(\delta + \beta_{ii}k_i^2)l_0^2 + \alpha_{ii}k_i^2 m_0^2](b + \alpha_{ii}k_i^2);$$

$$\Delta_{yy} = g^2(b + \alpha_{ii}k_i^2)l_0^2;$$

$$\Delta_{xx} = g^2(H + am_0 + \beta_{ii}m_0 k_i^2)m_0;$$

$$\Delta_{zz} = g^2[(H + \beta_{ii}k_i^2 m_0)m_0 + \alpha_{ii}k_i^2 l_0^2]; \quad \Delta = gm_0;$$

$$\alpha_{xx} = \alpha_{yy} = \beta_{xx} = \beta_{yy} = \alpha_\perp; \quad \beta_{zz} = -\alpha_{zz} = -\alpha;$$

$$\alpha_{ik} = \beta_{ik} = 0 \quad \text{for } i \neq k.$$

An analysis of expression (8) shows that for $\alpha_\perp = \alpha = 0$, these expressions coincide (except for the notation) with the relevant relations for the permeability of a metallic MSL from Ref. 2. Comparing expression (8) for $\alpha,\alpha_\perp \neq 0$ with similar expressions for an EP AFM in an external magnetic

field perpendicular to the difficult axis,[6–9] we must emphasize that the corresponding terms for $k_z \neq 0$ and $k_{x,y} \neq 0$ have opposite signs. This difference is due to the type of the ground state of the magnetic structure under investigation: the magnetic moments are ordered ferromagnetically in $XY$ layers and antiferromagnetically along the normal to the interface $0Z$ between the layers. The validity of relations (8) is confirmed by the fact that the expressions for the spectrum of normal magnon excitations $\omega_{F,AF}$ for a two-sublattice antiferromagnet in the limit $H=0$, $b=0$, $a=0$ coincide with the long-wave limit of the spectrum for a one-dimensional antiferromagnetic chain[10]:

$$\omega_{AF}^2 = \omega_F^2 = (2gM_0)^2 [\delta + \alpha_\perp (k_x^2 + k_y^2) - \alpha k_z^2]$$
$$\times [\alpha_\perp (k_x^2 + k_y^2) + \alpha k_z^2]. \tag{9}$$

Since the actual magnetic multilayered structure has a finite size, this circumstance can be taken into account correctly only by supplementing the system of dynamic equations with a system of boundary conditions. The system of boundary conditions for a semi-infinite MSL ($z<0$) with completely free spins on the surface ($z=0$) in the limit (4) can be written in the form

$$\frac{\partial \widetilde{\mathbf{m}}}{\partial z} = \frac{\partial \widetilde{\mathbf{l}}}{\partial z} = 0; \quad \mathbf{B}_m \cdot \mathbf{n} = \mathbf{B} \cdot \mathbf{n};$$

$$[\mathbf{H}_m \times \mathbf{n}] = [\mathbf{H} \times \mathbf{n}], \quad z=0 \tag{10}$$

($\mathbf{n} \| 0Z, \widetilde{\mathbf{m}}$ and $\widetilde{\mathbf{l}}$ are small oscillations of the ferromagnetism and antiferromagnetism vectors $\mathbf{m}$ and $\mathbf{l}$ respectively near the equilibrium orientation, and $\mathbf{B}_m$ and $\mathbf{H}_m$ ($\mathbf{B}$ and $\mathbf{H}$) are the magnetic induction and magnetic field vectors for the magnetic (nonmagnetic) media respectively).

Since we are interested in dipole-exchange oscillations localized near the surface $z=0$ of the MSL under investigation, the following conditions must also hold in addition to the boundary conditions (10):

$$|\widetilde{\mathbf{m}}|, |\widetilde{\mathbf{l}}|, |\mathbf{H}_m| \to 0 \quad \text{for } z \to -\infty;$$

$$|\mathbf{H}| \to 0 \quad \text{for } z \to \infty. \tag{11}$$

An analysis shows that in the model (7) of a semi-infinite MSL. the magnon spectrum taking into account the spatially inhomogeneous component of interlayer exchange for $k_\perp L \ll 1$ can be written in the form

$$\mu_{xx} \sin^2 \theta_k \cos^2 \varphi_k + \mu_{yy} \sin^2 \theta_k \sin^2 \varphi_k + \mu_{zz} \cos^2 \theta_k = 0$$

$$(\tan^2 \varphi_k = k_y^2/k_x^2; \quad \cot^2 \theta_k = k_z^2/(k_x^2 + k_y^2); \quad \mathbf{B} = \hat{\mu}\mathbf{h}). \tag{12}$$

It can be easily seen that if we disregard the nonlocal nature of the inter- and intralayer spin–spin exchange ($\alpha = \alpha_\perp = 0$), the energy–momentum relation (12) coincides with the analogous relation for the spectrum of spin waves of an infinite magnetic superlattice of the ferromagnetic–nonmagnetic metal type with the antiferromagnetic exchange between layers from Ref. 2 An analysis of expressions (8) and (12) shows that, in the absence of magnetic-dipole interaction, normal modes of the magnon spectrum of an infinite MSL (7) can be classified according to the type of their

excitation by high-frequency magnetic field $\mathbf{h}$ as quasi-ferromagnetic $\mathbf{h} \| \mathbf{H}(\omega_F)$ and quasi-antiferromagnetic $\mathbf{h} \| \mathbf{H}(\omega_{AF})$. Thus, these two modes in the model of an infinite MSL can interact only through long-range magnetic dipole fields. It follows from (8) that the frequencies $\omega_F(k=0)$ and $\omega_{AF}(k=0)$ can differ significantly depending on the applied magnetic field $\mathbf{H} \| 0Y$. This circumstance allows us to neglect the effect of high-frequency mode of antiferromagnetic resonance (AFMR) in the analysis of low-frequency dipole-exchange dynamics of MSL. We shall henceforth assume that the relation $\omega_{AF} \ll \omega_F$ holds for the MSL under investigation:

$$\delta^2 - H^2 \ll \frac{\delta + a}{b} \left( \frac{H}{2M_0} \right)^2. \tag{13}$$

In this case, it follows from (12) for the wave vectors $\mathbf{k}_\perp \perp \mathbf{H}$ satisfying the conditions

$$\delta \gg \alpha_\perp k_\perp^2, \quad \alpha k_\perp^2, \quad |4\pi(d_1 - d_2)2M_0/H| \ll 1, \tag{14}$$

that collective dipole-exchange spin-wave excitations propagating along the surface of the MSL under investigation form a two-partial type wave in view of the nonlocal nature of the interlayer exchange. Accordingly, the structure of magnetostatic potential $\varphi_m$, for example, for $z<0$, can be presented in the form ($\mathbf{k}_\perp \| 0Y$)

$$\varphi_m = \sum_{\lambda=1,2} A_\lambda \exp(i\omega t - i k_\perp y) \exp(-q_\lambda z). \tag{15}$$

Here $q_{1,2}$ are positive roots of the following characteristic equation obtained from (12) and conditions (13) and (14) for $k_z^2 \equiv -q^2$:

$$q^4 - P_1 q^2 + P_2 = 0;$$

$$P_1 = \frac{\omega_0^2 + [c^2(1+4\pi\chi_0) + c_\perp^2]k_\perp^2 - \omega^2}{c^2};$$

$$P_2 = k_\perp^2 \frac{(c_\perp^2 k_\perp^2 + \omega_0^2)(1+4\pi\chi_0) - \omega^2}{c^2}. \tag{16}$$

Here $\omega_0^2 = g^2(2M_0)^2\delta b$; $c^2 = g^2\delta 4M_0^2\alpha$; $c_\perp^2 = g^2\delta 4M_0^2\alpha_\perp$; $\chi_0 = 1/\delta$.

Using expressions (15) and (16), we can study the dependence of the localization of a dipole-exchange spin wave near the surface of the MSL under investigation on the wave number $k_\perp$ and the frequency $\omega$ of spin oscillations.

## POSSIBLE TYPES OF DIPOLE-EXCHANGE SPIN-WAVE EXCITATIONS

An analysis shows that if the frequency $\omega$ of spin oscillations and the wave number $k_\perp$ satisfy the conditions

$$\omega_+^2 < \omega^2 < B; \quad k^2 > k_*^2;$$

$$k_*^2 \equiv \frac{\omega_0^2(1+4\pi\chi_0)}{c^2(1+4\pi\chi_0) - 4\pi\chi_0 c_\perp^2};$$

$$\omega_-^2 > \omega^2 > 0;$$

$$\omega_\pm^2 \equiv A - 2c^2 k_\perp^2 \pm 2c k_\perp (c^2 k_\perp^2 + B - A)^{1/2};$$

$$A \equiv [c_\perp^2 + c^2(1 + 4\pi\chi_0)]k_\perp^2 + \omega_0^2;$$

$$B \equiv (\omega_0^2 + c_\perp^2 k_\perp^2)(1 + 4\pi\chi_0), \qquad (17)$$

a two-partial surface dipole-exchange spin wave ($q_{1,2}^2 > 0$) can be formed near the surface $z = 0$ of the MSL under investigation in view of the nonlocal nature of interlayer exchange ($c \neq 0$). If, however, the relation

$$\omega_-^2 < \omega^2 < \omega_+^2, \qquad (18)$$

holds, a two-partial generalized surface spin wave (Re $q_{1,2}^2 \neq 0$; Im $q_{1,2}^2 \neq 0$) can be formed in the MSL under consideration. If the frequency $\omega$ of spin oscillations and the wave number $k_\perp$ do not satisfy simultaneously relations (18) and (19), the formation of two-partial dipole-exchange excitations localized near the surface of the MSL (7) is ruled out. In particular, for

$$\omega^2 > (\omega_0^2 + c_\perp^2 k_\perp^2)(1 + 4\pi\chi_0) \qquad (19)$$

collective dipole-exchange spin-wave oscillations propagating along the surface of the MSL form a two-partial pseudo-surface spin wave ($q_1^2 > 0$, $q_2^2 < 0$). Finally, the formation of two-partial bulk ($q_{1,2}^2 < 0$) dipole-exchange excitations in the MSL under investigation takes place for

$$\omega_+^2 < \omega^2 < (\omega_0^2 + c_\perp^2 k_\perp^2)(1 + 4\pi\chi_0); \quad k_\perp^2 < k_*^2. \qquad (20)$$

However, relations (17) and (18) are only necessary conditions for the localization of collective dipole-exchange spin-wave excitations with the structure of the magnetic potential $\varphi_m$ (15) near the surface of the MSL in question.

## SURFACE DIPOLE-EXCHANGE SPIN WAVE

The energy–momentum relation for a surface dipole-exchange spin wave in the case of a semi-infinite MSL (10), (11) is a nontrivial solution of system (11) for the amplitudes $A_{1,2}$ (15) provided that $\omega$ and $k_\perp$ satisfy relations (17) or (18):

$$q_1 q_2 (q_1 + q_2) - k_\perp \left( \frac{\omega_0^2 + c_\perp^2 k_\perp^2 - \omega^2}{c^2} - q_1 q_2 \right) = 0. \qquad (21)$$

It can be easily seen that if we disregard the nonlocal nature of interlayer exchange ($\alpha = 0$), this type of surface spin-wave excitations does not exist. In the short-wave limit ($c_\perp^2 k_\perp^2 \gg 4\pi\chi_0 \omega_0^2$), the energy–momentum relation for the surface spin wave under consideration can be derived from (21) in an explicit form:

$$\omega^2 \cong (\omega_0^2 + c_\perp^2 k_\perp^2)(1 + 4\pi\chi_0) - 4(\pi\chi_0)^2 \frac{(\omega_0^2 + c_\perp^2 k_\perp^2)^2}{c^2 k_\perp^2}. \qquad (22)$$

A comparison of (22) with (17) and (18) shows that as the value of the wave number $k_\perp$ decreases, the nature of spatial localization of collective dipole-exchange spin-wave excitations with the energy–momentum relation (21) near the MSL surface changes since the type of collective dipole-exchange spin-wave excitations in MSL in the short-wave limit are two-partial ($q_{1,2}^2 > 0$) spin waves with the energy–

momentum relation (22), whose range on the plane of the parameters $\omega$ and $k_\perp$ is restricted by the condition $k_\perp^2 > k_*^2$ for $k_\perp$.

In order to obtain the spectrum of the surface collective spin-wave mode (21), (22) in the long-wave limit, we must take into account the finite size of the MSL: $2D = NL < \infty$ ($-D < z < D$). If the boundary conditions (10) are satisfied on both surfaces of the MSL, the energy–momentum relation for the spectrum of the mode of collective spin-wave excitations of the dipole-exchange type localized near the MSL surface for $D < \infty$ can be presented (taking into account relations (17), (18) and the symmetry of spin oscillations relative to the plane $z = 0$) in the form

$$q_1 \left( q_2^2 - \frac{\omega_0^2 + c_\perp^2 k_\perp^2 - \omega^2}{c^2} \right) [q_2 + k_\perp \coth(q_2 D)]$$

$$= q_2 \left( q_1^2 - \frac{\omega_0^2 + c_\perp^2 k_\perp^2 - \omega^2}{c^2} \right) [q_1 + k_\perp \coth(q_1 D)];$$

$$q_1 \left( q_2^2 - \frac{\omega_0^2 + c_\perp^2 k_\perp^2 - \omega^2}{c^2} \right) [q_2 + k_\perp \tanh(q_2 D)]$$

$$= q_2 \left( q_1^2 - \frac{\omega_0^2 + c_\perp^2 k_\perp^2 - \omega^2}{c^2} \right) [q_1 + k_\perp \tanh(q_1 D)].$$

$$(23)$$

It can easily be verified that, in the limiting case $k_\perp D \to \infty$, relations (23) coincide with the energy–momentum relation for the spectrum (21), (22) of surface spin–wave excitations in a semi-infinite MSL.

In the long-wave limit $k_\perp D \ll 1$, it follows from (23) that the spectrum of mode of dipole-exchange spin wave excitations, which is quasi-homogeneous over the thickness of the MSL under investigation, can be written in the form

$$\omega^2 \cong [\omega_0^2 + c_\perp^2 k_\perp^2 + D k_\perp (\omega_0^2 + c_\perp^2 k_\perp^2)(1 + 4\pi\chi_0)]$$

$$\times (1 + D k_\perp)^{-1}. \qquad (24)$$

A comparison of this expression with the results of the above classification of possible types of collective dipole-exchange spin-wave excitations in MSL (7) shows that if the MSL thickness $2D$ is smaller than a certain critical thickness

$$D_* \cong \frac{2c}{1 + 4\pi\chi_0} \left( \frac{4\pi\chi_0}{\omega_0^2} \right)^{1/2}, \qquad (25)$$

relation (24) for small $k_\perp$ defines a dispersion curve of the bulk mode ($q_{1,2}^2 > 0$) of the spectrum of dipole-exchange oscillations, which is quasi-homogeneous over the MSL thickness $2D$, transformed into the dispersion curve for a two-partial generalized surface spin wave for $k_\perp \neq 0$.

If, however, the condition $D > D_*$ is not satisfied (while the condition of the fine-layer structure of the magnetic superlattice is observed as before), formula (24) defines the energy–momentum relation for a generalized surface spin wave (Re $q_{1,2}^2 \neq 0$; Im $q_{1,2}^2 \neq 0$) for any $k_\perp D \ll 1$.

As regards other modes of the spectrum (7) of bulk dipole-exchange spin-wave excitations in MSL, whose energy–momentum relations are defined by formulas (23) under the conditions (9) and (10), it can be easily shown that

the nonlocal nature of interaction between the layers ($c \neq 0$) can lead to a resonant interaction between propagating bulk dipole-exchange oscillations with labels $\nu$ and $\rho$. In the vicinity of the point of intersection, their energy–momentum relation can be written in the form

$$(\omega^2 - \Omega_\nu^2)(\omega^2 - \Omega_\rho^2) - \xi_{\nu\rho}^2 \Omega_\nu^2 \Omega_\rho^2 \cong 0,$$

$$\Omega_\nu^2 = \left[ \omega_0^2 + c_\perp^2 k_\perp^2 + c^2 \left( \frac{\pi\nu}{D} \right)^2 \right] \left[ 1 + 4\pi\chi_0 \frac{k_\perp^2}{k_\perp^2 + (\pi\nu/D)^2} \right]. \quad (26)$$

$$(|\xi_{\nu\rho}^2| \leqslant 1; \quad \nu, \rho = 1, 2, \ldots).$$

The dimensionless parameter $\xi_{\nu\rho}^2$ is equal to zero if both outer surfaces of the MSL of finite thickness under investigation are metallized, while spins are rigidly fixed.

## CONCLUSION

The results of this research show that the nonlocal nature of indirect interlayer interaction through conduction electrons of a nonmagnetic layer in a magnetic superlattice of the ferromagnet–nonmagnetic metal type (taken into account consistently) may lead to the formation of a dipole-exchange spin wave near the MSL surface. It is shown that the localization of this type of collective spin-wave excitations near the MSL surface is determined to a considerable extent by the magnitude of the wave number $k_\perp$ and by the thickness $D$ of the magnetic superlattice.

The quasi-diagonal structure of the magnetic susceptibility tensor (8) analyzed here is typical of many kinds of equilibrium magnetic configurations, including antiferromagnets.[6] It can easily be proved that if a quasi-antiferromagnetic mode plays the role of the low-frequency mode in the spin-wave spectrum of such an infinite magnet, all the above calculations and conclusions remain in force

provided that $\mathbf{n} \perp \mathbf{h} \| \mathbf{k}_\perp \| \mathbf{H}$, and the spins on the surface of the magnet are completely free. If, however, the low-activation mode in the magnon spectrum is a quasi-ferromagnetic mode, the necessary condition for the formation of a generalized surface dipole-exchange spin wave on the basis of this mode is $\mathbf{k}_\perp \perp \mathbf{H} \| \mathbf{n} \perp \mathbf{h}$ under the same boundary conditions.

According to calculations, the type of the surface dipole–exchange spin wave analyzed by us can also be observed for a ferromagnet–nonmagnetic metal type MSL with $\mathbf{H} \| \mathbf{n}$.

*E-mail: bogdanov@host.dipt.donetsk.ua

[1] A. Fert, P. Grunberg, A. Barthelemy *et al.*, J. Magn. Magn. Mater. **140–144**, 1 (1995).

[2] N. S. Almeida and D. L. Mills, Phys. Rev. B **38**, 6698 (1988); *ibid.* **39**, 12339(E) (1989).

[3] N. Raj and D. R. Tilley, Phys. Rev. B **36**, 7003 (1987).

[4] F. G. Bass, A. A. Bulgakov, and A. P. Tetervov, *High-Frequency Properties of Semiconductors with Superlattices* [in Russian], Nauka, Moscow (1989).

[5] A. F. Zhuravlev and B. I. Khudik, Preprint Inst. Theor. Phys., National Academy of Sciences of the Ukraine, Kiev (1986).

[6] A. I. Akhiezer, V. G. Bar'yakhtar, and S. V. Peletminskiĭ, *Spin Waves*, No. Holland, Amsterdam, 1968.

[7] E. A. Turov, *Physical Properties of Magnetically Ordered Crystals*, Academic Press, NY, 1965.

[8] A. G. Gurevich, *Magnetic Resonance in Ferro- and Antiferromagnets* [in Russian], Nauka, Moscow (1973).

[9] M. I. Kaganov and V. M. Tsukernik, Zh. Éksp. Teor. Fiz. **34**, 106 (1958) [Sov. Phys. JETP **7**, 73 (1958)].

[10] D. Mattis, *The Theory of Magnetism*, New York (1965).

Translated by R. S. Wadhwa

# Magnetic structure of the ferro–antiferromagnet interface. II. Compensated interface

A. G. Grechnev

*Kharkov State University, 310077 Kharkov, Ukraine**

A. S. Kovalev

*B. Verkin Institute for Low Temperature Physics and Engineering,
National Academy of Sciences of the Ukraine, 310164 Kharkov, Ukraine***

A compensated ferro–antiferromagnet interface is studied in the framework of a discrete
classical spin model. The phase diagram is presented for the possible collinear and canted magnetic
structures of the interface. The change in magnetization upon a transition from a collinear
structure to canted form is studied.   © *1998 American Institute of Physics.*
[S1063-777X(98)00409-5]

The problem of coexistence of ferromagnetic (FM) and antiferromagnetic (AFM) phases was first encountered while studying cobalt microparticles with an oxidized (CoO) surface. Meiklejohn and Bean[1] discovered the phenomenon of hysteresis loop displacement (exchange bias) for this system. Almost simultaneously, Vlasov and Mitsek[2] began their investigations of disordered alloys of the type Co/CoO containing inclusions of AFM grains in the FM matrix. The discovery of the giant magnetoresistance effect triggered intensive theoretical and experimental studies of multilayered magnetic systems with alternating FM and AFM layers (Fe/Cr, Co/CoO, etc.).[3] The theoretical description of magnetic properties of interfaces is usually based on classical models of magnets in the exchange approximation. For example, Mauri *et al.*[4] and Koon[5] describe the phenomenon of exchange bias using the micromagnetic approach. Stamps *et al.*[6] studied FM resonance in two-layered FM/FM and FM/AFM systems and, in particular, in the system Co/CoO. In all these works, layers of finite thickness (several atomic spacings) are considered. It is found that the structure of boundaries and frequencies of spin waves are determined essentially by this thickness.

In this work as well as in our previous publication,[7] we have proposed simple theoretical models for the interface of semi-infinite easy-axis FM/AFM systems. These models can be used to analyze the magnetic structure of the interface and the existence of localized spin-wave modes in its vicinity. Two models with identical primitive cubic lattices of FM and AFM halfspaces but with different magnetic ordering of the AFM are considered. It is shown that for a layered AFM (Fig. 1a, model I proposed in Ref. 7) and an AFM with a staggered ordering (Fig. 1b, model II proposed in the present work), the systems have quite different static and dynamic properties. Although real systems usually have a more complicated geometry, the models proposed here provide a qualitative description of uncompensated[4,6] and compensated[5] FM/AFM interfaces, respectively.

From topological point of view, models I and II are quite different. In the first model, the period of the magnetic structure in a direction parallel to the interface coincides with the lattice period, while in the second case it is equal to double the atomic spacing. Hence the collinear structure with ''correct'' ordering of FM and AFM halfspaces in model I (Fig. 1a) corresponds to the ground state of the system for all values of the parameters of the magnets. In model II, a collinear structure with such an ideal order (Fig. 1b) corresponds to a totally frustrated FM/AFM interface. In case I, the domain walls parallel to the FM/AFM interface may intersect it and get transformed from FM to AFM wall. (The existence of such domain walls was first indicated by Mauri *et al.*[4]) Hence a description and classification of nontrivial states in a layered AFM was naturally carried out in terms of collinear and canted domain walls interacting with the interface of the magnets.[7] In the case of a compensated FM/AFM interface, the domain wall vanishes at the interface. Hence possible collinear and canted magnetic structures in this case differ significantly from those in model I.

In the present work, we study the static configurations of the interface between an FM and an AFM with a ''staggered ordering'' (model II). An analogous model without one-ion anisotropy was considered by Matsushita *et al.*[8] The magnetic structure of the interface changes radically if the easy-axis anisotropy is taken into consideration, leading to localization of magnetization nonuniformity in its vicinity. Unlike the case of a layered AFM, this problem cannot be reduced to the investigation of a one-dimensional spin chain normal to the FM/AFM interface: it can be seen from Fig. 1b that odd and even spin columns are in different states.

In the classical Heisenberg's model, the system is described by the Hamiltonian

$$H=\sum_{m,\delta} \frac{J_{m,\delta}}{2}\,(\mathbf{S}_m\cdot\mathbf{S}_{m+\delta})+\sum_m \frac{B_m}{2}\,(\mathbf{S}_m\cdot\mathbf{e})^2, \qquad (1)$$

where $m$ is a lattice site, $\delta$ its nearest neighbors, $\mathbf{S}_m$ the spin vector at this site, $J_{m,\delta}=-J_f$ and $J_{m,\delta}=J_a$, respectively, for FM and AFM halfspaces, $J_{m,\delta}=J_{fa}$ for exchange across the interface ($J_f, J_a, J_{fa}>0$), $B_m=B_f$ and $B_m=B_a$ are one-ion
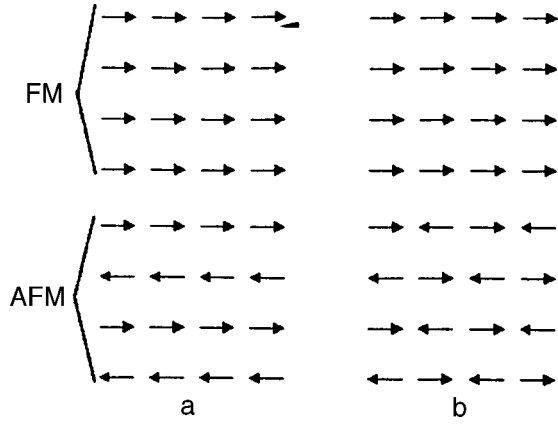
FIG. 1. Interface between an FM and an AFM for the case of a layered AFM (a), and for its ''staggered'' ordering (b).

anisotropy constants for FM and AFM halfspaces respectively, and $B_f$, $B_a > 0$ for the easy-axis anisotropy.

Depending on the values of the parameters $J$ and $B$, the ground state of the system for model II is one of the three collinear structures ($A$, $B$, and $C$), or the canted structure $S$ (see Fig. 2). Other collinear and canted structures are also possible for very large values of the anisotropy constant. They correspond to domain walls confined by the Peierls relief at a finite distance from the FM/AFM interface, and local energy minima. Since we are interested only in the ground state of the system, we shall not discuss such structures here.

Instead of the initial seven parameters of the model, it is expedient to consider four dimensionless quantities

$$\beta_f = \frac{B_f}{J_f}, \quad \beta_a = \frac{B_a}{J_a}, \quad \rho = \left(\frac{J_a}{J_f}\right)^{1/2} \frac{S_a}{S_f}, \quad j = \frac{J_{fa}}{\sqrt{J_a J_f}}. \quad (2)$$

The collinear structure energy values (per unit cell on the interface) are given by

$$E_A = 2J_{fa}S_a S_f = 2E_0 j, \quad E_B = 10J_f S_f^2 = \frac{10E_0}{\rho},$$

$$E_C = 10J_a S_a^2 = 10E_0 \rho, \quad (3)$$

where $E_0 = \sqrt{J_f J_a} S_f S_a$.

Let us find the relations between parameters corresponding to a bifurcation transition from collinear (CS) to canted (noncollinear) structure (NS). It is well known that if one of the eigenfrequencies of the system becomes equal to zero, it
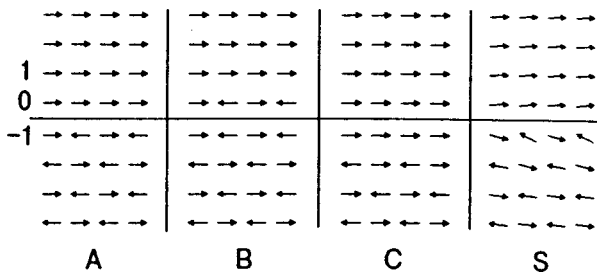


FIG. 2. Collinear interface structures ($A,B,C$) and the canted structure $S$ $\beta_f = 0.2$, $\beta_a = 0.3$, $\rho = 0.4$, $j = 0.9$.

undergoes a transition with a spontaneous symmetry breaking. Using the magnetization dynamics equation in polar coordinates (the $z$-axis coincides with the anisotropy axis)[9]

$$\sin \theta_m \frac{d\varphi_m}{dt} = -\frac{1}{\hbar S_n} \frac{\partial H}{\partial \theta_m}, \quad \sin \theta_m \frac{d\theta_m}{dt} = \frac{1}{\hbar S_m} \frac{\partial H}{\partial \varphi_m}, \quad (4)$$

where $\mathbf{S}_m = S_m(\sin \theta_m \cos \varphi_m, \sin \theta_m \sin \varphi_m, \cos \theta_m)$, we find that the quantity $d\varphi_m/dt = \omega$ in a CS defines the spin precession frequency around the easy axis, which vanishes at the CS–NS transition point.

In the equilibrium position of collinear structures, angle $\theta_m$ is equal to 0 or $\pi$. At the sites corresponding to $\theta_m = \pi$ in equilibrium, we introduce a new notation for the small angle of spin rotation $\theta_m \to \theta_m + \pi$. The CS–NS transition is determined by the condition of existence of nontrivial solutions of linearized static equations

$$\left. \frac{\partial H}{\partial \theta_m} \right|_{\theta_m \to 0} = 0. \quad (5)$$

The bulk Hamiltonian of the ferromagnet can be written in the form

$$H_F = -\sum_{m,\delta} \frac{J_f S_f^2}{2} \cos(\theta_m - \theta_{m+\delta}) + \sum_m \frac{B_f S_f^2}{2} \sin^2 \theta_m. \quad (6)$$

It can be seen from Fig. 1b that the system is periodic with a period $2a$ in the plane of the interface, $a$ being the lattice constant. Denoting by $\theta_n^{(1)}$ and $\theta_n^{(2)}$ the polar angles of even and odd spin columns, respectively, we obtain from (5) and (6) the equations for the ferromagnetic halfspace:

$$\theta_n^{(1)}(6+\beta_f) - 4\theta_n^{(2)} - \theta_{n-1}^{(1)} - \theta_{n+1}^{(1)} = 0,$$

$$\theta_n^{(2)}(6+\beta_f) - 4\theta_n^{(1)} - \theta_{n-1}^{(2)} - \theta_{n+1}^{(2)} = 0, \quad (7)$$

where $n$ is the layer number. These equations must be supplemented by the condition of decreasing $\theta_n^{(1)}$ and $\theta_n^{(2)}$ for $n \to +\infty$. The general solution of system (7) has the form

$$\theta_n^{(1)} = A_1 P_{f1}^n + A_2 P_{f2}^n, \quad \theta_n^{(2)} = A_1 P_{f1}^n - A_2 P_{f2}^n, \quad (8)$$

where

$$P_{f1} = P(\beta_f), \quad P_{f2} = P(8+\beta_f), \quad (9)$$

and

$$P(\beta) = 1 + \frac{\beta}{2} - \left(\beta + \frac{\beta^2}{4}\right)^{1/2}. \quad (10)$$

The solution for an antiferromagnet can be presented in an analogous form:

$$\theta_n^{(1)} = B_1 P_{a1}^{-n-1} + B_2 P_{a2}^{-n-1},$$

$$\theta_n^{(2)} = B_1 P_{a1}^{-n-1} - B_2 P_{a2}^{-n-1}, \quad (11)$$

where

$$P_{a1} = P(\beta_a), \quad P_{a2} = P(8+\beta_a). \quad (12)$$

Substituting the relations (8)–(12) into the static equations for four nonequivalent sites near the interface, we obtain a system of four linear homogeneous equations in un-
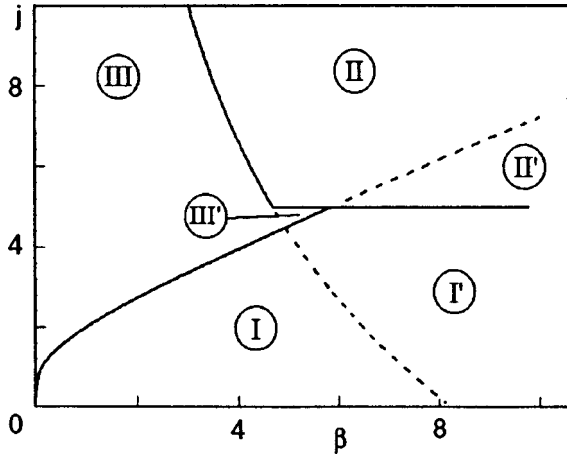
FIG. 3. Phase diagram of the FM/AFM interface for $\beta_f = \beta_a = \beta$ and $\rho = 1$.
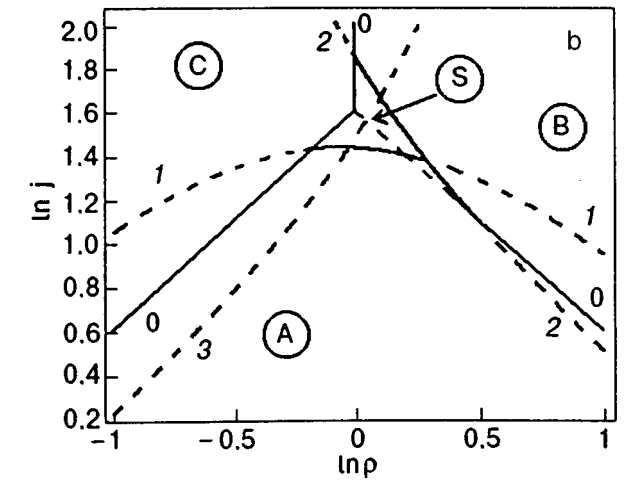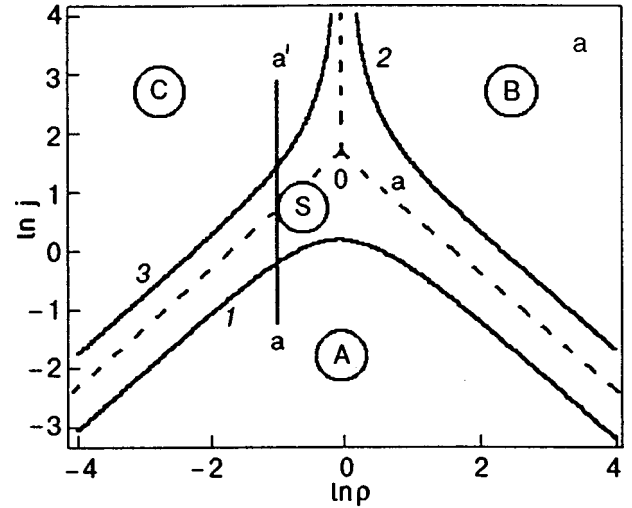


FIG. 4. Phase diagram of the FM/AFM interface for $\beta_f = 0.2$, $\beta_a = 0.3$ (a), and $\beta_f = 4$, $\beta_a = 5$ (b). Curves *1*, *2*, *3* are described by Eqs. (17), (18) and (19) respectively.

known parameters $A_1$, $A_2$, $B_1$ and $B_2$. For the collinear configuration $A$, for example, the equations for spin deviations (the number $n = 0$ corresponds to the first layer in the FM halfspace)

$$\theta_0^{(1)}(5 + \beta_f + \rho j) - 4\theta_0^{(2)} - \theta_1^{(1)} - \rho j \theta_{-1}^{(1)} = 0,$$

$$\theta_0^{(2)}(5 + \beta_f - \rho j) - 4\theta_0^{(1)} - \theta_1^{(2)} + \rho j \theta_{-1}^{(2)} = 0,$$

$$\theta_{-1}^{(1)}(5 + \beta_a + j/\rho) - 4\theta_{-1}^{(2)} - \theta_{-2}^{(1)} - j/\rho\,\theta_0^{(1)} = 0, \quad (13)$$

$$\theta_{-1}^{(2)}(5 + \beta_a - j/\rho) - 4\theta_{-1}^{(1)} - \theta_{-2}^{(2)} + j/\rho\,\theta_0^{(2)} = 0,$$

lead to the relations

$$A_1 F_{f1} + A_2 \rho j - B_2 \rho j = 0,$$

$$A_2 F_{f2} + A_1 \rho j - B_1 \rho j = 0,$$

$$B_1 F_{a1} + B_2 j/\rho - A_2 j/\rho = 0, \quad (14)$$

$$B_2 F_{a2} + B_1 j/\rho - A_1 j/\rho = 0,$$

where

$$F_{f,a1} = F(\beta_{f,a}), \quad F_{f,a2} = F(8 + \beta_{f,a}), \quad (15)$$

$$F(\beta) = \frac{\beta}{2} + \left(\beta + \frac{\beta^2}{4}\right)^{1/2}. \quad (16)$$

The equality to zero of the determinant of the system of equations (14) gives a relation between the critical values of the parameters $j$, $\rho$, $\beta_f$, and $\beta_a$:

$$j = \frac{F_{f1} F_{f2} F_{a1} F_{a2}}{(F_{f1}/\rho + F_{a1}\rho)(F_{f2}/\rho + F_{a2}\rho)}. \quad (17)$$

Analogously, we obtain

$$(\beta_f + F_{f1} + G_{f1})(-8 + \beta_f + F_{f2} + G_{f2})$$

$$= F_{f1} F_{f2}(\beta_f + G_{f1})(-8 + \beta_f + G_{f2}); \quad (18)$$

for structure $B$, and

$$(\beta_a + F_{a1} + G_{a1})(-8 + \beta_a + F_{a2} + G_{a2})$$

$$= F_{a1} F_{a2}(\beta_a + G_{a1})(-8 + \beta_a + G_{a2}), \quad (19)$$

for structure $C$, where

$$G_{f1,2} = j\rho\left(1 - \frac{1}{1 + F_{a1,2}\rho/j}\right),$$

$$G_{a1,2} = j/\rho\left(1 - \frac{1}{1 + F_{f1,2}/(\rho j)}\right). \quad (20)$$

Formulas (17)–(19) and (3) can be used to determine the ground state of the system as a function of the parameters $\beta_f$, $\beta_a$, $\rho$, and $j$. In other words, we can construct the phase diagram of the system in the four-dimensional space of these parameters.

Parameter $\rho$ characterizes the difference in the magnetic properties of FM and AFM, while parameter $j$ describes the role of the interface as a localized magnetic defect. For a graphic representation, let us first consider the particular case $\beta_f = \beta_a = \beta$ and $\rho = 1$, when magnets in two halfspaces are characterized by the same anisotropy constants and the same value of the exchange interaction. In this case, the interface affects the form of the ground state as a magnetic point defect. Figure 3 shows the $\beta$ vs. $j$ plane and the interfaces between various phases. In this case, formulas (18) and (19) coincide, and the collinear structures $B$ and $C$ have the same
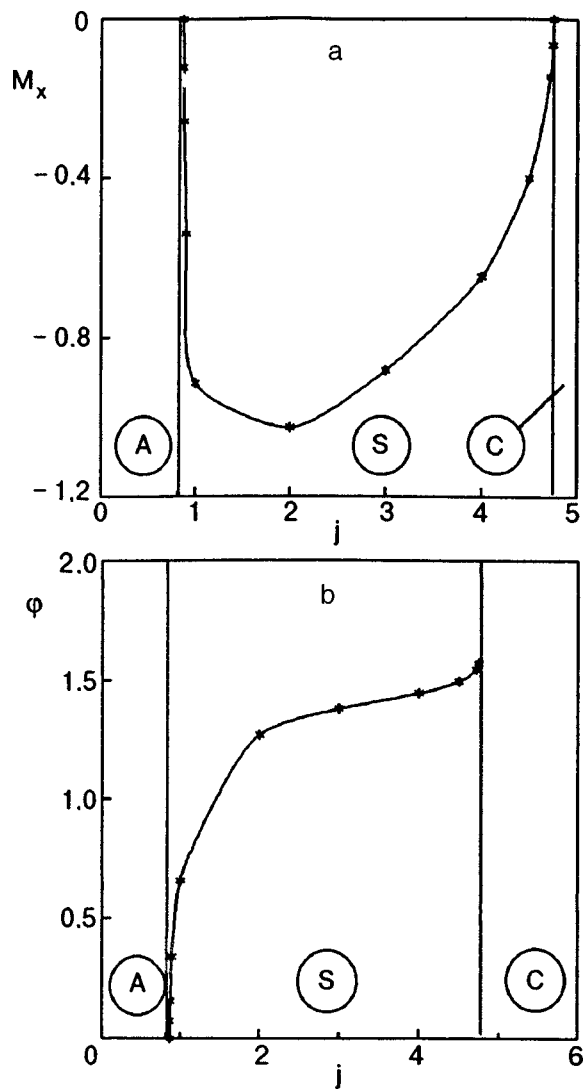
FIG. 5. Variation of the canted phase structure with $j$ for $S_f = S_a = 1$, $\beta_f = 0.2$, $\beta_a = 0.3$, $\rho = 0.4$; dependence of the $x$-component of the total magnetization (a). Angle of rotation of the antiferromagnetism vector in the AFM layer adjoining the interface (b).

energy. The collinear phase $A$ is the ground state in regions $I$ and $I'$. In addition to the principal energy minimum corresponding to phase $A$, the region $I'$ also contains additional local minima with higher energies corresponding to collinear phases $B$ and $C$. The principal minimum in regions $II$ and $II'$ corresponds to phases $B$ and $C$ (the metastable phase $A$ can also exist in the region $II'$). Finally, the regions $III$ and $III'$ correspond to the canted phases $S$, while metastable phases $B$ and $C$ can exist in the region $III'$.

In order to study the effect of nonidentical nature of magnets on the ground state of the system, we construct the phase diagram in the $(\ln \rho, \ln j)$ plane for fixed values of $\beta_f$ and $\beta_a$ (Fig. 4). Figure 4a shows the phase diagram for relatively small $\beta_f$ and $\beta_a$. In this case, the regions of three

collinear structures $A$, $B$, and $C$ are separated from one another by a canted structure $S$. On the straight line segments $j = 5/\rho$, $j = 5\rho$, and $\rho = 1$, the energies of two collinear phases become equal. Curves $1$, $2$, and $3$ separating the regions of collinear phases from the region of canted phase are described by Eqs. (17), (18) and (19) respectively. The phase diagram changes for large values of $\beta_f$ and $\beta_a$ (Fig. 4b). As before, the energies of collinear phases are equal on straight line segments, but these segments can now intersect with lines $1$, $2$, $3$ defined by Eqs. (17)–(19). The interfaces are marked in the figure by solid lines. It can be seen that for large anisotropies, a direct transition between collinear phases can occur without the formation of an intermediate canted phase. An analysis of formula (18) shows that the structure $B$ does not exist for $\beta_f < 0.011324$, while for $\beta_f > 8.234057$ it is a local energy minimum for all values of $\rho$ and $j$, and the bifurcation transition $B \rightarrow S$ does not occur. The same is also true for $\beta_a$ and the structure $C$.

The specific form of the canted structure was determined through a numerical search of the configuration with the lowest energy using the relaxation method. A change in the system parameters causes a rearrangement of the canted phase structure accompanied by a change in the total magnetization of the system and a rotation of the magnetization and antiferromagnetism vectors. Figure 5a shows the variation of the $x$ component of total magnetization (the $x$-axis is chosen in a direction perpendicular to the FM/AFM interface) upon a change in the parameter $j$ for fixed values of $\rho, \beta_f$ and $\beta_a$ ($\rho = 0.4$, $\beta_f = 0.2$, $\beta_a = 0.3$) i.e., along the line $aa'$ in Fig. 4a. Figure 5b shows the variation of the angle of rotation of the antiferromagnetism vector in the atomic layer adjoining the FM/AFM interface from the value $\varphi = 0$ in the $A$-phase to the value $\varphi = \pi/2$ in the $C$-phase.

*E-mail: grechnev@ilt.kharkov.ua
**E-mail: kovalev@ilt.kharkov.ua

[1] W. P. Meiklejohn and C. P. Bean, Phys. Rev. **102**, 1413 (1956).
[2] K. B. Vlasov and A. I. Mitsek, Fiz. Met. Metalloved. **14**, 487 (1962).
[3] R. E. Camley and R. L. Stamps, J. Phys.: Condens. Matter **5**, 3727 (1993).
[4] C. Mauri, H. C. Siegmann, P. S. Bagus, and E. Kay, J. Appl. Phys. **62**, 3047 (1987).
[5] N. C. Koon, Phys. Rev. Lett. **78**, 4865 (1997).
[6] R. L. Stamps, R. E. Camley, and R. J. Hicken, Phys. Rev. B **54**, 4159 (1996).
[7] A. G. Grechnev and A. S. Kovalev, Fiz. Nizk. Temp. **24**, 340 (1998) [Low Temp. Phys. **24**, L57 (1998)].
[8] Y. Matsushita, M. P. Gelfand, and C. Ishii, J. Phys. Soc. Jpn. **66**, 3648 (1997).
[9] A. M. Kosevich, B. A. Ivanov, and A. S. Kovalev, *Nonlinear Magnetization Waves. Dynamic and Topological Solitons* [in Russian], Naukova Dumka, Kiev (1983).

Translated by R. S. Wadhwa

# Instability of a one-dimensional quantum antiferromagnet under magnetic anisotropy

D. M. Apal'kov

*Kharkov State University, 310077 Kharkov, Ukraine;*
*B. I. Verkin Institute for Low Temperature Physics and Engineering, National Academy of Sciences of the Ukraine, 310164 Kharkov, Ukraine*

A. A. Zvyagin

*B. I. Verkin Institute for Low Temperature Physics and Engineering,*
*National Academy of Sciences of the Ukraine, 310164 Kharkov, Ukraine\**

It is shown by using the exact quantum-mechanical solution that a one-dimensional antiferromagnetic Heisenberg spin chain is unstable to the emergence of an easy-plane magnetic anisotropy in a real three-dimensional crystal. It is shown that the magnetic anisotropy is due to a Jahn–Teller type effect, i.e., a strong spin–lattice coupling. A change in the equilibrium position of ligands induces magnetic anisotropy in the spin chain. © *1998 American Institute of Physics.* [S1063-777X(98)00509-X]

Many theoretical and experimental works have been devoted in recent years to investigations of low-dimensional quantum antiferromagnets (AFM) at low temperatures. Low-dimensional low-symmetry magnets began to be studied in Kharkov over 30 years ago. The late A. I. Zvyagin, Corresponding Member of the National Academy of Sciences of the Ukraine, whose 60th birthday was celebrated recently, was one of the pioneers in the field of experimental studies in this field. One of the authors (A.A.Z) is deeply indebted to late A. I. Zvyagin for introducing him to this interesting field of physics.

Among other things, several quantum AFM in which the interaction of spins along certain directions is $10^2 - 10^4$ times stronger than along other directions of the crystal lattice have been synthesized during the last decade.[1,2] Such magnets usually undergo a phase transition to the ordered (three-dimensional) magnetic state at very low temperatures ($T_c \sim 1$ K). At temperatures higher than $T_c$ but lower than, or of the order of, the characteristic energy of exchange interaction along a preferred direction, such magnets display the properties of one-dimensional magnetic chains. Quantum fluctuations in one-dimensional systems are often enhanced due to singularities in the density of states. Hence approximate theoretical methods can give even qualitatively erroneous results for one-dimensional quantum systems. Thus, theoretical studies of essentially many-particle effects in a one-dimensional AFM spin chain require a precise quantum-mechanical approach like Abelian and non-Abelian bosonization and the Bethe ansatz method.[3]

Among the large number of low-dimensional spin systems studied in recent years, systems with lattice site spins $S = 1/2$ (e.g., $Cu^{2+}$ [Ref. 1] or $V^{4+}$ [Ref. 2] ions) are especially significant. The magnetic behavior of many rare-earth ions at low temperatures can be described by the effective Hamiltonian of spins $S = 1/2$. In other words, the lowest spin-doublets play the dominant role at low temperatures. It

should be noted, however, that such a description introduces a strong anisotropy in the magnetic properties of such models: these systems are transformed into Ising-type or $XY$-type systems depending on which two levels (doublets) of the total angular momentum of the corresponding $f$-orbital of the magnetic ion have a lower energy.[4]

It is well known that magnetic anisotropy plays a significant and fundamental role in the spin systems during a theoretical analysis of the magnetic properties of such systems at low temperatures.[5] Magnetic anisotropy is manifested in the removal of degeneracy (in the direction of quantization of the total spin of the system). Such a situation emerges in many-particle AFM spin systems in which the Heisenberg AFM spin–spin interaction is isotropic, and hence the spin directions along all lattice vectors are equivalent from the energy point of view. Magnetic anisotropy leads to a situation when some crystallographic directions become more advantageous from the energy point of view. In this case, the total spin of the system is no longer an integral of motion (in other words, its operator does not commute with the spin Hamiltonian of the system). The magnetic anisotropy is a manifestation of the crystal (electric) field of ligands (i.e., of the neighboring nonmagnetic ions).[4] This field interacts with the spin subsystem of electrons of magnetic ions through spin–orbit coupling (which is usually weak). Hence the variation (emergence) of magnetic anisotropy is due to a variation of the symmetry of neighboring nonmagnetic ionic lattice sites. The emergence of an axial magnetic anisotropy in the spin subsystem lowers the symmetry of spins from $SU(2)$ for the Heisenberg model to $U(1)$ for the axial model. The magnetic anisotropy may be of single-ion or interionic type.[4,5] In this work, we shall consider essentially many-particle spin systems, and hence consider the effect of interionic magnetic anisotropy at the very outset. As a matter of fact, the spin system $S = 1/2$ can exhibit only this type of anisotropy.

We shall show that at low temperatures, a one-dimensional AFM Heisenberg chain of spins $S = 1/2$ is unstable to the emergence of an easy-plane type magnetic anisotropy. This magnetic anisotropy appears owing to a slight distortion of nonmagnetic ions, i.e., of the three-dimensional (nonmagnetic) lattice and, as a result, a change in their crystal fields. The results are obtained in the mean-field approximation. This approximation is well substantiated since the lattice is three-dimensional in spite of the fact that the spin–spin exchange interaction in this system is one-dimensional. Hence we can certainly use the mean-field approach in this case. Moreover, we shall study the instability of magnetically isotropic homogeneous systems to uniform deformation which produces a uniform magnetic anisotropy along the entire chain. This means that we shall not consider the probability of phase transition to the noncommensurate phases (states). In other words, the phonon which removes the spin degeneracy has a commensurate wave vector (quasimomentum) and the instability of the AFM Heisenberg chain is mainly determined by this phonon. We shall also consider the effect of an external magnetic field and nonzero temperature on the above-mentioned instability.

The instability considered in this work is quite similar to a Peierls-type phase transition in the chain of spins $S = 1/2$ in the $XY$-model.[6,7] The spontaneous emergence of the biaxial magnetic anisotropy in the $XY$-model with spins $S = 1/2$ was predicted by Borovik and Zvyagin.[8] In all the above-mentioned works, the Hamiltonian of the $XY$ chain of spins was mapped (by using Jordan–Wigner transformation[9]) onto the Hamiltonian of a noninteracting linear chain of spinless fermions (whose Hamiltonian is a quadratic form of fermion operators of creation and annihilation of spinons). In other words, effectively noninteracting fermion systems were considered in Refs. 6, 7, and 8. We shall consider a one-dimensional Heisenberg AFM chain of spins $S = 1/2$ which can be mapped with the help of Jordan-Wigner transformation onto a one-dimensional spinless fermion system with two-particle interaction. Hence we shall essentially study the many-particle cooperative Jahn–Teller effect in an interacting one-dimensional quantum spin system.

The Hamiltonian of a periodic chain of $N$ spins $S = 1/2$ with antiferromagnetic interaction has the form

$$\mathcal{H}_0 = -\frac{1}{2}\sum_{n=1}^{N}(\sigma_n^x \sigma_{n+1}^x + \sigma_n^y \sigma_{n+1}^y + \Delta\sigma_n^z \sigma_{n+1}^z), \qquad (1)$$

where $\sigma_n^\alpha$ ($\alpha = x, y, z$) are Pauli operators of the $\alpha$-component of the spin in the $n$th position, the exchange constant is equal to unity, and $\Delta$ is the parameter of (interionic) magnetic anisotropy (note that $|\Delta| > 1$ corresponds to the "easy-axis" type anisotropy, while $|\Delta| < 1$ describes the "easy-plane" type magnetic anisotropy. The case $\Delta = -1$ corresponds to an isotropic AFM spin chain). The wave function with $M$ spins oriented downwards may be determined in the form of Bethe ansatz, i.e., in the form of a superposition of plane waves:

$$\Psi = \sum_{x_1 < x_2 < \ldots < x_M} \sum_P A_P \exp\left(i\sum_{j=1}^{M} p_{P_j} x_j\right)|x_1 \ldots x_M\rangle, \qquad (2)$$

where $x_j$ are coordinates of the downward oriented $j$-spin, $p$ are quasimomenta (conjugate to coordinates), and $P$ stands for all possible transpositions. The vector $|x_1 \ldots x_M\rangle = \sigma_{x_1}^- \ldots \sigma_{x_M}^-|0\rangle$ where $|0\rangle$ is the state with completely polarized spins: all spins are directed upwards (ferromagnetic state), and $\sigma_n^\pm = \sigma_n^x \pm i\sigma_n^y$ are the operators corresponding to an increase and decrease in the $z$-component of the spins. The energy of such an AFM chain with $M$ spins directed downwards is defined as

$$E_{\text{mag}} = -\frac{N\Delta}{2} + 2\sum_{j=1}^{M}(\Delta - \cos p_j). \qquad (3)$$

The values of the quasimomenta parametrizing the eigenfunctions and eigenvalues of the Schrödinger equation are obtained from the periodic boundary conditions in the form of the familiar Bethe ansatz equations:

$$Np_j = 2\pi I_j - \sum_{l=1, l\neq j}^{M} \theta(p_j, p_l), \qquad (4)$$

where

$$\theta(p_j, p_l) = 2\arctan$$
$$\times\left[\frac{\Delta\,\sin((p_j - p_l)/2)}{\cos((p_j + p_l)/2) - \Delta\,\cos((p_j - p_l)/2)}\right], \qquad (5)$$

and $I_j$ are integral (half-integral) numbers for odd (even) $M$. These numbers parametrize the eigenfunctions (2) and eigenvalues (3) in the quantum-mechanical problem under consideration. Obviously, the system is transformed into an isotropic $XX$ spin chain in the limit $\Delta \to 0$, and Eqs. (4) are transformed into the well-known periodic boundary conditions for a free one-dimensional lattice gas of fermions. Let $\Delta = -1 + x\delta$, where the parameter $x\delta$ characterizes the emergence of magnetic anisotropy ($x$ is the magnetoelastic constant and the parameter $\delta$ describes the distortion of symmetric configuration of nonmagnetic ligands). The magnetic anisotropy emerges due to a change in the crystal field of ligands and is therefore connected with a shift in the equilibrium position of the three-dimensional lattice of (nonmagnetic) ligands. In the first approximation in $\delta$, this process leads to an increase in the energy of the elastic subsystem:

$$E_{\text{el}} = NC\frac{\delta^2}{2}, \qquad (6)$$

where $C$ is the elastic constant. This means that a decrease in the magnetic energy in Eq. (3) caused by the magnetic anisotropy is accompanied (as expected) by an increase in the elastic energy. In other words, the removal of degeneracy of a Heisenberg AFM spin chain occurs owing to an effect of the type of the cooperative Jahn–Teller effect,[4] i.e., due to the effect of elastic subsystems on the electron subsystems. The energy of the spin subsystem defined by Eq. (3) can be determined exactly by using well-known results of classical

studies.[10] Let $\Delta \equiv -1 + x\delta = -\cos \mu$ ($x\delta > 0$) for the easy-plane type magnetic anisotropy. In this case, the Bethe ansatz equations (4) for an AFM spin chain can be solved in the thermodynamic limit (i.e., for $N \to \infty$, $M \to \infty$, and for a fixed value of $M/N$). These equations assume the form

$$\frac{\sin \mu}{\cosh \alpha - \cos \mu} = 2\pi\rho(\alpha)$$

$$+ \int_{-Q}^{Q} d\beta \rho(\beta) \frac{\sin 2\mu}{\cosh(\alpha - \beta) - \cos 2\mu},$$

$$(7)$$

where we have executed a change of variables from quasi-momenta $p_j$ to speeds $\alpha$ ($\rho(\alpha)$ is the density of quantum speeds $\alpha$ and these are the variables that will parametrize the eigenvalues and eigenvectors of the spin subsystem being considered here). The limits of integration $(-Q, Q)$ are defined by the quantity $M$ ($M = \int_{-Q}^{Q} d\alpha \rho(\alpha)$), i.e., they are connected with the total magnetization of our system. It was rigorously proved by Yang and Yang[10] that in the absence of an external magnetic field $h$, the speeds $\alpha$ completely cover the interval $[-\infty, \infty]$ for the AFM spin chain. The solution of Eq. (7) is obtained by using Fourier transformation. Substituting this solution into the thermodynamic limit of Eq. (3)

$$E_{\mathrm{mag}} = -\frac{N\Delta}{2} - N \int_{-Q}^{Q} d\alpha \rho(\alpha) \frac{2 \sin^2 \mu}{\cosh \alpha - \cos \mu}, \qquad (8)$$

we obtain for $h = 0$ ($Q = \infty$)

$$E_{\mathrm{mag}} = -N \sin \mu \int_{-\infty}^{\infty} dx \frac{\sinh(\pi - \mu)x}{\cosh(\mu x)\sinh(\pi x)} - N\Delta. \quad (9)$$

Let us find the minimum of the sum $E_{\mathrm{tot}} = E_{\mathrm{mag}} + E_{\mathrm{el}}$ over the distortion $\delta$ in the nonmagnetic lattice. The energy minimum for an AFM chain with ''easy plane'' type anisotropy is defined by the solution of the equation

$$C\delta_{\mathrm{eqv}} = \frac{\partial}{\partial \delta} \left[ \sin\{\mu(\delta)\} \right.$$

$$\left. \times \int dx \frac{\sinh[(\pi - \mu(\delta))x]}{\sinh(\pi x)\cosh[\mu(\delta)x]} + \Delta \right] \Bigg|_{\delta = \delta_{\mathrm{eqv}}}. \quad (10)$$

We construct the dependence of the total energy of the ground state (the lattice is assumed to be in the ground state irrespective of the complexity of the analysis) of the elastic and magnetic subsystems on the displacement $\delta$ of the three-dimensional nonmagnetic lattice of ligands. This dependence is shown in Fig. 1a for the value $C = 0.46$ of the elastic constant (note that we measure all quantities in units of isotropic exchange constant). It can be seen that the total energy minimum corresponds to a nonzero value of the lattice distortion. This means that the minimum energy in the ground state is associated with the displacement of three-dimensional nonmagnetic ions which, in turn, generates an electric field leading to a nonzero magnetic anisotropy of the one-dimensional AFM spin subsystem due to spin–orbit coupling.
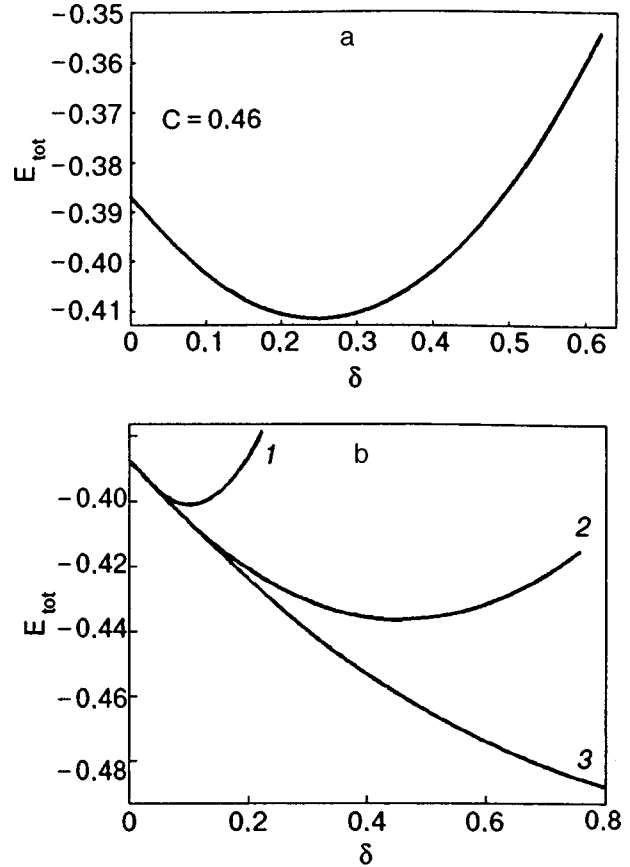


FIG. 1. Dependence of the total energy of the ground state of a magnetic and an elastic subsystems $E_{\mathrm{tot}}$ on the displacement $\delta$ of the position of nonmagnetic ions (ligands) in a crystal lattice for the elastic constant $C = 0.46$ (a) and for different values of $C$: 0.84 (1); 0.24 (2) and 0.14 (3) (b).

It can be asked whether such a behavior is observed for all values of the elastic constant $C$. Figure 1b shows the dependence of the total energy of the ground state of our system on displacement $\delta$ for several values of the elastic constant $C$. It can be observed that the minimum in $\delta$ associated with a nonzero displacement of ligand lattice is shifted towards decreasing $\delta$ upon an increase in the elastic constant $C$, while no minimum is observed for small $C$. This is obvious since the observation of the magnetic anisotropy effect in spin subsystems (which is usually quite small) requires quite large elastic displacements.

The analogous effect for $\Delta < -1$, i.e., for ''easy axis'' type magnetic anisotropy, can be studied in a similar manner. The Bethe ansatz equations (4) for this system are solved in the same way. After long but obvious computations, it is found that for all values of the elastic constant, the total energy minimum for the ground state of the spin and elastic subsystems corresponds to zero distortion $\delta$ of the three-dimensional ligand lattice. This means that there is no additional ligand electric field in this case, and hence there is no ''easy axis'' type magnetic anisotropy. This is an expected result since it is well known that in the case of Ising (''easy axis'') type magnetic anisotropy, the spectrum of low-lying excitations of an AFM chain of spins $S = 1/2$ in zero or weak magnetic fields is of gap (activation) type.

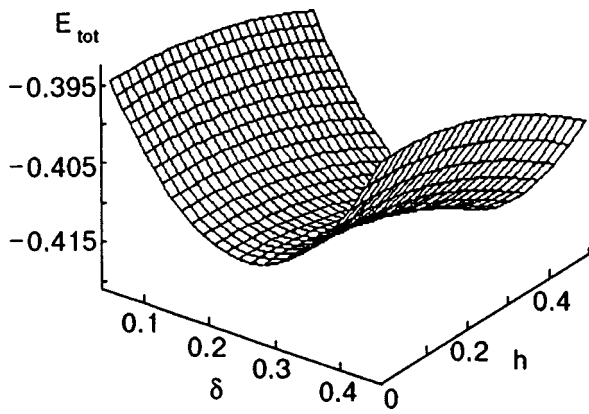Let us try to determine the behavior of such an unstable

FIG. 2. Dependence of the total energy of the ground state of a magnetic and an elastic subsystems $E_{tot}$ on the displacement $\delta$ and a weak applied magnetic field $h$.



FIG. 3. Dependence of the total free energy of a system on temperature $T$, lattice deformation $\delta$, and a weak applied magnetic field $h$. The temperatures are quite low in comparison with the exchange constant (unity).

one-dimensional Heisenberg AFM spin chain as a result of the emergence of ''easy plane'' type anisotropy in an external magnetic field $h$. We shall first consider the case of small magnetic fields $h \ll 1$. In this case, the Hamiltonian of the spin subsystem has the form

$$\mathcal{H} = H_0 - h \sum_n \sigma_n^z, \tag{11}$$

where $h = g\mu_B H$, $g$ is the gyromagnetic ratio, $H$ the magnetic field, and $\mu_B$ the Bohr magneton. Using the results obtained by Yang and Yang,[10] i.e., solving the integral equation (7) by the Wiener–Hopf method for very weak magnetic fields, we obtain

$$E_{mag} = E_{mag}\big|_{h=0} - Nh^2 \frac{\mu}{4\pi(\pi-\mu)\sin\mu}. \tag{12}$$

Having found the minimum of the total spin and elastic energy in the lattice displacement $\delta$, we can see that the ground state minimum energy for any weak field $h$ corresponds to the emergence of a nonzero minimum deformation $\delta$. The dependence of the total energy of the ground state of the spin and elastic subsystems on the external magnetic field $h$ and displacement $\delta$ of ligands in the three-dimensional lattice is shown in Fig. 2. It can be seen that for all magnetic fields $h$ there exists a minimum (corresponding to a nonzero displacement $\delta$) on the dependence of total energy on deformation.

In quite strong magnetic fields $h > h_c$, where $h_c$ is the critical field corresponding to a transition to the spin-polarized (''ferromagnetic'') state, the total energy $E_{tot}$ can be minimized in $\delta$, which gives

$$\delta_{eqv} = x/4C. \tag{13}$$

This means that in the present case, a strong external magnetic field also does not alter the situation significantly: the cooperative effect in the electric crystal spin subsystem and the distortion of the three-dimensional ligand lattice in the elastic subsystem lead to a nonzero ''easy plane'' type magnetic anisotropy. This means that the emergence of a ''easy plane'' type magnetic anisotropy in a Heisenberg AFM spin chain is independent of the applied magnetic field.
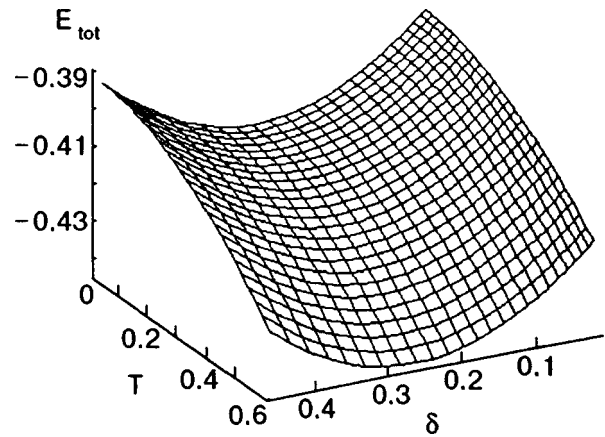
Earlier, we studied the properties of a Heisenberg quantum spin chain in the ground state. However, the behavior of the system at nonzero temperatures $T$ remains unclear. It can be easily shown that (in the present case of interionic magnetic anisotropy) the isotropic spin system will be stable at very high temperatures. This also follows from symmetry considerations: the high-temperature phase usually corresponds to a higher symmetry. It can be asked whether the critical temperature $T_c$ of such a cooperative Jahn–Teller type phase transition is equal to zero (which is usually true for one-dimensional systems in which 0 is the only singular point in temperature $T$), or a phase with a nonzero ''easy plane'' type magnetic anisotropy exists in a certain temperature interval for the spin chain $S = 1/2$. In order to answer this question, we can use the thermal Bethe ansatz[11] (for simplicity, we can consider only the low temperatures). At low temperatures, the familiar Sommerfeld expansion is valid (see, for example, Ref. 12):

$$E_{mag} = E_{mag} - N \frac{\pi T^2}{6v_F}, \tag{14}$$

where $v_F$ is the Fermi velocity of lowest excitations of the AFM chain (spinons). For zero magnetic field, this velocity can be determined easily: $v_F = \pi \sin(\mu)/\mu$.[10] We determine the minimum of the total free energy $E_{tot} = E_{mag} + E_{el}$ from the deformation $\delta$ of ligands (it should be recalled that we consider very low temperatures, i.e., assume that the elastic subsystem is still in the ground state). The assumption that the elastic subsystem is in the ground state is justified since its energy scale is usually higher than the energy scale of the magnetic subsystem. Figure 3 shows the dependence of the total free energy of the system on deformation $\delta$ and temperature (we consider the case of very low temperatures only). It can be seen that the minimum in the dependence on $\delta$ (corresponding to a nonzero displacement of the equilibrium, and hence to a nonzero magnetic anisotropy) exists at low temperatures and begins to vanish as the temperature is increased.
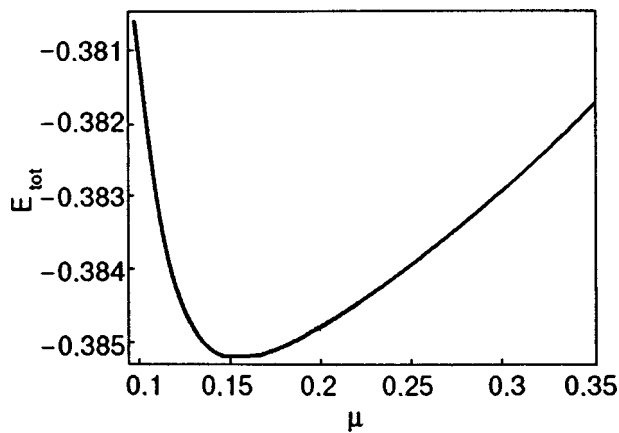
FIG. 4. Dependence of the total energy of the ground state of a magnetic and an elastic subsystems $E_{tot}$ on the displacement $\mu$ of nonmagnetic ions in the crystal lattice. The dependence of the magnetic anisotropy on the displacement parameter $\mu$ is nonlinear.

It can be assumed that an ''easy axis'' type magnetic anisotropy can also be expected for a fairly strong magnetic field (the field must be higher than the gap in an elementary spin excitation).

Note that the effect is independent of the manner in which a connection is established between the elastic and spin subsystems. The results are manifested qualitatively if we consider $E_{mag}$ as a function of $\mu$ and present the elastic energy in the form $E_{el}=NC\mu^2/2$ (see, for example, Ref. 7). Figures 4 and 5 show the dependence of the total energy of the magnetic and elastic subsystems in the ground state on displacement ($\mu$ in the present case), elastic constant $C$, and the magnetic field $h$ in the ground state. Figure 6 shows the dependence of the total free energy on temperature and displacement (at low temperatures). It can be seen that the energy minimum corresponds to a nonzero displacement of the ligand lattice. It is also obvious that the dependence of the total energy of the magnetic and elastic subsystems on the distortion of the three-dimensional nonmagnetic lattice does not depend qualitatively on the manner in which the displacement is caused, i.e., the effect does not depend on the choice of the model.

Unfortunately, we are not aware of experiments in systems with one-dimensional quantum AFM spin chains $S=1/2$ which could explicitly demonstrate the emergence of the spontaneous magnetic anisotropy. However, the results of recent experiments[13] on quasi-two-dimensional antiferromagnets $Ba_2CuGe_2O_7$ with $Cu^{2+}$ magnetic ions reveal that even for a fairly isotropic (square) spin lattice, the magnetic anisotropy must be taken into consideration for explaining the dependence of magnetization on the applied magnetic field. In our opinion, such an effect is an indirect confirmation of the predicted manifestation of the magnetic anisotropy, at least for a two-dimensional AFM Heisenberg system of spins 1/2. However, we believe that this effect must emerge for any AFM system of spins 1/2, whose ground state is not magnetically ordered and whose lowest excitations are gapless.

Summing up the results of our investigations, it can be stated that in this work we have studied a quantum one-
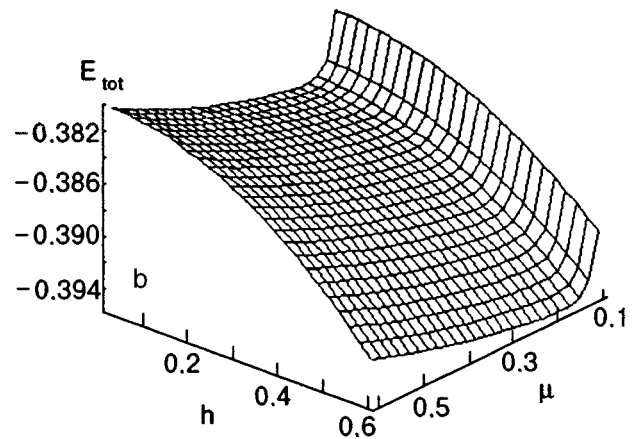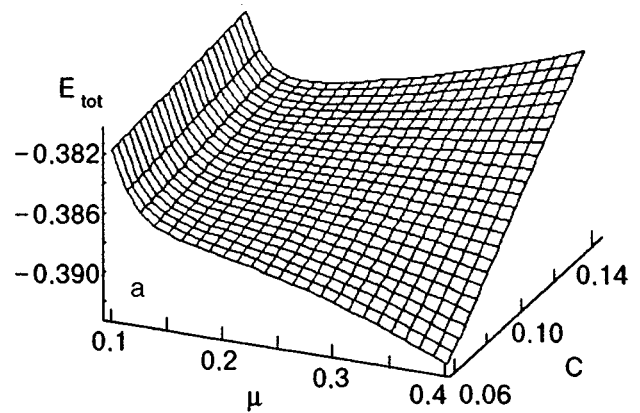


FIG. 5. Dependence of the total ground state energy of a magnetic and an elastic subsystems on the displacement $\mu$ and the elastic constant $C$ of the lattice (a) and on the weak applied magnetic field $h$ (b).

dimensional Heisenberg AFM chain of spins 1/2. It is shown that under the action of a three-dimensional lattice of nonmagnetic ions (ligands), the Heisenberg spin chain becomes unstable to the emergence of an ''easy plane'' type magnetic anisotropy. This cooperative Jahn-Teller type magnetoelastic effect is independent of the applied magnetic field. It is also shown that the phase with nonzero magnetic anisotropy exists in a certain nonzero interval of low temperatures. The instability studied in this work is analogous to the well-
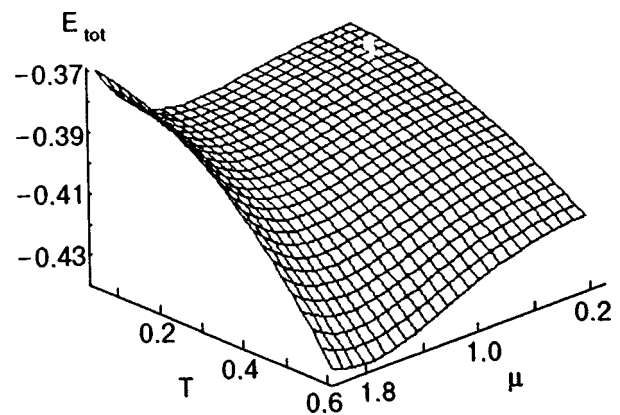


FIG. 6. Dependence of the total free energy of the system on temperature $T$ and lattice deformation $\mu$.

known Peierls instability of spin chains with $S = 1/2$.[6,7] However, this is the first theoretical work to our knowledge in which such cooperative effects are studied in a strongly interacting many-particle system. The microscopic source of the instability considered by us is the removal of degeneracy of the spin subsystem with an isotropic exchange interaction as a result of the emergence of magnetic anisotropy associated with a change in the electric field of nonmagnetic lattice ions.

*E-mail: zvyagin@ilt.kharkov.ua

[1] M. Hase, I. Terasaki, and K. Uchinokura, Phys. Rev. Lett. **70**, 3651 (1993).

[2] M. Isobe and Y. Ueda, J. Phys. Soc. Jpn. **65**, 1178 (1996); Y. Fujii, H. Nakao, T. Yosihama *et al.*, J. Phys. Soc. Jpn. **66**, 326 (1997); M. Isobe and Y. Ueda, Techn. Rep. ISSP **A3253** (1997).

[3] V. M. Korepin, N. M. Bogoliubov, and A. G. Izergin, *Quantum Inverse Scattering Method and Correlation Functions*, Cambridge Univ. Press, Cambridge (1993).

[4] A. K. Zvezdin, V. M. Matveev, A. A. Mukhin, and A. I. Popov, *Rare-earth Ions in Magnetically Ordered Crystals* [in Russian], Nauka, Moscow (1985).

[5] D. C. Mattis, *The Theory of Magnetism*, Springer-Verlag, Berlin (1981, 1985).

[6] P. Pincus, Solid State Commun. **22**, 1971 (1971); G. Beni and P. Pincus, J. Chem. Phys. **B57**, 3531 (1972); A. M. Kosevich and V. I. Khokhlov, Solid State Commun. **11**, 461 (1972).

[7] J. Y. Dubois and J. P. Carton, J. de Physique (Paris) **35**, 371 (1974); Y. Lepine and A. Caillé, J. Chem. Phys. **67**, 5598 (1977); C. Tannous and A. Caillé, Can. J. Phys. **57**, 508 (1979); Y. Lépine and A. Caillé, J. Chem. Phys. **71**, 3728 (1979); Y. Lepine, Phys. Rev. B **24**, 5242 (1981).

[8] A. E. Borovik and A. A. Zvyagin, Fiz. Tverd. Tela (Leningrad) **33**, 1587 (1991) [Sov. Phys. Solid State **33**, 894 (1990)].

[9] P. Jordan and E. Wigner, Z. Phys. **47**, 631 (1928).

[10] C. N. Yang and C. P. Yang, Phys. Rev. **150**, 327 (1966).

[11] M. Takahashi and M. Suzuki, Prog. Theor. Phys. **48**, 2187 (1972).

[12] H. W. J. Blöte, J. L. Cardy, and M. P. Nightingale, Phys. Rev. Lett. **56**, 742 (1986); I. Affleck, *ibid.*, p. 746.

[13] A. Zheludev, S. Maslov, G. Shirane *et al.*, Phys. Rev. B **56**, 14006 (1997).

Translated by R. S. Wadhwa

# Magnetic transport properties of semimagnetic semiconductor $Hg_{1-x-y}Cr_xMn_ySe$

V. D. Prozorovskiĭ, I. Yu. Reshidova, and A. I. Puzynya

*A. Galkin Physicotechnical Institute, National Academy of Sciences of the Ukraine, 340114 Donetsk, Ukraine**

S. Yu. Paranchich

*Yu. Fed'kovich State University, 274012 Chernovtsy, Ukraine*

Experimental results of investigations of monocrystalline samples of $Hg_{1-x-y}Cr_xMn_ySe$ solid solution indicate, first, a considerable influence of manganese atoms introduced in $Hg_{1-x}Cr_xSe$ on the absolute values of physical parameters such as magnetic susceptibility, phase-transition temperature, mobility of conduction electrons, and the period of time during which the samples go over to the equilibrium state, and second, the formation of materials with improved electrophysical and clearly pronounced magnetic characteristics as compared with $Hg_{1-x}Cr_xSe$ samples with the same concentration of chromium ions. © *1998 American Institute of Physics.* [S1063-777X(98)00609-4]

Intense development of science and technology in the field of fundamental and applied physics of semiconductors poses new and new problems whose solution involves application of new specially synthesized semiconducting materials and a detailed analysis of their physical properties. These materials include narrow-band semimagnetic semiconductor (SMSC). The continued interest of many researchers in this type of materials is due to their specific properties that make it possible to use them for solving problem in thermal detection, and quantum electronics, space communication in the infrared range by synthesizing material of appropriate composition. Practical application of narrow band SMSC is based on the effects of strong spin splitting of energy levels and Faraday's rotation due to the $sp-d$ exchange interaction. Spin splitting in mercury chalcogenides with Mn is manifested most clearly at liquid helium temperature. Hence the devices developed on the basis of these materials (like magnetic-field-controlled IR detectors and generators) can operate only in the helium temperature range. Experimental studies carried out by us on a number of representatives of this class of semiconductors made it possible to discover a wide spectrum of new physical effects in the $Hg_{1-x}Cr_xSe$ system[1–3] and to verify that strong spin splitting can takes place in this system in the nitrogen temperature range.[2] This important practical advantage of $Hg_{1-x}Cr_xSe$ solid solutions determines preferences given to the study of this material over other SMSC. However, the arrangement of energy levels of Cr ions in the conduction band of $Hg_{1-x}Cr_xSe$ leads to additional scattering of conduction electrons at these levels,[1,3,4] and hence to deterioration of electrical and physical parameters of this material. In this connection, attempts were made to obtain (on the basis of $Hg_{1-x}Cr_xSe$) a material with a lower concentration of Cr ions, but with the same or even improved magnetic and electrophysical parameters of the material. Since the impurity levels of Mn ions in mercury chalcogenides get in the valence band in contrast to energy

level of other impurity ions,[5] it should be expected that the introduction of Mn atoms into $Hg_{1-x}Cr_xSe$) would make it possible to obtain a material satisfying all these requirements. Following these principles, we obtained a new quaternary system $Hg_{1-x-y}Cr_xMn_ySe$ which will be described below.

## 1. ELECTRON SPIN RESONANCE AND MAGNETIC SUSCEPTIBILITY

In our previous investigations of the $Hg_{1-x}Cr_xSe$ system, we discovered and studied the electron spin resonance (ESR) spectrum on $Cr^{3+}$ ions.[1,3,4] The spectrum was observed in the range from helium to room temperatures and was determined by the concentration of Cr ions and temperature $T$. ESR and magnetic susceptibility studies revealed that a crystal cooled below a certain temperature $T_f$ displays cubic symmetry breaking in the lattice, and at a certain temperature $T_g < T_f$ a phenomenon interpreted by us as a transition of $Hg_{1-x}Cr_xSe$ to the spin glass phase takes place.

In order to establish the effect of Mn atomic impurity in $Hg_{1-x}Cr_xSe$ on the values of temperature $T_f$ at which the lattice starts being distorted and the phase-transition temperature $T_g$, as well as on magnetic susceptibility, we carried out complex studies based on ESR and magnetic susceptibility $\chi$ measurements on a number of $Hg_{1-x-y}Cr_xMn_ySe$ samples with the concentrations $N_{Cr} \approx 10^{20} \, cm^{-3}$ of chromium ions and $N_{Mn} \approx 5 \times 10^{18} \, cm^{-3}$ of the manganese ions, which were cut from different regions of an ingot.

The ESR spectrum was analyzed on a radiospectrometer with a working frequency 36.04 GHz. The values of $\chi$ were measured by using inductive technique on a setup which was a differential magnetometer with low-frequency field modulation, which was modified by us.[6] The setup was calibrated with a help of the superconducting lead replica of the sample under investigation. The amplitude of the ac magnetic field
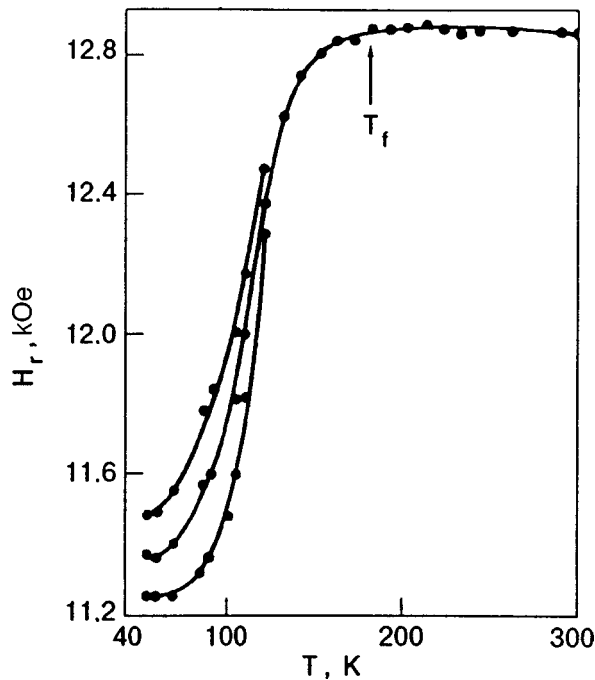
FIG. 1. Temperature dependence of resonant fields in the ESR spectrum of $Hg_{1-x-y}Cr_xMn_ySe$ corresponding to transition of $Cr^{3+}$ from top to bottom at 50 K$\leqslant T \leqslant$120 K): $|+\frac{1}{2}\rangle \leftrightarrow |+\frac{3}{2}\rangle$, $|+\frac{1}{2}\rangle \leftrightarrow |-\frac{1}{2}\rangle$, $|-\frac{1}{2}\rangle \leftrightarrow |-\frac{3}{2}\rangle$.



FIG. 2. Temperature dependence of magnetic susceptibility in $Hg_{1-x}Cr_xSe$ samples with $N_{Cr} \approx 10^{20}$ cm$^{-3}$ (curve *1*) and $Hg_{1-x-y}Cr_xMn_ySe$ samples with $N_{Cr} \approx 10^{20}$ cm$^{-3}$ and $N_{Mn} \approx 5 \times 10^{18}$ cm$^{-3}$ (curve *2*) recorded immediately after sample growth and after equilibrium stabilization in the second system (curve *3*).

inducing emf in the measuring coils of the setup and the frequency were varied smoothly in the intervals 0–5 Oe and 60–1100 Hz respectively. The temperature of the samples was stabilized during measurements and was measured to within $\pm 0.1$ K with the help of an electronic device.[7]

The temperature variation of ESR spectrum of $Cr^{3+}$ ions is shown in Fig. 1 for the $Hg_{1-x-y}Cr_xMn_ySe$ samples investigated by us. Until the temperature is lowered to a certain value, the spectrum contains a single symmetric isotropic line indicating that $Cr^{3+}$ is in a strictly cubic crystal field.[8] The resonant field $H_r$ of the absorption line is independent of $T$ in this case. As the temperature decreases further to $T \leqslant T_f$, the value of $H_r$ becomes a function of $T$, and the spectrum becomes axially anisotropic, which follows from the angular dependence of the ESR line. A subsequent decrease in $T$ gives rise to a fine structure of the spectrum, and the degree of anisotropy increases.

A comparison of the obtained temperature dependence of $H_r$ of the ESR spectrum on $Cr^{3+}$ ions in the $Hg_{1-x-y}Cr_xMn_ySe$ system with a similar dependence for the $Hg_{1-x}Cr_xSe$ system[3] with the same concentration $N_{Cr}$ shows that the nature of variation of the spectral structure with temperature is the same for both systems, but the temperature $T_f$ corresponding to the beginning of symmetry distortion in the lattice of the $Hg_{1-x-y}Cr_xMn_ySe$ system is $(20\pm3)$ K higher than in $Hg_{1-x}Cr_xSe$ system. The error in the measurements of $T_f$ was determined on the basis of a number of $H_r$ values obtained in this temperature range. It should be noted that no EPR spectrum of $Mn^{2+}$ ions was detected in our case for some reason.

Figure 2 shows the temperature dependence $\chi(T)$ of magnetic susceptibility measured on the same
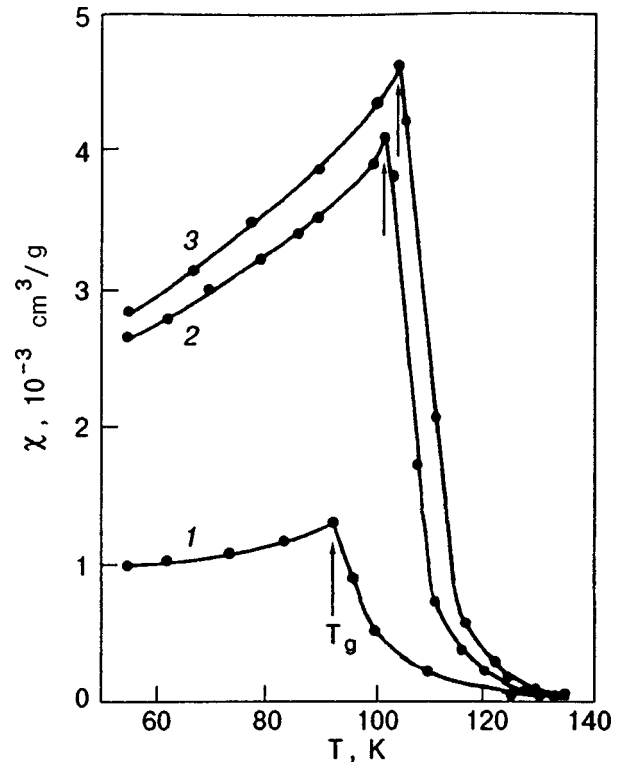
$Hg_{1-x-y}Cr_xMn_ySe$ samples immediately after the crystal growth (curve *2*) and after three months of storage under natural conditions, during which the system goes over to its equilibrium state (curve *3*). For the sake of comparison, the same figure shows the $\chi(T)$ curve[3] for $Hg_{1-x}Cr_xSe$ with $N_{Cr} \approx 10^{20}$ cm$^{-3}$ (curve *1*). A comparison of these curves indicates that the $\chi(T)$ curves for both materials are similar, the only difference being that the absolute values of $\chi$ in the phase-transition temperature region and at $T \leqslant T_g$ differ significantly. Besides, the phase-transition temperature $T_g$ for the $Hg_{1-x-y}Cr_xMn_ySe$ system is 12.5 K higher than for the $Hg_{1-x}Cr_xSe$ system with the same concentration $N_{Cr}$.

Thus, it follows from an analysis of the ESR spectrum on $Cr^{3+}$ ions and susceptibility measurements in $Hg_{1-x-y}Cr_xMn_ySe$ that the addition of Mn atoms to $Hg_{1-x}Cr_xSe$ changes the values of temperature $T_f$ corresponding to the beginning of lattice symmetry distortion of the crystal and the spin-glass phase transition temperature $T_g$ as well as the value of magnetic susceptibility in the phase transition temperature region and at $T \leqslant T_g$. This means that the addition of Mn atoms to $Hg_{1-x}Cr_xSe$ improves its magnetic characteristic $\chi(T)$ which becomes more expressive.

## 2. GALVANOMAGNETIC MEASUREMENTS

In order to determine the effect of Mn atoms introduced into $Hg_{1-x}Cr_xSe$ on the kinetic coefficients of the new system $Hg_{1-x-y}Cr_xMn_ySe$ obtained as a result, we chose $Hg_{1-x}Cr_xSe$ samples with the concentration
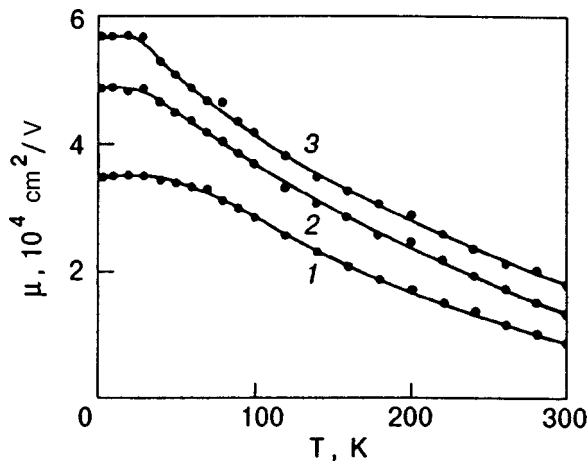
FIG. 3. Temperature dependence of conduction electron mobility in $Hg_{1-x}Cr_xSe$ samples with $N_{Cr} \approx 2 \times 10^{20}\,cm^{-3}$ (curve *1*) and $Hg_{1-x-y}Cr_xMn_ySe$ with $N_{Cr} \approx 10^{20}\,cm^{-3}$ and $N_{Mn} \approx 5 \times 10^{18}\,cm^{-3}$ (curve *2*) recorded immediately after sample growth and after equilibrium stabilization in the second system (curve *3*).

$N_{Cr} \approx 2 \times 10^{20}\,cm^{-3}$ since, according to Ref. 3, the magnetic susceptibility in this material in the temperature range $T \lesssim T_g$ is the same as that measured by us in $Hg_{1-x-y}Cr_xMn_ySe$ with $N_{Cr} \approx 10^{20}\,cm^{-3}$ and $N_{Mn} \approx 5 \times 10^{18}\,cm^{-3}$ (see Fig. 2). This allowed us to determine the variation of the Hall mobility $\mu$ in the quaternary system relative to the ternary system for equivalent magnetic parameters of the two systems.

Galvanomagnetic measurements proved that the concentration of electrons in both systems is $\approx 4.2 \times 10^{18}\,cm^{-3}$ and is independent of temperature $T$, while their mobilities differ significantly and are functions of $T$ (Fig. 3).

Thus, a comparison of the experimentally obtained $\mu(T)$ curves (see Fig. 3) shows that for similar magnetic characteristics $\chi(T)$ of both systems, the Hall mobility of conduction electrons in $Hg_{1-x-y}Cr_xMn_ySe$ is considerably higher than in the $Hg_{1-x}Cr_xSe$ system.

## 3. DISCUSSION AND CONCLUSIONS

The experimental results obtained by us and available data from the literature lead to the following interpretation of the phenomena observed in the $Hg_{1-x-y}Cr_xMn_ySe$ and $Hg_{1-x}Cr_xSe$ systems.

A comparison of experimental results obtained by us here for $Hg_{1-x-y}Cr_xMn_ySe$ samples ($N_{Cr} \approx 10^{20}\,cm^{-3}$ and $N_{Mn} \approx 5 \times 10^{18}\,cm^{-3}$) and for $Hg_{1-x}Cr_xSe$ samples with the same concentration of Cr atoms[3,4] leads to the conclusion that electrophysical and magnetic parameters of these systems display the same qualitative behavior, but differ quantitatively. For example, the introduction of Mn atoms with concentration $5 \times 10^{18}\,cm^{-3}$ into $Hg_{1-x}Cr_xSe$ causes a considerable increase in the temperature of transition of $Hg_{1-x-y}Cr_xMn_ySe$ to the spin glass phase. This experimental fact can be explained by using the concept of transition of SMSC to the spin glass state, which was proposed by Furdyna.[9]

This concept is based on the formation of clusters with a short-range antiferromagnetic order, which begins from local fluctuations in spin distribution. The size of clusters increases upon cooling. We can expect that at a certain temperature the cluster size will become large enough for correlated regions to ''touch'' one another. Such a process of establishment of contact between different clusters can be identified with spin freezing, and hence a transition of SMSC to the spin glass phase whose temperature $T_g$ is an increasing function of the magnetic ion concentration and the integral of exchange interaction between them. Consequently, an increase in the temperature corresponding to such a transition due to the introduction of Mn atoms into $Hg_{1-x}Cr_xSe$ is attributed by us to an increase in the number of clusters per unit volume, and hence their closer arrangement relative to one another. Besides, it was found by us earlier[3,4] that a change in the defect structure[1)] in the $Hg_{1-x}Cr_xSe$ system changes appreciably the magnitude and the form of variation of $\chi(T)$ as well as the stabilization of equilibrium state in the system, which is characterized by a decrease in the number of point defects and their ordering facilitating an increase in the values of $\chi$ and $\mu$. The results of our experiments indicate that a transition to the spin glass phase in samples with stabilized equilibrium state occurs at a higher temperature (see curves *2* and *3* in Fig. 2) and is accompanied by an increase in $\chi$ in the temperature range $T \lesssim T_g$ and in $\mu$ in the entire temperature range under investigation. (see curves *2* and *3* in Fig. 3). The experimental results obtained for the two systems and the conception described above apparently lead to the conclusion that the defect structure of a sample under investigation affects the conditions of the formation of a certain number of clusters as well as the rate of their growth upon cooling, which in turn leads to a change in the values of $T_g$ and $\chi$ and to a different $\chi(T)$ dependence in the region $T \lesssim T_g$.

Thus, the analysis of the effect of Mn atoms introduced into $Hg_{1-x}Cr_xSe$ on its physical parameters leads to the following results.

1. Immediately after crystal growth, the $Hg_{1-x-y}Cr_xMn_ySe$ system is metastable as well as the $Hg_{1-x}Cr_xSe$ system, but the time of stabilization of the equilibrium state in the former system is approximately one third of the corresponding time for the latter system (other conditions being equal).

2. The introduction of Mn atoms into $Hg_{1-x}Cr_xSe$ increases the phase transition temperature significantly.

3. The temperature dependence of magnetic susceptibility of $Hg_{1-x-y}Cr_xMn_ySe$ in the temperature range $T \lesssim T_g$ is pronounced more clearly, and the value of $\chi$ is several times higher than in $Hg_{1-x}Cr_xSe$ with the same concentration of Cr ions.

4. The mobility of conduction electrons is higher in the quaternary system, provided that the magnetic parameters of the two systems are identical.

It can be stated in conclusion that the introduction of $5 \times 10^{18}\,cm^{-3}$ Mn atoms into the solid solution of $Hg_{1-x}Cr_xSe$ results in the formation of the $Hg_{1-x-y}Cr_xMn_ySe$ system with a more clearly manifested magnetic characteristic and with a considerably improved

electrophysical characteristic for the same concentration of Cr ions in both systems.

[1] V. D. Prozorovskiĭ, I. Yu. Reshidova, S. Yu. Paranchich, and Yu. S. Paranchich, Fiz. Tverd. Tela (St. Petersburg) **34**, 882 (1992) [Sov. Phys. Solid State **34**, 472 (1992)].

[2] V. D. Prozorovskiĭ, I. Yu. Reshidova, S. Yu. Paranchich, and Yu. S. Paranchich, Ukr. Fiz. Zh. **40**, 1005 (1995).

[3] V. D. Prozorovskiĭ, I. Yu. Reshidova, A. I. Puzynya, and Yu. S. Paranchich, Fiz. Nizk. Temp. **21**, 1057 (1995) [Low Temp. Phys. **21**, 813 (1995)].

[4] V. D. Prozorovskiĭ, I. Yu. Reshidova, A. I. Puzynya, and Yu. S. Paranchich, Fiz. Nizk. Temp. **22**, 1396 (1996) [Low Temp. Phys. **22**, 1058 (1996)].

[5] T. Dietl, J. Cryst. Growth **101**, 808 (1990).

[6] A. Goldshtein, S. D. Williamson, and S. Founer, Pribory Nauchn. Issled. No. 9, 70 (1965) [Rev. Sci. Instrum. **36**, 1356 (1965)].

[7] V. D. Prozorovskiĭ and Yu. M. Nikolaenko, Author Cert. No. 1319000, Bull. Izobr. No. 23 (1987).

[8] S. A. Al'tshuler and B. M. Kozyrev, *Electron Paramagnetic Resonance of Intermediate Group Compounds* [in Russian], Nauka, Moscow (1989).

[9] J. K. Furdyna, J. Appl. Phys. **64**, R29 (1988).

Translated by R. S. Wadhwa

# Formation and growth dynamics of domains under phase transitions in an external field

## L. I. Stefanovich

*Physics and Engineering Institute, National Academy of Sciences of Ukraine, 72 R. Luxemburg St., 340114, Donetsk, Ukraine*[*)]

The formation and the growth dynamics of 180°-domains in ferroelectrics in external field are investigated with the use of the statistical approach within the Ginzburg–Landau model. It is shown that despite the polarizing role of an external field the formation of an intermediate polydomain structure is found to be more preferable than immediate transfer to the monodomain ordering state. © *1998 American Institute of Physics.* [S1063-777X(98)00709-9]

## INTRODUCTION

The fact that the really observed structure of solids is often nonequilibrium is largely determined by the dynamics of transformations occurring there. These transformations may have the character of both phase separation[1] and ordering[2]. In multicomponent alloys both of the aforesaid processes can proceed simultaneously[3]. In this paper we are concerned with the ordering processes and in large measure their dynamic aspect, which consists in tracing the paths of establishing one or another stable or metastable state and in revealing the reasons influencing this choice.

The structural phase transitions in ferroelectrics associated with the appearance of macroscopic regions of the crystal where the spontaneous electric polarization is not equal to zero are the basic object of our investigation in this work.

To characterize quantitatively the state change of a system passing through the critical temperature point $T_c$ of a phase transition, one or more values called order parameters are introduced. In the case of the ferroelectric phase transition the projection of the polarization vector on a certain crystallographic direction is used as a long-range order parameter.

It is known[4] that, in the absence of external field at the temperatures below $T_c$, i.e., in low-symmetrical phase, the states correspond to the different (with respect to the sign) values of the order parameter $\pm\eta$. In the early stages of the ordering, when the relaxation of the short-range order has already been proceeded basically, the appearance of the structures of the type $+\eta$ or $-\eta$ proves to be quite accidental and therefore the regions of both the signs $\pm\eta$ (called usually 180°-domains) must exist in different points of the crystal. It is obvious that the spatial size of the domains is assumed to be much larger than the lattice parameter. As was shown by us earlier[2], the evolution of these inhomogeneities of the order parameter in the absence of the external field will proceed along one of two basic paths, depending on the initial conditions—either the formation of a single-domain state or the formation of a polydomain structure followed by increasing (for diffusion time) the spatial scale of this structure up to the crystallite size.

Our goal is to clear up how the long-range order

evolution character will change in an initially disordered system if at the moment of quenching is finished some external field $\varepsilon$ conjugating with the order parameter $\eta$ will be imposed on it rapidly enough. The question is, if the homogeneous (monodomain) ordering will occur, or can a sufficiently developed polydomain structure formed, in some situations? In the case of a ferroelectric an uniform steady-state electric field should be meant when speaking about an external field. The time of its establishing ($\tau_\varepsilon = \varepsilon/\dot{\varepsilon}$) is considered to be small in comparison with the time of the forming ($\tau_d$) and certainly it is much less than the time of coalescence ($\tau_c$) of the domain structure ($\tau_\varepsilon \ll \tau_d \ll \tau_c$).

## GENERAL DESCRIPTION OF THE MODEL

In order to describe the ordering within the framework of Landau theory we shall assume further that, despite the proximity of temperature to the critical one $(T_c - T)/T_c \ll 1$ the system lies outside the fluctuation region. In this situation a nonequilibrium addition to the thermodynamic potential in the presence of external field can be presented in the form of Ginzburg–Landau functional[5]:

$$\Phi\{\eta, \nabla\eta\} = \int \left[ \frac{1}{2} A\eta^2 + \frac{1}{4} B\eta^4 + \frac{1}{2} \delta(\nabla\eta)^2 - \eta E \right] dV. \tag{1}$$

Here the coefficient $A$ is proportional to $(T_c - T)$. Since the characteristic energy scale in this problem is $T_c$ it may be considered that $B \sim T_c$, and $\delta \sim T_c r_0^2$, where $r_0$ is the interaction radius; i.e., the value of the order of interatomic distance; $E$ is the external field, which we believe for the simplicity to be homogeneous one.

In order to describe the dynamics of nonequilibrium system we shall use the Landau–Khalatnikov equation[2] for a nonconserved order parameter:

$$\frac{\partial\eta}{\partial t} = -\gamma \frac{\delta\Phi}{\delta\eta}, \tag{2}$$

where $\gamma$ is the kinetic coefficient which can be represented in the form $(\tau T_c)^{-1}$, so $\tau$ can be interpreted to be the time

required for an elementary rearrangement of the system (for example, a displacement of an atom or interchange of neighboring atoms).

If, now, distance is measured in units of $r_0$ and time in units of $\tau$, then Eq. (2) can be written, in view of Eq. (1), in the form:

$$\partial \eta / \partial t = \Delta \eta + \alpha \eta - \eta^3 + \varepsilon. \tag{3}$$

Here $\Delta$ is the Laplacian and we have introduced two parameters: $\alpha = (T_c - T)/T_c$ is a dimensionless parameter that characterizes the proximity of temperature $T$, up to that of the specimen cooled, to the temperature of ordering $T_c$; $\varepsilon = E/T_c$ is the external field in corresponding units.

It should be emphasized that the initial state of order-disorder system must be given statistically, considering that, first, inhomogeneities of an order parameter are formed as a result of rapid cooling of specimen randomly arranged in space; second, there are thermal fluctuations of order parameters all along. The spatial scale of appropriate inhomogeneities is assumed to be much larger than the lattice parameter.

To solve the problem it is necessary to have an initial condition to Eq. (3), i.e., the meaning of order parameter $\eta(\mathbf{r}, t)$ at the initial moment of time should be given, $\eta(\mathbf{r}, 0) \equiv \eta_0(\mathbf{r})$. Since this initial function is random, the order parameter is a random function of coordinates for $t \neq 0$ as well. Therefore, Eq. (3) will describe spatial-time evolution of the order parameter random field operating in the spatially uniform (and determinate) field $\varepsilon$.

## THE DERIVATION OF BASIC EQUATIONS

To describe the relaxation processes taking place in the system undergoing the phase transition, there is no need to know the spatial distribution of the order parameter $\eta(\mathbf{r}, t)$ in detail over the total specimen. Therefore, we shall deal with the search for the main physically significant characteristics of this function in the subsequent discussion, such, for example, as the average (over crystalline grain) value of the order parameter $\langle \eta(\mathbf{r}, t) \rangle \equiv \bar{\eta}(t)$ and the two-point correlation function

$$\langle \xi(\mathbf{r}, t) \xi(\mathbf{r}, t) \rangle \equiv K(\mathbf{s}, t), \quad \mathbf{s} = \mathbf{r} - \mathbf{r}', \tag{4}$$

where we have introduced the centered order parameter $\xi(\mathbf{r}, t) \equiv \eta(\mathbf{r}, t) - \bar{\eta}(t)$, and have used the standard assumption that the order parameter field is statistically uniform.

The equations for $\bar{\eta}(t)$ and $K(\mathbf{s}, t)$ are derived from the basic equation (3) both by averaging the equation itself and by averaging after premultiplying both sides of Eq. (3) by $\eta(\mathbf{r}', t)$.

To obtain a closed system of equations for $\bar{\eta}(t)$ and $K(\mathbf{s}, t)$, the possible asymmetry are neglected here, i.e., we suppose that

$$\langle \xi^2(\mathbf{r}) \xi(\mathbf{r}') \rangle = 0 \tag{5}$$

for all the $\mathbf{r}$ and $\mathbf{r}'$. For correlation function of the type $\langle \xi^3(\mathbf{r}, t) \xi(\mathbf{r}', t) \rangle$ we shall use the unlinking of the form

$$\langle \xi^3(\mathbf{r}, t) \xi(\mathbf{r}', t) \rangle = \langle \xi^2(t) \rangle \langle \xi(\mathbf{r}, t) \xi(\mathbf{r}', t) \rangle$$
$$\equiv K(0, t) K(\mathbf{s}, t). \tag{6}$$

One of the justifications for this procedure is the availability of only one spatial scale in the problem considered.

It would appear natural, then, that the functional dependence of the fourth order correlation function $\langle \xi^3(\mathbf{r}) \xi(\mathbf{r}') \rangle$ of $|\mathbf{r} - \mathbf{r}'|$ would be an accurate copy the functional dependence of the distance between points $\mathbf{r}$ and $\mathbf{r}'$ for the second order correlation function $\langle \xi(\mathbf{r}) \xi(\mathbf{r}') \rangle \equiv K(|\mathbf{r} - \mathbf{r}'|)$. It has been known that for the Gaussian random field the unlinking (6) will be an accurate one, if the right-hand side of Eq. (6) is multiplied by a coefficient which is equal to three. In our case the Eq. (6), without any doubt, is an approximation, in which the choice of the coefficient is determined by the fact that in the problem considered, for long times in particular, the one-point distribution function is significantly different from Gaussian form. It follows from physical considerations based on the equivalency of states that are equal in magnitude but opposite in sign, of order parameters, that for the sufficiently long times ($t \gg \alpha^{-1}$) are close to the curve with two sharp maxima at the equilibrium values of the order parameter. Here, of course, we are dealing with a centered order parameter $\xi$. As it is immediately evident from the calculation, for such a distribution function the coefficient mentioned above is close to unity.

As a consequence of Eq. (3) and assumptions (5) and (6), we obtain, finally, the system of equations for the functions: $\bar{\eta}(t)$ and $K(\mathbf{s}, t)$

$$\begin{cases} \dfrac{d\bar{\eta}}{dt} = \dfrac{1}{2} (\alpha \bar{\eta} - 3K(0,t)\bar{\eta} - \bar{\eta}^3 + \varepsilon), & (7) \\[2mm] \dfrac{\partial K(\mathbf{s}, t)}{\partial t} = \Delta K(\mathbf{s}, t) + [\alpha - K(0,t) - 3\bar{\eta}^2] K(\mathbf{s}, t). & (8) \end{cases}$$

The system of Eqs. (7) and (8) contains two physically meaningful parameters: $\alpha$ and $\varepsilon$. Owing to the nonlinearity contained in the right-hand sides of Eqs. (7) and (8), our system cannot be solved by analytical methods. However, as shown in[2], due to the distinctive degeneracy, the similar system can be reduced to a system of nonlinear ordinary differential equations for the average value of order parameter $\bar{\eta}(t)$ and dispersion of it $D = D(t)$ with the help of the Fourier transformation of the Eq. (8) on the spatial variable $\mathbf{s}$

$$\begin{cases} \dfrac{d\bar{\eta}}{dt} = \dfrac{1}{2} [(\alpha - 3D - \bar{\eta}^2)\bar{\eta} + \varepsilon], \\[2mm] \dfrac{dD}{dt} = (\alpha_{\mathrm{eff}}(t) - D - 3\bar{\eta}^2)D, \end{cases} \tag{9}$$

where the following notations are introduced: $D = D(t) = K(0, t)$;

$$\alpha_{\mathrm{eff}}(t) \equiv \alpha - 1/r_c^2(t). \tag{10}$$

Here we have used a natural determination of the correlation radius $r_c(t)$ by Fourier transform, $\tilde{K}(\mathbf{q}, t)$, of the correlation function:

$$\frac{1}{r_c^2(t)} \equiv \int q^2 \tilde{K}(\mathbf{q}, t) d^3q \bigg/ \int \tilde{K}(\mathbf{q}, t) d^3q. \tag{11}$$

As it is shown in Ref. 2, the correlation radius at an arbitrary moment of time is determined by the value of the correlation

function $K(\mathbf{s},t)$ at the initial moment of time, i.e., $K(\mathbf{s},0)$. The last must be specified as the initial condition of the problem. The temporal dependence of the coefficient $\alpha_{\text{eff}}$, in accordance with (10), is determined completely by the evolutionary character of the system correlation radius $r_c(t)$ (in our case it is associated with the characteristic spatial scale of ordered region or domain size).

For all the ''acceptable'' initial correlation functions, $K(\mathbf{s},0)$, as it is shown in Ref. 2, the temporal dependence of the correlation radius $r_c(t)$ has the form:

$$r_c(t) = \sqrt{r_c^2(0) + 2t/3}, \qquad (12)$$

where $r_c(0)$ is the correlation radius of the system at the initial moment of time ($t=0$). The last formula confirms the well-known conclusion that domain sizes grow with time according to a diffusion law in proportion to $\sqrt{t}$ [provided, of course, that $t \gg r_c^2(0)$]. Thus, the system of equations (9) for $\bar{\eta}(t)$ and $D(t)$, in the terms of the Eqs. (10) and (12), takes the form

$$\begin{cases} \dfrac{d\bar{\eta}}{dt} = \dfrac{1}{2}\left[(\alpha - 3D(t) - \bar{\eta}^2)\bar{\eta} + \varepsilon\right], \\[2mm] \dfrac{dD(t)}{dt} = \left[\alpha - \{2/3t + r_c^2(0)\}^{-1} - D(t) - 3\bar{\eta}^2\right]D(t). \end{cases} \qquad (13)$$

## ASYMPTOTIC BEHAVIOR OF SYSTEM FOR LONG-TIMES

It is of greatest interest to study the system of Eqs. (13) close to the ordering temperature $T_c$, when $\alpha \ll 1$ and the initial correlation length is not too large, so that the condition $r_c^2(0) \ll (1/\alpha) \ll d^2$ can satisfied, where $d$ is the characteristic crystallite size (we recall that time is measured in units of $\tau$ and distance is measured in units of $r_0$, i.e., the interatomic interaction length). Then, asymptotically, i.e., at times $t \gg 1/\alpha$, the system of Eqs. (13) transforms into a system of equations with constant coefficients

$$\begin{cases} \dfrac{d\bar{\eta}}{dt} = \dfrac{1}{2}\left[\{\alpha - 3D(t) - \bar{\eta}^2\}\bar{\eta} + \varepsilon\right], \\[2mm] \dfrac{dD(t)}{dt} = \left[\alpha - D(t) - 3\bar{\eta}^2\right]D(t), \end{cases} \qquad (14)$$

with the initial conditions

$$\bar{\eta}(0) = \bar{\eta}_0; \quad D(0) = D_0. \qquad (15)$$

The solution of the system of Eqs. (14) with initial conditions (15) allows us to obtain information about the closing stages of the ordering process.

Let us perform qualitative analysis of the system (14) with use of the concept of phase pattern[6] (in the present case, in the variables $\bar{\eta}$ and $D$ (see Fig. 1).

As it is shown, the singular (stationary) points of the system (14) can be found from the fact that $(d\eta/dt) \to 0$ and $(dD/dt) \to 0$ as $t \to \infty$; therefore,

$$\begin{cases} \varepsilon + \alpha\bar{\eta} - 3D\bar{\eta} - \bar{\eta}^3 = 0, \\ (\alpha - D - 3\bar{\eta}^2)D = 0. \end{cases} \qquad (16)$$
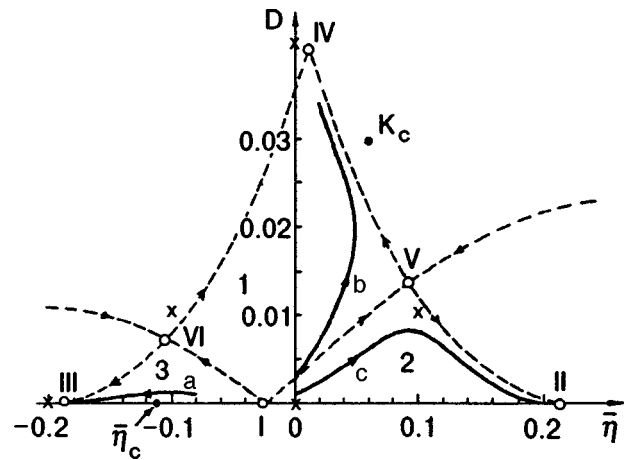


FIG. 1. Phase pattern of order-disorder system. The singular points of the system (14) at $\varepsilon = 0$ are marked by symbol (X); the singular points (I–VI) for the system (14) at $\varepsilon \neq 0$ are marked by circles (○) and separatrices are indicated by dotted lines. The bifurcation points (at $\varepsilon = \varepsilon_c$) for the system (14) ($\eta_c$ and $K_c$) are shown by black circles (●). Here solid lines a–c are the phase trajectories as a result of numerical integrating of the total system (13) for $\alpha = 0.04$; $\varepsilon = 0.001$; $r_c(0) = 10$ at different initial conditions $\{\bar{\eta}_0, D_0\}$: $\{-0.08; 0.001\}$ (a); $\{0; 0.003\}$ (b); $\{0; 0.001\}$ (c).

This is a system of two algebraic equations in variables $\bar{\eta}$ and $D$. The roots of the above-mentioned system yield the coordinates of singular points in the plane ($\bar{\eta}$, $D$).

For $\alpha < 0$, i.e., at a temperature above the critical point, there is only one singular point, which is a stable node. The coordinates of this point for the small $\varepsilon$ are $\bar{\eta} = \varepsilon/|\alpha|$, $D = 0$. This means that, irrespective, of the initial conditions, the system will pass into a disordered state. First of all, it should be noted here that, even though the field $\varepsilon$ is as small as possible, the average value of order parameter $\bar{\eta}$ becomes nonvanishing everywhere over the temperature region. Owing to the external field, among other things, the phase transition appears to be ''blurred'' i.e., it takes place some temperature interval away from critical point $T_c$.

For $\alpha > 0$, i.e., at $T < T_c$, and not-too-strong field there is a whole system of singular points. However, only the points located in the upper half-plane of the phase pattern (in variables $\bar{\eta}$, $D$) will have physical meaning. Let us analyze, initially, the positions of the singular points in the case of weak field ($\varepsilon \ll \alpha^{3/2}$).

The first singular point I [$\bar{\eta} = -(\varepsilon/\alpha)$, $D = 0$], which corresponds to a homogeneous disordered state, is an unstable node (Fig. 1).

The second point II [$\bar{\eta} = \sqrt{\alpha} + (\varepsilon/2\alpha)$, $D = 0$] corresponds to a homogeneous ordered state ''aligned with the external field'' and it is a stable node (Fig. 1).

The third point III [$\bar{\eta} = -\sqrt{\alpha} + (\varepsilon/2\alpha)$, $D = 0$] corresponds to homogeneous ordering, but it is ''opposite to the field.'' This point is also a stable node (Fig. 1).

Both the second and the third singular points correspond to single-domain types of the specimen ordering.

All the rest of the singular points (with $D \neq 0$) correspond to inhomogeneous ordering, i.e., to one or the another polydomain structures.

The fourth point IV ($\bar{\eta} = \varepsilon/2\alpha$; $D = \alpha - 3\varepsilon^2/4\alpha^2$)

(Fig. 1) is a stable node and corresponds to the possibility of the polydomain structure realization. The fact that $\bar{\eta} \neq 0$ in this state corresponds to some non-equivalency of domains of two types. However, in weak fields this distinction is small (to the extent of the ratio $\varepsilon/\alpha$).

And finally, there are another two singular points of the saddle type. One of them V ("right saddle") with coordinates ($\bar{\eta} = \sqrt{\alpha}/2 - \varepsilon/4\alpha$; $D = \alpha/4 + 3\varepsilon/4\sqrt{\alpha}$) (Fig. 1) corresponds to a possibility for realizing such a quasi-stationary polydomain structure, where the volume fraction of domains of the same type (e.g., with polarization vector, aligned with field) substantially exceeds the volume fraction of the other type domains (opposed to the field).

The other point ("left saddle") with coordinates ($\bar{\eta} = -\sqrt{\alpha}/2 - \varepsilon/4\alpha$; $D = \alpha/4 - 3\varepsilon/4\sqrt{\alpha}$) (the point VI, Fig. 1) corresponds to a possibility for realizing the quasi-stationary polydomain structure as well. However, in this situation the volume fraction of domains with the polarization vector oriented opposite to the field substantially exceeds a volume fraction of domains aligned with the field.

Two separatrices, leaving the origin of coordinates and passing through the "left" and "right" saddle points, divide the phase pattern into the three sectors. The upper central sector (1) is the "attraction region" of the inhomogeneous (polydomain) state, the lower right-hand (2) and lower left-hand sectors (3) correspond to two attraction regions of homogeneous single-domain states. Depending on the initial conditions ($\bar{\eta}_0, D_0$) the phase trajectories of the system will be located in one of the above-mentioned sectors. This is illustrated on the phase pattern (Fig. 1), where, apart from the singular points founded analytically and the separatrices of the asymptotic system of equations (14), a number of results of numerical integrating (curves a–c) of the complete system of equations (13) are presented.

If in the initial state the average value of order parameter $|\bar{\eta}_0 \neq 0|$ and it is greater than the fluctuations of order parameter, the system will transfer immediately into one of the single-domain states. The sign of the order parameter in the state of thermodynamic equilibrium is determined by what side of the first singular point the value $\bar{\eta}_0$ is located on. We emphasize that the availability of external field ($\varepsilon \neq 0$), with weak inhomogeneity of order parameter, will make the system to go over into single-domain state, even though $\eta_0 = 0$. The choice between two single-domain states is predetermined by the field direction.

The deflection of the system to one or another side in magnitude of the order parameter with respect to the first singular point can occur, in general, for various reasons, both random and determinate character.

If, however, at the initial state inhomogeneities are sufficiently developed and the average value of the order parameter at the initial moment of time $\bar{\eta}_0$ is close to $-(\varepsilon/\alpha)$, the developed polydomain structure will be formed in the system over a time $t \sim \alpha^{-1}$. The characteristic size of the domains, just as the characteristic size of the transition layer (domain boundary) between them, will achieve the value of order $\alpha^{-1/2}$ by this moment.

Further, in accordance with (12), the domain sizes will grow in keeping with the diffusion law $\sim \sqrt{t}$, while the thickness of the domain boundaries remains unchanged at the level $\alpha^{-1/2}$.

Strictly speaking, if the long-range interaction is not counted, the polydomain state is not stable thermodynamically. The state of interest may be considered to be long-lived and its characteristic lifetime is $\alpha^{-1} \ll t \ll d^2$. That is, in the situation being considered the system will pass to the thermodynamically stable monodomain state as well. However, this transition does not proceed immediately, but it goes through the stage of forming and growing the domains. This growth proceeds for as long as the domain sizes will become of the order of the crystallite size, when by the influence of external field $\varepsilon$ the system will give the preference to the domain of certain sign.

## CONCLUSIONS

In this paper we have used a statistical approach[1] to investigate the ordering dynamics under the second order phase transitions in the presence of the external field. This has allowed us to show that the imposition of a not-too-strong field to the ordering system leads to the asymmetry of the ordering process, removing the degeneracy on the sign of the order parameter, i.e., it makes monodomain states with the order parameters $+\eta$ and $-\eta$ nonequivalent. However both in the weak field and at the absence of the field the formation of a polydomain ordered structure is most likely. Despite its thermodynamic instability, the structure of this kind will evolve rather slowly to the thermodynamic equilibrium monodomain type of ordering. The influence of a weak external field on the polydomain structure lies only in the fact that the volume redistribution of an energetically disadvantageous regions (oriented opposite to the field) and advantageous regions (aligned with the field) will occur in favor of the latter. The homogeneous (monodomain) state of ordering is realized just in sufficiently strong fields in excess of the critical value $\varepsilon_c$ (which is generally dependent on the temperature), irrespective of the initial conditions. The field $\varepsilon_c$ is nothing but a coercive field.

*)E-mail: listef@host.dipt.donetsk.ua

[1] E. P. Feldman and L. I. Stefanovich, Zh. Éksp. Teor. Fiz. **96**, 1513 (1989) [Sov. Phys. JETP **69**, 858 (1989)].
[2] E. P. Feldman and L. I. Stefanovich, Pis'ma Zh. Éksp. Teor. Fiz. **63**, 933 (1996) [JETP Lett. **63**, 983 (1996)].
[3] J. W. Cahn and A. Novic-Cohen, J. Stat. Phys. **76**, 877 (1994).
[4] I. M. Lifshits, Zh. Éksp. Teor. Fiz. **42**, 1354 (1962) [Sov. Phys. JETP **15**, 939 (1962)].
[5] L. D. Landau and E. M. Lifshits, *Statistical Physics*, Nauka, Moscow (1976) [English translation published by Pergamon Press, Oxford].
[6] A. A. Andronov, E. A. Leontovich, I. I. Gordon, and A. G. Mayer, *Qualitative Theory of Second-Order Dynamic Systems* [in Russian], Fizmatgiz, Moscow (1996).

# Generalization of equal-module exchange magnetic classes

Kh. Sh. Borlakov

*Karachaevo-Cherkes Technological Institute, 357100 Cherkessk, Karachaevo-Cherkes Republic, Russia\**
(Submitted March 23, 1998)

It is shown that in addition to equal-module exchange structures satisfying the criterion for the existence of the Andreev–Marchenko and Bar'yakhtar–Yablonskii spin scalar, other equal-module exchange structures also exist. In contrast to the structures obtained from the condition for the existence of a spin scalar, the latter follow from thermodynamic conditions and correspond to thermodynamically stable phases. Besides, these structures are not related to the restrictions imposed on the dimensionality of irreducible representation typical of the structures of the former kind.   © *1998 American Institute of Physics.* [S1063-777X(98)00809-3]

## INTRODUCTION

The magnetic symmetry of magnetically ordered crystals in the exchange approximation is higher than in the case when relativistic interactions are taken into consideration. A group theory method of determining the symmetry of exchange structures was proposed by Andreev and Marchenko[1] and by Bar'yakhtar and Yablonskii[2] on the basis of the condition for the existence of a certain invariant function formed by spin components (spin scalar). The exchange magnetic structures obtained by using this approach are equal-module structures, i.e., the magnitude of spin moment is the same in all magnetic positions of the crystal. Gufan *et al.*[3] used a model example to prove the existence of exchange structures with different modules. We propose a method for obtaining exchange magnetic structures which is more general than magnetic classes obtained from the condition for the existence of a spin scalar.

For this purpose, a general approach is required, which would not require any information other than that provided by the magnetic symmetry group of the paramagnetic phase and the population density of magnetic atoms in positions in the space group of the crystal. If such information is available, all possible types of exchange structures for the given crystal can be determined on the basis of the group theory method of determining low-symmetry phases proposed in Refs. 4–6.

## GENERAL METHOD OF DETERMINING EXCHANGE MAGNETIC STRUCTURES

The magnetic symmetry of the paramagnetic phase of a crystal is characterized by the exchange paramagnetic group $M$ that can be reduced to a direct product of the space group $G$ and the three-dimensional group of spin rotations $O(3)$, i.e., $M = G \times O(3)$.[7] Each space group is characterized by a set of crystallographic orbits or a regular system of points (RSP).[8] Any point belonging to a RSP is transformed into a point from the same RSP under the action of symmetry elements of the space group $G$, i.e., RSP is transformed into itself under the action of elements from group $G$. Accordingly, any system of functions defined on RSP is transformed into itself under the action of symmetry elements from $G$, i.e., forms the basis of the irreducible representation (IR) of this group. In addition to the symmetry group, a given crystal is characterized by the diagram of population of various RSP by atoms. Some crystallographic orbits in a magnetic crystal are populated completely or partially by magnetic atoms. Each such orbit can be presented by the spin density function $\mathbf{S}(\mathbf{r})$. We expand this function in the basis functions from the IR of the group $M$:

$$\mathbf{S}(\mathbf{r}) = \sum_{a=1}^{3} \sum_{i=1}^{n} S_a^i \varphi_i(\mathbf{r}) \mathbf{e}^a = \sum_i \mathbf{S}_i \varphi_i(\mathbf{r}), \tag{1}$$

where $\varphi_i(\mathbf{r})$ are the basis functions of the IR of the group $G$, $\mathbf{e}^a$ is the orthonormal basis in the spin space (the basis of the vectorial IR of the $O(3)$ group), $a$ the index labelling unit vectors in the spin space, and $i$ the index labelling basis functions of the IR. Thus, the type of magnetic ordering is determined by the set of the mixing coefficients $S_a^i$. The last two factors on the right-hand side of formula (1) form the IR $D = \Gamma \times V$ of the $G \times O(3)$ group, where $\Gamma$ is the IR of the $G$ group, whose basis is just formed by functions appearing in (1), and $V$ is the vectorial IR of the group of three-dimensional spin rotations. Spin group transformations correspond to transpositions of atoms within a crystallographic orbit. In addition to lattice site coordinates, magnetic atoms are also characterized by spin. However, the direction and magnitude of spin do not change upon a transposition of an atom, i.e., spin rotations and space transformations are carried out independently. This is a formally logical realization of the condition corresponding to the absence of a coupling between the spin subsystem and the lattice, which is executed by relativistic interactions. Thus, the transformation properties of each component of the spin density function are similar to transformation properties of variation of electric charge density. Let us clarify this statement. The variation $\delta \rho(\mathbf{r})$ of electric charge density has two components[9]: the variation of the form of the function $\delta \rho(\mathbf{r})$ and the variation of the function due to a change in the argument:

$$\delta\rho(\mathbf{r}) = \delta\rho(\mathbf{r}) + \frac{\partial\rho}{\partial\mathbf{r}}\,\mathbf{u}(\mathbf{r}), \tag{2}$$

where $\mathbf{u}(\mathbf{r})$ is the vector function of atomic displacements.

The variation of the form of the function describes purely phase transitions associated with atomic ordering. The second term on the right-hand side of (2) characterizes purely displacement-type transitions. The transformation properties of the spin density function components are identical just with the transformation properties of the function $\delta\rho$ describing atomic ordering. The (reducible) representation according to which the function $\delta\rho(\mathbf{r})$ is transformed is called the transposition representation.[8] Thus, the spin density function can be expanded in the basis functions of the IR appearing in the transposition representation.[8]

Atomic ordering can be described by a set of scalar basis functions and a set of mixing coefficients $\mathbf{c} = (c_1, c_2, \ldots, c_n)$ forming the so-called stationary vector (statvector).[3,6] In order to describe the exchange magnetic ordering, we need a set of scalar basis functions and three statvectors

$$(S_1^1, S_2^1, \ldots, S_n^1), (S_1^2, S_2^2, \ldots, S_n^2), (S_1^3, S_2^3, \ldots, S_n^3). \tag{3}$$

The statvector $\mathbf{c}$ can be regarded a vector of a certain vector space ($\varepsilon$-space in the terminology of Gufan $et\ al.$[3]) Different symmetry positions of the statvector in this space correspond to different subgroups of the group $G_D \subset G$ of the high-symmetry phase. Each of these subgroups describes the crystal symmetry corresponding to atomic ordering wit certain mixing coefficients.

The three statvectors (3) can be conveniently combined into a stationary matrix (statmatrix) of dimensionality $n \times 3$:

$$\hat{\mathbf{S}} = \begin{pmatrix} S_1^1, S_2^1, \ldots, S_n^1 \\ S_1^2, S_2^2, \ldots, S_n^2 \\ S_1^3, S_2^3, \ldots, S_n^3 \end{pmatrix}. \tag{4}$$

The exchange magnetic ordering symmetry is determined by the least symmetric of the three statvectors appearing in statmatrix (4). If we go over to the spherical coordinates in the spin space, the statmatrix assumes the form

$$\hat{\mathbf{S}} = \begin{pmatrix} S_1\sin\theta_1\cos\varphi_1; & S_2\sin\theta_2\cos\varphi_2; & \ldots; & S_n\sin\theta_n\cos\varphi_n \\ S_1\sin\theta_1\sin\varphi_1; & S_2\sin\theta_2\sin\varphi_2; & \ldots; & S_n\sin\theta_n\sin\varphi_n \\ S_1\cos\theta_1; & S_2\cos\theta_2; & \ldots; & S_n\cos\theta_n \end{pmatrix}. \tag{5}$$

In the general case, statmatrix (5) defines an essentially three-dimensional magnetic structure. If, however, one of the spherical angles $\theta_i$ or $\varphi_i$ does not depend on the number $i$ of the column, the statmatrix can be reduced to a form with a single zero line by rotation of the spin axes. Such a statmatrix corresponds to two-dimensional exchange structures. If the other spherical angle is also the same for all the column, the rotation of spin axes can nullify two rows of the matrix $S$, and such a matrix corresponds to a collinear antiferromagnetic exchange structure.

A unit IR of the space group $G$ corresponds to the ferromagnetic spin ordering within each crystallographic orbit. Other one-dimensional IR appearing in the transposition representation at the crystal lattice sites occupied by magnetic atoms correspond to collinear antiferromagnetic exchange structures. Two-dimensional IR appearing in the transposition representation correspond two-dimensional antiferromagnetic structures. Irreducible representations with a dimensionality higher than three and appearing in the transposition representation correspond to essentially three-dimensional antiferromagnetic structures. Obviously, a change in the number of independent parameters in the statmatrix corresponds to a transition from one exchange phase to another as in the case of an atomic ordering.

It should be noted that by the dimensionality of an IR we meant the dimensionality of real-valued IR or the dimensionality of physically-irreducible representations of complex IR.

## EQUAL-MODULE EXCHANGE STRUCTURES

Let us consider the exchange structures obtained from the condition for the existence of the Andreev–Marchenko spin scalar. Raising both sides of equality (1) to the second power, we obtain

$$S^2(\mathbf{r}) = \sum_{a,i}\sum_{b,k} S_a^i S_b^k \varphi_i(\mathbf{r})\varphi_k(\mathbf{r})\mathbf{e}^a \cdot \mathbf{e}^b. \tag{6}$$

The left-hand side of this equation is a scalar relative to transformations from space group $G$. Consequently, the right-hand side of this relation must also assume a form invariant to spatial transformations:

$$S^2(\mathbf{r}) = \sum_a S_a^2 \sum_i |\varphi_i(\mathbf{r})|^2. \tag{7}$$

A comparison of the right-hand sides of (6) and (7) shows that the mixing coefficients must satisfy the following orthogonality condition:

$$S_a^i S_b^k = S_a^2 \delta_{ik} \delta_{ab}, \tag{8}$$

where $\delta_{ik}$ and $\delta_{ab}$ are Kronecker deltas. For the sake of visualization, it is convenient to write relations (1), (6)–(8) in matrix form. We introduce the column vector

$$\varphi(\mathbf{r}) = \begin{pmatrix} \varphi_1(\mathbf{r}) \\ \varphi_2(\mathbf{r}) \\ \ldots\ldots \\ \varphi_n(\mathbf{r}) \end{pmatrix},$$
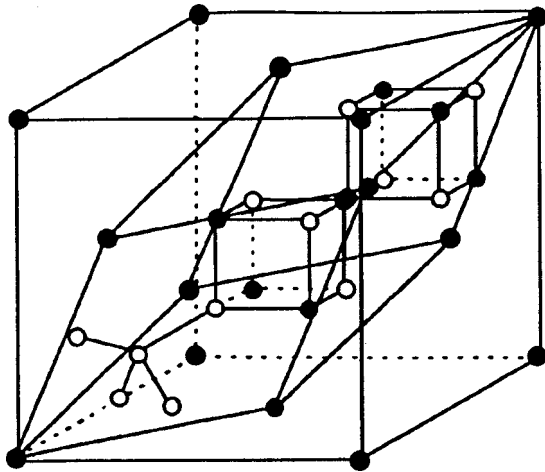
FIG. 1. Primitive cell of a spinel crystal. Light circles correspond to 32(e) positions occupied by anions, dark circles to 16($d$) positions (octahedral sublattice); and hatched circles to 8($a$) positions (tetrahedral sublattice).
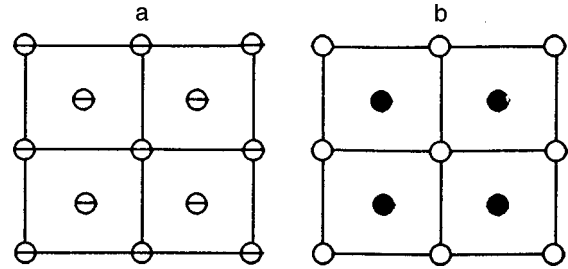


FIG. 2. Projection of tetrahedral ions on the $(x,y)$ plane in a unit cell of the spinel. Disordered (paramagnetic) phase (a) and ordered (antiferromagnetic) phase (b). The orientation of the average value of spin in positions marked by dark circles is opposite to the orientation of atomic spins occupying positions marked by light circles. The direction of the antiferromagnetism vector relative to crystallographic axes is arbitrary.

and denote the line vector by $\varphi(\mathbf{r})$. Then expansion (1) can be written in the matrix form

$$\mathbf{S}(\mathbf{r}) = \hat{S}\varphi(\mathbf{r}),$$

and expression (7) can be written as

$$S^2(\mathbf{r}) = \varphi(\mathbf{r})\hat{S}^T\hat{S}\varphi(\mathbf{r}),$$

where $\hat{S}^T$ is the transposed statmatrix. We present the statmatrix $\hat{S}$ in the form of the row

$$\hat{S} = (\mathbf{S}_1, \mathbf{S}_2, \ldots, \mathbf{S}_n),$$

where the vectors $\mathbf{S}_i$ are defined in the three-dimensional spin space. In such a case, the condition (8) of invariance of the square of spin density module assumes the form

$$\hat{S}^T\hat{S} = \begin{pmatrix} \mathbf{S}_1 \\ \mathbf{S}_2 \\ \ldots \\ \mathbf{S}_n \end{pmatrix}(\mathbf{S}_1, \mathbf{S}_2, \ldots, \mathbf{S}_n) = \mathbf{S}^2\hat{E}. \qquad (9)$$

This relation (9) indicates that the $n$ vectors $\mathbf{S}_i$ forming the statmatrix are mutually orthogonal and have equal modules. However, the three-dimensional spin space cannot have more than three such vectors. Consequently, the maximum dimensionality of IR describing equal-module exchange structures does not exceed three in accordance with the results obtained in Refs. 1 and 2.

### EQUAL-MODULE EXCHANGE PHASES WITH COINCIDING MAGNETIC AND CRYSTALLOCHEMICAL UNIT CELLS IN CRYSTALS WITH SPINEL STRUCTURE

Let us consider crystals with a spinel structure by way of illustration of the above discussion. These crystals have the stoichiometric formula $AB_2O_4$, where A and B are cations of metals and O anions of oxygen. Figure 1 shows a primitive cell of a spinel. The crystal lattice symmetry of the spinel is characterized by the space group $O_h^7$. The A and/or B ions can be magnetic ions of $3d$ elements. These ions occupy crystallographic orbits of the type 8($a$) (tetrahedral sub-

lattice) and 16($d$) (octahedral sublattice) of the space group $O_h^7$, while anions occupy positions of the type 32($e$).

Let us consider commensurate magnetic structures induced by the IR of a space group, which satisfy the Lifshitz condition.[10] For the space group $O_h^7$, the Lifshitz condition is satisfied by 22 IR.[6,8] However, the dimensionality of the IR belonging to the star of the wave vector $\mathbf{k}_{11}=0$ does not exceed three. Here and below, we use the same notation for the wave vector stars and IR as in Ref. 8. The dimensionality of the remaining Lifshitz-type IR is higher than three. It is well known[11] that the parameters of magnetic and crystal-lochemical unit cells for exchange structures described by the star of a wave vector equal to zero coincide.

From the ten IR of the wave vector $\mathbf{k}_{11}$, the transposition representation includes[5] 11-1 and 11-4 IR in positions 8($a$), 11-1 and 11-7 IR in positions 16($d$), 11-1 IR being a unit IR according to which magnetic ordering takes place (within a crystallographic orbit). Thus, each sublattice is characterized by a spontaneous magnetization vector. The crystal is ferromagnetic as a whole if the magnetizations of the sublattices are parallel, while the spinel is ferrimagnetic if the magnetizations are antiparallel. Finally, if the magnitudes of magnetization are equal in the latter case, the spinel is a collinear antiferromagnet. Obviously, considerations based on the group theory give no information on mutual orientation of the magnetizations of sublattices, and we must use purely physical arguments concerning the magnitude and sign of intersublattice exchange constants. Let us consider a one-dimensional even IR 11-4 describing an atomic 1:1 ordering in a tetrahedral sublattice. Such an ordering in exchange magnets corresponds to a collinear antiferromagnetic structure. The emergence of the 1:1 ordering lowers the crystal symmetry: $O_h^7 \to T_d^2$. For ordinary phase transitions of the order–disorder type, such a symmetry lowering has the obvious meaning. What is the meaning of such a lowering for a magnetic exchange ordering? The crystal lattice symmetry of a spinel in the paramagnetic and magnetically ordered phases is the same (Fig. 2). This means that neutron diffraction studies of the magnetic structure makes it possible to detect the symmetry group $T_d^2$, while x-ray diffraction analysis gives the symmetry group $O_h^7$ of the crystal lattice. Thus, the transformation of the magnetic symmetry of an exchange-ordered crystal requires two space groups. Exchange ordering ac-

TABLE I. Exchange structures induced by the IR 11-7 of group $O_h^7$.

| $\mathbf{S,S,S}$ | $\mathbf{S}, 0, 0$ | $\mathbf{S}_1, \mathbf{S}_2, \mathbf{S}_2$ | $\mathbf{S}_1, \mathbf{S}_2, \mathbf{S}_3$ |
|---|---|---|---|
| $D_{3d}^5$ | $D_{2h}^{28}$ | $C_{2h}^2$ | $C_i^l$ |

cording to the 11-4 IR leads to a magnetic structure whose symmetry is described by a binomial symbol $(O_h^7, T_d^2)$.

Let us now consider the exchange ordering according to the three-dimensional IR 11-7. Table I contains stationary vectors and corresponding symmetry groups for the IR 11-7.

In order to determine the exchange structures induced by the IR 11-7, we supplement Table I with one more table giving the basis functions of this IR in positions $16(d)$. The number 16 in the notation of a crystallographic orbit is the number of points belonging to the given crystallographic orbit and located in a unit cubic cell of the space group $O_h^7$. The primitive cell (see Fig. 1) of this symmetry group contains four nonequivalent positions of the type $16(d)$. In the calculation of basis functions, these four positions are strictly labelled and have the coordinates given in Table II. The vectors of the primitive cell in Table II can be expressed in terms of the vectors of the fcc Bravais unit cell[8]:

$$\mathbf{a}_1 = \frac{1}{2}(\mathbf{A}_2 + \mathbf{A}_3); \quad \mathbf{a}_2 = \frac{1}{2}(\mathbf{A}_1 + \mathbf{A}_3);$$

$$\mathbf{a}_3 = \frac{1}{2}(\mathbf{A}_1 + \mathbf{A}_2).$$

We can now obtain scalar basis functions calculated for these four atoms[12] (Table III).

Substituting the basis functions from Table III and the elements of statmatrix from Table I into formula (1), we obtain the average value of the spin moment for each magnetic atom in the position $16(d)$ (Table IV).

Table IV shows that the total magnetic moment of a primitive cell is equal to zero for all the four phases as it should be in the case of the antiferromagnetic ordering. One-parametric phases $(\mathbf{S,S,S})$ and $(\mathbf{S},0,0)$ correspond to collinear antiferromagnetic structures, the latter phase corresponding to an Andreev–Marchenko equal-module exchange structure. The two-parametric phase $(\mathbf{S}_1, \mathbf{S}_2, \mathbf{S}_2)$ corresponds to a two-dimensional antiferromagnetic structure. The three-parametric phase with the lowest symmetry corresponds to an essentially three-dimensional antiferromagnetic structure. If the three vectors $\mathbf{S}_1, \mathbf{S}_2, \mathbf{S}_3$ have equal magnitudes and are mutually orthogonal, they satisfy conditions (8) and (9), and we again have a three-dimensional equal-module antiferromagnetic structure. Under certain thermodynamic conditions,

TABLE III. Scalar basis functions for IR 11-7 for positions $16(d)$.

| Atom number | Basis functions | | |
|---|---|---|---|
| | $\varphi_1$ | $\varphi_2$ | $\varphi_3$ |
| 1 | 1 | 1 | 1 |
| 2 | $-1$ | $-1$ | 1 |
| 3 | $-1$ | 1 | $-1$ |
| 4 | 1 | $-1$ | $-1$ |

three vectors $\mathbf{S}_1, \mathbf{S}_2, \mathbf{S}_3$ can accidentally become equal in magnitude and mutually orthogonal, but these conditions do not correspond to any thermodynamic phase since the conditions (7) and (8) for the existence of an equal-module structure are not thermodynamic conditions. Conversely, the equal-module structure corresponding to the one-parametric solution $(\mathbf{S},0,0)$ is obtained under certain thermodynamic conditions and corresponds to a stable (in certain limits) equal-module exchange structure.

## CONCLUSION

We can summarize the results of the above analysis as follows. Equal-module exchange structures that can be formed in crystals belong to two essentially different classes. The first class includes thermodynamically stable exchange structures characterized by their own magnetic symmetry. The second class includes the structures appearing under conditions (7) and (8). These structures can be singled out from a thermodynamically stable exchange structure by imposing the additional nonthermodynamic condition (8) and have no magnetic phase with its own magnetic symmetry corresponding to them. The problem of exchange structures is not only of academic interest and does not serve just as an exercise in the methods of the group theory. The results of numerous experiments show that magnetic phases (see Refs. 13 and 14) whose thermodynamic properties are determined only by the exchange interaction can be formed in some magnetic crystals. For this reason, the symmetry of exchange structures exactly corresponds to the symmetry of isotropic magnetic phases in these crystals.

TABLE II. Coordinates of atoms in $16(d)$ position.

| Atom number | Position of atom in primitive cell |
|---|---|
| 1 | $(5/8)(\mathbf{a}_1 + \mathbf{a}_2 + \mathbf{a}_3)$ |
| 2 | $(1/8)(\mathbf{a}_1 + 5\mathbf{a}_2 + 5\mathbf{a}_3)$ |
| 3 | $(1/8)(5\mathbf{a}_1 + \mathbf{a}_2 + 5\mathbf{a}_3)$ |
| 4 | $(1/8)(5\mathbf{a}_1 + 5\mathbf{a}_2 + \mathbf{a}_3)$ |

TABLE IV. Magnetic moments of atoms in positions $16(d)$ for antiferromagnetic exchange structures induced by IR 11-7.

| Atom number | Statmatrices | | | |
|---|---|---|---|---|
| | $\mathbf{S,S,S}$ | $\mathbf{S}, 0, 0,$ | $\mathbf{S}_1, \mathbf{S}_2, \mathbf{S}_2$ | $\mathbf{S}_1, \mathbf{S}_2, \mathbf{S}_3$ |
| 1 | $3\mathbf{S}$ | $\mathbf{S}$ | $\mathbf{S}_1 + 2\mathbf{S}_2$ | $\mathbf{S}_1 + \mathbf{S}_2 + \mathbf{S}_3$ |
| 2 | $-\mathbf{S}$ | $-\mathbf{S}$ | $-\mathbf{S}$ | $-\mathbf{S}_1 - \mathbf{S}_2 + \mathbf{S}_3$ |
| 3 | $-\mathbf{S}$ | $-\mathbf{S}$ | $\mathbf{S}$ | $-\mathbf{S}_1 + \mathbf{S}_2 - \mathbf{S}_3$ |
| 4 | $-\mathbf{S}$ | $\mathbf{S}$ | $\mathbf{S}_1 - 2\mathbf{S}_2$ | $\mathbf{S}_1 - \mathbf{S}_2 - \mathbf{S}_3$ |

*E-mail: kchti@com2com.ru;
hborlakov@hotmail.com

[1] A. F. Andreev and V. I. Marchenko, Usp. Fiz. Nauk **130**, 39 (1980) [Sov. Phys. Usp. **23**, 21 (1980)].

[2] V. G. Bar'yakhtar and D. A. Yablonskii, Fiz. Nizk. Temp. **6**, 345 (1980) [Sov. J. Low Temp. Phys. **6**, 164 (1980)].

[3] Yu. M. Gufan, E. I. Kut'in, V. L. Lorman *et al.*, Pis'ma Zh. Éksp. Teor. Fiz. **46**, 228 (1987) [JETP Lett. **46**, 287 (1987)].

[4] Yu. M. Gufan, *Structural Phase Transitions* [in Russian], Nauka, Moscow (1982).

[5] V. P. Sakhnenko, V. M. Talanov, and G. M. Chechin, Fiz. Met. Metalloved. **62**, 847 (1986).

[6] V. P. Sakhnenko, V. M. Talanov, and G. M. Chechin, Dep. VINITI, dep. No. 638-82, Moscow (1982).

[7] Yu. A. Izyumov, V. I. Naish, and R. P. Ozerov, *Neutron Diffraction Analysis of Magnets* [in Russian], Atomizdat, Moscow (1981).

[8] O. V. Kovalev, *Irreducible and Induced Representations and Corepresentations of Fedorov Groups* [in Russian], Nauka, Moscow (1986).

[9] N. N. Bogoliubov and D. V. Shirkov, *Introduction to the Theory of Quantized Fields* [in Russian], Nauka, Moscow (1976).

[10] L. D. Landau and E. M. Lifshitz, *Statistical Physics* [in Russian], Part I, Nauka, Moscow (1976).

[11] V. L. Indenbom, Sov. Phys. Crystallogr. **5**, 115 (1960).

[12] V. P. Sakhnenko, V. M. Talanov, and G. M. Chechin, Dep. VINITI, dep. No. 6379-83, Moscow (1983).

[13] Kh. Sh. Borlakov, Preprint SAO RAN No. 116 T (1997).

[14] Kh. Sh. Borlakov, Preprint SAO RAN No. 117 T (1997).

Translated by R. S. Wadhwa

# Phase diagram of Ising model ($S=1$) with easy-plane anisotropy in a magnetic field

A. A. Loginov and Yu. V. Pereverzev

*B. Verkin Institute for Low Temperature Physics and Engineering, National Academy of Sciences of the Ukraine, 310164 Kharkov, Ukraine**

The surfaces corresponding to the loss of stability and equilibrium of paramagnetic and antiferromagnetic states are found in the mean field approximation with temperature, field, and anisotropy as variables. The characteristic temperatures at which the topology of phase diagram sections changes are determined. © *1998 American Institute of Physics.* [S1063-777X(98)00909-8]

## 1. INTRODUCTION

This paper is devoted to an analysis of the phase diagram for an Ising antiferromagnet with a spin $S=1$ at each lattice site, which exhibits one-ion anisotropy of the type of an easy plane normal to the Ising axis and is in a magnetic field **H** parallel to this axis. Such a model is exotic from the point of view of magnetic systems since Ising anisotropy of spin–spin interactions is usually associated with a strong one-ion anisotropy of the easy-axis type. However, such a model can exist as an equivalent model for some structural phase transitions. For example, if the coordinate which is active in a transition under consideration has an effective crystal potential with three minima, the classical configuration integral of states in the first approximation at low temperatures can be reduced to the partition function in the Ising model ($S=1$). This is true if the minima differ insignificantly in energy and are all deep enough to be approximated by quadratic potentials in the temperature range significant for the transition in question. In this case, the partition function from the Ising model is obtained if the elastic constants of the potential wells have the same values. If the values of these constants are different, the partition function is modified by additional weight factors determined by the ratio of elastic constants. We shall not go beyond these tentative considerations concerning the possible origin of the model under investigation. Its behavior is quite peculiar, and the problem is of independent interest from the point of view of the ''zoology'' of phase diagrams. The relation between such a model and the experimentally observed structural phase transition[1] induced by a magnetic field is based on considerations described in Ref. 2 and will be analyzed more thoroughly in a separate publication.

We shall analyze the model in the mean field approximation.

## 2. FORMULATION OF EQUATIONS

The model under investigation is described by the Hamiltonian

$$\hat{H} = \frac{1}{2} \sum J_{fg} S_f^z S_g^z - H \sum S_f^z + D \sum (S_f^z)^2, \tag{1}$$

where $J_{fg} > 0$ is the exchange interaction parameter, $H$ the magnetic field (in energy units), $D > 0$ the one-ion anisotropy constant, and $S_f^z$ is the $z$-component of spin at the $f$th lattice site, $S_f^z = 0, 1, -1$. The summation is carried out over nearest pairs of sites of the three-dimensional lattice containing $2N$ sites.

The model free energy[2] in the molecular field approximation in the class of two sublattice structures (we assume that the nearest neighbors at one lattice site cannot be nearest neighbors relative to each other) has the form

$$F_{\text{mod}} = NJ_0 f, \quad J_0 = \sum_g J_{fg},$$

$$f = \sigma_1 \varphi(x_1) + \sigma_2 \varphi(x_2) + \varphi(x_1) \varphi(x_2) - t[\ln Z(x_1) + \ln Z(x_2)], \tag{2}$$

$$Z(x) = q + \cosh x, \quad \varphi(x) = \frac{\partial \ln Z}{\partial x} = \frac{\sinh x}{q + \cosh x},$$

$$x_i = (\sigma_i - h)/t \quad (i=1,2), \quad q = \frac{1}{2} \exp(d/t),$$

where $t = T/J_0$, $h = H/J_0$, $d = D/J_0$, and $\sigma_{1,2}$ are self-consistence parameters. The values of $\sigma$ can be determined from the conditions of the minimum value of $f$. The stability condition for $f$ in $\sigma$ can be expressed by the equations

$$\sigma_1 + \varphi(x_2) = 0, \quad \sigma_2 + \varphi(x_1) = 0 \tag{3}$$

and coincide with the self-consistency conditions

$$\sigma_1 = \langle S_1^z \rangle, \quad \sigma_2 = \langle S_2^z \rangle, \tag{4}$$

where the averaging $\langle ... \rangle$ is carried out over the Gibbs state with the molecular field Hamiltonian of the form

$$\hat{H}_m = -J_0 \sigma_1 \sigma_2 + (J_0 \sigma_2 - H) S_1^z + (J_0 \sigma_1 - H) S_2^z + D[(S_1^z)^2 + (S_2^z)^2]. \tag{5}$$

The necessary condition for stability loss, i.e.,

$$\det \left\| \frac{\partial^2 f}{\partial \sigma_i \partial \sigma_j} \right\|_{i,j=1,2} = 0 \tag{6}$$

can be reduced to the form

$$\varphi'(x_1)\varphi'(x_2)=t^2 \tag{7}$$

and defines, together with Eqs. (3), the boundaries for the existence and stability of all local minima of the model free energy. It should be noted that since the inequality $\varphi'(x) > 0$ is satisfied identically in the case under consideration, the necessary condition for stability $\varphi'(x_1)\varphi'(x_2)<t^2$ is also a sufficient condition since $\partial^2 f/\partial\sigma_1^2=t^{-1}\varphi'(x_1)$ at the stationary points.

Equations (3) have paramagnetic ($\sigma_1=\sigma_2$) and antiferromagnetic (AFM, $\sigma_1\neq\sigma_2$) solutions. It is convenient to describe these solutions by the order parameter $l_0$ (the antiferromagnetism parameter) and the mean spin $m_0$:

$$\sigma_1=m_0+l_0, \quad \sigma_2=m_0-l_0. \tag{8}$$

We can write the steady-state conditions (3) in these variables for the paraphase ($l_0=0$) and AFM ($l_0\neq0$) solutions separately. For $l_0=0$, we obtain

$$m_0=-\varphi(m), \quad m=(m_0-h)/t. \tag{9}$$

In view of the monotonicity of the function $\varphi$, the paraphase solution obviously exists in all cases and is unique. For AFM solutions, Eqs. (3) have the form

$$t=\xi[q\cosh m+\cosh l]/\Delta, \quad \xi=\sinh l/l, \quad l=l_0/t, \tag{10}$$

$$h=-mt-\sinh m[q\cosh l+\cosh m]/\Delta, \tag{11}$$

$$\Delta=[q\cosh l+\cosh m]^2-(q^2-1)\sinh^2 l. \tag{12}$$

In these variables, condition (7) assumes the form

$$(q\cosh m+1)Z^{-2}(m)=t; \tag{13}$$

for paraphase solutions, and

$$\cosh m=[(1-q^{-2})(\xi^2-1)^{-1}]^{1/2}\sinh l-q^{-1}\cosh l, \tag{14}$$

for AFM solutions. We do not write here standard equations of phase equilibrium, which are also required for constructing a phase diagram in the regions of existence of several stable time-independent solutions.

A complete analysis of Eqs. (3), (7), or (9)–(14) (as well as phase-equilibrium conditions) cannot be carried out. For this reason, we shall use the combination of numerical and analytic methods in various limiting cases.

Let us study the phase diagram in the space of controlling parameters $(h,t,d)$. Since the plane $h=0$ is a symmetry plane, we shall assume that $h>0$. We shall henceforth indicate explicitly only states with $l>0$ ($\sigma_1>\sigma_2$) since if $(l,m)$ is a solution of steady-state equations, $(-l,m)$ is also a solution. Taking this into consideration, we can write $0\leq\sigma_1\leq1$ and $-1\leq\sigma_2\leq\min(1,h)$ (it should be noted that $\sigma_2\leq0$ for $h\leq\sigma_1$).

The most important element of the phase diagram is the stability loss surface for the paraphase state (PS). We begin the analysis of the results with the description of this surface.

## 3. STABILITY LOSS SURFACE FOR PARAPHASE STATES

The boundary of the PS stability region in the space of controlling parameters $(h,t,d)$ is described by the equations
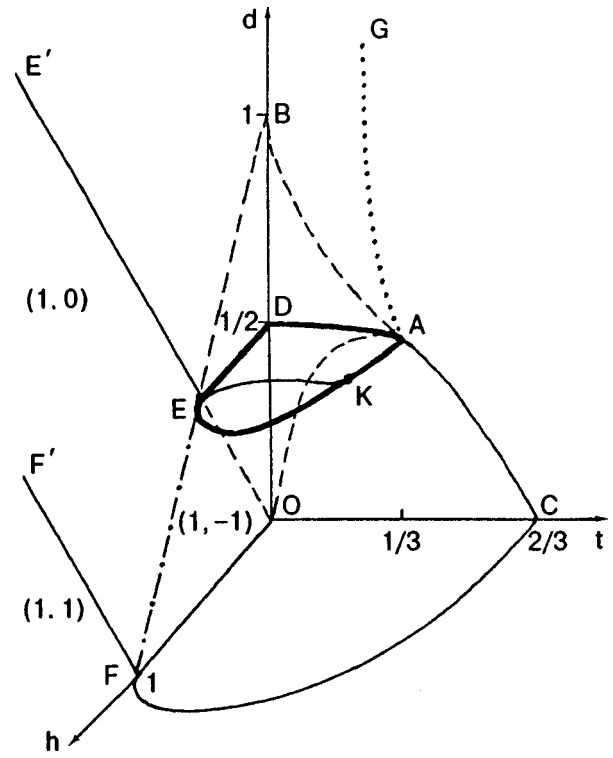


FIG. 1. Schematic phase diagram in the variables $t$, $h$, and $d$. Fine curve KE and bold curve AKE are spatial curves, the remaining curves lie on the coordinate planes. Fine curves are the intersections of the PT2 with coordinate planes and with the PT1 surface, the dotted curve AG is the projection of the PT2 surface on the plane $h=0$. Dashed lines are intersections of the stability loss surfaces with the coordinate planes. The dot-and-dash line describes the divergence of $\partial m/\partial h$.

$$h=h_i(t,d), \quad i=1,2, \tag{15}$$

where

$$h_i(t,d)=d+t\ln\left[\frac{y_i+(y_i^2-4t^2/q^2)^{1/2}}{4t}\right]$$
$$+\frac{(y_i^2-4t^2/q^2)^{1/2}}{y_i+2t},$$

$$y_{1,2}=1-2t\pm(1-4t+4t/q^2)^{1/2}.$$

These equations together with the initial equations (9) and (13) make it possible to describe the shape of the surface under investigation. Its projection on the $(t,d)$ plane is the region

$$1-q^{-2}\leq(4t)^{-1} \quad \text{for } d\geq\tfrac{1}{3}\ln 4, \quad t\leq1/3, \tag{16}$$

$$1+q\geq t^{-1} \quad \text{for } 0\leq d\leq\tfrac{1}{3}\ln 4, \quad t\geq1/3. \tag{17}$$

The boundary of this region (adjoining the $d$-axis) is shown in Fig. 1 by the CAG curve. The curve CA corresponds to the equality in (17), while the AG curve corresponds to the equality in (16), the latter having the asymptotic form $t=1/4$. The entire curve OAC can also be described by the equality in (17) (if $t$ varies in the interval $(0, 2/3)$) and is the intersection of the surface (15) with the $(t,d)$ plane. The

field $h_2$ is not defined at points under the OAC curve. The PS instability region for these points is described by the inequality $h < h_1$. A part of the $(t,d)$ plane bounded by the OAG curve is covered by surface (15) twice. In this case, the region of unstable PS lies in the field interval $h_2 < h < h_1$. The surface (15) intersects the $(t,h)$ plane along the curve CF described by the equation $h = h_1(t,0)$. For $t \to 0$, its asymptotic form is

$$h_1(t,0) \simeq 1 - t \ln t. \tag{18}$$

In general, the asymptotic form of the fields $h_1, h_2$ for $t \to 0$ is

$$h_1(t,d) \simeq d + 1 - t \ln t, \quad h_2(t,d) \simeq d + t \ln t. \tag{19}$$

It can be seen that the surface (15) touches the plane $t = 0$ along two parallel straight lines $h = d$ and $h = d + 1$ (OEE$'$ and FF$'$), respectively. The PS instability region in this plane lies between these straight lines and goes to infinity. Other sections of the surface (15) by the planes $t = \text{const}$ are shown in Fig. 2 and can be described as follows. For $t$ belonging to the interval $(0, 1/4)$, these are two lines OE$'$ and FF$'$ going to infinity as before (see Fig. 2a), which converge for $t \to 1/4$ for large $h$. For $t > 1/4$, it is a single curve OF (see Figs. 2b and 2c) bounding a finite PS instability region. For $t > 2/3$, there are no points of stability loss.

We must now consider the existence of stable AFM solutions other than the AFM solutions generated in the case of paraphase stability loss. This is associated with the possibility of first-order phase transitions (PT1). It is well known[4] that a general mechanism of such transitions is associated with degeneracy of the ground state for certain values of controlling parameters. If the Peierls stability condition[4] is satisfied in this case, such values of the parameters must lie at the edge of the PT1 surface existing for small $t > 0$ (The Peierls condition indicates that the energy of local excitations above the ground state increases not more slowly than the number of boundary excitation sites). For this reason, it is expedient to analyze the phase diagram first in the low-temperature range.

## 4. LOW-TEMPERATURE RANGE

Let us first describe the phase diagram for $t = 0$, which is obtained from an analysis of the ground states of the molecular field Hamiltonian (5). It must correspond to the phase diagram constructed on the basis of free energy for $t \to 0$.

In the region $h < d$ on the plane $t = 0$ (above the ray OE$'$ in Fig. 1), the state $(S_1^z, S_2^z) = (0,0)$ is the self-consistent ground state for the Hamiltonian (5) (the stability condition for the state at $t = 0$). In the region $h + d < 1$ (under the BF curve in Fig. 1), the self-consistent ground state is $(1, -1)$. Thus, there exist two stable states within the triangle BEO with energies coinciding on the segment DE of the straight line $d = 1/2$. Consequently, a PT1 occurs on this segment from the AFM state $(1, -1)$ which is in equilibrium for $d < 1/2$ to the PS $(0,0)$ which is in equilibrium for $d > 1/2$.

In the region on the plane bounded by the line E$'$EFF$'$ ($0 < h < d + 1$ and $h + d > 1$), the only stable state is $(1,0)$, while the only stable state in the region $h > d + 1$ (under the
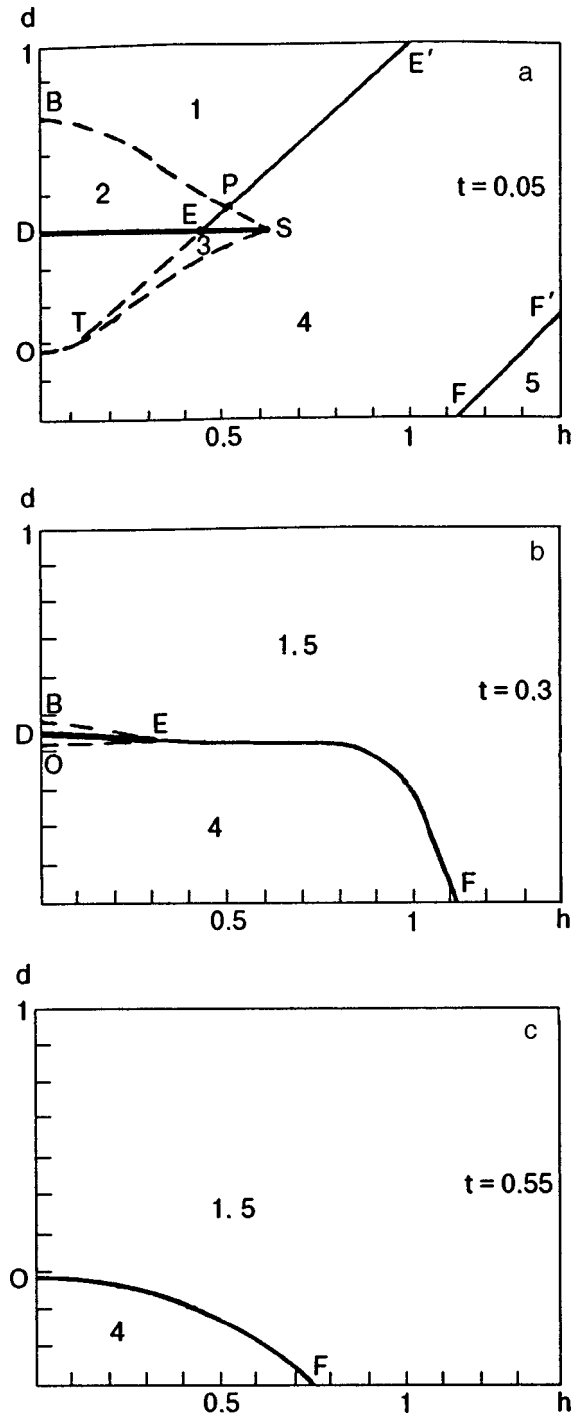


FIG. 2. Temperature sections of the phase diagram for $t = 0.05$ (a), 0.3 (b), and 0.55 (c). Fine curves correspond to PT1, thick line to PT1, while dashed curves characterize the loss of stability.

line FF$'$) is the PS $(1,1)$. The stability loss lines EE$'$, EF, and FF$'$ are equilibrium lines for adjacent pairs of states. This distinguishes them significantly from the PT1 line DE, although the equilibrium states also change jumpwise in this case. The lines FF$'$ and OE$'$ correspond to the limiting ($t \to 0$) expression for the PS stability loss surface (19).

It is expedient to compare these results with the results of analysis of the ground states of the exact Hamiltonian (1) and the Peierls condition mentioned above. The ground states of Hamiltonian (1) at all internal points in the above-

described regions coincide with equilibrium states obtained by the molecular field method. The ground state is also doubly degenerate on the DE line, the Peierls stability condition being satisfied in this region. This ensures the existence of a PT1 surface emerging from the segment DE at low temperatures. As regards the line E'EFF', we can easily verify that the number of ground states on this line is infinitely large. For example, proceeding from the state $(1, -1)$ on EF, we can transform any number of sites with $S^z = -1$ to a state with $S^z = 0$ so that neighboring sites are only typical of coexisting phases $(1,0)$ and $(1,-1)$. In particular, we can construct in this way periodic ground states with an arbitrary period and relative concentration of coexisting phases on this line. In the situation described above, the Peierls condition is violated, and the lines EE' and FF' can be continued to the region $t > 0$ as surfaces of a continuous PT2 according to (19). Conversely, the line EF has no continuation to the region $t > 0$ (this will be clear from the subsequent description of all possible states) and remains isolated special line on the phase diagram for $t = 0$. It is manifested in actual practice as a line on which the susceptibility $\partial m / \partial h$ diverges as we approach the line from the region $t > 0$ (for example, if we approach the EF line along the surface $d + h = 1$, we can prove that $\partial m / \partial h \sim 1/(8t)$ for $t \to 0$).

Let us now consider the phase diagram for small $t$. The PS stability loss surface is described above by formulas (19), and hence it remains for us to describe the behavior of AFM solutions. Let us consider the asymptotic form of the phase diagram for $t/d \to 0$. The region of existence of AFM solutions is bounded by stability loss surfaces which are defined by the system of equations (10), (11) and (14). As $t \to 0$ on this surface, $l_0$ necessarily tends to $d$. Taking this into consideration, we omit rapidly decreasing terms of the type $t^{-1} \exp(-d/t)$ or $t^{-1} \exp(-l/t)$ in the equations of the surface (this can be done if $d$ does not tend to zero for $t \to 0$). In this case, Eqs. (10), (11), and (14) can be written in the form

$$d = l_0 - t \ln r, \tag{20}$$

$$r = (l_0 - 0.5)t^{-1} + [(l_0 - 0.5)^2 t^{-2} + 1]^{1/2},$$

$$m_0 = t[(l - r)^2 - 1]^{1/2}, \tag{21}$$

$$h = m_0 + t \ln(l - r + m_0/t). \tag{22}$$

These formulas (20)–(22) define the $l_0$-parametric representation of cross sections of the stability loss surface by the planes $t = \text{const} \leqslant d$ ($l_0$ varies in the interval $[0.5 - 0.5\sqrt{1 - 4t}; 0.5 + 0.5\sqrt{1 - 4t}]$). These formulas are equilibrium asymptotic approximations (for $t \to 0$) for exact equations in the entire range of controlling parameters $h$ and $d$ except a small neighborhood of points with $d = 0$. As a result of the latter restriction, the solutions corresponding to values of $l_0$ in the vicinity of the lower boundary of the admissible interval of its variation are incorrect and require the inclusion of the omitted terms. It should be noted, however, that even in the vicinity of such points, the formulas give a correct limiting value of the surface cross section ($t = 0$).

The calculation of the derivatives $\partial d / \partial l_0$ and $\partial h / \partial l_0$ shows that the cross sections of the surface under

consideration by the planes $t = \text{const}$ have two branches. One branch corresponds to values of $l_0 < 0.5$ and is described by a monotonically increasing function $d_1(h)$ with zero derivative at the point with $l_0 = 0.5$. The other branch corresponds to $l_0 > 0.5$ is described by a monotonically decreasing function $d_2(h)$ whose derivative at the point with $l_0 = 0.5$ is also equal to zero. Figure 2a shows a section of the phase diagram by the plane $t = 0.05$, where the functions $d_{1,2}$ are described by the curves TS and BS (the curve corresponding to $d_1$ for small values of $l_0$ is plotted according to exact solutions, and the point T corresponds to $l_0 = 0$). These curves form a "beak" ($l_0 = 0.5$) with the coordinates $(h, d)$ and the magnetization given by

$$h = \sqrt{1/4 - t} + t \ln[0.5t^{-1} - 1 + 0.5t^{-1}\sqrt{1 - 4t}]$$
$$\approx 0.5 + t \ln(1/t), \quad d = 0.5, \tag{23}$$

$$m_0 = \sqrt{1/4 - t} \approx 0.5 - t. \tag{24}$$

A comparison with (19) shows that the "beak," and hence both surfaces corresponding to the loss of stability of AFM solutions are within the region of instability of the paraphase. Using formulas (20)–(22), we can verify that the extreme positions of the $d_1$ and $d_2$ curves for $t = 0$ coincide with the segments OE and BE respectively in Fig. 1. The curve $d_1$ for low temperatures lies completely in the region of instability of the paraphase solution (see Fig. 2a). There is no continuation to the region with $t \neq 0$ for segment EF in Fig. 1 (see above).

It was mentioned above that the surface under investigation for a fixed (although small) temperature cannot be described correctly by formulas (20)–(22) for points with small $d$. In fact, the $d_1$ curve terminates at a certain point T (see Fig. 2a) lying on the stability loss line OE' for the paraphase solution. At this point, the AFM and the paraphase states coincide ("merging of curves"). We can obtain the condition for merging the surfaces corresponding to the loss of stability of paraphase and AFM solutions along a certain curve (the curve of tricritical points whose section is point T in Fig. 2a) as well as the equation for this curve from a qualitative analysis of the steady-state equation.

Such an analysis allows us to interpret the section of the phase diagram corresponding to low temperatures (see Fig. 2a) as follows. In region *1* lying above the BPE' curve, only one (paraphase) solution exists. In region *2* bounded by the curve BPTO, two stable (PP and AFM) solutions exist. Region *3* bounded by the "triangle" TSP corresponds to two stable AFM solutions one of which is generated on the segment TP of the stability loss curve for the paraphase and loses its stability on the TS curve. The condition for the emergence of AFM minima on the stability loss surface for the paraphase (which is not connected with the low value of temperature) is the inequality

$$3[\varphi''(x)]^2 - 2t\varphi'''(x) \geqslant 0, \quad x = (\sigma - h)/t. \tag{25}$$

The equality in (25) and Eqs. (3) and (13) ($m = x$ in the latter case) are equations of the curve of tricritical points. These equations can be used for obtaining relations connecting magnetization $\sigma$ and temperature

$$\sigma^6 - 2\sigma^4(1-2t) + \sigma^2(1-4t+5t^2) - 2t^2(1/3-t) = 0 \tag{26}$$

as well as expressions for the field and anisotropy:

$$h = \sigma - 0.5t\ \ln[(t+\sigma^2-\sigma)(t+\sigma^2+\sigma)^{-1}], \tag{27}$$

$$d = t\ \ln\{2(1-t-\sigma^2)[(t+\sigma^2)^2-\sigma^2]^{-1/2}\}. \tag{28}$$

For small $t$, the only solution satisfying the system of equations (3), (13), and (26) corresponds to the root of equation (26) tending to zero as $t\to 0$. For small $t$, this gives the coordinates $(d,h)$ of the point T:

$$\sigma \approx \sqrt{2/3}\,t, \quad d \approx t\ \ln(t^{-1}) + 0.5t\ \ln 12,$$

$$h \approx t[\sqrt{2/3} + \ln(\sqrt{3}+\sqrt{2})]. \tag{29}$$

This point marks the segment OT on the stability loss curve for the paraphase, on which no AFM solutions are generated. We shall return to the tricritical curve while considering higher temperatures after completing the description of the structure of the low-temperature section of the phase diagram (see Fig. 2a). In each of the regions *2* and *3* described above, two minima coexist, and hence each of these regions contains an equilibrium curve, i.e., the PT1 curve. We are aware of two point on this curve: one point can be obtained as an asymptotic curve for the parameter $d$ for $h=0$ and $t\to 0$ (Sec. 5), and the other point is the ''beak.'' Intermediate points were obtained numerically, the corresponding line being DS (bold line). In region *4* bounded the OTSPE$'$ and FF$'$ curves, only one AFM minimum is observed, while region *5* corresponds to the paraphase solution only.

Thus, the low-temperature section of the phase diagram (see Fig. 2a) contains the PT1 curve (DES), the PT2 curve branching from it at point E (EE$'$), and the PT2 curve (FF$'$). On the segment DE, a PT1 from the AMF phase to the paraphase takes place (upward motion), while on segment ES a PT1 between AFM states occurs (terminating with the critical state at point S).

## 5. GENERAL STRUCTURE OF PHASE DIAGRAM

Let us first consider the section of the diagram by the plane $h=0$ (shown in Fig. 1). The stability loss curve OAC for the paraphase is described in Sec. 3. A qualitative analysis of Eqs. (3) leads to the conclusion that the stability loss curve BA of the AFM phase merges with it at the tricritical point A with the coordinates

$$t = 1/3, \quad d = \tfrac{1}{3}\ln 4 \approx 0.462. \tag{30}$$

This point is the intersection of the tricritical points curve described above with the plane $h=0$. The equilibrium curve for the phases coexisting in the ''triangle'' OAB connects point A with the point $d=1/2$, $t=0$ (the AD line) and can be described in the vicinity of points D and A by the asymptotic formulas

$$d \approx 0.5 - (1-t)\exp(-0.5t^{-1}),$$

$$\sigma = 1 - \exp(-0.5t^{-1}); \tag{31}$$

for $t\to 0$ and

$$d \approx \frac{1}{3}\ln 4 + \left(\frac{3}{2}-\ln 4\right)\left(\frac{1}{3}-t\right) + \frac{27}{32}\left(\frac{1}{3}-t\right)^2,$$

$$\sigma^2 \approx \frac{15}{2}\left(\frac{1}{3}-t\right) \tag{32}$$

for $t\to 1/3$. It should be noted for comparison that the $d(t)$ dependence near point A for stability loss curves of the AFM and paraphase solutions (AB and AO curves) differ from (32) only in the coefficient of the last term, which is equal to $9/4$ and $-27/8$, respectively in these cases.

It can be seen that $t=1/3$ is one of the points at which the topology of the temperature sections of the phase diagram changes.

Another characteristic temperature is that at which the tricritical point T merges with the critical point S (see Fig. 2a). We shall call such a point a degenerate critical point. At this temperature, region *3* shrinks to a point and vanishes upon a further increase in temperature. From the point of view of phase states, two AFM minima and a paraphase peak merge in this case. The corresponding equations can be derived on the basis of the following considerations.

Using the second equation from (3), we can express the free energy (2) as a function of only one parameter $\sigma_1$, i.e., $f_1(\sigma_1) = f[\sigma_1, \sigma_2(\sigma_1)]$. The remark following formula (7) and the expressions for the second derivative of the function $f_1$ at its stationary points, i.e.,

$$f_1'' = t^{-1}\varphi'(x_1)[1 - t^{-2}\varphi'(x_1)\varphi'(x_2)] \tag{33}$$

lead to the conclusion that local minima of the function $f_1$ correspond to local minima of the model free energy $f$, and vice versa. Consequently, equating to zero the first consecutive derivatives of the function $f_1$, we obtain successively the steady-state equations for the stability loss surface as well as the lines of critical, tricritical, and finally the degenerate critical point. The equality to zero of the third, fifth, and seventh derivatives is a consequence of the previous equations if $l_0=0$. For the critical points, we obtain a system consisting of Eqs. (3) and (7), and the equality $f_1'''=0$:

$$[\varphi'(x_1)]^3(\varphi''(x_2))^2 = [\varphi'(x_2)]^3[\varphi''(x_1)]^2. \tag{34}$$

For the tricritical points, we obtain the system (26)–(28) again, while for the degenerate critical point this system is supplemented with the equality to zero of the sixth derivative. Taking into account other equations of the system, it can be presented in the form

$$2t\varphi^{(5)} - 15\varphi^{(4)}\varphi^{(2)} + \tfrac{40}{3}(\varphi^{(3)})^2 = 0, \tag{35}$$

$$\varphi^{(k)} \equiv \partial^k\varphi/\partial x^k.$$

The system (26)–(28), (35) has a unique solution and gives the following parameters for the degenerate critical point K (see Fig. 1):

$$t_k = \frac{62}{225} \approx 0.276,$$

$$h_k = \frac{2\sqrt{2}}{225} - \frac{31}{225}\ln\left[\frac{(7-3\sqrt{2})^2}{31}\right] \approx 0.382,$$

$$d_k = \frac{31}{225}\ln 31 \approx 0.473, \quad \sigma_k = \frac{2\sqrt{2}}{15} \approx 0.189. \quad (36)$$

Thus, the segment KA of the curve for tricritical points lies at the edge of the surface PT1, while the remaining part of the curve (connecting points O and K and not shown in the figure) lies under this surface in the region of metastable states (point T in Fig. 2a).

The sequence of temperatures at which the topology of temperature sections of the phase diagram changes is given by

$$0 < 0.25 < t_k < 1/3 < 2/3. \quad (37)$$

The phase diagram shown in Fig. 1 is described in Sec. 4 at $t = 0$. The first rearrangement takes place at the emergence of a nonzero temperature. The OE line (see Fig. 1) bifurcates, giving rise to a ''triangular'' region TPS (see Fig. 2a in which two AFM minima exist. As the value of $t$ increases, this region first expands, and then shrinks to a point at a temperature $t_k$. The structure of the section in the interval (0, 0.25) is shown in Fig. 2a and is described in the same Sec. 4. In the interval $(0.25, t_k)$, the PT1 in the AFM phase still exists, but the stability loss line of the paraphase becomes connected, and the region of AFM states becomes bounded. We shall not illustrate this by a figure which can be easily visualized, but is difficult to plot on a scale such that both the singularities mentioned above are seen clearly since the segment SE is very small, and the OE and FF' lines merge far away. In the temperature interval $(t_k, 1/3)$, there is no critical point in the AFM phase, and the PT1 curve passing the tricritical point is transformed into the PT2 line. A typical section is shown in Fig. 2b for $t = 0.3$. The interval (1/3, 2/3) contains only the PT2 line (see Fig. 2c) which contracts to the origin upon an increase in temperature, and only the paraphase solution exists for $t > 2/3$.

Thus, the general pattern of phase diagram can be explained by the set of the figures presented in this work. The PT1 surface is a nearly horizontal piece of the surface bounded by the bold AKED curve in Fig. 1 (AD is the line of its section by the plane $h = 0$, while the surface itself can be continued symmetrically to the region $h < 0$). The PT2 surface emerges from the fine line on this surface connecting points K and E. (The point on this line in Fig. 2a correspond to point E, while the line EE' corresponds to the PT2 sur-

face.) The remaining ''reference'' elements on the PT2 surface are the arcs AK, AC, CF, FF', and EE'. The curve of critical points (bold line EK) is covered by this surface and lines within this surface in the instability region of the PS.

## 6. CONCLUSION

We studied the general structure of the phase diagram of the Ising model under investigation. Figure 1 shows qualitatively its main elements. The results of numerical calculations of the temperature sections of the phase diagram are presented in Fig. 2. The described geometric structure of the diagram and the asymptotic formulas derived for various limiting cases as well as the values of some characteristic parameters makes it possible to calculate reliably various elements of the phase diagram. A typical feature of the PT1 surface is that it is concentrated in the anisotropy parameter $d$ in a very small neighborhood of its value equal to 1/2. The deviation (in the downward direction) amounts to less than 0.03. If we consider direct interpretation of the model in question, experimental observation of such a transition is is hampered in view of limited possibility of controlling the parameter $d$. It was mentioned in Introduction, however, that this model is equivalent to a certain model of structural phase transition induced by a magnetic field. In this case, the parameter $d$ can be controlled by the same field a over wide interval of values. It should also be noted that as we approach another observable element of the phase diagram, viz., segment EF (see Fig. 1, $t = 0$) from the region where $t > 0$, the susceptibility $\partial m/\partial h$ diverges (this is analogous to Lifshitz transitions in electron systems).[5]

*E-mail: pereverzev@ilt.kharkov.ua

[1] V. I. Kut'ko, M. I. Kobets, V. A. Pashchenko, and E. N. Khats'ko, Fiz. Nizk. Temp. **21**, 441 (1995) [Low Temp. Phys. **21**, 345 (1995)].
[2] Yu. V. Pereverzev, Fiz. Nizk. Temp. **22**, 289 (1996) [Low Temp. Phys. **22**, 226 (1996)].
[3] S. V. Tyablikov, *Methods in the Quantum Theory of Magnetism*, Plenum Press, NY, 1967.
[4] Ya. G. Sinai, *Theory of Phase Transition* [in Russian], Nauka, Moscow (1980).
[5] A. A. Abrikosov, *Fundamentals of the Theory of Metals*, No. Holland, Amsterdam, 1988.

Translated by R. S. Wadhwa

## LOW-DIMENSIONAL AND DISORDERED SYSTEMS

# On electron states localized at intercrystallite and twin boundaries

E. P. Feldman and V. M. Yurchenko

*A. Galkin Physicotechnical Institute, National Academy of Sciences of the Ukraine, 340114 Donetsk, Ukraine**

It is stated that an electron can be in a state localized at an intercrystallite or twin boundary or stacking fault irrespective of the specific structure of the transition region. It is important that the crystal containing such a boundary must be non-periodic ''as a whole.'' The one-dimensional model (two abutting Kronig–Penney lattices for which the spectrum of localized states is determined) is considered. The bands containing one or two discrete levels alternate in a complex way in the spectrum. © *1998 American Institute of Physics.* [S1063-777X(98)01009-3]

**1.** It was established by Tamm[1] that an electron can be bound by the external surface of a crystal. The electron wave function in such a state localized near the surface decreases exponentially towards the bulk of the crystal and in the outward direction. The electron is as if trapped by the potential barrier from the outer side and by the periodic potential relief from the inner side. Tamm proposed a simple one-dimensional model that makes it possible to prove the emergence of discrete levels, to estimate their position in the band structure, and to find the radii of localization of the corresponding wave functions. Essentially, the presence of a surface in Tamm's model is not reduced to a local change in potential energy. The corresponding quantum-mechanical problem can be solved exactly and not in accordance with the perturbation theory.

In real crystals, the electron spectrum can be affected significantly not only by outer surfaces, but also by inner interfaces. We are speaking primarily of intercrystallite boundaries separating regions with identical structure, which are disoriented and/or shifted relative to each other. Specularly symmetric crystallites are in contact along twin boundaries.

Interfaces of this type violate the periodicity globally (on a macroscopic scale) so that a polycrystal as a whole is certainly not periodic in spite of the periodicity of the structure of individual crystallites. This peculiar nonhomogeneity of the material is responsible for qualitatively new properties such as the emergence of grain-boundary sound waves,[2] and extra electrical and thermal resistance.[3] The curves describing the dependence of the energy of a bicrystal on the angle of disorientation of adjacent crystallites acquire sharp minima for preferred angles corresponding to a high density of coinciding lattice sites, i.e., to a small size of the lattice of coinciding sites.[4] At the same time, these boundaries introduce local imperfections in the polycrystal, which are associated with the structure of the transition layer (the thickness of the layer is usually of the order of atomic spacing), which

differs considerably from the structure of adjacent crystallites.

Such type of boundaries determines the specific form of potential energy of an electron moving in the crystal (we use the one-electron approximation). For simplicity, we consider a bicrystal with an interface coinciding with the $yz$ plane. Obviously, the potential of the electron in the bicrystal in the general case cannot be represented as the sum of the potential periodic in the entire space and a perturbation localized near $x=0$. Such a representation ignores the lack of global periodicity and takes into account only the changes in the structure of the transition region.

For example, for a symmetric tilt boundary (see Fig. 1) or a twin, the potential of the right crystallite ($x>0$) is a mirror image of the left crystallite potential $U(x) = U(-x)$. If the boundary is a stacking fault, the right crystallite is shifted relative to the left one by a distance differing from the lattice period. In these examples, the structure of the bicrystal as a whole is non-periodic, the local distortions in the transition layer being virtually absent.

In contrast to the situation analyzed by Tamm, localization of states at intercrystallite boundaries is associated with electron trapping between two potential lattices. The electron energy can be higher or lower than the height of the potential barrier that may or may not exist in the transition region. The parameters of a barrier affect only the details of the spectrum (e.g., the arrangement of discrete levels in forbidden bands of a perfect crystal) but not the very fact of localization or the classification of states. The latter is determined only by the loss of global periodicity. Thus, for an arbitrarily small angle of disorientation of the crystallites (in the case of a tilt boundary) or an arbitrarily small relative shift of the crystallites (in the case of a stacking fault or a microcrack), the potential energy of an electron cannot be presented as the sum of an unperturbed periodic potential and a local perturbation. Accordingly, some important parameters of the discrete spectrum formed (naturally, against the background
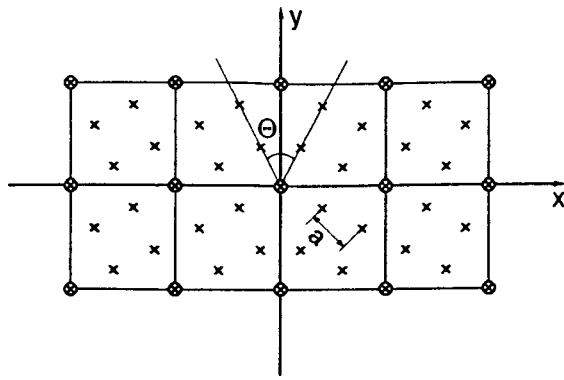
FIG. 1. Schematic diagram of a symmetric tilt boundary. The circles show the lattice of coinciding sites.



FIG. 2. Schematic diagram of a potential relief.

of the band structure of a perfect crystal) differ from the characteristics of the spectrum which can be determined, for example, by the method of degenerate local Lifshits perturbations (see, for example, Refs. 5 and 6. For example, two discrete levels can emerge in certain forbidden bands (for an arbitrary shift of the lattices), while the theory of local perturbations predicts the emergence of not more than one level in each such band. This difference is due to rotation of the entire macroscopic region, e.g., the right crystallite relative to the left one.

**2.** A rigorous analysis of the problem of localization in a real three-dimensional crystal involves the following main difficulties: (a) atoms in the boundary layers are displaced relative to their positions in a perfect crystal; (b) volume energy bands in a three-dimensional crystal can overlap, and (c) the solution of the Schrödinger equation is generally not factorized into the product of functions each of which depends on only one coordinate.

However, the main parameters of localized states (localization radius and energy) as well as the classification of states can be obtained by generalizing the results of analysis of one-dimensional models. The arguments used in this case (and given, for example, in Refs. 1, 10 and 11) are the same for the outer surface and for internal interfaces and can be reduced to the statement that the modulating factor $\exp(i\mathbf{k}\cdot\mathbf{r})$ plays a decisive role in Bloch's function. Instead of one (localized) state in the one-dimensional model, we have a large number of states in the three-dimensional case differing in the projection of the quasiwave vector on the plane of the boundary. The remaining characteristics of these states are of the same type and can be determined from an analysis of the one-dimensional model in a direction perpendicular to the plane of the boundary.

In order to obtain a quantitative (and if possible simple) estimate of the localization of states generated by internal boundaries, we introduce a symmetric one-dimensional relief shown in Fig. 2. This relief is a potential barrier of height $U_0$ for $-s/2 < x < s/2$, while on the intervals $-\infty < x < -s/2$ and $s/2 < x < \infty$ it is a Kronig–Penney lattice. In other words, the potential relief in Fig. 2 is constructed from an ideal Kronig–Penney lattice, which is infinitely large in both directions, by cutting it at the point $x=0$ and subsequent displacement of the right-hand part relative to the left-hand part by $2c+s$
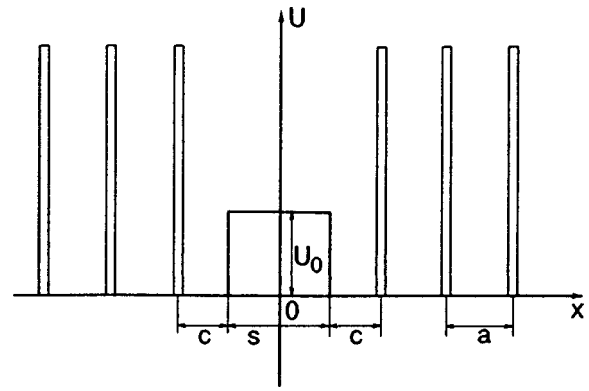
$-a$ ($a$ is the lattice constant) and inserting a potential barrier in the formed gap. Such a model was considered by Sokolov[7] for energies $E < U_0$ and for macroscopic values of $s \gg a$. Naturally, Tamm's surface states must be formed in the limit $s \to \infty$. We shall be interested in the states localized near the origin. The corresponding wave functions must decrease exponentially on both sides of the boundary (i.e., for $x \to \infty$ as well as for $x \to -\infty$). For $x > s/2$, the required wave function has the Bloch form $\psi(x) = \exp^{(i\alpha x)} u_\alpha(x)$, and the complex exponent $\alpha$ must have a positive imaginary component (such a function corresponds to states in the forbidden band of a perfect lattice). Since the potential is symmetric, the wave function are either symmetric, or antisymmetric. If the right-hand ''half-lattice'' is shifted relative to the left-hand one by a microscopic distance $|2c+s-a| \sim a$, it is expedient to analyze localized states not only with energies $E < U_0$, but rather with energies exceeding the barrier height $E > U_0$.

The calculation of the wave functions of localized states and corresponding energy levels of the discrete spectrum in the one-dimensional model under investigation is a standard quantum-mechanical problem. For this reason, the details of calculations are not given here. However, some aspects of the solution should be clarified and the required formulas will be considered.

The analysis is carried out in the framework of the exactly solvable model. The relation between the decrement $\alpha$ and the electron energy $E$ in the Kronig–Penney model has the familiar form[1]:

$$\cos(\alpha a) = P \frac{\sin \xi}{\xi} + \cos \xi \equiv S(\xi). \tag{1}$$

Here $P$ is the dimensionless power of the potential, $\xi \equiv (\sqrt{2mE}/\hbar)a$.

The energy values for which $|S(\xi)| < 1$ correspond to allowed bands, while for $|S(\xi)| > 1$ we are dealing with forbidden bands. It is well known that forbidden bands in one-dimensional models of periodic structures alternate with allowed bands, i.e., the bands do not overlap. In the Kronig–Penney model, the upper edges of the allowed bands (i.e., the lower edges of forbidden bands) are located at the points $\xi_n = n\pi$ ($n=1,2,\ldots$). Each energy interval $n\pi < \xi < (n+1)\pi$ ($n=0,1,2,\ldots$) contains one forbidden band (below) and one allowed band (above). In accordance with such an

arrangement, it is convenient to label the forbidden bands as 0,1,2,... . In the $n$th forbidden band, the inequality $n\pi<\xi<(n+\gamma_n)\pi$ is observed, the quantity $\gamma_n$ defining the position of the upper edge of this band being smaller than unity ($\gamma_n<1$). For asymptotically large $n$ such that $n\gg P$, we have $\gamma_n\sim 2P/(n\pi)$. Another relation between $\alpha$ and $E$ (in addition to (1)) follows from the condition of joining wave functions and their derivatives at the points $x=\pm s/2$. If the electron energy is larger than the barrier height, we can write for even wave functions

$$e^{i\alpha a}=\frac{2P\,\sin\,\xi}{\xi}+\cos\,\xi-\sin\,\xi$$

$$\times\frac{\cos(\varepsilon\sqrt{\xi^2-q^2})\sin\,\delta\xi+\sqrt{1-(q^2/\xi^2)}\sin(\varepsilon\sqrt{\xi^2-q^2})\cos\,\delta\xi}{\cos(\varepsilon\sqrt{\xi^2-q^2})\cos\,\delta\xi+\sqrt{1-(q^2/\xi^2)}\sin(\varepsilon\sqrt{\xi^2-q^2})\sin\,\delta\xi},$$
(2)

where the following notation is introduced: $q^2\equiv 2ma^2U_0/\hbar^2$; $\varepsilon\equiv s/2a$; $\delta\equiv c/a$.

A relation similar to (2) was also obtained for odd wave functions, but it will not be given here. For energies smaller than the barrier height, Eq. (2) is transformed by analytic continuation. Equations (1) and (2) form a system whose solutions give energy levels and localization radii for wave functions. It should be emphasized once again that localized states correspond only to solutions for which $\alpha$ is a complex quantity with a positive imaginary component, Im $\alpha>0$, Re $\alpha=n\pi/a$, where $n$ is an arbitrary integer. The elimination of $\alpha$ from Eqs. (1) and (2) leads to the following equation for the required energy levels:

$$\left(\frac{\xi\,\sin\,\xi}{P}-\cos\,\xi\right)\left[1-\frac{q^2}{2\xi^2}\pm\frac{q^2}{2\xi^2}\,\cos(2\varepsilon\sqrt{\xi^2-q^2})\right]$$

$$=\pm\cos[\xi(1-2\delta)]\left[\left(1-\frac{q^2}{2\xi^2}\right)\cos(2\varepsilon\sqrt{\xi^2-q^2})\right.$$

$$\left.\pm\frac{q^2}{2\xi^2}\right]\pm\left(1-\frac{q^2}{\xi^2}\right)^{1/2}\sin[\xi(1-2\delta)]$$

$$\times\sin(2\varepsilon\sqrt{\xi^2-q^2}).$$
(3)

Here the plus and minus signs correspond to even and odd wave functions, respectively. Equation (3) corresponds just to above-the-barrier states for which $\xi^2>q^2$. However, this equation can be easily transformed by analytic continuation for under-the-barrier states also. In this case, the corresponding trigonometric functions are transformed into hyperbolic functions.

The transcendental equation (3) contains several parameters; for this reason, its analysis in the general case is complicated and is not necessary. For this reason, we shall consider here the following two most interesting cases.

1. The barrier width $s$ tends to infinity, $c=a$, and $q^2>\xi^2$. In this case, Eq. (3) can be transformed into the classical Tamm's equation[1] for surface energy levels:

$$\xi\,\cot\,\xi=\frac{q^2}{2P}-\sqrt{q^2-\xi^2}.$$
(4)

For large but finite values of $s$, when $s/a\gg 1$, each Tamm level splits into two energy levels, the magnitude of the splitting being exponentially small ($\sim\exp^{-s/a}$). This results follows directly from Eq. (3) (see also Ref. 7).

2. Let us now suppose that the barrier height is zero ($q=0$). This means that we neglect the change in the structure in the transition layer, and the boundary is formed only by relative displacement of the right- and left-hand ''half-lattices'' by $2c+s-a\equiv b$. The reflection of the structure relative to a point separated by a distance $(a+b)/2$ from an ideal lattice site gives the same result as the displacement.

In the case under investigation, Eq. (3) is simplified considerably:

$$G(\xi)\equiv\frac{\xi\,\sin\,\xi}{P}-\cos\,\xi=\pm\cos\frac{b}{a}\,\xi.$$
(5)

It should be noted that the magnitude of the function $G(\xi)$ is smaller than unity just in forbidden bands. An analysis of the graphs of the functions on the left- and right-hand sides of Eq. (5) shows that there are two solutions of this equation in all bands (probably except the zeroth band) (for definiteness, we assume that $b/a<1$). Localized boundary (grain boundary) states correspond to only those solutions of (5) whose energy decreases with increasing $b$. This follows from simple physical consideration (since the average electron potential in the structure under investigation decreases with increasing $b$) and is confirmed by an analysis of the system of equations (1) and (2) after the substitution of the solutions of Eq. (5) into these equations. The main result of this analysis lies in the fact that for an arbitrary value of $b/a$, the spectrum of grain boundary states has as a rule a complex irregular structure of the ''devil's staircase'' type and cannot be reduced to the spectrum of a periodic system with a local perturbation. For example, it we can find positive integers $m$ and $n$ such that the inequality

$$n<m\,\frac{a}{b}<n+\gamma_n,$$
(6)

is satisfied, the $n$th band will contain two energy levels. The bands that do not satisfy inequality (6) contain only one energy level. Since $\gamma_n\lesssim 1$, we can find examples (at least for not very large $n$) when inequality (6) holds for a large number of bands. For example, if the ratio $a/b$ is equal to an integral $M$ plus a small correction $\mu\ll 1$, i.e., the lattice period $a$ is almost a multiple of the shift $b$, inequality (6) holds for bands with numbers $n=M, 2M, 3M,\ldots$ as long as $m\mu$ is smaller than $\gamma_n$. Since the value of $\mu$ can be indefinitely small, each $M$th band will contain in the limit two discrete levels, while the remaining bands will contain only one level. In actual practice, the alternation of bands with two and one energy levels for finite $\mu$ is extremely complex and cumbersome and is determined by the shift $b$ as well as the ''power'' $P$ of the potential according to the dependence $\gamma_n(P)$.

If the shift almost coincides with the lattice period, almost all bands contain two energy levels. If the equality is satisfied exactly, half the localized states disappear (are delocalized and ''drive into'' allowed bands) so that strictly

one level remains in each forbidden band. In other words, for $b \to a$, the spectrum is rearranged radically. This statement corresponds to the actual physical pattern since in contrast to the case when $b \neq a$, the potential energy of an electron for $b = a$ can be presented as the sum of an unperturbed periodic potential and a local perturbation. However, it was shown by Lifshits and Kosevich[5,6] that in this case each band must contain exactly one energy level, and hence only one localized state (the rank of the perturbation operator is equal to unity). A rough estimate of localization radii for grain boundary states gives $r_{loc} \sim a^2/Pb$ and weakly depends on the band number.

**3.** Thus, one of the distinguishing properties of a polycrystal, viz., the absence of a global periodicity as a whole, generates (independent of the specific structure of transition layers) electron states localized at intergranular boundaries and leads to a generally complicated and intricate sequence of lines in the spectrum. However, the spectrum again becomes regular for boundaries of special type. Apparently we can put in correspondence (at least conditionally to a certain extent) the commensurability of the shift with the lattice parameter in the one-dimensional model considered above with the formation of a lattice with coinciding sites (see, for example, Ref. 8) for certain angles of disorientation of three-dimensional crystallites (see Fig. 1). It is known[4,9] that the energy of intercrystallite boundaries for these angles has sharp minima relative to neighboring angles. This fact can be attributed to ''sudden'' ordering of the spectrum of states localized at such boundaries.

Naturally, it should be borne in mind that in a real three-dimensional crystal we are dealing not with discrete levels, but with surface bands corresponding to states localized near boundaries. The number of such states is of the order of the number of atoms at the boundary, i.e., of the order of

$10^{14}$ cm$^{-2}$. The density of surface states per unit energy interval has the form of a step which is ''thrown over'' the volume density of states.[10] Consequently, the spectrum rearrangement considered above is manifested in the formation or disappearance of steps on the spectral density curve.

It should be noted in conclusion that the grain boundary states can play a significant role in the formation of some properties (such as conductivity), especially of semiconductors. This role can be comparable with (or even more significant than) the role of the outer surface[10] since the total area of internal interfaces is much larger than the area of the outer surface as a rule.

[*]E-mail: feldman@host.dipt.donetsk.ua

[1] I. Tamm, Phys. Z. Soviet Union **1**, 733 (1932).

[2] V. P. Naberezhnykh, E. P. Feldman, B. I. Selyakov, and V. M. Yurchenko, Poverkhnost': Fiz., Khim., Mekh. **5**, 21 (1986).

[3] V. P. Naberezhnykh, V. V. Sinolitskii, and E. P. Feldman, Zh. Éksp. Teor. Fiz. **78**, 165 (1980) [Sov. Phys. JETP **51**, 82 (1980)].

[4] V. P. Naberezhnykh, E. P. Feldman, and V. M. Yurchenko, Fiz. Tverd. Tela (Leningrad) **24**, 187 (1982) [Sov. Phys. Solid State **24**, 103 (1982)].

[5] I. M. Lifshits, Sov. Phys. JETP **17**, 1076 (1947).

[6] I. M. Lifshits and A. M. Kosevich, in *Collected Works of I. M. Lifshits* [in Russian], Nauka, Moscow (1987).

[7] A. A. Sokolov, Zeits. für Physic **90**, 520 (1934).

[8] M. L. Kronberg and F. N. Wilson, J. Met. **1**, 501 (1949).

[9] T. Schober and R. W. Ballufi, Philos. Mag. **21**, 109 (1970).

[10] S. Davison and J. Levine, *Surface States*, Academic Press, London (1970).

[11] S. I. Pekar and I. M. Lifshits, Sov. Phys. Usp. **56**, 531 (1955).

Translated by R. S. Wadhwa

## QUANTUM EFFECTS IN SEMICONDUCTORS AND DIELECTRICS

# Theory of Aharonov–Bohm oscillations resulting from a charge density wave condensate flowing across an array of columnar defects in a magnetic field

Alexander S. Rozhavsky*[)]

*Centre de Recherches sur les Tres Basses Temperatures, laboratoire associe a l'Universite Joseph Fourier, C. N. R. S., BP 166, 38042 Grenoble-Cedex 9, France*

We propose a microscopic theory for the Aharonov–Bohm oscillations, observed by Latyshev *et al.* in the magnetotransport experiment in NbSe$_3$ with a charge density wave (CDW). The CDW slides across an array of columnar defects in a high magnetic field. For the charge carrying quanta of CDW these defects are elementary solenoids carrying a magnetic flux. The quantum CDW current acquires a component oscillating with the flux, with the period $hc/2e$. Its magnitude is proportional to the concentration of columnar defects. The lower limit to the phase breaking length for these oscillations is set by the minimal Lee–Rice coherence length. © *1998 American Institute of Physics.* [S1063-777X(98)01109-8]

The sliding charge density and spin-density waves (CDW and SDW) in quasi-one-dimensional metals represent amazing examples, apart from the superconductivity, of collective transport by a moving quantum ground state at high enough temperatures.

The most striking feature is the existence of a nonlinear dc-current along the high conducting direction produced by the Fröhlich collective mode (see the review papers[1]). The Fröhlich conductivity emerges in electric fields exceeding the threshold value $E_T$ ($E > E_T$). Until recently, all the CDW-transport experiments had been more or less successfully explained by the theories which had considered CDW in a classical manner: either phenomenologically as a rigid object moving in a periodic potential, or microscopically, as a deformable medium in which the topologically stable domain walls (the CDW solitons) serve as the elementary CDW-charge carriers (see Ref. 1).

The pioneer experiment which had evidently shown the quantum nature of the CDW-solitons was performed by Latyshev *et al.*,[2] A thin film of a CDW-conductor NbSe$_3$ was irradiated by heavy ions of Xe. The Xe-ions produced an array of identical parallel tracks [columnar defects (CD)] piercing the film, and the host lattice inside the CD was destroyed. The radius $R$ of each CD is of the order of 100 Å. The irradiated film was placed in a strong magnetic field $H \approx 20$ T (Fig. 1) and the nonlinear conductance was measured. In electric fields above the threshold, $E > E_T$, the transport current appeared to be an oscillatory function of the magnetic field with the period of oscillation

$$\delta H \cong \frac{hc}{2e\pi R^2}.$$

The relative magnitude of the oscillatory component of the transport current is of the order of 0.25%.

The oscillatory dependence on $H$ clearly indicates the Aharonov–Bohm effect (ABE) nature of the observed phenomenon, the period of the ABE-oscillations with the magnetic flux being $\Delta\Phi = hc/2e$.

The striking feature of this ABE is that it is observed at such high temperatures ($T \approx 50$ K) when single-electron ABE is totally suppressed by the electron-phonon scattering. Therefore, it was assumed in[5] that those oscillations can be attributed to the quantum CDW-solitons which encircle the CDs pierced by the magnetic field thus affecting the collective Fröhlich current. In other words, the CDs serve as the elementary solenoids for quantum solitons.

To summarize, the experiment[2] is really the first evidence for a high-temperature quantum coherent effect in a non-superconducting material. It brings us to a qualitatively new level in understanding the nature of a CDW current state: it demonstrates unambiguously the quantum origin of a collective current which was masked in all the previous studies. It demands therefore a new theoretical description of transport phenomena in CDW-conductors.

A theory that aims to describe the ABE in CDW transport should include the quantum description of the CDW charge carriers and should explain the anomalously large CDW phase breaking length $L_\varphi^{\text{CDW}}$, strongly exceeding the one for a single electron transport at such temperatures, which makes ABE observable at high temperatures.

In this paper we develop such a theory, using the concepts, formulated in,[3,4] where the idea of the CDW charge carriers quantization has been put forward and the persistent current of the CDW-condensate has been studied for the first time.

It is well known that the ABE in conductors can be observed in two ways: (i) as oscillations of a diamagnetic moment (of persistent currents) in isolated loops, and (ii) as oscillations of conductance in open circuits containing loops.
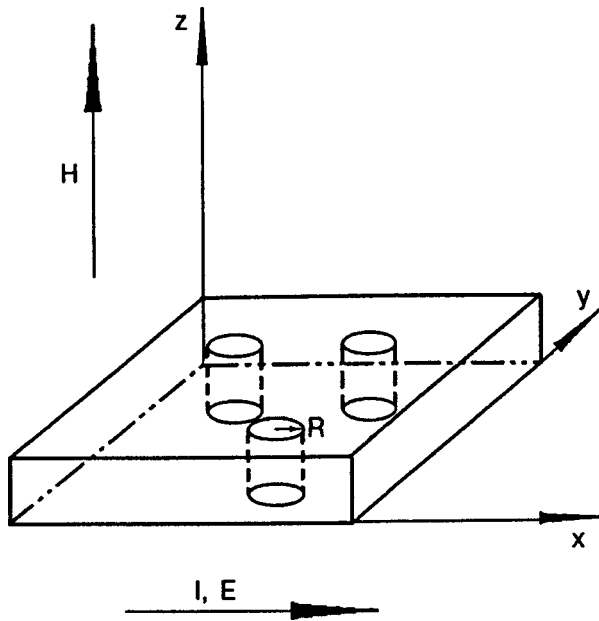
FIG. 1. Geometry of the experiment.[2] Magnetic field **H** is oriented along the axis of the columnar defects of radius $R$ (z-axis), the transport current **I** flows along the electric field **E** (x-axis).

As the ABE is intimately connected to the topological structure of a charge carrier wave function in a multiply connected conductor, the basic period of oscillations with flux in both those schemes is the same.

The qualitative theory of persistent currents in CDW in the idealized model of a single-chain CDW loop was first proposed by Krive and the author[3] and was elaborated later on in a series of papers.[4] It was shown there that the persistent current in CDW is formed by the topologically nontrivial CDW-excitations, viz, solitons and instantons. The basic period of the persistent current oscillations with magnetic flux is found to be $\Phi_S = hc/2e$, just as in the experiment.[2] Although the measurements of a persistent current in CDW are beyond the present technology facilities, the understanding of the role of the topological CDW-excitations in the ABE is essential for solution of the quantum transport problem. The qualitative picture of the AB-oscillations in the geometry of interest was first discussed by the author.[5]

The paper is organized as follows.

In the first chapter, we give a proper method of CDW quantization and formulate an exactly solvable model of a quantum CDW transport along a single chain with a loop pierced by a magnetic flux. Such a loop mimics a columnar defect.

In the second chapter, we propose a model of a columnar defect in a CDW-material. In the third part, we show that the long range CDW-coherence allows us to reduce the problem of a transport current through a dilute array of CDs to the one studied in the first chapter, and calculate the transport current oscillating with flux. The relative magnitude of the oscillatory current estimated along our formulas for the parameters of the experiment[2] is of the order of $10^{-2}-10^{-3}$, which is in a good agreement with the experimental data.

# 1. MATHEMATICAL FORMALISM. AHARONOV–BOHM OSCILLATIONS OF A CDW TRANSPORT CURRENT IN A TOY 1D MODEL

The Peierls–Fröhlich order parameter is $\Delta \exp(i\varphi)$ where $\Delta$ is the gap in a single electron spectrum and the gradients of $\varphi$ define, via the Fröhlich relations,[1] the collective CDW current, $j$, and the charge density fluctuations, $\rho$, in a single chain:

$$j = -\frac{e}{\pi}\frac{\partial\varphi}{\partial t}, \tag{1a}$$

$$\rho = \frac{e}{\pi}\frac{\partial\varphi}{\partial x}, \tag{1b}$$

where $e$ is the electron charge, and $x$ denotes the coordinate along the chain.

Note that the Eqs. (1) have, at first glance, an incorrect vector dimensionality. Indeed, the Eq. (1a) comprises a scalar operator that acts on a scalar to give a vector quantity, and the Eq. (1b) comprises the vector operator acting on a scalar to give a scalar. It is necessarily the case that there is an implicit direction implied. Such a direction is the one along the chains. The phase $\varphi$ (the CDW variable), strictly speaking, is a quantum Bose field. This can easily be seen in the path integral formulation of the Peierls–Fröhlich problem (see, e.g., the review by Krive *et al.* in Ref. 1). Accordingly, the Eqs. (1) are the operator equations. The measured current is:

$$j_t = -\frac{e}{\pi}\left\langle\frac{\partial\varphi}{\partial t}\right\rangle = j_c + j_q, \tag{2}$$

where the brackets denote quantum averaging. In electric field above the threshold, $E > E_T$, the transport current (2) has two components: the classic $j_c$ and the quantum, $j_q$. The former is produced by the mean component of the order parameter, and the latter by its fluctuations. The theory of a classic CDW dc-transport is well developed (see Ref. 1). For our purposes we must find the quantum dc-current $j_q$ expressed in terms of wavefunctions of individual CDW-charge carriers. In the Aharonov–Bohm geometry, the wavefunctions are sensitive to magnetic flux variations providing oscillations of a transport current. To quantize CDW, we use the Bose–Fermi duality transformations in $1D$.[6] This powerful tool allows us to map the results of the electron theory of metals and semiconductors onto quantum CDW. In particular, quantum solitons of CDW, which serve as elementary charge carriers, turn out to be equivalent to spinless conduction electrons in a $1D$ semiconductor (see, e.g., Ref. 7). Evidently, the oscillatory ABEs, existing in mesoscopic conductors, have their analogs in CDW.

The dual transformations for the normally ordered operators are (see, e.g., Ref. 7):

$$\frac{1}{\sqrt{\pi}}\,\partial_t\varphi \rightleftarrows \bar{\psi}\sigma_x\psi \tag{3}$$

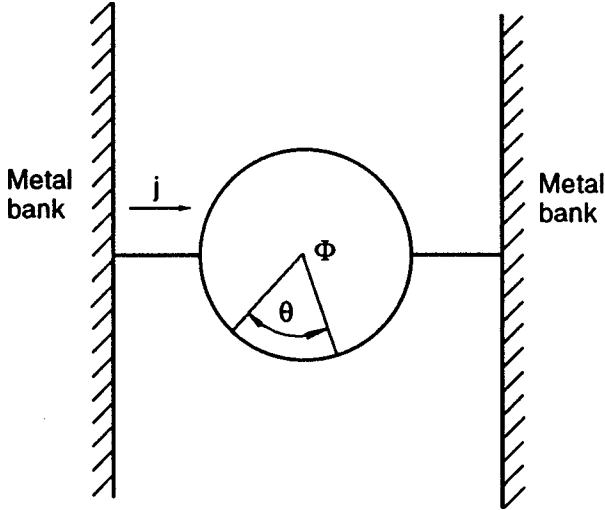$$\frac{1}{\sqrt{\pi}}\,\partial_x\varphi \rightleftarrows -\bar{\psi}\sigma_y\psi,$$

FIG. 2. Schematic view of a CDW-transport along a single chain containing a loop with a perimeter $L$, pierced by the magnetic flux $\Phi$; $j$ is the transport current density; $\theta$ is the angle variable.

where $\psi$ is a two-component Dirac spinor, $\bar{\psi} = \psi^+ \sigma_y$, $\sigma_\mu$ are the Pauli matrices.

The qualitative picture underlying the transformations (3) is that the statistics in $1D$ are ill defined. One cannot merely place two solitons at one point which, roughly speaking, allows us to treat them as fermions. The Eqs. (3) introduce explicitly the desired description of a CDW in terms of the wave-functions of the CDW charge carriers (solitons and antisolitons).

To show how this scheme works, consider the AB-oscillations of $j_q$ in a single chain with a loop, of a perimeter $L$, pierced by a magnetic flux $\Phi$ (Fig. 2). Consider for simplicity an incommensurate CDW described by Lagrangians:

$$\mathcal{L} = N_0 \left\{ \frac{1}{2}(\partial_t \varphi)^2 - \frac{c_0^2}{2}(\partial_x \varphi)^2 \right\} \tag{4a}$$

in linear chains connected to the loop, and

$$\mathcal{L} = N_0 \left\{ \frac{1}{2}(\partial_t \varphi)^2 - \frac{2\pi^2 c_0^2}{L^2}(\partial_\theta \varphi)^2 \right\} - \frac{e\Phi}{\pi c L}(\partial_t \varphi) \tag{4b}$$

in a loop.

Here $N_0 = \hbar/\alpha^2 v_F$, $\alpha = c_0/v_F < 1$ is the parameter of adiabaticity in the Peierls–Fröhlich theory, $c_0$ is the phase velocity of CDW.

The Lagrangian (4a) is well known in the theory of CDW. The Lagrangian (4b) contains the topological term which describes coupling of a Fröhlich current (1a) to a vector potential $A = \Phi/L$ in the loop:

$$\mathcal{L}_{\text{int}} = \frac{jA}{c}. \tag{4c}$$

The topological term in (4b) was introduced for the first time in the paper by Bogachek *et al.*, Ref. 4. On a microscopic level, it arises nonperturbatively due to the chiral anomaly phenomenon in a $1D$ CDW.[7,8] The doubling of the electron charge in (4b) is the result of a summation over spin projections of electrons out of which the CDW is formed.

The effective charge $2e$ leads to the oscillations of the persistent and transport currents with flux with the period $\Phi_s = hc/2e$.[4,5]

To obtain the $j_q$ one has to find the transparency of the loop. It is highly unacceptable to do it in terms of $\varphi$-field using for example the instanton approach.[4] It is more convenient to use the dual fermion language in which this problem can be reduced to the one already solved in Ref. 9. Indeed, the Lagrangians (4a) and (4b) take the Dirac form:

$$\mathcal{L} = N_0 i \bar{\psi} \gamma_\mu \partial_\mu \psi \tag{5a}$$

and

$$\mathcal{L} = N_0 i \bar{\psi} \gamma_\mu \left( \partial_\mu - i \frac{e}{\pi c L} \Phi \delta_{\mu,x} \right) \psi, \tag{5b}$$

where $\gamma_\mu = (\sigma_y, c_0 \sigma_x)$, $\mu = (t, x)$.

The scattering problem of interest has been solved in Ref. 9 for a nonrelativistic electron. One can easily show that the results obtained in Ref. 9 remain valid in our case.

The CDW quantum transport current takes the form:[10]

$$j_q(\Phi) = \frac{2e}{h} \int d\varepsilon\, g(\varepsilon) [f_L(\varepsilon) - f_R(\varepsilon)]. \tag{6}$$

The integration is performed over the energy $\varepsilon$. Here $g(\varepsilon)$ is the transmission probability, which depends explicitly on the CDW wave functions, $f_{R,L}$ are the distribution functions of the left and right moving dual fermions. For simplicity, we assume that the relaxation occurs in leads, which means that

$$f_{R,L} = f_0(\varepsilon \pm p v_D), \tag{6a}$$

where $f_0$ is the Fermi function and $v_D$ is the drift velocity. For sliding CDW, $v_D$ is not zero in electric fields above the threshold $E_T$. It is convenient to rewrite (6) in the form:

$$j_q(\Phi) = j_c \int d\varepsilon\, g(\varepsilon) \frac{[f_0(\varepsilon + p v_D) - f_0(\varepsilon - p v_D)]}{2 p v_D}, \tag{7}$$

where $j_c$ is the classic current at zero temperature along a chain free of a loop:

$$j_c = \frac{e \tilde{p}_F v_D(E)}{\pi \hbar}. \tag{8}$$

The Fermi energy for dual fermions is of the order of $\Delta$. This is the maximum kinetic energy which the CDW soliton (the dual fermion) possesses.[11] Correspondingly the cut-off to the Dirac theory, for dual fermions is:

$$\tilde{p}_F \sim \frac{\Delta}{c_0} \sim \frac{\hbar}{\alpha \xi_0}, \tag{9}$$

where $\xi_0 = \hbar v_F/\Delta$ is the amplitude coherence length.

The function $g(\varepsilon)$ was calculated in Ref. 9 to be:

$$g(\varepsilon) = \frac{4\eta^2 \cos^2(\pi\Phi/\Phi_s)\sin^2(\pi k)}{\eta^2 \sin^2(2\pi k) + p^2(k, \eta, \Phi)}, \tag{10}$$

where

$$p(k,\eta,\Phi)=b^2\,\cos\!\left(\frac{2\pi\Phi}{\Phi_s}\right)+a^2-(1-\eta)\cos(2\pi k),\tag{11}$$

$$k=\frac{\varepsilon L}{2\pi\hbar c_0}.$$

The phenomenological parameter $\eta$, $0\le\eta\le1/2$, determines the connection between the linear chain and the loop. The coefficients $a$, $b$ are:

$$a=\frac{1}{2}\left[(1-2\eta)^{1/2}-1\right],\quad b=\frac{1}{2}\left[(1-2\eta)^{1/2}+1\right].\tag{12}$$

The value of $\eta$ will be specified in the Ch. 2.

Note that the Eqs. (6) and (10) are valid when the perimeter of a loop is small compared to the phase breaking length $L_\varphi^{\mathrm{CDW}}$. In a sliding $1D$ CDW the lower limit to $L_\varphi^{\mathrm{CDW}}$ is set by the Lee–Rice phase coherence length $l_\parallel$ which is typically $1$–$10$ $\mu$m.[1] This clearly shows why the CDW ABE is observed at sufficiently high temperatures, when the single electron ABE, characterized by $L_\varphi^{(e)}\sim10^3-10^3$ Å, is suppressed. A three-dimensional sample of NbSe$_3$ is characterized by three coherence lengths: $l_\parallel$ along the chains in $x$-direction, $l_\perp$ along the $y$ direction and $l_d$ along the less conducting axis, $z$: $l_d\ll l_\perp\ll l_\parallel$, and, correspondingly, by three phase velocities $c_z\ll c_y\ll c_0$. In an actual experiment,[2] the phase breaking length is governed by the sample thickness $d$ in a less conducting direction. In this context, the oscillatory effect in CDW is the mesoscopic one in spite of it resemblance to the flux quantization in superconductors.

Under the conditions of the experiment,[2] the CD hole diameter contains several tens of chains and the model has to be reformulated keeping safe two basic features: (i) a qualitative picture of the quantum transport of CDW along a single chain [Eqs. (6) and (10)], and (ii) the long distance phase coherence in a sliding CDW.

## 2. A MODEL OF A COLUMNAR DEFECT IN A CDW MATERIAL

According to Ref. 2, the CD is a real hole with a diameter $10$–$12$ nm surrounded by a damaged region which adds a further $2$–$4$ nm to the effective diameter.

Consider the distribution of a phase around a single cylindric CD with the radius $R$ (Fig. 3). Inside the CD, the host material is destroyed and, accordingly, $\Delta=0$. This local defect creates Friedel oscillations of the electron charge that compete with the CDW charge modulation over an atomic distance scale $\delta_1\sim10$ Å.[12] The suppressed $\Delta$ causes a strong phase gradients $|\partial\varphi/\partial\mathbf{r}|\gg|\mathbf{I}|^{-1}$ localized around the CD within a strip of width $\delta_2$ which is of the order of several $\xi_0$.[12] The potential barrier created by these phase gradients is of the order of $\Delta$[12] (Fig. 4). It separates the phase $\varphi$ inside $\delta_1$ from the bulk. The local phase $\varphi$ in the region $R+\delta_1\propto r\ll R+\delta_2$ is adjusted to a certain optimal value $\varphi_0$ that matches the Friedel oscillations. The value $\varphi_0$ differs from the one established in the bulk, its excitations can be regarded as the edge states. We make a plausible assumption that inside the layer $\sim\delta_1$ there exists random $1D$ chain paths encircling the CD, along which the CDW current is again
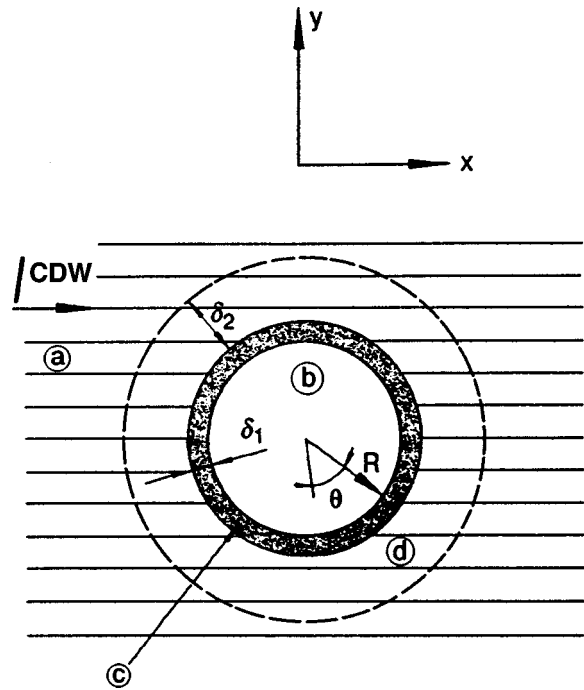


FIG. 3. The model of CD adopted in the theory: (a) conducting chains are oriented along the $x$-axis; (b) the real hole; (c) the region of the edge states of the width $\sim\delta_1$; (d) the interface layer of the width $\sim\delta_2$ around the CD containing large phase gradients. The high energy heavy ion produces a round hole which pierces the sample along the $z$-axis. The CD-hole is surrounded by a layer of width $\delta_1$, within which the phase is confined to $\varphi=\varphi_0$ (see the text). We assume that the positions of conducting chains are not disturbed away from the CD: $|x|>R|\cos\theta|$, $|y|>R|\sin\theta|$. $I^{\mathrm{CDW}}$ is the transport current; $\theta$ is the angle variable.

given by the Eq. (1a). The CDW edge state phase velocity along those $1D$ paths is $\bar{c}$ where $c_y<\bar{c}<c_0$. Such random chains emerge as the result of a strong damage of a host lattice caused by a heavy ion. The average phase $\varphi$ in the bulk away from the CD still remains correlated over the Lee–Rice lengths.[12] This qualitative picture is an assumption of our model.

Consider the scattering of the classic and quantum CDW excitations on a CD. In the classical picture the excitations of $\varphi_0$ (the edge states) are confined to a CD in a radial direction, they have only the azimuthal momenta and do not contribute to the current flow. The classic current spreads around the CD in the way plotted in Fig. 5(a). The characteristic spreading length $L_x$ can be estimated from the equation of motion for a $3D$ CDW Lagrangian:

$$\mathscr{L}=n_2N_0\int dx\,d\mathbf{r}_\perp\left\{\frac{1}{2}(\partial_t\varphi)^2-\frac{c_0^2}{2}(\partial_x\varphi)^2\right.$$
$$\left.-\frac{2ZT_c^2}{\pi\hbar v_F N_0}\cos(\varphi_{\mathbf{r}_\perp}-\varphi_{\mathbf{r}_\perp+1})\right\},\tag{13}$$

where $n_2$ is the $2D$ density of conducting chains, $T_c$ is the critical temperature of a $3D$ phase transition, and $Z$ is the number of the nearest neighbor chains. Assuming the thickness of a sample $d\ll l_d$ and putting $\partial x\sim1/L_x$, $\partial y\sim1/L$, we get an estimate:
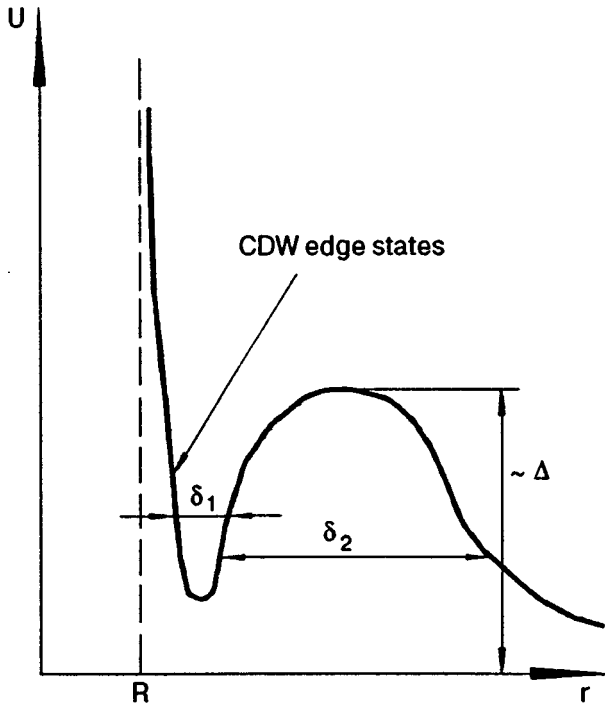
FIG. 4. The potential $U$ created by the CD for the CDW excitations as a function of the radial coordinate $r$. The destroyed host material occupies the region $r < R$. The potential barrier of the order of $\Delta$ produced by the large phase gradients in the region $R + \delta_1 < r < R + \delta_2$ separates the edge states localized at $R < r < R + \delta_1$ from the bulk. $R$ is the CD radius.

$$L_x \sim L \frac{c_0}{c_y} \sim L \frac{\varepsilon_\mathbf{r}}{T_c} \gg L, \tag{14}$$

where

$$c_y = \frac{\sqrt{2Z}T_c}{\hbar n_2^{1/2}} \quad \alpha \ll c_0. \tag{15}$$

In NbSe$_3$ $c_y \approx 0.1 c_0$. Classic trajectories (14) contribute to the magnetoresistance but not to the ABE.

Contrary to the classic picture, the quantum CDW-particles encircle the CD in a quite different way (Fig. 5b). Quantum particles propagate freely along the chain away from the CD, then penetrate under the potential barrier (Fig. 4) and mix with the edge states localized near the hole. Because the dispersion of the edge state trajectories is small as far as $\delta_1 \ll L$ and $\tilde{k}_F \delta_1 \approx 1$, the CDW quanta encircle the CD along a path of a fixed length $L$. Quantum paths obviously contribute to the AB-oscillations.

Now we can formulate a quantum model of a CDW which contains a single CD.

Save $N_0$, the excitations of the phase localized in the chains away from the CD are described by the Lagrangian:

$$\mathscr{L} = \sum_n i\bar{\psi}_n \gamma_\mu \partial_\mu \psi_n, \tag{16}$$

where $n$ labels the chain. There are $N_\Phi$ chains which connect the CD:
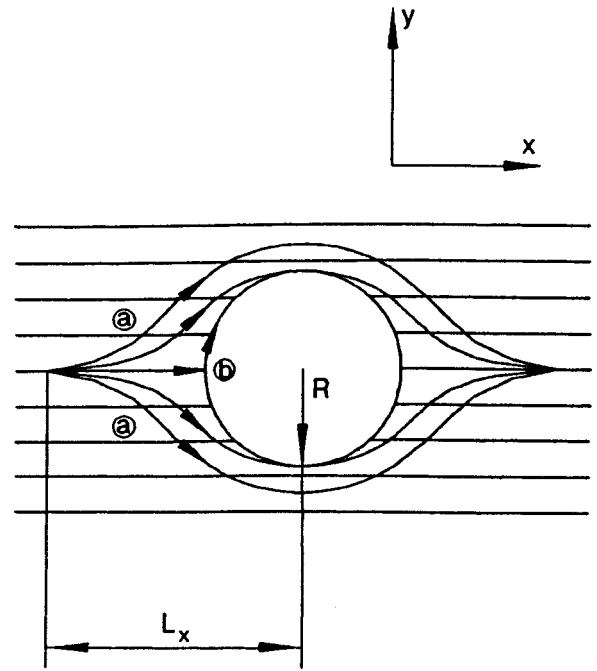
$$N_\Phi \approx \frac{Ld}{4\pi} n_2. \tag{17}$$



FIG. 5. The trajectories along which the classic current (a) and quantum current (b) encircle the CD. $L_x$ is the classical current spreading length (14).

The edge excitations of $\varphi_0$ are described by the Lagrangian:

$$\mathscr{L} = \sum_n i\bar{\psi}_n \gamma_\mu \left( \partial_\mu - i \frac{e}{\pi cL} \Phi \delta_{\mu,x} \right) \psi_n, \tag{18}$$

where $n$ runs over the $Ld(\tilde{k}_F \delta_1)$ values, $\partial x \to 1/R \partial_\theta$, $v_F \to v_F(\bar{c}/c_0)$.

The phases in all the $N_\Phi$ chains that are connected to the CD (17) are correlated provided $L \ll l_y$, $d \ll l_d$. This means that all the dual fermions located in these chains have the same transmission probability $g(\varepsilon)$ (10), in which $k$ [Eq. (11)] is replaced by $k(c_0/\bar{c})$. Thus, the flux-dependent transport current carried by the bunch of $N_\Phi$ chains is nothing but $N_\Phi j_q(\Phi)$ where $j_q(\Phi)$ is given by Eq. (7). The parameter of transparency $\eta$ can be estimated quasiclassically:

$$\eta \sim \exp\left( -\frac{\delta_2 (m_{\text{CDW}} \Delta)^{1/2}}{\hbar} \right), \tag{19}$$

where $m_{\text{CDW}} = \alpha^{-2} m^*$, $m^*$ is the band mass in NbSe$_3$. Taking $m^* = 1.8 m_0$, $\xi_0 = 30$ Å, $\Delta = 350$ K, $\alpha \approx 0.5$ (see, e.g., Grüner[2]), we get:

$$\eta \approx 0.03 - 0.05 \tag{19a}$$

for $\delta_2/\xi_0 \approx 6 - 7$ [Refs. 12 and 13]. Note, however, that the ratio $\delta_2/\xi_0$ was estimated for a point defect. For a CD, the estimate can differ though not crucially.

## 3. CALCULATION OF A FLUX-DEPENDENT TRANSPORT CURRENT

The total current $I^{\text{CDW}}$ is the sum over the single chain currents. At small concentration of CDs[1] one can neglect the contribution of chains connecting the different loops (random loop approximation) we then get

$$I^{CDW} \approx Nj_c + \sum_{loops} j_q(\Phi) = I_0^{CDW} + I^{CDW}(\Phi), \qquad (20)$$

where $N$ is the total number of chains in a sample, $I_c^{CDW} = Nj_c$.

The sum over loops is estimated as

$$\sum_{loops} \approx N_\Phi N_{CD}, \qquad (21)$$

where $N_{CD}$ is the total number of loops (of CDs) in a sample:

$$N_{CD} = n_d L_\parallel L_\perp, \qquad (22)$$

where $n_d$ is the concentration of CDs, $L_\parallel$ is the distance between the electrodes along the $x$-direction, $L_\perp$ is the size of a sample in the $y$-direction. Collecting together Eqs. (7), (20), and (21) we obtain

$$I^{CDW}(\Phi) = \frac{Ld}{\pi} n_2 n_d L_\parallel L_\perp j_q(\Phi)$$

$$= \frac{LL_\parallel}{2\pi} n_d I_0^{CDW} \frac{1}{\tilde{p}_F v_D} \int d\varepsilon \, g(\varepsilon)[f_0(\varepsilon + \tilde{p}_F v_D) - f_0(\varepsilon - \tilde{p}_F v_D)]. \qquad (23)$$

To calculate the integral over the energy, we make use of the periodicity of $g(\varepsilon)$:

$$g(\varepsilon) = g(\varepsilon + 2\pi T_0), \qquad (24)$$

where

$$k_B T_0 = \frac{\hbar \bar{c}}{L} \qquad (25)$$

is the interlevel spacing in a one-dimensional isolated ring. We get:

$$\frac{1}{\tilde{p}_F v_D} \int d\varepsilon \, g(\varepsilon)[f_0(\varepsilon + \tilde{p}_F v_D) - f_0(\varepsilon - \tilde{p}_F v_D)]$$

$$= \frac{1}{\tilde{p}_F v_D} \int_0^{2\pi T_0} d\varepsilon \, g(\varepsilon + \tilde{\varepsilon}_F) \sum_{n=-\infty}^{\infty} [f_0(\varepsilon + \tilde{\varepsilon}_F + 2\pi n T_0 + \tilde{p}_F v_D) - f_0(\varepsilon + \tilde{\varepsilon}_F + 2\pi n T_0 - \tilde{p}_F v_D)], \qquad (26)$$

where $\tilde{\varepsilon}_F$ is the Fermi energy for dual fermions.

Making use of the Poisson summation formula

$$\sum_n p(n) = \int dn \, p(n) + 2 \sum_{k=1}^{\infty} \int dn \, p(n) \cos(2\pi kn), \qquad (27)$$

we get

$$\sum_{n=-\infty}^{\infty} [f_0(\varepsilon + \tilde{\varepsilon}_F + 2\pi n T_0 + \tilde{p}_F v_D) - f_0(\varepsilon + \tilde{\varepsilon}_F + 2\pi n T_0 - \tilde{p}_F v_D)] = \frac{T}{T_0} \sum_{k=1}^{\infty} \frac{\sin(k\tilde{p}_F v_D / T_0) \sin(k\varepsilon/T_0)}{\sinh(\pi k T/T_0)}. \qquad (28)$$

Making use of the inequality $v_D \ll \bar{c}$, we eventually obtain the following equation for $I^{CDW}(\Phi)$:

$$I^{CDW}(\Phi) = \frac{LL_\parallel n_d}{2\pi} \frac{T}{T_0} I_0^{CDW}$$

$$\times \sum_{k=1}^{\infty} k \sinh^{-1}(\pi k T/T_0) F(\Phi, \eta, T_0), \qquad (29)$$

where

$$F(\Phi, \eta, T_0) = \int_0^{2\pi T_0} d\varepsilon \, \sin(k\varepsilon/T_0) g(\varepsilon + \tilde{\varepsilon}_F). \qquad (30)$$

In an actual experiment,[2] the ratio $\pi T/T_0 \approx 10$ which allows us to keep only the first harmonics with $k=1$ in the r.h.s. of Eq. (29). The exponential decrease with temperature is a typical feature of the AB-transport current (see, e.g., Ref. 14), as well as of the persistent current.[4]

The integral over the energy (30) has to be calculated at $\eta \ll 1$ [see Eq. (19a)]:

$$F \approx 4\eta^2 \cos^2(\pi\Phi/\Phi_s) \int_0^{2\pi T_0} d\varepsilon \frac{\sin(\varepsilon/T_0)\sin^2((\varepsilon + \tilde{\varepsilon}_F)/2T_0)}{\eta^2 \sin^2((\varepsilon + \tilde{\varepsilon}_F)/2T_0) + [\cos^2(\pi\Phi/\Phi_s) - \eta - \cos((\varepsilon + \tilde{\varepsilon}_F)/2T_0)]^2}. \qquad (31)$$

The main contribution to $F$ comes from those points in which the denominator of the integrand is close to zero. We get the asymptotes:

$$\frac{1}{T_0} F \approx \begin{cases} -\dfrac{1}{2} \eta \sin\left(\dfrac{\tilde{\varepsilon}_F}{T_0}\right)\left(1 + \pi^2\left(\dfrac{\Phi - n\Phi_s}{\Phi_s}\right)^2\right), & \text{when } |\Phi - n\Phi_s| \ll \eta\Phi_s, \quad |\Phi - (n\pm 1/4)\Phi_s| \gg \eta\Phi_s, \\[3mm] \dfrac{1}{4} \eta \cos\left(\dfrac{\tilde{\varepsilon}_F}{T_0}\right)\left(1 \mp 2\pi\left(\dfrac{\Phi - (n\pm 1/4)\Phi_s}{\Phi_s}\right)\right), & \text{when } |\Phi - n\Phi_s| \gg \eta\Phi_s, \quad |\Phi - (n\pm 1/4)\Phi_s| \ll \eta\Phi_s, \\[3mm] \dfrac{1}{\sqrt{2}} \eta^{3/2} \sin\left(\dfrac{\tilde{\varepsilon}_F}{T_0}\right) 2\pi^2\left(\dfrac{\Phi - (n\pm 1/2)\Phi_s}{\Phi_s}\right)^2, & \text{when } |\Phi - (n\pm 1/2)\Phi_s| \ll \eta\Phi_s, \quad |\Phi - n\Phi_s| \gg \eta\Phi_s. \end{cases} \qquad (32)$$

Here $n = [\Phi/\Phi_s]$ is an integer.

In an actual experiment,[2] $n_d L_\| L \approx 10^3 - 10^4$ and we obtain the following estimate for the relative magnitude of the oscillatory component of $I^{\text{CDW}}$:

$$\frac{I^{\text{CDW}}(\Phi)}{I_0^{\text{CDW}}} \approx 10^{-2} - 10^{-3} \tag{33}$$

which is in good agreement with the experimental data.[2]

To conclude, we have constructed, for the first time, a microscopic theory of the AB-oscillations phenomenon in a transport CDW-current which flows through a sample containing a large number of identical tiny holes (CD) placed in a strong magnetic field. The quantum CDW excitations view these holes as elementary solenoids which carry magnetic flux and the quantum transport current acquires terms oscillating with the magnetic flux with the period $hc/2e$. The oscillatory component of current is proportional to the concentration of CDs. Because of the long-range CDW rigidity, all the holes contribute additively to the current and the oscillations exist at sufficiently high temperature $T \approx 50$ K. At such temperatures, the single electron oscillations, periodic with $hc/e$, are exponentially suppressed by the electron-phonon phase-breaking scattering and cannot be observed.

The presented theory of the ABE in CDW is based on the quantum description of the CDW charge carriers in one dimension by means of the Bose–Fermi equivalence procedure. This method, together with the idea of a long range CDW coherence within an array of $1D$ chains, allows us to reduce this $3D$ problem to an exactly solvable model of a single chain connected to a loop pierced by a magnetic flux. This simple picture gives good agreement with the experimental data.

*)Permanent address: B. I. Verkin Institute for Low Temperature Physics and Engineering, 47 Lenin Ave., 310164 Kharkov, Ukraine

[1] For a review see *Electronic Properties of Inorganic Quasi One-Dimensional Compounds*, P. Monceau (Ed.), Reidel Company, Dordrecht (1985), Parts 1 and 2; *Charge Density Waves in Solids*, L. Gork'ov and G. Grüner (Eds.), *Modern Problems in Condensed Matter Sciences* 25, North-Holland, Amsterdam (1989); *Electronic Crystals, ECRYS-93*, S. Brazovskii and P. Monceau (Eds.), J. Phys. (France) IV Coloq. **C2**, (1993); *Density-Waves in Solids*, G. Grüner (Ed.), Addison-Wesley, Reading, Massachusets (1994); I. V. Krive, A. S. Rozhavsky, and I. O. Kulik, Fiz. Nizk. Temp. 12, 1123 (1986) [Sov. J. Low Temp. Phys. **12**, 635 (1986)].

[2] Yu. I. Latyshev, O. Laborde, P. Monceau, and S. Klaumünzer, Phys. Rev. Lett. **78**, 919 (1997).

[3] I. V. Krive and A. S. Rozhavsky, in *Topological Phases in Quantum Theory*, World Scientific, Singapore (1989) p. 291; *Proc. Int. Seminar on "Geometric Aspects of Quantum Theory"*, Dubna, USSR (1989).

[4] E. N. Bogachek, I. V. Krive, I. O. Kulik, and A. S. Rozhavsky, Phys. Rev. B **42**, 7614 (1990); E. N. Bogachek, I. V. Krive, I. O. Kulik, and A. S. Rozhavsky, Zh. Éksp. Teor. Fiz. **97**, 603 (1990) [Sov. Phys. JETP **70**, 336 (1990)]; E. N. Bogachek, I. V. Krive, and A. S. Rozhavsky, Teor. Mat. Fiz. **83**, 115 (1990) [Sov. Theor. Mat. Phys. **83**, 1 (1990)]; I. V. Krive and A. S. Rozhavsky, Int. J. Mod. Phys. B **6**, 1255 (1992).

[5] A. S. Rozhavsky, Fiz. Nizk. Temp. **22**, 462 (1996) [Low Temp. Phys. **22**, 360 (1996)].

[6] S. Coleman, Phys. Rev. D **11**, 2088 (1975); S. Mandelstam, Phys. Rev. D **11**, 3026 (1975).

[7] I. V. Krive and A. S. Rozhavsky, Usp. Fiz. Nauk **152**, 33 (1987) [Sov. Phys. Usp. **152**, (1987)].

[8] I. V. Krive and A. S. Rozhavsky, Phys. Lett. **113A**, 313 (1985); Z.-B. Su and B. Sakita, Phys. Rev. Lett. **56**, 9 (1986).

[9] M. Büttiker, Y. Imry, and M. Ya. Azbel, Phys. Rev. A **30**, 1982 (1984).

[10] Y. Imry, in *Directions in Condensed Matter Physics*, G. Grinstein and G. Mazenko (Eds.), World Scientific, Singapore (1986), p. 101.

[11] A. S. Kovalev, Yu. V. Pershin, and A. S. Rozhavsky, Phys. Rev. B **53**, 16227 (1996).

[12] I. Tüttö and A. Zawadowski, Phys. Rev. B **32**, 2449 (1985); J. R. Tucker, Phys. Rev. B **40**, 5447 (1989); P. A. Lee and T. M. Rice, Phys. Rev. B **19**, 3970 (1979).

[13] S. Abe, J. Phys. Soc. Jpn. **54**, 3494 (1985); M. Inui, P. P. Hall, S. Doniach, and A. Zettl, Phys. Rev. B **38**, 13047 (1988); C. M. Marcus, S. H. Strogatz, and R. M. Westervelt, Phys. Rev. B **40**, 5588 (1989).

[14] M. R. Geller, D. Loss, and G. Kirczenow, Phys. Rev. Lett. **77**, 5110 (1996).

## PHYSICAL PROPERTIES OF CRYOCRYSTALS

# The structure and the orientational order parameter of Ar–CO$_2$ solid solutions

M. A. Strzhemechny, A. A. Solodovnik, and S. I. Kovalenko

*B. Verkin Institute for Low Temperature Physics and Engineering,
National Academy of Sciences of the Ukraine, 310164 Kharkov, Ukraine**

Electron diffraction studies of the structural characteristics of Ar–CO$_2$ solid solutions are carried out over the entire range of their mutual concentrations. The regions of low concentrations of both components are analyzed in detail and the relative excess volumes $\Delta v/v$ are determined for the CO$_2$ impurity in solid Ar ($\Delta v/v \simeq 0.8$), and for the Ar impurity in solid CO$_2$ ($\Delta v/v \simeq 0.28$). The experimental results and relationships are compared with the results obtained from the semi-quantitative theory on the basis of known atom–atom potentials. An expression relating the intensity of superstructural reflections $I_{(super)}$ (including the reflection 210) with the long-range orientational order parameter $\eta$ is obtained. It is found that $I_{210} \propto \eta^2$ to a high degree of precision. The experimental dependence of the orientational order parameter $\eta$ on the argon concentration in solutions rich in CO$_2$ is obtained. © *1998 American Institute of Physics.* [S1063-777X(98)01209-2]

## 1. INTRODUCTION

All molecular cryocrystals made of linear molecules have orientationally ordered phases.[1] In most cases, the symmetry of these phases under saturated vapor pressure is described by a $Pa3$ group symmetry.[1)] The physics of the orientational order and the nature of the corresponding phase transition (if such a transition does occur) to the disordered phase have been studied quite extensively for classical as well as quantum behavior of the rotational subsystem (see, for example, Ref. 1). Doping of the rotationally ordered phase (of the molecular component M) by particles of "orientationally neutral" modifications or atomic impurities (component A) leads to the destruction of the orientational order. Materials exhibiting this phenomenon include ortho–parahydrogen solutions,[3] as well as alloys of rare gases with linear diatomic[4,5] and triatomic (CO$_2$) molecules.[6–8] Replacement of one of the molecules in the orientationally ordered phase by an "orientationally neutral" rare gas atom leads to the disappearance of the anisotropic interaction component (which was responsible for the orientational order in the entire ensemble) from the bonds between this atom and the surrounding molecules. The molecules surrounding the atom will be in a molecular field whose intensity decreases by $1/z$ in comparison with its value in the regular case ($z$ is the number of nearest neighbors).[2)] It is obvious from a physical point of view that of substitutional atoms for a certain concentration $x^{cr}$, the orientational subsystem loses its long-range order.

Thus AM-type cryoalloys (i.e., those formed by linear molecules and rare gas atoms) form a disordered system in which the multicomponent (quadrupolar in the case considered by us) order is violated as a result of dilution by indistinguishable particles (without a quadrupole moment, which is responsible for the long-range order). The behavior of dilute systems undergoing ordering and the magnitude of the critical concentration $x^{cr}$ depend on the nature of the long-range order, crystal structure and other factors. Hence the investigation of any specific system is interesting in itself. Figure 1 shows a phase diagram of AM solid solutions. Such a diagram is characteristic of ortho–parahydrogen solutions, as well as AM solutions based on a diatomic molecular component. States with orientational long-range order for large values of $x$ are replaced by states without long-range order for concentrations $x \simeq 50\%$ and below. These two regions are separated by the hcp–fcc phase-transition curve. A decrease in temperature in high-concentration phases without long-range order leads to a freezing of molecular orientations into a state called the quadrupolar glass.[9] For lower concentrations ($x < 15\%$) of the M-component, a region is formed whose physical properties are determined by the nature of the system (see below).

The destruction of the purely quadrupolar order has been studied most extensively on the example of ortho–parahydrogen,[3] where molecules in the spherically symmetric para state are the orientationally neutral particles. In this case, the critical concentration $x_{para}^{cr} = 45\%$. In the region of low ortho-concentrations, the thermodynamics is completely determined by the number of "pair clusters" of closely spaced ortho molecules (isolated ortho molecules do not contribute to the thermodynamics).

Dilute quadrupolar systems based on diatomic molecules N$_2$ and CO have been studied quite intensively (see, for example, the reviews by Hochli *et al.*,[4] Strzhemechny *et al.*,[5] and Manzhelii *et al.*[10]).[3)] One of the factors hampering the investigation of these disordered systems in a
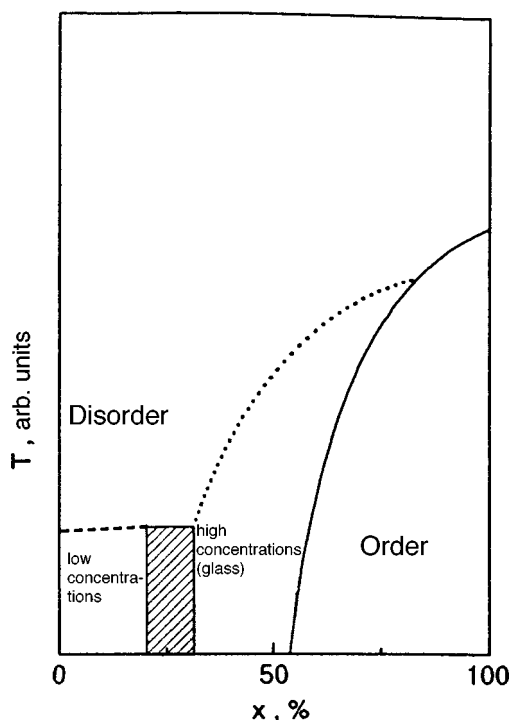
FIG. 1. Typical phase diagram of AM solid solutions. The solid curve describes the orientational order–disorder phase transition, while the dashed curve defines the conditional boundary of orientational glass formation.

macroscopically homogeneous solid solution is their tendency to separate into regions rich in molecular and atomic components respectively. In some cases,[11] the homogeneity region is so narrow that it is not even possible to determine the solubility boundary in the solid solution. However, there are several examples of highly nonequilibrium alloys based on diatomic molecular crystals. For these systems, the low-concentration region (see Fig. 1) is in a specific orientational-glass state for which the energy spectrum is the sum of the rotational spectra of isolated molecules, and randomization of each individual spectrum occurs as a result of the dilatational action of all the remaining impurities.[12] The universal laws governing such a glass-like state have been studied most intensively in the system $Kr-^{14}N_2$.[10,13]

One of the characteristic features of these two systems is the presence of an fcc–hcp structural transition, which is apparently induced by a change in the frustrational energy parameters upon dilution of the $Pa3$ structure by rotationally neutral impurities[4] (see for example, Ref. 15). Thus, the effect of dilution cannot be studied in a cubic structure, and experiments on orientational glass formation are carried out in structures with a different symmetry, where the existence of a long-range order imposed by the quadrupole interaction remains doubtful.

In this connection, the use of triatomic linear molecules as the molecular component has a number of advantages, as well as several distinguishing features as compared to diatomic linear molecules. First, it can be expected that the detection of superstructural reflections in mixtures with a suppressed long-range order will be more reliable, especially in electron diffraction measurements. Second, the inhibited

mobility of individual particles as well as layers in the case of triatomic molecules allows us to obtain long-lived metastable solid solutions with high mutual concentrations. This leads to the third advantage according to which the lattice of the mixture remains cubic for all mutual concentrations and it becomes possible to study the effect of dilution on orientational order in pure form. These peculiarities have been reported in our earlier communications about $CO_2$-based systems with atomic components Kr,[6] Ar,[7] and Xe.[8]

An equally interesting problem concerns the thermodynamics in the region of low M-concentrations ($x \leqslant 15\%$) in which a glass-like state with predominantly indirect interaction (through the field of elastic deformations) must be realized, the more so because the rotational spectrum in this case must differ from that of solutions based on diatomic molecules. Studies of dilute ($x \sim 1\%$) solutions provide information about the regions of mixing which constitute one of the factors that determine the magnitude of the elastic fields around the molecular impurity.

The possibility of the formation of a glass-like structure in orientational states localized at the atomic impurities of the orientationally ordered lattice and interacting through elastic static fields remains an open question although some experimental data speak about the anomalies in the heat capacity of AM-type solid solutions.[16]

In this communication, we present the results of detailed investigations of the structure of $Ar-CO_2$ alloys in the entire range of concentrations. The main attention was paid to the following issues: low concentrations (at both ends of the phase diagram) for obtaining mixing volumes per Ar atom in solid $CO_2$ and $CO_2$ molecules in solid Ar, detailed studies of the behavior of superstructural reflections as functions of the Ar concentration and temperature, and a theoretical estimate of quantities concerning the structural and energy characteristics of the system under consideration. The obtained experimental data are compared with the conclusions of the semiquantitative theory constructed on the basis of phenomenological potentials. The mathematical and computational problems are considered in the Appendices.

## 2. EXPERIMENT

Investigations were carried out by the transmission electron diffraction technique using a special helium cryostat. Samples were prepared *in situ* by depositing gaseous mixtures at various deposition temperatures $T_d$. Measurements were made at temperatures ranging from 6 K to the sublimation temperature of pure argon (28–30 K, depending on the thickness). The effective thickness of the deposited films varied from 80 to 200 Å. Samples were deposited on substrates made of polycrystalline Al films which also served as the internal reference material. In the photographic technique of recording, such a reference material ensures a more precise evaluation of the lattice parameter $a$. Since we dealt with solid solutions, the diffraction rings could be quite weak and blurred (depending on the composition), thus considerably increasing the error in determining $a$, which varied from 0.1 to 0.3%.
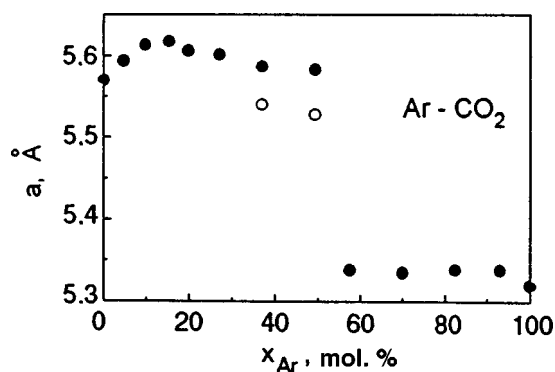
The composition was varied over the entire range of

FIG. 2. Lattice parameter of solid Ar–CO$_2$ mixtures as a function of argon concentration at $T=25$ K. The deposition temperature $T_d=25$ K. Light circles correspond to the argon-rich phase.



FIG. 3. Densitometric profile region for an Ar–CO$_2$ samples with 37% Ar, $T=25$ K; $T_d=25$ K. The indices of peaks for the diffraction pattern are marked on top; $s=4\pi \sin \theta/\lambda$ is the diffraction vector modulus, where $\theta$ is Bragg's angle and $\lambda$ is the electron wavelength.

mutual concentrations. The concentration of the gaseous phase was determined by measuring the partial pressure of components with the help of a sensitive manometer. The total volume of the mixture being prepared was increased in order to increase the accuracy of measurements of the pressure of highly diluted components for argon molar concentrations $x_{Ar}$ close to 0 and 1.

The supply of the gaseous mixture at low pressures (ensuring a growth rate from 1 to 3 Å/s) minimized not only the risk of separation during transportation at liquid nitrogen temperature, but also the condensation overheating which could cause uncontrollable or undesirable separation in the solid phase. Judging by the experimental data, the prepared solid solutions were found to be quite homogeneous (see discussions below).

## 3. EXPERIMENTAL RESULTS

Analysis of the electron diffraction patterns showed that, in the entire range of compositions, the solid solutions have cubic symmetry, or an fcc structure for argon-rich solutions, or a $Pa3$ structure for solutions rich in the molecular component. Let us consider some peculiarities in the dependence of the lattice parameter of solutions on the composition (Fig. 2). The concentration range can be divided arbitrarily into three regions. For solutions in which carbon dioxide predominates ($0 \leqslant x_{Ar} \leqslant 35\%$), we observed a set of $Pa3$ reflections which give the lattice parameter varying significantly with the argon impurity concentration. This fact as well as a qualitative theoretical analysis (see Sec. 4) lead to the inference that we are dealing with a nearly homogeneous impurity distribution, at least for argon concentrations up to about 10 percent. For nearly equimolar concentrations ($35\% \leqslant x_{Ar} \leqslant 55\%$), we observed a number of reflections against the background of reflections corresponding to the CO$_2$-based solutions. These reflections were attributed to the argon-rich phase. Figure 3 shows a typical densitogram of a CO$_2$–Ar (37% Ar) sample in the region of principal reflections. It can be stated on the basis of a rough estimate obtained by using the values for excess volume (see below) that these reflections may correspond to the argon-based solutions with a relatively high (about 15%) concentration of the M-component. Thus we can speak of the classical separation of
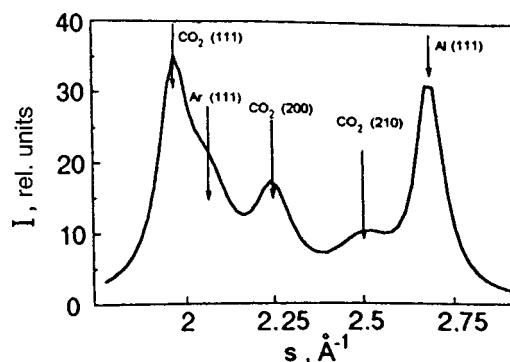
solutions only in this relatively narrow intermediate range of concentrations of the M-component. For higher argon concentrations ($60\% \leqslant x_{Ar}$), we observed only one set of reflections. The lattice parameter of the solutions was found to depend weakly on the composition except in a very narrow interval $x_{CO_2} \leqslant 3\%$ in which a relatively weak dependence $a(x_{CO_2})$ was observed.

A characteristic feature of solid solutions is the non-monotonic dependence of the lattice parameter (and molar volume) on composition for small admixtures of argon (from 0 to 25%) at deposition temperatures $T_d=25$ K, which was reported by us earlier.[7] In order to find the nature of this nonmonotonicity, we performed the experiments at lower temperatures $T_d=6$ and 15 K. The obtained results are presented in Fig. 4. It can be seen that the shape of the curves $a(x_{Ar})$ is preserved although the effect itself is modified: the height of the peak is lowered considerably as $T_d$ decreases; the peak itself shifts towards lower values of $x_{Ar}$. The authors are not in a position to explain this effect.

It was mentioned above that one of the aims of our research was a meticulous measurement of the dependence of the lattice parameter $a$ (molar volume) of the mixtures for low concentrations of the A- or M-component. For low Ar concentrations, presumably homogeneous solutions were easily obtained, and hence the excess volume per argon
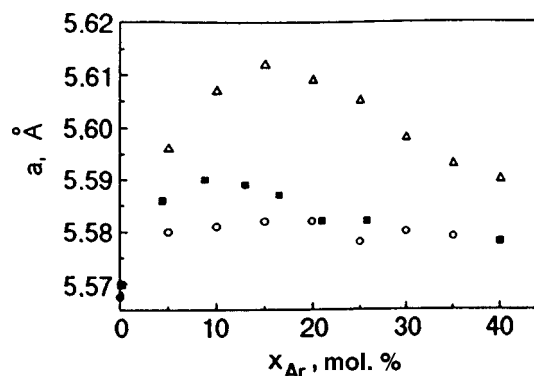


FIG. 4. Lattice parameter of solid Ar–CO$_2$ mixtures as a function of argon concentration at three deposition temperatures $T_d$ (in K); 6 (circles), 15 (squares) and 25 (triangles).
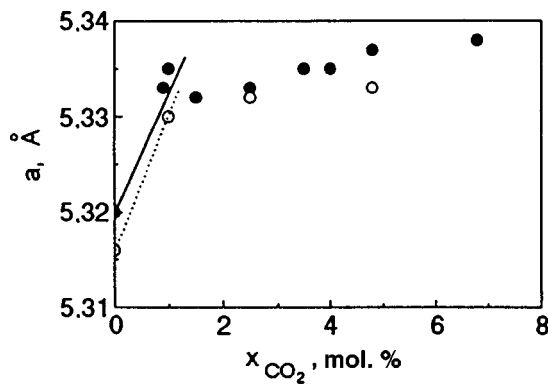
FIG. 5. Lattice parameter of Ar–$CO_2$ solutions for low concentrations of carbon dioxide at two deposition temperatures $T_d = 6$ and 25 K.

impurity could be determined without any difficulty. In view of the above peculiarities in the dependence of the lattice parameter on composition for low concentrations of $CO_2$, we made a number of experiments for extremely low concentrations of $CO_2$ (see Fig. 4) at which the attainable degree of precision allows us to determine the excess volume.

By definition, the relative excess volume $\Delta v/v = \Omega(A/M)$ per impurity particle of the substance A in the crystal M is given by the expression

$$\Omega(A/M) \equiv \lim_{x_A \to 0} \frac{V(x_A) - V(0)}{x_A V(0)}, \tag{1}$$

where $x_A$ is the concentration of the substance A and $V(x_A)$ is the molar volume of the solution for the concentration $x_A$. Using the data from Fig. 3 (see also Fig. 7), we obtain

$$\Omega(\text{Ar}/CO_2) = \lim_{x_{Ar} \to 0} \frac{V(x_{Ar}) - V(0)}{x_{Ar} V(0)} = 0.28 \pm 0.04, \tag{2}$$

i.e., the argon impurity occupies a considerably larger volume (1.28) than the $CO_2$ molecule in the crystal. This effect is discussed in Sec. 4.

Analogous measurements of the molar volume for extremely low concentrations of $CO_2$ (below 1%) made it possible to determine the excess volume of a single $CO_2$ impurity. Using the data of Fig. 5 showing the results of deposition at temperatures 6 and 25 K, we obtain

$$\Omega(CO_2/\text{Ar}) = 0.8 \pm 0.2. \tag{3}$$

Within the limits of the error indicated above, the value of $\Omega$ is practically independent of the deposition temperature.

## 4. INTENSITY OF SUPERSTRUCTURE LINES AND THE ORIENTATIONAL ORDER PARAMETER

A problem of fundamental importance considered in this work concerns the behavior of the orientational order parameter $\eta$ in the investigated solid solutions Ar–$CO_2$. The structural analysis and, in particular, electron diffraction studies are among the very few techniques available for obtaining a direct quantitative information about the value of $\eta$. For this purpose, we use the lines that are present in the spectrum for the $Pa3$ lattice and do not appear for the fcc structure.

The orientational order parameter of the crystal formed by symmetric linear molecules is, by definition, the thermodynamic average of the corresponding spherical function

$$\eta \equiv (5/4\pi)^{1/2} \overline{P_{20}(\omega)}, \tag{4}$$

where the unit vector $\omega$ determines the orientation of the axis of the molecule, while for the reference frame we chose one of the directions of the type $\langle 111 \rangle$ along which the molecules are oriented in the $Pa3$ structure. In an impurity-free crystal, the quantity $\eta$ is the same in all four sublattices of this structure. In a doped crystal, the order parameter can be written in the form

$$\eta = \langle Y_{20}(\omega) \rangle = \sum_i \hat{c}_i \int d\omega Y_{20}(\omega) \rho_i(\omega). \tag{5}$$

Here the summation is carried out over the lattice sites $i$; the operator $c_i$ assumes the value 1 if the site is occupied by a $CO_2$ molecule and 0 if the site is occupied by an argon atom which naturally does not make any contribution to the orientational order parameter; the quantity $\rho_i(\omega)$ is the weight function which defines the angular distribution of the orientation probability of molecules. This distribution is determined by the dynamics of the rotational angular momentum in given molecular and crystal fields, while the latter are determined by temperature and deviations of the closest environment from uniformity (crystals containing impurities or other defects). Thus, dilution of solid carbon dioxide by rotationally neutral argon atoms leads to two effects causing a decrease in the value of $\eta$, viz., the direct substitution simply puts some of the sites ''out of play'' (i.e., increases the number of sites at which $c_i$ vanishes), and an additional (apart from temperature-related) broadening and deformation of the weight function $\rho(\omega)$ takes place and lowers the value of the integral in Eq. (5). Unlike the temperature broadening by phonons, which is of a dynamic nature, the latter effect has a static origin. As a rough approximation which is valid only for low concentrations of the atomic impurity, Eq. (5) can be written in the form $\eta = (1 - x_{Ar}) \tilde{\eta}$, where $\tilde{\eta}$ can be conditionally called the order parameter at sites occupied by molecules.

For the measure of the orientational order parameter, we chose the intensity of the superstructural reflection 210 whose relative values are presented in Fig. 6 for a number of compositions. It will be shown below that, to a good degree of precision, the intensity of this superstructural reflection can be assumed to be proportional to the square of the orientational order parameter: $I_{210}(x_{Ar}) \propto \eta^2(x_{Ar})$. The values of the intensity presented in Fig. 3 were obtained for various samples with different thicknesses and other parameters. Hence we used a modified reduction procedure[6] for reflection intensities which is substantiated in Appendix 1.

The evaluation of the orientational order parameter in Ar–$CO_2$ alloys requires an analysis of the line intensities. For pure orientationally ordered crystals, the generally accepted method for estimating the absolute value of the orientational order parameter is to calculate the intensities and reflection widths by using the effective lengths of molecules whose shortening is associated with zero-point or thermal
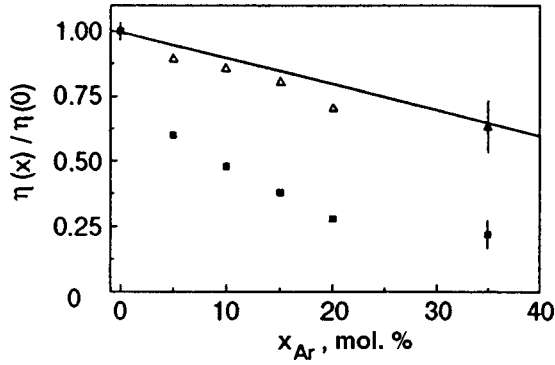
FIG. 6. Relative orientational order parameter (triangles) as a function of argon concentration in solid $CO_2$. Squares indicate the relative values of the intensity of the superstructure reflection 210 in solid Ar–$CO_2$ mixtures, and the solid line corresponds to the theoretical calculation in the molecular field approximation reflecting only the substitution by argon which leads to a suppressio of the 210 line in proportion to the argon concentration.

librations.[17] Such an approach is applicable for cases in which the librational movement is not too intense. This method cannot be used for solutions, especially those with an appreciable spherical impurity concentration.

We shall consider alloys that are rich in the M-component and whose lattice structure has the $Pa3$ symmetry. For reasons that will be explained below, we shall discuss in detail the lines 200 and 210, the former existing in the sets of both fcc and $Pa3$ structures, while the latter is a superstructural line and is therefore used as a measure of the orientational order.

The intensity of electron scattering $I$ as a function of the transferred momentum $\mathbf{q}$ can be represented in the general case in the form

$$I = \left| \sum_{s=1}^{N} \sum_{\gamma} f_{s\gamma}(\mathbf{q}) \exp i\mathbf{q}\cdot\mathbf{R}_{s\gamma} \right|^2 = \left| \sum_{s} F_s(\mathbf{q}) \exp i\mathbf{q}\cdot\mathbf{R}_s \right|^2. \quad (6)$$

Here $s$ stands for summation over unit cells, and $\gamma$ for summation over scattering centers within a unit cell, $\mathbf{R}_{s\gamma} = \mathbf{R}_s + \mathbf{R}_\gamma$ where where $\mathbf{R}_\gamma$ is the radius vector of the scattering center $\gamma$ within a unit cell.

Averaging, as usual,[18] over the positions of the Ar impurity atoms, we obtain the following expression for the mean structural amplitude:

$$F_s = \sum_c e^{i\mathbf{q}\cdot\mathbf{R}_c}\{x_{AR}f_{AR}(\mathbf{q}) + (1-x_{Ar})F_C(\mathbf{q})$$

$$+ (1-x_{Ar})^2 f_O(\mathbf{q}) \cos[\mathbf{q}\cdot\mathbf{g}_c x]\}. \quad (7)$$

Here $f_i(\mathbf{q})$ is the scattering factor for the $i$th atom (for convenience, we shall not indicate explicitly the dependence of the scattering factors on $\mathbf{q}$). Summation over $c$ indicates summation over positions which can be occupied by carbon atoms, while the summation over oxygen atoms for each position $c$ can be presented explicitly by using the following notation: $\mathbf{g}_c$ is the unit vector along a $CO_2$ molecule in the position $c$, $x = d/(a\sqrt{3}) = 0.0120$ for $CO_2$ at low temperatures, $d$ being half the length of the molecule and $a$ the lattice parameter. The first two terms contribute only to the reflec-

tions that are common for fcc and $Pa3$ structures. The last term also contributes to the regular reflections, but completely determines the intensity of superstructural amplitudes.

The amplitude $F_s$ can also be presented in the form

$$F_s = \sum_c e^{i\mathbf{q}\cdot\mathbf{R}_c}\{x_{Ar}f_{Ar} + (1-x_{Ar})(f_C + 2f_O)$$

$$+ (1-x_{Ar})2f_O(1 - \cos[\mathbf{q}\cdot\mathbf{g}_c x])\}, \quad (8)$$

whose only advantage is that the term which vanishes as the length of the molecule formally tends to zero is clearly singled out. This is convenient for determining the relation between the intensity of the superstructural line and the orientational order parameter $\eta$ defined by Eq. (4). It is implied that the averaging is carried out over dynamic (thermal vibrations) as well as static factors (atomic displacements in a solid solution).

Let us consider a superstructural line. The amplitude of such reflections is determined only by the last term under the summation sign in Eq. (8):

$$F_s^{super} = 2f_O(1 - x_{Ar})\sum_c e^{i\mathbf{q}\cdot\mathbf{R}_c}(1 - \cos[\mathbf{q}\cdot\mathbf{g}_c x]). \quad (9)$$

For simplicity, we shall assume that static displacements concern only rotational degrees of freedom of molecules, i.e., the directions of molecules $\mathbf{g}_c$ vary from site to site, while the positions of the centers of gravity $\mathbf{R}_c$ of molecules remain unchanged. In this case, averaging of $F_s$ over dynamic and static disorder will affect only the cosine. Presenting vector $\mathbf{q}$ for the reflection 210 in the form $\mathbf{q} = q\mathbf{n}$, where $q = 2\pi\sqrt{5}$ and $\mathbf{n} = (1/\sqrt{5})(2,1,0)$, we can expand the expression in the parentheses into a series in spherical harmonics[19]

$$1 - \cos[\mathbf{q}\cdot\mathbf{g}_c x] = 8\pi\sum_{l\geqslant 2} j_l(2\pi xq)[Y_l(\mathbf{n})\cdot Y_l(\mathbf{g}_c)]. \quad (10)$$

Here $j_l(y)$ are spherical Bessel functions, the summation is carried out over even $l$, and

$$[Y_l(\mathbf{n})\cdot Y_l(\mathbf{g}_c)] = \sum_{m=-1}^{l} Y_{lm}^*(\mathbf{n})Y_{lm}(\mathbf{g}_c), \quad (11)$$

where $Y_{lm}$ are spherical functions in standard normalization.[19] It follows from Eq. (10) that the expansion over spherical harmonics begins from $l=2$. Subsequent terms with $l=4,6,\ldots$ are corrections that cannot be reduced to $\eta$. It can be shown easily that after averaging, the term with $l=2$ must give the exact value of the orientational order parameter:

$$\overline{Y_{lm}(\mathbf{g}_c)} = \eta Y_{lm}(\mathbf{g}_{c0}), \quad (12)$$

where $\mathbf{g}_{c0}$ are unit vectors along the corresponding diagonals of the cube in the $Pa3$ structure. Equation (12) was derived under the following assumptions. First, it is assumed that statically disoriented molecules have a symmetric distribution relative to the corresponding $\mathbf{g}_{c0}$ so that we can confine the analysis to just one order parameter $\eta$ and disregard the anisotropy of the order parameter $\zeta = (Y_{22} - Y_{2\bar{2}})$. Second, the averaging is carried out by disregarding significant static
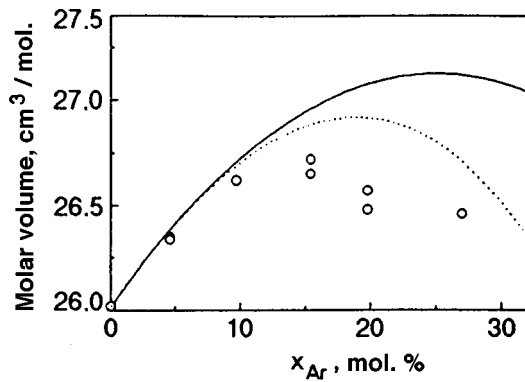
FIG. 7. Molar volume of Ar–CO₂ solid solutions as a function of argon concentration. The deposition temperature $T_d = 25$ K; measurements were made at 25 K. The solid curve was obtained from the semiquantitative theory taking into account only paired clusters of Ar impurity, while the dashed curve corresponds to the theory for an analogous model taking into account triple clusters also (see Sec. 4).

displacements of centers of gravity of both A and M particles. These displacements can alter the line intensity. However, since we shall adopt in the following a specific procedure for reducing the intensity of superlines against regular ones (of the 200 type), it can be stated confidently that this additional intensity variation does not occur in the reduced variables.

Let us evaluate the role of high-order ($l > 2$) spherical harmonics in Eq. (10) for the reflection 210 as compared with the term with $l = 2$. We shall first consider an ideal crystal for $T = 0$ and $\eta = 1$. In this case, $\mathbf{n} = (1/\sqrt{5})(2,1,0)$; $x = 0.120$ (we shall take the value $xq = 0.269$ for pure carbon dioxide). Numerical estimates show that the ratio of the expressions under the summation sign in (10) with $l = 4$ and $l = 2$ is about 0.055. Disregarding this correction, we find from (1) that $I_{210}$ is proportional to the square of the orientational order parameter: $I_{210} \propto \eta^2$.

## 5. DISCUSSION OF RESULTS

Let us consider in detail the dependence of the molar volume of Ar–CO₂ solid solutions for low Ar concentrations (see Fig. 7). For solid carbon dioxide diluted weakly with argon, two opposing processes are operative. On the one hand, the dissolution of smaller argon particles (the Lennard–Jones parameter $\sigma$ for CO₂ is about 17% larger than for argon, which amounts to about 62% in terms of volume) must lead to a compression of the crystal. On the other hand, it must be taken into consideration that if a CO₂ molecule at any site is replaced by an argon atom, 12 CO₂–CO₂ bonds are replaced by an equal number of much weaker CO₂–Ar bonds. This causes a weakening of the attraction due to the anisotropic part of the interaction, and eventually leads to a swelling of the crystal. The change $\Delta v$ in the volume caused by the introduction of a substitutional impurity in the cubic lattice can be presented in the form[20,21]

$$\Delta v = \frac{1}{3B} \sum_f R_f F(R_f), \tag{13}$$

where the summation is carried out over the lattice sites $f$ with the radius vector $\mathbf{R}_f$, $B$ is the compressibility modulus, $\mathbf{F} = -V\Phi_{i0}$; $\Phi_{i0} = \varphi_{i0} - \varphi_{00}$; $\varphi_{i0}$ and $\varphi_{00}$ are the potentials of "guest–host" and "host–host" interactions, respectively, i.e., $\mathbf{F}$ is the impurity-induced additional force acting on the nearest regular neighbor. In the nearest neighbor approximation, this expression assumes the form

$$\Delta v = \frac{4R_0 F(R_0)}{B}, \tag{14}$$

where $R_0$ is the distance to the nearest neighbor in the new equilibrium position.

Using an analogous formula, we can also take into consideration the second factor (vanishing of the binding energy due to anisotropic forces). In this case, we should use for the additional force in Eq. (13) the expression $\partial U_{anis}/\partial R$, where $U_{anis}$ is the part of the binding energy which vanishes as a result of substitution by argon. Finally, we obtain the following expression for this part of the dilatational volume:

$$\Delta v \simeq \frac{4}{B} \sum_i \gamma_i U_i. \tag{15}$$

Here $i$ labels three (quadrupole, valence, and dispersion) contributions to the energy of anisotropic interaction of CO₂ molecules, $\gamma_i$ and $U_i$ are the corresponding Grüneisen constants and the anisotropic interaction energy components respectively. The values for the latter parameters are borrowed from Ref. 22. For CO₂, the value of the modulus is $B = 76.6$ kbar.

Using the numerical data (some of which are presented in Appendix 3), we obtain for the parameters of all three isotropic interaction potentials (CO₂–CO₂, CO₂–Ar and Ar–Ar) a theoretical estimate for the excess volume per argon impurity in CO₂: $\Delta v/v = 0.34$, which is in quite good agreement with the magnitude and sign of the experimentally obtained value 0.28 [see Eq. (2)]. Thus, it turns out that for weak dilutions with the argon impurity, the vanishing of the anisotropic part of the binding energy of two CO₂ molecules is a more significant factor. Hence the introduction of smaller but more weakly interacting argon particles into solid CO₂ ultimately causes a dilatation of the lattice rather than its compression.

As the concentration of Ar in the solution increases, the description on the basis of the excess volume per isolated impurity becomes less and less appropriate. The behavior of the molar volume for appreciable concentrations ($x > 5\%$) can be explained by using the cluster approach which can be applied for concentrations up to 30% if we take triple clusters into consideration. If we confine the analysis to pair clusters for simplicity, the average molar volume $V$ can be represented in the form

$$V = V_M + x_s \Delta v_s + x_p \Delta v_p. \tag{16}$$

Here $V_M$ is the molar volume of a pure crystal M, $x_i$ and $\Delta V_i$ are the molar concentration and excess volume of single and pair clusters respectively, and $x_{Ar} = x_s + 2x_p$ by definition. Each isolated (single) argon impurity has an excess volume associated with it, which is proportional to the number $Z$ of

nearest neighbors and to the corresponding additional (negative for the system considered by us) force: $\Delta V_s = Z\varphi$ (see below). If two Ar atoms form a pair cluster, it can be easily shown that the number of $CO_2$–$CO_2$ bonds vanishing from the pure crystal is $2Z-4$ and not $2Z$. For simplicity, we disregard the difference between the isotropic parts of the M–M and M–A interactions. This gives $\Delta v_p = (2Z-4)\varphi$. Transforming (16), we obtain

$$V = V_M + (x - 2x^2)\Delta v_s. \tag{17}$$

Figure 7 shows the dependence of the molar volume recalculated by using the data of Fig. 4 for $T_d = 25$ K. The solid curve corresponds to formula (16) with a theoretical value $\Delta v_s(\text{Ar}/CO_2)$ (see above). Consideration of triple clusters lowers the peak and displaces it to the left (dashed curve in Fig. 7).

The excess volume for the $CO_2$ impurity in solid argon was calculated by taking into account the renormalization of the isotropic part of the Ar–$CO_2$ interaction to a finite length of the molecule (see Appendix 2) and on the basis of the potentials proposed by Mirsky.[27] The excess volume is estimated theoretically at $\Delta v/v = 2.78$, which differs significantly from the experimentally obtained value (3). The theoretical result indicates that if dilatation is taken into consideration, the $CO_2$ molecule occupies a four-times larger volume than a regular argon atom. Consequently, the deformations around the $CO_2$ impurity are so large that it may occupy two different equilibrium positions in the Ar lattice. The value of the excess volume obtained in (3) may be due to a poor solubility of $CO_2$ in solid argon.

All things considered, the indicated value of quasistatic displacements and the estimate of the corresponding barrier heights indicate that the $CO_2$ molecule in argon cannot perform hindered tunnel rotation (like a nitrogen molecule in any rare gas crystal). The rotational transitions of the molecule must occur between librational levels in the appropriate orientational potential well. In turn, this determines the considerable difference of the glass state of this binary system in the region of indirect interaction between molecules from solutions with diatomic molecular impurities.

Let us return to our discussion of the phase whose lattice parameters are shown in Fig. 2 in the form of light circles. If we accept the theoretical estimate for the excess volume per $CO_2$ molecule, we find that the concentration of the component M is $\sim 2.5$–$4\%$. It should also be noted that the large linewidth of what was indexed as the 111 reflection of Ar (Fig. 3) indicates that the crystallites of the precipitated Ar-based phase are very small.

The behavior of the orientational order parameter $\eta$ in $CO_2$-rich solutions differs from that of $N_2$-based solutions. The order parameter $\eta$ in Ar–$CO_2$ solutions varies smoothly with the Ar concentration. The dependence $\eta(x_{\text{Ar}})$ does not tend to zero for moderate Ar dilutions unlike those in the case of nitrogen.[23] With increasing Ar concentration (above 55%), the $CO_2$ impurity begins to precipitate, apparently in the form of a low-dispersive fraction whose crystallites cannot form individually detectable coherent reflections in the course of the experiment. In the absence of such a sharp variation in the morphology, it could be expected that the

orientational order would ''survive'' until quite large concentrations of argon (80–85%) are attained since cubic symmetry, unlike hexagonal symmetry, is not a factor in itself that would obstruct the existence of a long-range orientational order. This hypothesis is confirmed by the NMR data[24] obtained in Ar-rich $N_2$–Ar solutions in the range of $N_2$ concentrations close to the percolation threshold where these solid solutions have a fcc structure.

In conclusion, the authors are pleased to express their gratitude to A. I. Èrenburg for providing an opportunity to go through some of his unpublished results, and for a discussion of several problems associated with the topics considered in this work. Thanks are also due to V. G. Manzhelii and N. V. Krainyukova for discussion of the results and for valuable comments.

## APPENDIX 1: REDUCTION OF SUPERSTRUCTURE REFLECTION INTENSITIES

The problem of determining the absolute values of the orientational order parameter is quite complex even in pure molecular crystals. In solutions, this problem is considerably complicated in view of the fact that the impurities are responsible for the emergence of several factors which strongly influence the intensity and shape of reflections. Hence the procedure of reduction of reflection intensities becomes quite complicated. The idea behind the procedure laid down in the present work is based on the method described earlier by Sandor and Farrow,[17] but modified by taking into account the results obtained by us, including those described in Appendix 4. We shall carry out the reduction by using the reflections 200 and 210. The line 200 is used because it is quite intense and remains clearly distinguishable even for high mutual concentrations.

The experimental value of the intensity of the $hkl$ line for a given sample with argon concentration $x$ (we ignore the subscript Ar for the sake of simplification) can be presented in the form

$$I_{hkl}^{(\text{exp})}(x) = B(x)I_{hkl}^{(0)}(x), \tag{A1.1}$$

where the quantity $B(x)$, which takes into account all parameters of the experiment (scattering volume, primary beam intensity, etc.), is the same for all reflections of the given sample. Using (8), we can represent the intensity of the regular reflection $I_{200}^{(0)}(x)$ approximately in the form $B(x)F_{200}^2(x)$. On the other hand, the intensity of the superstructural reflection 210 from a sample with concentration $x$ can be given in the form $I_{210}^{(\text{exp})}(x) = B(x)I_{210}^{(0)}(x) \simeq B(x)CF(\eta)$, where we have made use of the conclusion that the scattering intensity for the reflection 210 is proportional to $\eta^2(x)$ with a certain proportionality factor $C$.

We introduce a physically significant relation

$$R(x) \equiv \frac{I_{210}^{(\text{exp})}(x)}{I_{200}^{(\text{exp})}(x)}, \tag{A1.2}$$

which does not involve the factor $B(x)$ which is difficult to determine. From (A1.2) we obtain

$$\frac{R(x)}{R(0)} = \frac{I_{200}^{(0)}(0)}{I_{200}^{(0)}(x)} \frac{F(\eta(x))}{F(\eta(0))}, \tag{A1.3}$$

whence

$$\frac{\eta(x)}{\eta(0)} = \left(\frac{R(x)}{R(0)}\right)^{1/2} \frac{\overline{F_{200}(x)}}{\overline{F_{200}(0)}}, \tag{A1.4}$$

where $F_{hkl}$ are the corresponding structural amplitudes.

Since the random static displacements lead to analogous variations of the intensities of all lines, the reduction procedure presented here essentially excludes the effect of this important factor on the estimate for the orientational order parameter. The structure amplitude $F_{200}$ averaged over the impurity positions and appearing in the above expression is calculated with the help of Eq. (8) in which we put $\mathbf{g}_c = \mathbf{g}_{c0}$.

## APPENDIX 2: ACCOUNT OF FINITE LENGTH OF MOLECULES

The anisotropic part of the interaction between two (generally different) molecules or a molecule and an atom can be presented as the sum of three components, viz., the multipole electrostatic interaction and two components associated with valence and dispersion forces. The form of the direct electrostatic interaction is obvious. The valence- based anisotropic component is usually estimated by using the atom–atom approach, while the dispersive anisotropic component is "constructed" either by using the concept of anisotropy of polarizability of a molecule, or by using the atom–atom approach again. We shall use a unified atom–atom approximation for valence as well as dispersive parts of anisotropic interactions. The analytic representation of these interactions is fraught with the problem concerning the choice of the potential. Usually, one confines the expansion in $\xi = 2d/R_0$ to the first nontrivial term ($2d$ is the "length" of the molecule and $R_0$ the separation between the interacting particles). Each term in such an expansion "carries" a corresponding spherical function of angles defining the orientation of the molecule. This function is just the potential acting on the angular variables of the molecule. To a certain extent, such a procedure can be assumed to be justified for short (diatomic) molecules, although good numerical estimates for such molecules can be obtained by considering the first few terms in the expansion in $\xi$ in the coefficients of the corresponding spherical harmonics. Even for triatomic linear molecules, such a procedure becomes quite cumbersome and irrespective of the number of terms of the expansion used in the analysis, there is no guarantee that the principal part has been taken into consideration.

Hence we propose an alternative approach for constructing the anisotropic part of the interaction.[25] By way of an example whose results have been used actively in the main text, we consider the part of anisotropic interaction between a molecule and an atom which is associated with valence forces.

Thus, the repulsive part of the interaction energy $E_{MA}$ of a linear symmetric molecule M with an atom A is estimated in the atom–atom approximation. In this case, $E_{MA}$ will have the form (relative to the axis passing through the atom A and the center of the molecule)

$$E_{MA} = \sum_a E_a(\mathbf{R}_a). \tag{A2.1}$$

Here the summation is carried out over the atoms $a$ of the molecule, and $\mathbf{R}_a = \mathbf{R}_0 + \mathbf{r}_a$ is the radius-vector of separation between the atom A and the atom $a$ of the molecule ($\mathbf{r}_a$ is the radius-vector of the atom $a$ relative to the center of the molecule). It is assumed that the interaction of the atom A with the atom $a$ of the molecule is the same as with an isolated atom $a$ (the energy $E_a$ of this interaction depends only on the separation $R_a$). It can be easily shown that (A2.1) can be represented in the form

$$E_{MA} = \sum_N F(N0) Y_{N0}(\omega), \tag{A2.2}$$

where the index $N$ runs through even values $0, 2, \ldots$ for a symmetric molecule, $Y_{N0}(\omega)$ is a spherical function, and $\omega$ is a unit vector along the molecular axis. The coefficients $F(N0)$ have the form

$$F(N0) = \sum_a A_a(R_0) f_N(\xi_a), \tag{A2.3}$$

where $\xi_a = r_a/R_0$, and $A_a(R_0)$ is the constant of interaction energy between the atom under consideration and atom $a$ in the molecule. The function $f_N(r_a/R_0)$ is the total "intensity" of the $N$th rotational harmonic summed over all powers of ratio $\xi_a$.

For valence interaction, a convenient and fruitful approximation is the Lennard–Jones representation $A(R) \propto R^{-12}$. Experience shows that it is convenient to confine the expansion in spherical functions to terms with $N \geq 4$. Let us represent the specific values of the spherical amplitudes of interactions of an atom of a rare gas R with a diamotic nitrogen molecule $N_2$ and a triatomic carbon dioxide molecule $CO_2$. Introducing the notation

$$\eta = \frac{2\xi}{1+\xi^2}, \tag{A2.4}$$

we obtain for $N_2$

$$F(00) = 4\pi^{1/2} A \frac{(5 + 10\eta^2 + \eta^4)}{4(1-\eta^2)^5}; \tag{A2.5}$$

$$F(20) = 8(\pi/5)^{1/2} A \frac{\eta^2(7+\eta^2)}{(1-\eta^2)^5}; \tag{A2.6}$$

$$F(40) = \frac{192\pi^{1/2}}{5} A \frac{\eta^4}{(1-\eta^2)^5}. \tag{A2.7}$$

Here,

$$A = \frac{A_{NR}}{(1+\xi^2)^6 R^{12}}; \tag{A2.8}$$

where $A_{NR}$ is the constant for the valence part of the Van der Waals potential of interaction between a nitrogen atom N and a rare gas atom R. Note that the only coefficient $F(00)$ tends to a nonzero value $4\pi^{1/2}A_{NR}$ as $\eta$ (or $\xi$) tends to zero. Hence the corresponding coefficient in (A2.2) tends to $2A_{NR}$.

It can be seen from (A2.5)–(A2.7) that for $R = d$ (i.e., for $\xi = \eta = 1$), all coefficients of expansion in harmonics have a divergence which is quite obvious from physical considerations for a Lennard–Jones type hard-core potential. This moment cannot be revealed for any arbitrarily large and finite number of terms of expansion in $\xi$.

Similarly, we can write the coefficient $F(00)$ for the interaction between a rare gas atom R and a carbon dioxide molecule in the form

$$F(00) = 4\pi^{1/2}A\frac{(5 + 10\eta^2 + \eta^4)}{5(1 - \eta^2)^5} + 2\pi^{1/2}\frac{A_{OR}}{R^{12}}, \qquad (A2.9)$$

where $A$ is defined by formula (A2.8) with the obvious substitution $A_{CR}$ for $A_{NR}$, and $A_{OR}$ is the constant of valence interaction between an oxygen atom and a rare gas atom R.

The remaining coefficients $F(N0)$ coincide with the corresponding expressions (A2.5) and (A2.6) in which the substitution $A_{NR} \rightarrow A_{CR}$ is made. The expansion for $F(00)$ for the exponential form of representation for the valence interaction (in a diatomic molecule) has the form

$$F(00) = 4\pi^{1/2}\frac{A\exp(-\rho)}{\rho^2}\left[(1 + \rho)\frac{\sinh\rho\xi}{\xi} - \rho\cosh\rho\xi\right], \qquad (A2.10)$$

where $\rho = \alpha R$, $\alpha$ being the spatial parameter of the potential. The potential can be easily generalized for a symmetric triatomic molecule, as for the representation $R^{-12}$ (see (A2.8)).

Let us also consider all terms of the expansion for the anisotropic part of the dispersion interaction. In this case we use functions of the type $B(R) = -B/R^6$ instead of the functions $A \propto R^{-12}$. As a result, we obtain for the lowest harmonic amplitude (for the diatomic molecule $N_2$)

$$F(0,0) = -4\pi^{1/2}\frac{B_{NR}}{R^6}\frac{1 + \xi^2}{(1 - \xi)^4}. \qquad (A2.11)$$

## APPENDIX 3: INTERACTION POTENTIALS

The theoretical estimates obtained in this work are based on the following potentials.

The potential of interaction between two argon atoms, or the *AA potential*, has the Lennard–Jones form:

$$V_{AA} = \frac{A_{AA}}{R^{12}} - \frac{B_{AA}}{R^6}, \qquad (A3.1)$$

where $A_{AA} = 4\varepsilon\sigma^{12}$; $B_{AA} = 4\varepsilon\sigma^6$; $\varepsilon$ and $\sigma$ are the Lennard–Jones potential parameters defined in the standard manner. Presenting $R$ in the above equation in Å and choosing the values of $\sigma$ and $\varepsilon$ as recommended by Barker,[26] we obtain $A_{AA} = 1.164 \times 10^9$ K×Å$^{12}$; $B_{AA} = 7.47 \times 10^5$ K×Å$^6$.

We shall also use the potential proposed by Mirsky,[27] especially the AA potential

$$V_{AA} = C_{AA}\exp(-\alpha_{AA}R) - \frac{B_{AA}}{R^6}, \qquad (A3.2)$$

where $R$ is in Angströms, $B_{AA} = 7.88 \times 10^5$ K×Å$^6$; $C_{AA} = 3.93 \times 10^7$ K; and $\alpha_{AA} = 3.305$ Å$^{-1}$.

The potential of interaction of an Ar atom with a $CO_2$ molecule, i.e., the *AM potential*, consists of an isotropic and an anisotropic part:

$$V_{AM} = V_{AM}^{(iso)} + V_{AM}^{(anis)}. \qquad (A3.3)$$

It can be expected[12] that the main contribution to the excess mixing volume for low concentrations of $CO_2$ comes from the first term. Hence it must be evaluated with the highest degree of precision, taking into account the nonzero length of the molecule (see Appendix 2). For a ''long'' molecule like $CO_2$ such a renormalization turns out to be quite significant.

Using the atom–atom approach for valence- as well as dispersive contribution to the anisotropic part of the interaction, we can present $V_{AM}^{iso}$ in the final form

$$V_{AM}^{(iso)} = V_{val}^{(iso)} + V_{disp}^{(iso)}. \qquad (A3.4)$$

Using (A2.11), we can write

$$V_{disp}^{(iso)} = -\frac{B_{AC}}{R^6} - \frac{2B_{AO}}{R^6}\frac{1 + \xi^2}{(1 - \xi)^4}, \qquad (A3.5)$$

where $R$ is the separation between the center of a $CO_2$ molecule and an Ar atom.

The form of the valence contribution depends on the choice of the initial potential. For the form $R^{-12}$, we obtain (see (A2.9))

$$V_{val}^{(iso)} = \frac{2A_{AO}}{R^{-12}}\frac{(5 + 10\eta^2 + \eta^4)}{5(1 - \eta^2)^5} + \frac{A_{OC}}{R^{12}}, \qquad (A3.6)$$

where $A_{AO}$ and $A_{AC}$ are the constants of valence interaction between the corresponding atoms. If the valence contribution is exponential in form, we obtain

$$V_{val}^{(iso)} = C_{AC}\exp(-R\alpha_{AC})$$
$$+ \frac{2C_{AO}e^{-\rho}}{\rho^2}\left[(1 + \rho)\frac{\sinh\rho\xi}{\xi} - \rho\cosh\rho\xi\right], \qquad (A3.7)$$

where $C_{AC}$ and $C_{AO}$ are the constants of the corresponding atom–atom valence potentials, $\rho = R\alpha_{AO}, \alpha_{AC}$ and $\alpha_{AO}$ being the spatial parameters of these potentials.

The second term in (A3.3) determines, among other things, the energy levels of an isolated impurity $M$ in the matrix $AS$, i.e., the thermodynamics of the impurity subsystem as well.

The potential of interaction between $CO_2$ molecules, i.e., the *MM potential*, was chosen in the form proposed by Kohin[28] (see Ref 1 for details). The isotropic part also includes a contribution that is of valence origin and is averaged over rotations of both molecules.[28] The anisotropic part of

the interaction consists of the valence and dispersion contributions plus the direct electrostatic quadrupole–quadrupole interaction.

---

*E-mail: strzhemechny@ilt.kharkov.ua

[1)] The only exception is oxygen. Moreover, a large variety of phases with different positional and orientational structures was observed under high pressures when direct repulsion forces begin to play a significant role.[2]

[2)] An anisotropic interaction (AM) of nonmultipole type exists between an atom (spherical impurity) and a molecule. Henceforth, we shall disregard this interaction for two reasons. First, its intensity is much lower than for intermolecular (MM) anisotropic interaction. Second, this AM interaction does not contribute to the characteristic crystal field associated with the harmonic $P_{20}(\omega)$, where $\omega$ is the unit vector of the molecular axis orientation.

[3)] Alloys based on $O_2$ form a special case because of a strong additional contribution to the anisotropic interaction, i.e., the exchange interaction of electron spins.

[4)] We shall not consider the question of equilibrium of the transition itself. This problem has been discussed by Yantsevich *et al.*[14]

---

[1] V. G. Manzhelii, Yu. A. Freiman, M. L. Klein, and A. A. Maradudin (Eds.), *Physics of Cryocrystals* (Eds.), AIP Press, New York, 1996).

[2] Yu. A. Freiman, Fiz. Nizk. Temp. **16**, 955 (1990) [Sov. J. Low Temp. Phys. **16**, 559 (1990)].

[3] A. B. Harris and H. Meyer, Can. J. Phys. **63**, 3 (1985).

[4] V. T. Hochli, K. Knorr, and A. Loidl, Adv. Phys. **39**, 408 (1990).

[5] M. A. Strzhemechny, A. I. Prokhvatilov, and L. D. Yantsevich, Physica B **B198**, 267 (1994).

[6] S. I. Kovalenko and A. A. Solodovnik, Fiz. Nizk. Temp. **18**, 889(1992) [Sov. J. Low Temp. Phys. **18**, 626 (1992)].

[7] M. A. Strzhemechnǐ, S. I. Kovalenko and A. A. Solodovnik, Fiz. Nizk. Temp. **18**, 1387 (1992) [Sov. J. Low Temp. Phys. **18**, 967 (1992)].

[8] S. I. Kovalanko and A. A. Solodovnik, Fiz. Nizk. Temp. **19**, 336 (1993) [Low Temp. Phys. **19**, 238 (1993)].

[9] N. S. Sullivan, M. Devoret, B. P. Cowan, and C. Urbina, Phys. Rev. B **B12**, 5016 (1978).

[10] V. G. Manzhelii, M. I. Bagatskii, I. Ya. Minchina, and A. N. Aleksandrovskii, to be published in Proc. Cryocrystals'97, Wroclaw, Sept. 1997; J. Low Temp. Phys. **111**, 257 (1998).

[11] A. I. Prokhvatilov and L. D. Yantsevich, Fiz. Nizk. Temp. **12**, 882 (1986) [Sov. J. Low Temp. Phys. **12**, 502 (1986)].

[12] S. E. Kal'noǐ and M. A. Strzhemechnǐ, Fiz. Nizk. Temp. **14**, 514 (1988) [Sov. J. Low Temp. Phys. **14**, 283 (1988)].

[13] M. I. Bagatskǐ, V. G. Manzhelǐ, M.A . Ivanov, *et al.*, Fiz. Nizk. Temp. **18**, 1142 (1992) [Sov. J. Low Temp. Phys. **18**, 801 (1992)].

[14] L. D. Yantsevich, A. I. Prokhvatilov, I. N. Kurpskǐ, and A. S. Baryl'nik, Fiz. Nizk. Temp. **12**, 300 (1986) [Sov. J. Low Temp. Phys. **12**, 170 (1986)].

[15] H. Klee, H.O. Karmesin, and K. Knorr, Phys. Rev. Lett. **61**, 1855 (1988).

[16] V. G. Manzhelǐ, G. P. Chausov, and Yu. A. Freiman, Fiz. Tverd. Tela (Leningrad) **13**, 3441 (1971) [Sov. Phys. Solid State **13**, 2802 (1971)].

[17] E. Sándor and R. F. C. Farrow, Discuss. Faraday Soc. **48**, 78 (1969).

[18] M. A. Krivoglaz, *Theory of X-ray and Thermal Neutron Scattering by Real Crystals,* Plenum Press, NY (1969).

[19] D. A. Varshalovich, A. N. Moskalev and V. K. Khersonskǐ, *Quantum Theory of Angular Momentum* [in Russian], Nauka, Leningrad (1975).

[20] H. Kanzaki, J. Phys. Chem. Solids **2**, 27 (1957).

[21] A. P. Brodyanskǐ and M. A. Strzhemechnǐ, Fiz. Nizk. Temp. **16**, 367 (1990) [Sov. J. Low Temp. Phys. **16**, 203 (1990)].

[22] B. I. Verkin and A. F. Prikhot'ko (Eds.), Cryocrystals [in Russian], Naukova Dumka, Kiev (1983).

[23] A. A. Solodovnik and M. A. Strzhemechnǐ, Fiz. Nizk. Temp. (to be published).

[24] J. A. Hamida, S. Pilla, and N. S. Sullivan, to be published in Proc. Cryocrystals'97, Wroclaw, Sept. 1997; J. Low Temp. Phys. **111**, 365 (1998).

[25] M. A. Strzhemechnǐ, D. Sc. Thesis, Kharkov (1990).

[26] J. A. Barker, in Rare Gas Solids, Vol. 1. (Ed. by M. L. Klein and J. A. Venables), Academic Press, New York, (1976), p. 212.

[27] K. Mirsky, Chem. Phys. **60**, 445 (1980).

[28] B. Kohin, J. Chem. Phys. **33**, 882 (1960).

Translated by R. S. Wadhwa

## LATTICE DYNAMICS

# Low-temperature field reconstruction of atomic nanoclusters at tungsten surface

T. I. Mazilova

*National Sciences Center ''Kharkov Institute of Physics and Engineering,'' 310108 Kharkov, Ukraine*

Low-temperature field reconstruction of atomic clusters at a closely packed face of a metal is observed for the first time by the method of field ion microscopy. It is found that compact clusters disintegrate into non-closely packed zigzag atomic chains.  © *1998 American Institute of Physics.* [S1063-777X(98)01309-7]

Most of clean metal surfaces have an atomic structure corresponding to an ideal cross section of a three-dimensional lattice. The structure of such atomically clean surfaces does not differ from structures lower-lying atomic planes. However, some metals at elevated temperatures undergo a rearrangement of the first surface layer as a rule, which was called surface reconstruction.[1,2] Reconstructed surfaces are characterized by a modified lattice symmetry or the size of a unit cell (as compared to an ideal lattice). In strong electric fields inducing the dipole–dipole interaction of atoms, a special type of surface reconstruction associated with a virtually activationless displacement of atoms from the steps of closely packed faces to field-stabilized metastable positions is observed.[3,4] Combined thermal and field influence can lead to the disintegration of compact atomic clusters at closely packed faces of metals.[5] Detailed information on the reconstruction of configurations of atomic complexes in strong electric fields is required, for example, to ensure reliable interpretation of images of scanning tunnel microscopes and the reproducibility of maintenance parameters of nanotechnological devices developed on their basis.[6,7] Surface relaxation and reconstruction of the surface of macroscopic objects were studied in detail by the methods of slow electron diffraction.[1,2] However, there is virtually no information concerning these phenomena in surface atomic nanoclusters.

In this communication, we report on the observation of low-temperature field reconstruction of compact atomic nanoclusters at the (110) face of tungsten by using the field ion spectroscopy. The experiments were made in a two-chamber field ion microscope on samples cooled by liquid nitrogen. The sample temperature was monitored from the data on the temperature dependences of the threshold strength of evaporating field and the resolution of the microscope.[3] In electric field measurements, the reference point was the threshold strength of the evaporating field for tungsten taking into account anisotropy of field evaporation.[8] The residual gas pressure in the working chamber was $10^{-8}–10^{-6}$ Pa, and the pressure of the imaging gas (helium) was $10^{-3}–10^{-2}$ Pa. Needle-shaped samples oriented along the crystallographic direction [110] were prepared by electrochemical etching from grained tungsten wire with a purity 99.98%. After mounting in the microscope, the samples were subjected to field evaporation in an electric field of strength $(5.7–6.5)\times10^8$ V/cm until a perfect atomically smooth surface was formed. The radii of curvature of samples at the tip after the formation varied from 4.5 to
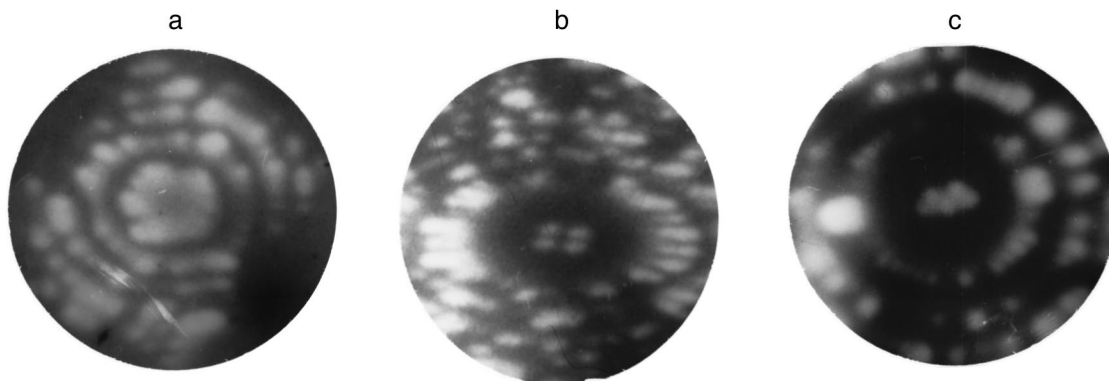


FIG. 1. Field ion microscopic images of a compact nanocluster (a) and non-closely packed atomic groups (b and c) formed during low-temperature field evaporation of the {110} face of tungsten.
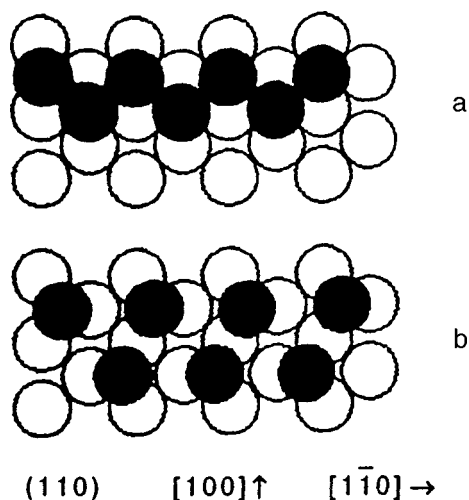
FIG. 2. Schematic diagram of arrangement of tungsten atoms on the {110} face in closely packed (a) and non-closely packed (b) zigzag chains.

50 nm. Evaporation was carried out at 78 K by applying a positive voltage of $1-25$ kV.

Circular atomic nanocomplexes (Fig. 1a) were formed in the course of controlled low-temperature field evaporation of the upper atomic layer (110). The configuration of the complex approximately corresponded to the circular trace left by the intersection of the crystallographic (110) plane with the hemisphere enveloping the surface. For needle-shaped samples with radii of curvature exceeding $12-15$ nm, circular configuration was preserved during field evaporation of complexes. For smaller radii of curvature, field evaporation from the steps of the upper (110) layer led to a jumpwise disintegration of a cluster and to the formation of non-closely packed atomic groups with various configurations (Figs. 1b and c). Evaporation of samples with the radii of curvature at the vertex smaller than $7-8$ nm was accompanied by the formation of zigzag chains (see Fig. 1c) similar to those observed earlier for thermal and field treatment of microscopic crystals.[5] An analysis of the change in the configuration of atomic chains in the course of low-temperature evaporation proved that links of the chains are formed by pairs of atoms separated by distances exceeding the atomic diameter $a/2$ [111]. The accuracy of direct measurements of the angles between adjacent links of the chains is comparatively low in view of partial overlapping of atomic images, and the error amounts to $10-15°$. The error of calculations of angles taking into account the width and length of zigzag chains and the number of atoms in them is smaller by a factor of $3-4$. According to calculations, the angles between pairs of atoms in ion-microscopic images change upon a decrease in the chain length during evaporation. The links of chains consisting of $9-10$ atoms are oriented along the $[1\bar{1}3]$ and $[\bar{1}13]$

directions to within the errors of measurements. In the course of evaporation of the chains, the angle between adjacent atoms increases continuously, attaining the value of $(60 \pm 5)°$. In strong electric fields, atoms can go over to a metastable position corresponding to the arrangement of the lower-lying layer {100} above the triple of atoms.[3] The recorded continuous change in the angles between adjacent atomic dumb-bells on ion-microscopic images cannot reflect the actual distribution of metastable positions of atoms on a closely packed face. An analysis of 100 microphotographs of atomic chains revealed that such a change in angles on ion-microscopic images is associated with nonuniformity of local magnification above a non-axisymmetric cluster. As the length of the chains decreases, the principal radii of curvature of the perturbed region on the effective electron surface level out, the anisotropy of magnification of the microscope above the non-axisymmetric cluster decreases,[9] and the angle between pairs of atoms on the images increases, approaching the actual angle between the links in the chains. Figure 2 shows the schematic diagram of the arrangement of atoms in the (110) face in the nearest lattice sites (a) and in the non-closely packed zigzag chain formed during low-temperature field reconstruction (b). While constructing the diagram in Fig. 2b, we assumed that surface atoms are in metastable surface states stabilized by the electric field. The driving force in the observed disintegration of nanoclusters is apparently dipole–dipole repulsion[4] of atoms in a nanocluster, which is induced by strong electric fields.

Thus, we discovered a special type of low-temperature field reconstruction, viz., disintegration of atomic nanoclusters at a closely packed face.

In conclusion, the author expresses her deep gratitude to A. S. Bakaĭ and I. M. Mikhaĭlovskiĭ for fruitful discussions.

[1] M. A. Vasil'ev, *Structure and Dynamics of the Surface of Transition Metals* [in Russian], Naukova Dumka, Kiev (1988).

[2] A. G. Naumovets, Fiz. Nizk. Temp. **20**, 1091 (1994) [Low Temp. Phys. **20**, 857 (1994)].

[3] E. W. Muller and T. T. Tsong, *Field Ion Microscopy*, American Elsevier Publ. Company, New York (1969).

[4] A. L. Suvorov, *Structure and Properties of Surface Layers of Metals* [in Russian], Energoatomizdat, Moscow (1989).

[5] S. Nishigaki and S. Nakamura, Jpn. J. Appl. Phys. **14**, 769 (1975).

[6] V. A. Ksenofontov, I. M. Mikhailovskij, V. M. Shulaev *et al.*, in *Physics, Chemistry, and Application of Nanostructures* (ed. by V. E. Borisenko *et al.*), Belarusian State University of Informatics and Radioelectronics, Minsk, 244 (1995).

[7] S. N. Magonov and M.-H. Whangbo, *Surface Analysis with STM and AFM*, Springer-Verlag, Berlin (1996).

[8] I. M. Mikhaĭlovskiĭ, V. A. Ksenofontov, and T. I. Mazilova, Pis'ma Zh. Éksp. Teor. Fiz. **65**, 521 (1997) [JETP Lett. **65**, 537 (1997)].

[9] I. M. Mikhaĭlovskiĭ and V. S. Geĭsherik, Radiotekhnika i Elektronika **19**, 1490 (1974).

Translated by R. S. Wadhwa

## BRIEF COMMUNICATIONS

# Renormalization of acoustic phonon spectrum and space distribution of the induced charge in a double-layer quantum Hall system

D. V. Fil

*Institute of Single Crystals, National Academy of Sciences of the Ukraine, 310001 Kharkov, Ukraine**

The frequency renormalization of acoustic phonons interacting with a double-layer composite fermion system is calculated. The space distribution of the density of the charge induced by an external electrostatic potential in a double-layer composite fermion system is determined. It is shown that for a filling factor for which states with the interlayer statistical interaction and without it can be realized, the emergence of such an interaction causes a jump in the phase velocity of a finite-frequency acoustic phonon and changes the space distribution of the charge induced by the external potential. These effects can be used for observing a transition in a double-layer electron system under the conditions of the fractional quantum Hall effect to a new ground state upon a decrease in the separation between the layers. © *1998 American Institute of Physics.* [S1063-777X(98)01409-1]

A double-layer electron system in a strong magnetic field is characterized by a hierarchy of noncompressible states with fractional filling factors, which differs from a monolayer hierarchy. The possibility of such states was predicted by Halperin[1] who proposed a new class of wave functions with are a generalization of the Laughlin function[2] to multicomponent systems. New states were detected experimentally by Suen *et al.*[3] and Eisenstein *et al.*[4] who observed the fractional quantum Hall effect with a filling factor $\nu = 1/2$.

Lopez and Fradkin[5] proposed a model for description of the fractional quantum Hall effect in a double-layer system, which is a generalization of the model of composite fermions developed earlier for monolayer systems.[6–8] The concept of composite fermions lies in that the ground state of the system described by the wave function[1,2] corresponds to the ground state of fermions interacting with the Chern–Simons gauge field. As a result of such an interaction, the external magnetic field is partially screened, and the fractional quantum Hall effect for electrons appears as the integral Hall effect for composite quasiparticles. In the case of a double-layer system, a composite fermion can be regarded as a quasiparticle carrying a statistical charge (each layer is characterized by its own type of charge), the flux of the gauge field $\varphi$ corresponding to the statistical charge in the same layer, and the flux of the gauge field $s$ corresponding to charges in the other layer. In particular, for $s = 0$ the interlayer statistical interaction is absent, and the ground state in each layer coincides with the ground state of the monolayer system. The Fermi statistics of composite quasiparticles imposes constraints on the magnitudes of the fluxes: the parameter $\varphi$ is even and $s$ is integral (even or odd) in the units of flux quanta.

In the case of two equivalent layers, the filling factors corresponding to Hall plateaus are defined as

$$\nu = 2\nu_i = \frac{2N}{N(\varphi + s) \pm 1}, \tag{1}$$

where $\nu_i$ is the filling factor per layer and $N$ the integer corresponding to the number of filled Landau levels in the effective field $B_{\rm eff} = B[1 - \nu(\varphi + s)/2]$. The upper (lower) sign in Eq. (1) and below corresponds to the parallel, $B_{\rm eff} > 0$ (antiparallel, $B_{\rm eff} < 0$) direction of effective field relative to the external magnetic field.

According to Eq. (1), different generalized Laughlin states corresponding to different states of parameters $\varphi$, $s$, and $N$ in the composite Fermi approach can exist for certain fixed filling factors. As the separation $d$ between the layers decreases, a phase transition from state with $s = 0$ (existing for $d \gg l_B$, where $l_B$ is the magnetic length) to a state with the statistical interaction between layers ($s \neq 0$) can occur.[9] For example, for $\nu = 4/7$, a transition from the state with $\varphi = 4$, $s = 0$, $N = 2$ to a state with $\varphi = 2$, $s = 1$, $N = 2$ can be expected.

The rearrangement of the ground state might be observed experimentally while studying collective properties of a double-layer system. Among other things, a change in the ground state can modify the spectrum of collective modes.[5] In this communication, we analyze the interaction of acoustic phonons with a double-layer system of composite fermions as well as the screening of external electrostatic potential by such a system. The above-mentioned effects applicable to monolayer systems were considered by us in Refs. 10 and 11. Here we prove that a transition of a double-layer system to a new ground state must be manifested in the change in the frequency of the phonon mode interacting with composite fermions and in a change in the space distribution of the charge induced by an external potential.

Let us consider a double-layer system of completely po-

larized composite fermions in an external magnetic field perpendicular to the layers. The Hamiltonian of the system has the form

$$H = \sum_{i=1}^{2} d^2 r \Psi_i^+(\mathbf{r}) \frac{1}{2m} [-i\nabla + e\mathbf{A}_{\text{eff}}(\mathbf{r}) - \mathbf{a}_i(\mathbf{r})]^2 \Psi_i(\mathbf{r})$$

$$+ \frac{1}{2} \sum_{i,j=1}^{2} \int d^2 r \int d^2 r' \, \delta n_i(\mathbf{r}) V_{ij}(|\mathbf{r} - \mathbf{r}'|) \delta n_j(\mathbf{r}'),$$
(2)

where $\Psi$ is the fermion field, $m$ the quasiparticle mass, $\mathbf{A}_{\text{eff}}$ the vector potential of the field $B_{\text{eff}}$,

$$V_{ij}(r) = \frac{e^2}{\varepsilon} [\delta_{ij} r^{-1} + (1 - \delta_{ij})(r^2 + d^2)^{-1/2}]$$
(3)

the Coulomb potential, $\varepsilon$ the dielectric permittivity,

$$\mathbf{a}_i(\mathbf{r}) = \sum_{j=1}^{2} \int d^2 r' [\varphi \delta_{ij} + s(1 - \delta_{ij})]$$

$$\times \delta n_j(\mathbf{r}') \frac{\hat{\mathbf{z}} \times (\mathbf{r} - \mathbf{r}')}{|\mathbf{r} - \mathbf{r}'|^2}$$
(4)

the sum of vector potentials of gauge field fluctuations, $\hat{\mathbf{z}}$ the unit vector along the field $B$, $\delta n_i(\mathbf{r}) = \Psi_i^+(\mathbf{r}) \Psi_i(\mathbf{r}) - n_0$; $n_0$ being the average concentration of electrons in the layer.

The polarization tensor of system (2) in the random-phase approximation is defined as

$$\hat{K}^{-1}(q, \omega) = [\hat{K}^{(0)}(q, \omega)]^{-1} - \hat{V}(q),$$
(5)

where $\hat{K}^{(0)}(q, \omega)$ is the polarization tensor in the zeroth approximation and $\hat{V}(q)$ the interaction matrix. In Eq. (5), the quantities $K$, $K^{(0)}$, and $V$ are $4 \times 4$ matrices whose each component has two indices corresponding to the numbers of the layers, the other two indices corresponding to the zeroth and transverse current components. The matrix $K^{(0)}$ has the block-diagonal form

$$K^{(0)}_{\mu\nu ij}(q, \omega) = \delta_{ij} \left[ D^{(0)}_{\mu\nu}(q, \omega) + \frac{n_0}{m} \delta^{\mu\nu}(1 - \delta^{\mu 0}) \right],$$
(6)

where $D^{(0)}_{\mu\nu}(q, \omega)$ is the Fourier component of the temporally ordered current–current correlator in the zeroth approximation:

$$D^{(0)}_{\mu\nu}(r, t; r', t') = -i \langle T\{j_{i\mu}(r, t) j_{i\nu}(r', t')\} \rangle_0.$$
(7)

The calculation of $K^{(0)}$ at $T = 0$ gives

$$K^{(0)}_{\mu\nu ij}(q, \omega) = \delta_{ij} \frac{1}{2\pi\omega_c} \begin{pmatrix} q^2 \Sigma_0 & \mp iq\omega_c \Sigma_1 \\ \pm iq\omega_c \Sigma_1 & \omega_c^2 (\Sigma_2 + N) \end{pmatrix},$$
(8)

where $\omega_c = e|B_{\text{eff}}|/m = 2\pi n_0/mN$ is the effective cyclotron frequency, and

$$\Sigma_k = e^{-x} \sum_{n=0}^{N-1} \sum_{m=N}^{\infty} \frac{n!}{m!} \frac{x^{m-n-1}(m-n)}{(\omega/\omega_c)^2 - (m-n)^2} [L_n^{m-n}(x)]^{2-k}$$

$$\times \left[ (m-n-x)L_n^{m-n}(x) + 2x \frac{dL_n^{m-n}(x)}{dx} \right]^k,$$
(9)

where $x = (ql_{\text{eff}})^2/2$, $l_{\text{eff}} = (e|B_{\text{eff}}|)^{-1/2}$ is the effective magnetic length, and $L_n^{m-n}(x)$ is the generalized Laguerre polynomial. Expressions similar to (8) and (9) were obtained for the first time for anyon systems (see, for example, Ref. 12).

The interaction matrix has the form

$$V = \begin{pmatrix} V_{11} & V_{12} \\ V_{21} & V_{22} \end{pmatrix},$$
(10)

where

$$V_{11} = V_{22} = \frac{2\pi}{q} \begin{pmatrix} e^2 \varepsilon^{-1} & -i\varphi \\ i\varphi & 0 \end{pmatrix},$$
(11)

$$V_{12} = V_{21} = \frac{2\pi}{q} \begin{pmatrix} e^2 \varepsilon^{-1} \exp(-qd) & -is \\ is & 0 \end{pmatrix}.$$
(12)

The solution of Eq. (5) for polarization density–density functions gives

$$K_{1100} = K_{2200} = \tfrac{1}{2} (K_{\text{in}} + K_{\text{out}}),$$
(13)

$$K_{1200} = K_{2100} = \tfrac{1}{2} (K_{\text{in}} - K_{\text{out}}),$$
(14)

where

$$K_{\text{in(out)}} = \frac{1}{2\pi\omega_c} \frac{q^2 \Sigma_0}{\Delta_{\text{in(out)}}},$$
(15)

$$\Delta_{\text{in(out)}} = (\varphi_{\text{in(out)}} \Sigma_1 \mp 1)^2 - \varphi_{\text{in(out)}}^2 \Sigma_0 (N + \Sigma_2) - V_{\text{in(out)}} \Sigma_0.$$
(16)

In the last equation (16), we have $\varphi_{\text{in}} = \varphi + s$, $\varphi_{\text{out}} = \varphi - s$, $V_{\text{in}} = (e^2 q/\varepsilon\omega_c)[1 + \exp(-qd)]$, $V_{\text{out}} = (e^2 q/\varepsilon\omega_c)[1 - \exp(-qd)]$.

Let us consider the renormalization of the spectrum for acoustic phonons interacting with a double-layer system of composite fermions. For $q \perp B$, Green's function for phonons satisfies the following equation:

$$G^{-1}(q, \omega) = [G^{(0)}(q, \omega)]^{-1} - g_i g_j K_{ij00}(q, \omega),$$
(17)

where $G^{(0)}(q, \omega)$ is Green's function for free phonons, $g_i = g_j = \Lambda q (2\rho d_l \omega_q)^{-1/2}$ the matrix element of interaction between phonons and composite fermions, $\Lambda$ the deformation potential, $\rho$ the density of the elastic medium, $d_l$ the thickness of the layer in which the phonon mode propagates,[1] and $\omega_q = cq$ the nonrenormalized phonon frequency. According to Eqs. (13)–(17), the renormalization of the phonon phase velocity for finite $q$ has the form

$$\frac{\Delta c(q)}{c} = \frac{\Lambda^2 q^2 \Sigma_0(q, \omega_q)}{2\pi\rho d_l c^2 \omega_c \Delta_{\text{in}}(q, \omega_q)}.$$
(18)

The dependence $\Delta c(q)/c$ for $\nu = 4/7$, $4/5$ is shown in Fig. 1 for $s = 0, 1$. We used the parameters $n_0 = 10^{11}$ cm$^{-2}$, $m = 0.25 m_e$, $\varepsilon = 12.6$, $c = 4 \times 10^5$ cm/s, $\Lambda = 7.4$ eV, $\rho = 5.3$ g/cm$^3$, $d = 3l_B$ and $d_l = 10^3$ Å. It can be seen from the curves in Fig. 1 that statistical interaction emerging between the layers changes qualitatively the dependence of the renormalization of the phase velocity of an acoustic phonon on $q$.
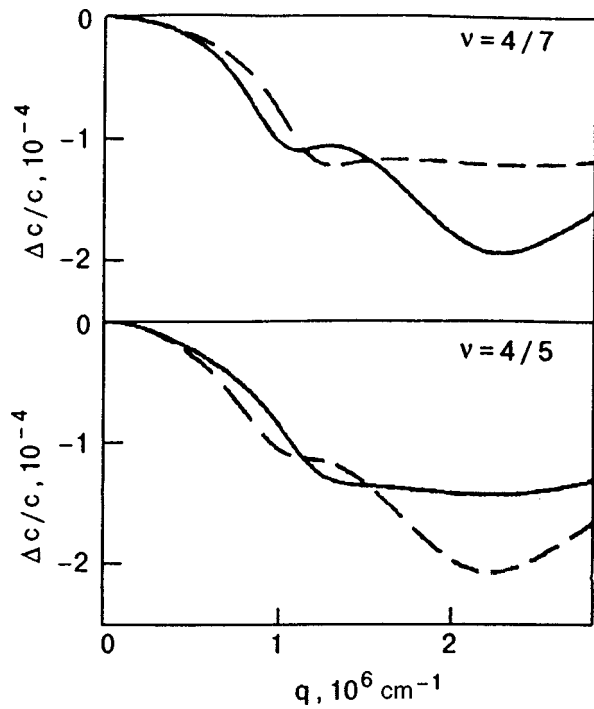
FIG. 1. Dependence of the renormalization of the phase velocity of an acoustic phonon on the wave vector. The solid curves correspond to a system with a statistical interaction between layers ($s=1$), while the dashed curves correspond to a system without a statistical interaction between layers ($s=0$).



FIG. 2. Spatial distribution of the induced charge in a double-layer system for $\nu=4/7$ (a) and 4/5 (b). The solid curves correspond to $s=1$ and the dashed curves to $s=0$, $\rho^{\mathrm{ind}}$ is in units of $n_0$.

For a given $q$, the phase velocity jump observed during the transition of the system to a new ground state can become comparable with the renormalization.

Let us now consider the screening of electrostatic potential in a double-layer system. To be more specific, we analyze the situation when a test charge of magnitude $-e$ and with coinciding $x$ and $y$ coordinates is located near each layer. In the random-phase approximation, the Fourier component of the density of the charge induced in the $i$th layer is defined by the equation

$$e\rho_i^{\mathrm{ind}}(q)=e^2 K_{ij00}(q,0)\varphi_j(q), \tag{19}$$

where $\varphi_i(q)=\varphi_j(q)=-(2\pi e/\varepsilon q)[1+\exp(-qd)]$ is the Fourier component of the external electrostatic potential created by test charges. Taking into account Eqs. (13)–(16), we obtain the following expression for $\rho_i^{\mathrm{ind}}(q)$:

$$\rho_i^{\mathrm{ind}}(q)=\frac{V_{\mathrm{in}}\Sigma_0(q,0)}{\Delta_{\mathrm{in}}(q,0)}. \tag{20}$$

The inverse Fourier transform for formula (20) gives the space distribution of the induced charge $\rho^{\mathrm{ind}}(r)$. The $\rho^{\mathrm{ind}}(r)$ curves for the filling factors $\nu=4/7$ and 4/5 for $s=0, 1$ are shown in Figs. 2a and 2b. In our calculations, we used the parameters of the electron system given above. The curves in Fig. 2 are analogs to Friedel oscillations in a system of composite fermions. It can be seen that the statistical interaction between the layers changes significantly the space distribution of the charge.

Thus, the renormalization of the acoustic phonon frequency for finite wave vectors and the space distribution of
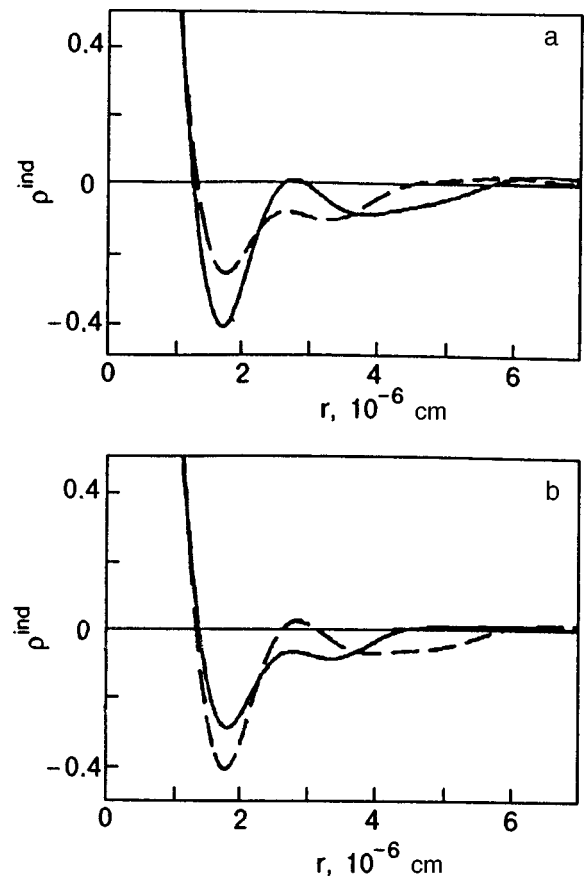
the charge induced in a double-layer system of composite fermions are modified significantly upon a transition of the system to a state with interlayer statistical interaction. The observation of the effect considered above can be used as an indicator of the formation of a new electron state of a double-layer Hall system upon a decrease in the separation between the layers.

[1)]In the case of a solitary double-layer system, the physical situation considered above can correspond to the propagation of a surface acoustic wave. In this case, the parameter $d_l$ is the attenuation length for the surface wave. The renormalization of the spectrum of bulk phonons can be observed in a superlattice of double quantum wells. In this case, $d_l$ is the superlattice parameter.

[1] B. I. Halperin, Helv. Phys. Acta **56**, 75 (1983).
[2] R. B. Laughlin, Phys. Rev. Lett. **50**, 1395 (1983).
[3] Y. W. Suen, L. W. Engel, M. B. Santos *et al.*, Phys. Rev. Lett. **68**, 1379 (1992).
[4] J. P. Eisenstein, G. S. Boebinger, L. N. Pfeiffer *et al.*, Phys. Rev. Lett. **68**, 1383 (1992).
[5] A. Lopez and E. Fradkin, Phys. Rev. B **51**, 4347 (1995).
[6] J. K. Jain, Phys. Rev. Lett. **63**, 199 (1989).
[7] A. Lopez and E. Fradkin, Phys. Rev. B **44**, 5246 (1991).
[8] B. I. Halperin, P. A. Lee, and N. Read, Phys. Rev. B **47**, 7312 (1993).

[9] D. Yoshioka, A. H. MacDonald, and S. M. Girvin, Phys. Rev. B **39**, 1932 (1989).

[10] A. L. Zazunov and D. V. Fil, Fiz. Nizk. Temp. **23**, 1345 (1997) [Low Temp. Phys. **23**, 1010 (1997).

[11] D. V. Fil, Functional Materials **5**, 14 (1998).

[12] Y. H. Chen, F. Wilczek, E. Witten, and B. I. Halperin, Int. J. Mod. Phys. B **3**, 1001 (1989).

Translated by R. S. Wadhwa

# Current-phase relation for a superconducting point contact with a tunneling barrier

G. A. Gogadze

*B. Verkin Institute for Low Temperature Physics and Engineering, National Academy of Sciences of the Ukraine, 310164 Kharkov, Ukraine\**
(Submitted April 10, 1998)

The microscopic theory of the dc Josephson effect for a short clean superconducting point contact with a tunnel barrier is developed. The influence of the ordinary quasiparticle scattering on the nondiagonal potential $\Delta$ of the superconductor is studied. It is shown that such processes may be significant in high-$T_c$ superconductors for the case of a barrier with high transmittance. The current-phase relation for a point contact at arbitrary temperatures is calculated. © *1998 American Institute of Physics.* [S1063-777X(98)01509-6]

The microscopic theory of the current states of clean superconducting point contacts was first constructed by Kulik and Omelyanchouk[1,2] They studied the model of a point contact in the form of a small orifice in an opaque screen through which electrons can penetrate ballistically from one superconducting bank to the other. It was shown that the Josephson current of the point contact is defined as

$$J = \frac{\pi \Delta(T)}{eR_N} \sin(\Phi/2) \tanh \frac{\Delta(T)\cos(\Phi/2)}{2k_B T},$$

$$-\pi < \Phi < \pi, \tag{1}$$

where $2\Delta$ is the band gap of the superconductor, $\Phi$ is the phase difference in the order parameter of the contacting superconductors, $R_N$ the point contact resistance in the normal state, $T$ the temperature and $k_B$ the Boltzmann constant. Near the superconducting transition temperature $T_c$, formula (1) has a form reminiscent of the result obtained by Ambegaokar and Baratoff[3] for a tunnel junction ($j \sim \sin \Phi$), but has a current dependence of the phase in the form $\sin(\Phi/2)$ at $T = 0$, the current suffering a discontinuity at the points $\Phi = \pm \pi$.

The results obtained in Refs. 1 and 2 were subsequently generalized by Haberkorn *et al.*[4] and Zaitsev[5] to the case of a point contact containing a tunnel barrier of arbitrary transparency $0 < D_0 < 1$:

$$J = \frac{\pi \Delta(T)}{2eR_N} \frac{\sin \Phi}{\sqrt{1 - D_0 \sin^2(\Phi/2)}}$$

$$\times \tanh \left[ \frac{\Delta(T)}{2k_B T} \sqrt{1 - D_0 \sin^2(\Phi/2)} \right], \tag{2}$$

where $R_N$ is the resistance of the point contact, $R_N^{-1} = e^2 k_F^2 S D_0 / (4\pi^2 \hbar)$, $k_F$ the Fermi wave vector and $S$ the contact area.

It can be seen that formula (2) tends to the classical expression obtained in Ref. 3 for $D_0 \ll 1$. Upon an increase in $D_0$ (as well as a decrease in $T$), the current-phase relation deviates from the $\sin \Phi$ dependence. In the limit of a clean contact ($D_0 \to 1$), formula (2) is transformed to formula (1).

Beenakker[6] derived formula (2) for the case of a superconductor-normal metal-superconductor (*SNS*) junction, when the normal interlayer can be described by an arbitrary disordered potential.

The current through a weak link is carried by quasiparticles which are transported coherently from one superconducting bank to the other. For a clean *SNS* junction, this was demonstrated for the first time by Kulik[7] who studied the quantum states of excitations with energy $E < \Delta$. It was shown that Andreev reflection of quasiparticles at *NS*-boundaries leads to the formation of coupled states (Andreev levels) in the normal interlayer,[8] their spectrum depending significantly on the phase difference $\Phi$ of order parameters at the contact banks. The superfluid current is transported through these Andreev levels, and the current states of the weak link are parametrized by the phase difference $\Phi$. It was stated[7,9] that Andreev quantization and Josephson tunneling in *SNS* junctions are closely related concepts. Later, it was established remarkably that Josephson current through a tunnel junction is also transported through coupled states localized in the vicinity of the tunnel barrier. Furusaki and Tsukada[10,11] showed that the passage of current through a tunnel junction leads to the formation of discrete levels in the band gap ($E < \Delta$). The emergence of coupled states is accompanied by the processes of conversion of Cooper pairs into quasiparticles (and vice versa) near the insulating barrier, so that the current is transported through the barrier by quasiparticles. Hence a comparison of formulas (1) and (2) leads to the following conclusion. Andreev reflection of quasiparticles is considered during calculation of the current through weak links in both cases. However, normal scattering of quasiparticles at the barrier during their passage through the contact is also taken into consideration while deriving formula (2). It was shown by Bagwell[12] that the introduction of an individual impurity into a weak link also suppresses the Josephson current.

In this communication, we report on the influence of a new mechanism of potential scattering of quasiparticles on the Josephson current through a clean point contact containing a tunnel barrier (Fig. 1). This phenomenon is associated with the normal scattering of excitations at the nondiagonal potential $\Delta$ leading to the scattering of a particle into a
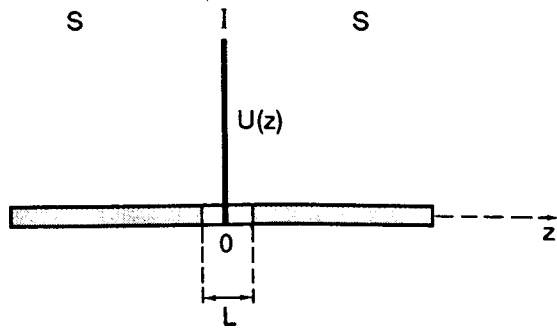
FIG. 1. Schematic diagram of a short point contact with a tunnel barrier.

''particle'' and a hole into a ''hole''. The probability of such processes can be calculated easily and is of the order of $(\Delta/\zeta)^2$ for energies $E<\Delta$ ($\zeta$ is the chemical potential of the metal). For conventional superconductors, this probability is so low that such processes are usually disregarded during calculations of quantum effects in weak links (the so-called Andreev approximation). However, it was shown in recent experiments[13,14] that the parameter $\eta_0 \equiv \Delta/\zeta$ for a number of high-$T_c$ superconductors (and may attain values of the order of 0.1). Hence such processes in these materials may be significant in the calculations of quantum effects. In a recent publication,[15] we derived a general dispersion equation describing the spectrum of quasiparticles in a *SINIS* structure taking into account the Andreev scattering as well as the normal scattering of quasiparticles at the interfaces between the media and at the potential $\Delta$.

In order to calculate the current, we must calculate the spectrum of quasiparticles in a point contact containing an insulating barrier. We assume that the transition is translationally invariant in the $(x,y)$ plane. The transverse size of a point contact is assumed to be small in comparison with the field penetration depth, and hence we can disregard the vector potential from the equations.[16] We proceed from the Bogoliubov-De Gennes equation[17]:

$$\hat{H}\Psi = E\Psi. \tag{3}$$

Here $\Psi = \binom{\psi}{\varphi}$ is the two-component wave function of quasiparticles, and $E$ its energy. If the $z$-axis is directed along the normal to the tunnel barrier and the nondiagonal potential $\Delta$ of the superconductor and the diagonal potential $U$ depend only on $z$, the matrix $\hat{H}$ describes the one-dimensional problem

$$\hat{H} = \begin{pmatrix} \hat{T} & \Delta \\ \Delta^* & -\hat{T} \end{pmatrix} \quad \text{where} \quad \hat{T} = -\frac{\hbar^2}{2m}\left(\frac{d^2}{dz^2} + \frac{2m\tilde{\zeta}}{\hbar^2}\right) + U(z);$$

$\tilde{\zeta} = \zeta - \mathbf{q}^2/2m$; $\mathbf{q}(q_x,q_y,0)$ is the component of quasimomentum parallel to the interface, and $m$ the electron mass.

For simplicity, we use a model with the $\delta$-functional potential $U(z) = W\delta(z)$, where $W$ characterizes the intensity of normal scattering of electrons at the barrier. The superconducting order parameter $\Delta(z)$ on both sides of the barrier is described in the form

$$\Delta(z) = \begin{cases} \Delta \exp(i\Phi_+), & z>0, \\ \Delta \exp(i\Phi_-), & z<0. \end{cases} \tag{4}$$

A point contact is assumed to be short if its length $L$ satisfies the conditions $a_0 \ll L \ll \xi_0$ (here $a_0$ is the lattice constant and $\xi_0$ the coherence length of the superconductor). The spectrum is calculated by using the model of abrupt variation of the magnitude of order parameter of an *SNS* junction, i.e., by disregarding the proximity effect. The efficiency of this model is the higher, the stronger the scattering of quasiparticles at the insulating barrier.

We are interested in the states of quasiparticles with energy $E<\Delta$. We shall solve the Bogoliubov-de Gennes equations by using the boundary conditions, i.e., the continuity of the two-component wave function at the point $z=0$ and the existence of a jump in this derivative at the same point. As a result, we arrive at a homogeneous system of four equations for determining the unknown coefficients for the amplitudes of wave functions in the media. We shall use the requirement of zero determinant of the system to find the dispersion equation for the quasiparticle spectrum of a point contact with a barrier. It is convenient to introduce the following quantities: $Z = mW/\sqrt{2m\tilde{\zeta}}$ (the dimensionless parameter $Z$ characterizes the intensity of the potential barrier; $Z=0$ in the absence of a barrier), and $\lambda = \sqrt{1+i\eta t}$, $t \equiv t(E) = \sqrt{1-E^2/\Delta^2}$ ($\lambda$ is the dimensionless quasimomentum in $\sqrt{2m\tilde{\zeta}}$ units). The parameter $\eta = \Delta/\tilde{\zeta}$ takes into account normal (potential) quasiparticle scattering at the nondiagonal potential $\Delta$ (the case $\eta = 0$ corresponds to the Andreev approximation). Using these parameters, we can write the dispersion equation in the form

$$2\gamma^2(|\lambda|^2+1)\cos\Phi - 2|\lambda|^2(1-\gamma^2) - 2\gamma^2$$
$$-(1-\gamma^2)^2[2Z^2 + Z\eta t] - 2|\lambda|^2\gamma^4$$
$$+ iZ(1-\gamma^2)^2(\lambda - \lambda^*) = 0. \tag{5}$$

Here

$$\gamma = \frac{\Delta}{E + i\sqrt{\Delta^2 - E^2}} \quad (E<\Delta);$$

$\Phi = \Phi_+ - \Phi_-$ is the phase difference for the order parameters of the banks of the contact. Assuming that $Z$ is arbitrary, we take into account in (5) only the second-order terms in $\eta$. In this case, Eq. (5) assumes the form

$$(1-\gamma^2)^2\left[1 + \left(\frac{\eta t}{2}\right)^2 + \left(Z + \frac{\eta t}{2}\right)^2\right] + 4\gamma^2\left[1 + \left(\frac{\eta t}{2}\right)^2\right]$$
$$\times \sin^2\frac{\Phi}{2} = 0. \tag{6}$$

Let us suppose that $Z=0$; in the absence of an insulating barrier, ordinary scattering at a nondiagonal potential $\Delta$ gives a correction of the order of $\eta^2$ to the quasiparticle spectrum of a short point contact. Beyond the Andreev approximation, this gives the following expression for energy levels ($\alpha = \arccos E/\Delta$):

$$\cos\alpha = \frac{E^\pm}{\Delta} = \pm\sqrt{\cos^2(\Phi/2) + (\eta^2/4)\sin^4(\Phi/2)}, \tag{7}$$

which coincides with the result obtained by Hurd and Wendin.[18] For traditional superconductors, the parameter

$\eta \sim 10^{-3} - 10^{-4}$, and this correction to the spectrum can be neglected.

It is interesting to consider a point contact made of a HTSC material for which the insulating barrier has a high transparency:

$$1 \sim Z \gg \eta t/2. \tag{8}$$

We can now retain in Eq. (6) only first-order terms in $\eta$. Then the expression for the spectrum has the form

$$E^{\pm}(\Phi; \mathbf{q}) = \pm \Delta \{1 - D \sin^2(\Phi/2)$$
$$\times [1 - \eta D \sqrt{1 - D} \sin(\Phi/2)]\}^{1/2}. \tag{9}$$

We have introduced the notation $D = 1/(1 + Z^2)$ for the transparency of the potential barrier. Spectrum (9) satisfied the condition $dE/d\Phi|_{\Phi = \pi} = 0$.[10–12] Both functions $D = D(\mathbf{q})$ and $\eta = \eta(\mathbf{q})$ depend on $\mathbf{q}$. It can be seen that when perturbation (ordinary scattering of quasiparticles at the barrier and at the potential $\Delta$) is taken into consideration, the spectrum of Andreev levels acquires an energy gap, which suppresses the Josephson critical current of the point contact. For $\Phi = \pi$, the gap is

$$E'_g = 2\Delta \sqrt{1 - D[1 - \eta D(1 - D)^{1/2}]}$$
$$\approx 2\Delta \sqrt{1 - D} + \Delta \eta D^2.$$

In the Andreev approximation ($\eta = 0$) for a point contact with a barrier, the gap is $2\Delta\sqrt{1-D}$,[12] while for a clean barrierless point contact ($D = 1$) and a finite $\eta$, its value coincides with the result obtained by Hurd and Wendin.[18]

Generally speaking, the Josephson current contains contributions of discrete and continuous spectra of a weak link. However, while calculating the current through a short point contact, we can confine ourselves to the contribution from the discrete spectrum only.[6,10–12]

The current through discrete Andreev levels can be calculated by the formula[19]

$$J(\Phi) = \frac{2e}{\hbar} \sum_{\mathbf{q}} \left[ \frac{dE^+}{d\Phi} f(E^+) + \frac{dE^-}{d\Phi} f(E^-) \right], \tag{10}$$

where $f(E)$ is the Fermi function for quasiparticles. Considering that $E^+ = -E^-$ and $f(E^+) = 1 - f(E^-)$, substituting spectrum (9) into (10), and integrating with respect to $q$, we obtain the following expression for current:

$$J(\Phi) \approx \frac{\pi \Delta(T)}{2eR_N}$$

$$\times \frac{\sin \Phi [1 - 3/2 \eta D_0 \sqrt{1 - D_0} \sin(\Phi/2)]}{[1 - D_0 \sin^2(\Phi/2) + \eta_0 D_0^2 \sqrt{1 - D_0} \sin^3(\Phi/2)]^{1/2}}$$

$$\times \tanh \left[ \frac{\Delta(T)}{2k_B T} [1 - D_0 \sin^2(\Phi/2)$$

$$+ \eta_0 D_0^2 \sqrt{1 - D_0} \sin^3(\Phi/2)]^{1/2} \right]. \tag{11}$$

Here $D_0$ and $\eta_0 = \Delta/\zeta$ are the maximum values of the transparency coefficient and parameter $\eta$ (the maximum current through the barrier is connected with the value $\mathbf{q} = 0$).

Expression (11) is valid for superconductors with $\eta_0 \approx 0.1$ under the condition (8). It can be seen that the presence of ordinary scattering of quasiparticles at potential $\Delta$ reduces the Josephson current.

It is interesting to note that the first-order correction in $\eta$ to current vanishes in the following two limiting cases: (1) the barrier transparency $D_0 \to 0 (Z \to \infty)$, and (2) $D_0 \to 1 (Z \to 0)$. In these cases, the corrections to the current have a higher order of smallness. For a tunnel junction ($Z \gg 1$), this is associated with a suppression of coherence at the contact banks. For a clean contact ($Z \to 0$), the processes of normal scattering of quasiparticles by the potential $\Delta$ make a contribution just of the order of $\eta^2$ to the current [see formula (7)]. Upon the application of a potential barrier, the intensity of particle-particle scattering processes increases. For a highly transmitting barrier ($Z \sim 1$), the contribution to the current is of the order of $\eta$, i.e., the decrease in current is stronger than for a clean barrierless point contact.

The experimental detection of an additional contribution to the contact current from the processes of particle-particle scattering by nondiagonal potential $\Delta$ is not a simple problem. The current passing through the contact must be measured to a high degree of precision. This imposes severe constraints on the quality of tunnel junctions in the point contact. In particular, the interfaces between media must be perfect to the atomic scale. Bozovic and Eckstein[20] have reported on the fabrication of a high-temperature *SIS* tunnel junction. The technology developed by them makes it possible to prepare tunnel junctions and multilayers with sharp interfaces on the atomic scale, thus demonstrating the high reproducibility of the experimental results. The technology of obtaining tunnel junctions with a mechanically adjustable gap (MAG) between metals[21] has its advantages for precise measurements of current and its comparison with the theory. Akimenko *et al.*[22] used the MAG technique to obtain $Bi_2Sr_2CaCu_2O_{8+\delta}$ single crystal junctions with clean and sharp cleavage surfaces (on the atomic scale) of quite large area. For a small gap between electrodes (tunnel regime), a microjunction with adjustable contact resistance can be realized.

*E-mail: gogadze@ilt.kharkov.ua

[1] I. O. Kulik and A. N. Omelyanchouk, Fiz. Nizk. Temp. **3**, 945 (1977) [Sov. J. Low Temp. Phys. **3**, 459 (1977)].
[2] I. O. Kulik and A. N. Omelyanchouk, Fiz. Nizk. Temp. **4**, 296 (1978) [Sov. J. Low Temp. Phys. **4**, 142 (1978)].
[3] V. Ambegaokar and A. Baratoff, Phys. Rev. Lett. **10**, 486 (1963); **11**, 104(E) (1963).
[4] W. Haberkorn, H. Knauer, and J. Richter, Phys. Status Solidi A **47**, K161 (1978).
[5] A. V. Zaitsev, Zh. Éksp. Teor. Fiz. **86**, 1742 (1984) [Sov. Phys. JETP **59**, 1015 (1984)].
[6] C. Beenakker, Phys. Rev. Lett. **67**, 3876 (1991).

[7] I. O. Kulik, Zh. Éksp. Teor. Fiz. **57**, 1745 (1969) [Sov. Phys. JETP **30**, 944 (1969)].

[8] A. F. Andreev, Zh. Éksp. Teor. Fiz. **46**, 1823 (1964) [Sov. Phys. JETP **19**, 1228 (1964)].

[9] I. O. Kulik, D.Sc. Thesis, Kharkov (1972).

[10] A. Furusaki and M. Tsukada, Physica B **165−166**, 967 (1990).

[11] A. Furusaki and M. Tsukada, Phys. Rev. B **43**, 10164 (1991).

[12] P. F. Bagwell, Phys. Rev. B **46**, 12573 (1992).

[13] J. R. Kirtley, Int. J. Mod. Phys. **4**, 201 (1990).

[14] K. Karrai, E. J. Choi, F. Dunmoro *et al.*, Phys. Rev. Lett. **69**, 152 (1992).

[15] G. A. Gogadze and A. M. Kosevich, Fiz. Nizk. Temp. **24**, 716 (1998) [Low Temp. Phys. **24**, 540 (1998)].

[16] K. K. Likharev, Rev. Mod. Phys. **51**, 101 (1979).

[17] P. G. de Gennes, *Superconducting of Metals and Alloys*, Benjamin, New York (1966).

[18] M. Horde and G. Wendin, Phys. Rev. B **49**, 15258 (1994).

[19] P. W. Anderson, in *Ravello Lectures on the Many-Body Problem*, Vol. 2 (Ed. by E. R. Gianello) Acad. Press, New York (1963).

[20] I. Bozovic and J. N. Eckstein, Appl. Surf. Sci. **113−114**, 189 (1997).

[21] C. J. Muller, J. M. van Ruitenbeek, and L. J. de Jongh, Phys. Rev. Lett. **69**, 140 (1992).

[22] A. I. Akimenko, T. Kita, J. Yamasaki, and V. A. Gudimenko, J. Low Temp. Phys. **107**, 511 (1997).

Translated by R. S. Wadhwa

## LETTERS TO THE EDITOR

# Spontaneous incommensurate crystal phase in the Jahn–Teller KDy(MoO$_4$)$_2$ crystal?

N. F. Kharchenko and Yu. N. Kharchenko

*B. Verkin Institute for Low Temperature Physics and Engineering,
National Academy of Sciences of the Ukraine, 310164 Kharkov, Ukraine*[*)]

R. Szymczak and M. Baran

*Institute of Physics, Polish Acad. Sci., 02-668 Warsaw, Poland*
(Submitted May 14, 1998)
Fiz. Nizk. Temp. **24**, 915–919 (September 1998)

Investigations of magnetic and spontaneous birefringence properties of a KDy(MoO$_4$)$_2$ crystal
under the Jahn–Teller phase transformation reveal some features indicating the existence
of two spontaneous phase transitions at temperatures close to 14.3 and 11.0 K. The characteristic
changes in birefringence in these transitions suggest that the crystal of KDy molybdate has
a modulated incommensurate lattice structure in the temperature range from 11.0 to 14.3 K.
© *1998 American Institute of Physics.* [S1063-777X(98)01609-0]

The KDy(MoO$_4$)$_2$ crystal (Fedorov symmetry group $D_{2h}^{14}(Pbcn)$),[1,2] which is orthorhombic at room temperatures, belongs to the family of layered crystal of double alkaline-earth molybdates. Many crystals of this family exhibit at low temperatures spontaneous instability associated with cooperative Jahn–Teller effect. A distinguishing feature of this effect in KDy(MoO$_4$)$_2$ is nonferrodistortion ordering of its Jahn–Teller distortions.[3–6] Paramagnetic compounds based on rare-earth Jahn–Teller ions are characterized by a high sensitivity of their crystal lattice structures to magnetic field at low temperatures.[7–9]

Leask et al.[5] discovered that a magnetic field in a paramagnetic KDy(MoO$_4$)$_2$ crystal oriented along a direction close to the direction of the axis with the maximum value of the $g$-factor of spectroscopic splitting for one half of Dy$^{3+}$ ions (and along the axis with the lowest value of the $g$-factor for the other half of these ions) leads to a structural phase transition similar to the metamagnetic transition in strongly anisotropic antiferromagnets. Optical and magnetic investigations of this transition revealed that the transformation from the low-field to the high-field crystal phase occurs not though a single phase transition, but through two phase transitions with the formation of an intermediate phase.[10,11] Extrapolation of temperature dependences of the two critical fields led to the conclusion that the intermediate crystal state must also exist in zero magnetic field.

This research aims at experimental verification of conclusions concerning the spontaneous formation of the intermediate crystal phase in a KDy(MoO$_4$)$_2$ crystal.

We analyzed the temperature dependences of spontaneous linear birefringence and magnetization. The magnetization was measured in magnetic fields of strength up to 10 kOe. The linear birefringence method is widely used for studying magnetic and structural phase transformations.[12,13] The application of the magnetic method was dictated by the

fact that the parameters and orientations of the principal axes of $g$-tensors of magnetic sites in Dy$^{3+}$ change significantly in the structural transformation under investigation.[4,14]

The experiments were made on samples having a size $\sim 4 \times 3 \times 0.2$ mm. The sample quality was tested by conventional optical–polarization methods. The samples contained plane-parallel regions with a size $\sim 0.5 \times 1$ mm in which the extinction of light was uniform. Birefringence was studied on spots of diameter $200 \mu$mm just in these regions. The direction of light propagation always coincided with the $c$-axis ($a = 5.07$ Å, $b = 7.95$ Å, $c = 18.23$ Å) perpendicular to the cleavage plane. The phase shift between normal optical modes emerging from the crystal was measured by using the modulation technique.[13]

For birefringence measurements at low temperatures, we used an optical cryostat without ''cold'' windows. The sample was in vacuum and was ''freely'' attached to the cold finger by using the technique described earlier.[10] The sample temperature was varied smoothly at a rate $\sim 0.25$ K/min. Temperature measurements were made with the help of a carbon resistance thermometer. The error in determining the temperature difference for the sample was of the order of 0.02 K, while the error in the measurement of the absolute value of sample temperature is estimated by us as 0.3 K.

The magnetic properties of the crystal were studied on a SQUID magnetometer MPMS-5. In order to avoid the emergence of mechanical stresses in the sample during cooling, which could affect the phase transition, the sample was placed in a special cell consisting of two quartz plates and three quartz supports whose thickness was close to the sample thickness. Quartz parts were glued together by an adhesive containing no magnetic impurities. The sample itself was not glued. The error in the sample orientation relative to the magnetic field direction did not exceed 2°.
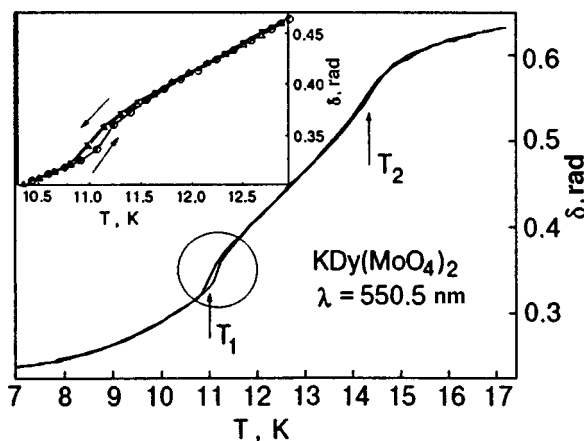
FIG. 1. Variation of phase shift between optical modes propagating in a KDy(MoO$_4$)$_2$ crystal at right angles to the cleavage plane during the structural phase transformation.
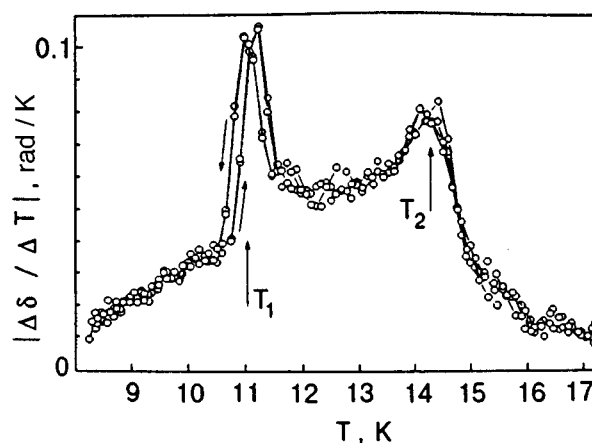


FIG. 2. Peculiarities in the behavior of the first derivative of birefringence of light with respect to temperature in the vicinity of temperatures $T_1$ and $T_2$.

First of all, we studied the extinction of light in the sample in the temperature interval covering the phase transition temperature. According to visual observations, extinction of light in crossed polarizers was complete and uniform over the entire field of sample image at all temperatures. Extinction of light in polarizers crossed at 45° was studied in quasi-monochromatic light. No changes in the pattern of extinction and its depth in the course of phase transformation of the crystal were observed. The invariability of extinction conditions indicates that the macroscopic symmetry of optical properties of the sample did not change as a result of the phase transformation. This property can be an evidence of the fact that if the point symmetry of the crystal is lowered as a result of the transition, the twins formed during the transition must have walls parallel to the plane of cleaved surface of the sample, and domains themselves must have a thickness smaller than the thickness which could be visually observed in polarized light at step edges of the sample.

Figure 1 shows the temperature dependences of the phase shift $\delta$ between the normal optical modes with the wavelength 550.5 nm in the temperature range of phase transformation. In order to illustrate high reproducibility of the experimental values, the dependences obtained in two cooling–heating cycles are presented. The change in the phase shift $\delta$ over the entire region of the structural transformation is $\sim 0.35$ rad. If we disregard the change in the crystal size, this value of $\delta$ corresponds to a change in birefringence by $\sim 1.2 \times 10^{-4}$.

The $\delta(T)$ dependences display two clearly manifested temperatures $T_1 = 11$ K and $T_2 = 14.3$ K at which singularities are observed: a jump (near $T_1$) and a kink ($T_2$). Different types of singularities are manifested more clearly on the temperature dependence of the derivative of birefringence with respect to temperature, which reflects to a certain extent the temperature variation of heat capacity in the vicinity of the phase transition.[12,13]

The temperature dependence of $\Delta\delta/\Delta T$ is shown in Fig. 2. The peculiar behavior of birefringence at $T_1$ and $T_2$ can be due to phase transitions in the crystal. It can be clearly seen from Fig. 1 that a temperature hysteresis loop of width

$\sim 0.1$ K takes place in the vicinity of 11 K. The hysteresis is slightly asymmetric: its branch corresponding to sample cooling is less steep than the branch corresponding to heating. The hysteresis loop has tails extending to the regions occupied by neighboring phases. The shape of the hysteresis loop depends on the temperature variation rate and the temperature of heating only slightly.

The observed singularities suggest that $T_1$ and $T_2$ are the temperatures corresponding to two phase transitions. Jumpwise changes in $\delta$ and the hysteresis loop indicate that the transition at $T_1$ is a first-order phase transition. However, this transition must be close to a second-order phase transition since the jump-wise variation of $\delta$ amounts to less than 20% of the entire change in $\delta$ (from the value near 11 K from the side of high temperatures to saturation which is almost attained at the lowest experimental temperature of 6.7 K.

The existence of a phase transition near 14.3 K follows from the temperature dependence of birefringence. The $\delta(T)$ dependence is close to linear in the temperature range from 11.5 to 13.5 K. A further increase in temperature leads to more rapid changes, after which the $\delta(T)$ dependence attains saturation. The absence of a hysteresis loop and the jump-wise change in the derivative $\Delta\delta/\Delta T$ near $T_2$ from the side of high temperatures suggest that the phase transition at $T_2$ is a second-order phase transition.

The temperature dependences of crystal magnetization, which were obtained for different samples with the magnetic field orientation along the crystallographic $b$-axis and at angles to the $c$-axis have clearly manifested singularities in the neighborhoods of the same temperatures $T_1$ and $T_2$. Figure 3 illustrates the temperature behavior of magnetization in a magnetic field oriented along the crystallographic axis $b$. For other field orientations, singularities can be observed in the coordinates $(M/H) \times T = f(T)$ and in the temperature dependences of the derivatives $\Delta[(M/H) \times T]/\Delta T = f'(T)$. The observed singularities indicate that the positions of O$^{2-}$ ions surrounding a Dy$^{3+}$ ion and determining the orientation of the axes of the $g$-tensor of spectroscopic splitting change in the temperature interval $T_1 < T < T_2$.

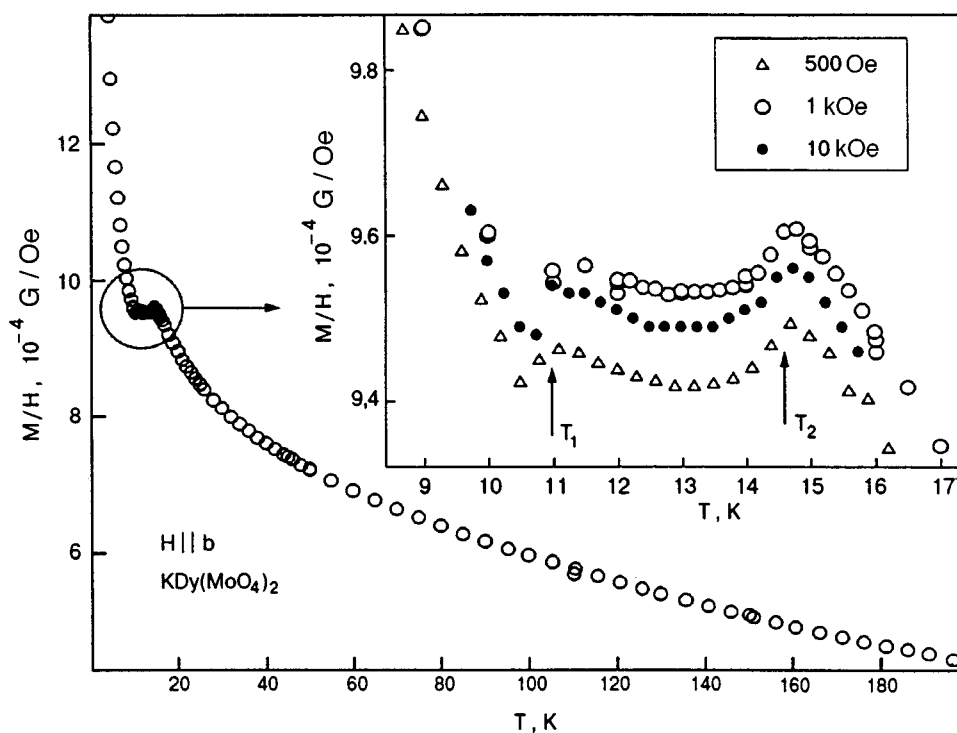The peculiarities in the temperature dependence of

FIG. 3. Behavior of magnetization of a $KDy(MoO_4)_2$ crystal in weak magnetic fields oriented parallel to the crystallographic axis $b$ ($b = 7.97$ Å) in the cleavage plane during the spontaneous structural phase transformation.

birefringence and magnetization considered above indicate that the phase transformation in $KDy(MoO_4)_2$ occurs through two phase transitions. The peculiar behavior of birefringence, i.e., the continuity in the transition at $T_2$, smooth and monotonic variation upon a decrease in temperature to $T_1$, the jump and the small characteristic hysteresis loop in the low- temperature transition at $T_1$, suggests that a modulated crystal structure is formed in the temperature interval $T_1 < T < T_2$. In this case, the phase transition at $T_2$ must be of the type of a transition between the normal and modulated structures, while the transition at $T_1$ is a lock-in transition for the modulation phase. The absence of step-wise changes in the interval from $T_1$ to $T_2$ and the hysteresis loop in the vicinity of $T_1$ indicate that higher modulation harmonics become significant only near $T_1$, where the pinning of incommensurabilities formed takes place. Such a temperature behavior of linear birefringence and heat capacity is normally observed during the normal–modulated–incommensurate phase transformation in many crystals.[15–19]

The absence of visible crystal domains at temperatures below $T_2$ has a simple explanation: the symmetry of linear crystallo-optical properties of the incommensurate phase is the same as for the high-temperature normal phase.[20]

The following remarks can be made regarding the structure of the modulated phase and the mechanism of its formation. The regularities in the displacement of the lowermost electron energy bands during phase transition, which were observed by spectroscopic methods, indicate the Jahn–Teller mechanism of this structural transformation.[3,4,6] The role of the soft mode in a transition to the modulated structure can be played by the hybrid mode formed by interacting Jahn–Teller vibronic oscillations of the ligand polyhedron surrounding a $Dy^{3+}$ ion, transverse and longitudinal phonon modes, and rotational oscillations of $(MoO_4)^{2-}$ complexes.

The modulation wave vector is determined by the dependence of the intensity of interaction between modes within the Brillouin zone on the direction and magnitude of the wave vector. We can expect that its direction is determined by the direction of coinciding wave vectors of optical and acoustic phonons with the lowest energies. According to Refs. 21 and 22, these oscillations propagate along the $c$-axis. Naturally, an unambiguous answer to the question whether the structure of $KDy(MoO_4)_2$ is modulated in this temperature range can be obtained only by direct methods based on diffraction of x-rays, neutrons and electrons and providing information on the wave vector of this structure.

*)E-mail: kharchenko@ilt.kharkov.ua

[1] R. F. Klevtsova and S. V. Borisov, Dokl. Akad. Nauk SSSR **177**, 1333 (1967) [Sov. Phys. Dokl. **12**, 1095 (1967)].
[2] I. Spitsyn and V. K. Trunov, Dokl. Akad. Nauk SSSR **185**, 854 (1969).
[3] A. I. Zvyagin, T. S. Stetsenko, V. G. Yurko, and R. A. Vaĭshnoras, Pis'ma Zh. Éksp. Teor. Fiz. **17**, 190 (1973) [JETP Lett. **17**, 135 (1973)].
[4] A. H. Cooke, M. M. Davidsen, N. J. England *et al.* J. Phys. C **9**, L573 (1976).
[5] M. J. Leask, A. C. Tropper, and M. R. Wells, J. Phys. C **14**, 3481 (1981).
[6] D. Michalovic, J. F. Ryan, and M. C. K. Wiltshire, J. Phys. C **20**, 3047 (1987).
[7] G. A. Gehring and K. A. Gehring, Rep. Prog. Phys. **38**, 1 (1975).
[8] M. D. Kaplan and G. O. Zimmermann, Phys. Rev. B **52**, 1 (1995).
[9] V. I. Kut'ko, M. I. Kobets, V. A. Pashchenko, and E. N. Khatsko, Fiz. Nizk. Temp. **21**, 441 (1995) [Low Temp. Phys. **21**, 345 (1995)].

[10] Yu. N. Kharchenko, Fiz. Nizk. Temp. **22**, 394 (1996) [Low Temp. Phys. **22**, 306 (1996)].

[11] N. Kharchenko, Yu. Kharchenko, R. Szymczak, and M. Baran, Czech. J. Phys. **46**, S4, 2141 (1996).

[12] G. A. Gehring, J. Phys. C **10**, 531 (1977).

[13] J. Ferre and G. A. Gehring, Rep. Prog. Phys. **47**, 513 (1984).

[14] V. A. Bagulya, A. I. Zvyagin, A. A. Stepanov, and A. S. Zaika, Fiz. Nizk. Temp. **14**, 493 (1988) [Sov. J. Low Temp. Phys. **14**, 270 (1988)].

[15] H. Z. Gummins, Phys. Rep. **185**, 211 (1990).

[16] S. V. Mel'nikova and A. T. Anistratov, Fiz. Tverd. Tela (Leningrad) **25**, 848 (1983) [Sov. Phys. Solid State **25**, 485 (1983)].

[17] A. V. Kityk and V. P. Suprunyuk, Ukr. Fiz. Zh. **38**, 147 (1993).

[18] I. Polovinko, S. Sveleba, V. Kapustianyk *et al.*, Ferroelectrics **153**, 327 (1994).

[19] D.-Y. Kim, Y. S. Cho, and S.-I. Kwun, J. Phys. Soc. Jpn. **65**, 3926 (1996).

[20] V. A. Golovko and A. P. Levanyuk, Zh. Éksp. Teor. Fiz. **77**, 1556 (1979) [Sov. Phys. JETP **50**, 780 (1979)].

[21] V. A. Bagulya, A. I. Zvyagin, V. I. Kut'ko *et al.* Fiz. Nizk. Temp. **14**, 1215 (1988) [Sov. J. Low Temp. Phys. **14**, 671 (1988)].

[22] V. I. Kut'ko, Fiz. Nizk. Temp. **24**, 383 (1998) [Low Temp. Phys. **24**, 291 (1998)].

Translated by R. S. Wadhwa